

AN ANALYSIS OF THE FINE STRUCTURE
OF LANGMUIR WAVE EMISSIONS

by

George Blair Hospodarsky

An Abstract

Of a thesis submitted in partial fulfillment
of the requirements for the Doctor of
Philosophy degree in Physics
in the Graduate College of
The University of Iowa

December 1994

Thesis supervisor: Professor Donald A. Gurnett

ABSTRACT

Highly structured Langmuir waves produced by energetic electrons streaming into the solar wind have been detected under a variety of conditions by the wideband plasma wave instrument on the Galileo spacecraft. These include Langmuir waves associated with Type III solar radio bursts, and Langmuir waves observed upstream of the bow shocks of Venus and Earth. These observations provide a rare opportunity to study Langmuir waves produced under widely different conditions with the same spacecraft. The Langmuir waves share many similar characteristics. The smallest scale structure corresponds to spatial scales of a only few tens of Debye lengths. The peak electric field strengths are approximately 1 to 10 mV/m, which are too small for a strong turbulence process to be important. The most striking similarity is the occurrence of many beat-type waveforms. The beat frequencies range from approximately 150 to 650 Hz for the waves observed in association with the Type III event, and from approximately 150 to 7000 Hz for the waves observed upstream of the bow shocks of Earth and Venus. The beat-type waveforms are strongly suggestive of parametric decay. In a parametric decay process, nonlinear interactions cause the beam-driven Langmuir wave to decay into a Langmuir wave and a low-frequency ion sound wave. Comparison of the observed beat frequency are in good agreement with theoretical predictions for a three-wave parametric decay process. Weak low-frequency emissions are also sometimes detected at the predicted frequency of the ion sound wave. At Earth and Venus large upshifts and downshifts in the Langmuir wave emission frequency are often observed. These shifts in frequency are correlated with the

downstream distance from the tangent field line, implying that the shifts in frequency are controlled by the electron beam velocity.

Abstract approved:


Thesis supervisor

Professor, Physics and Astronomy
Title and department

Dec 6, 94
Date

AN ANALYSIS OF THE FINE STRUCTURE
OF LANGMUIR WAVE EMISSIONS

by

George Blair Hospodarsky

A thesis submitted in partial fulfillment of the
requirements for the Doctor of
Philosophy degree in Physics
in the Graduate College of
The University of Iowa

December 1994

Thesis supervisor: Professor Donald A. Gurnett

Graduate College
The University of Iowa
Iowa City, Iowa

CERTIFICATE OF APPROVAL


PH.D. THESIS


This is to certify that the Ph.D. thesis of

George Blair Hospodarsky

has been approved by the Examining Committee
for the thesis requirement for the Doctor of
Philosophy degree in Physics at the December 1994
graduation.


Thesis committee:


Thesis supervisor


Member


Member


Member


Member

ACKNOWLEDGMENTS

I wish to express my sincere appreciation to Professor Don Gurnett for his valuable help and advice over the years of my graduate studies. He is always willing to answer questions and explain any concept, repeatedly if necessary. I would like to thank Dr. Kivelson, Dr. Khurana, Dr. Strangeway, and S. Joy for providing the Galileo magnetometer data and for calculating the depth parameter. I would also like to thank Dr. Williams and Dr. McEntire for providing the Galileo energetic electron data. IMP-8 and Pioneer Venus solar wind data was obtained from the National Space Science Data Center (NSSDC). Dr. Bill Kurth and Dr. Iver Cairns have contributed many useful suggestions during the course of this project.

Very special thanks to Kathy Kurth for typing the many revisions of this thesis. Without her help, I would still be pecking away at the computer. I would also like to thank Joyce Chrisinger for the many figures in the thesis, and for putting up with the far too many revisions. I would like thank Larry Granroth, Scott Allendorf, and Joe Groene for provided many of the computer programs that process and display the data, and also Janice Cook-Granroth for making many of the spectrograms used in this study.

I would like to thank my many friends for making graduate school enjoyable. Special thanks to Tami and Rick, Lee, Jim and Lucy (thanks for the house), Kevin (rocketman), Jerry, Bill and Robin, Lucy, Chris, Jim, Tak, Billy-Bob, Jay, Glen, Brent, Fred, and the many others who I have forgotten to mention. A special thanks to Karen whose encouragement has kept me going, and who made me realize that there is other thing in life besides physics. I am forever

grateful for the love, support and encouragement of my family, especially my mother Jean. Without the support from all of my family and friends, I would never have made it.

I would also like to thank Professor Paul Kleiber for showing me that I could do physics at a time I had my doubts, and lastly, I would like to thank Dr. Nicholson, Dr. Goertz, Dr. Smith, and Dr. Shan for the all to brief period that I knew them. You will never be forgotten.

This research has been supported by contract 958779 with the Jet Propulsion Laboratory and by an Iowa Space Grant Consortium Grant through NASA.

ABSTRACT

Highly structured Langmuir waves produced by energetic electrons streaming into the solar wind have been detected under a variety of conditions by the wideband plasma wave instrument on the Galileo spacecraft. These include Langmuir waves associated with Type III solar radio bursts, and Langmuir waves observed upstream of the bow shocks of Venus and Earth. These observations provide a rare opportunity to study Langmuir waves produced under widely different conditions with the same spacecraft. The Langmuir waves share many similar characteristics. The smallest scale structure corresponds to spatial scales of a only few tens of Debye lengths. The peak electric field strengths are approximately 1 to 10 mV/m, which are too small for a strong turbulence process to be important. The most striking similarity is the occurrence of many beat-type waveforms. The beat frequencies range from approximately 150 to 650 Hz for the waves observed in association with the Type III event, and from approximately 150 to 7000 Hz for the waves observed upstream of the bow shocks of Earth and Venus. The beat-type waveforms are strongly suggestive of parametric decay. In a parametric decay process, nonlinear interactions cause the beam-driven Langmuir wave to decay into a Langmuir wave and a low-frequency ion sound wave. Comparison of the observed beat frequency are in good agreement with theoretical predictions for a three-wave parametric decay process. Weak low-frequency emissions are also sometimes detected at the predicted frequency of the ion sound wave. At Earth and Venus large upshifts and downshifts in the Langmuir wave emission frequency are often observed. These shifts in frequency are correlated with the

downstream distance from the tangent field line, implying that the shifts in frequency are controlled by the electron beam velocity.

TABLE OF CONTENTS

	Page
LIST OF TABLES	viii
LIST OF FIGURES	ix
 CHAPTER	
I. INTRODUCTION	1
II. DESCRIPTION OF INSTRUMENT AND DATA	4
III. LANGMUIR WAVES ASSOCIATED WITH A TYPE III RADIO BURST ...	9
Description of the Type III Event Detected by Galileo	12
Electric Field Amplitudes	18
Fine Structure	18
Discussion	20
Soliton Collapse	22
Parametric Decay	26
IV. LANGMUIR WAVES UPSTREAM OF THE BOW SHOCK AT VENUS ...	34
Galileo Observations from the Venus Flyby	37
Electric Field Amplitudes	46
Fine Structure	47
Discussion	49
Soliton Collapse	50
Parametric Decay	50
V. LANGMUIR WAVES UPSTREAM OF THE BOW SHOCK AT EARTH ...	53
Galileo Observations at Earth	54
Data from the First Earth Flyby	54
Electric Field Amplitudes	63
Data from the Second Earth Flyby	65
Electric Field Amplitudes	72
Discussion	73
Soliton Collapse	75
Parametric Decay	77
VI. CONCLUSIONS	80

REFERENCES	213
------------------	-----

LIST OF TABLES

		Page
Table 1.	Wideband Waveform Receiver Modes	84
Table 2.	Energetic Particle Experiment	85
Table 3.	Characteristics of the Langmuir Wave Emissions: Type III	86
Table 4.	Plasma Parameters and Langmuir Wave Characteristics: Type III	87
Table 5.	IMP-8 Solar Wind Parameters: Type III	88
Table 6.	Characteristics of the Langmuir Wave Emissions: Venus	89
Table 7.	Plasma Parameters and Langmuir Wave Characteristics: Venus	90
Table 8.	IMP-8 Solar Wind Parameters: Earth 1	91
Table 9.	Plasma Parameters and Langmuir Wave Characteristics: Earth 1	92
Table 10.	Plasma Parameters and Langmuir Wave Characteristics: Earth 2	93
Table 11.	IMP-8 Solar Wind Parameters: Earth 2	94

LIST OF FIGURES

	Page
Figure 1. A block diagram of the Galileo plasma wave instrument. The main electronics package consists of three spectrum analyzers and a high-resolution wideband waveform receiver. An electric dipole antenna is used to detect electric fields and two search coil magnetometers are used to detect magnetic fields.	95
Figure 2. A diagram showing the scheme for sampling the spectrum analyzer receivers. The time required to obtain a complete spectrum from one antenna is 18.67 seconds. For most of this study, the low- and medium-frequency spectrum analyzers were cycled between the electric and magnetic antennas, providing alternating electric and magnetic spectrums. This cycling between the antennas results in a sampling period of 37.33 seconds between complete electric field spectrums. The high-frequency analyzer is always connected to the electric antenna.	97
Figure 3. Representative waveforms for the four modes of the wideband waveform receiver. Table 1 summarizes the characteristics of the four wideband waveform receiver modes used in this study.	99
Figure 4. A sketch of the two-step mechanism involved in the generation of a type III solar radio burst. First, the electron beam produces Langmuir waves near the plasma frequency f_{pe} by a beam-plasma instability. Second, the Langmuir waves are converted to electromagnetic radiation at both the fundamental f_{pe} and the harmonic $2f_{pe}$ by nonlinear processes. As the electron beam moves outward from the Sun, the Langmuir waves are produced at progressively lower frequencies due to the decrease in the density of the solar wind plasma with increasing distance from the Sun. The decrease in the plasma frequency with distance from the Sun produces the characteristic frequency-time spectrum in which the frequency decreases with increasing time.	101
Figure 5. A four-hour frequency-time spectrogram from the spectrum analyzer for this event. The onset of the type III burst was first detected at ~0743 UT in the high-frequency spectrum analyzer. The event shows an intense band of noise sweeping downward in frequency with increasing time, which is the characteristic signature of a type III solar radio burst. Several other weaker type III bursts can also be seen in the spectrogram at 0713 UT, 0720 UT, 0945 UT, and 0955 UT. The Langmuir waves are the narrowband emissions that can be seen at	

	about 24 kHz starting at ~ 0835 UT and continuing sporadically until ~ 1020 UT.	103
Figure 6.	Channel plots from the medium-frequency spectrum analyzer receiver and the energetic particle instrument. The top panel shows the electric field intensities from 45.6 to 49.5 kHz, which spans $2f_{pe}$. The middle panel shows the electric field intensities from 21.6 to 25.1 kHz, which spans the electron plasma frequency f_{pe} . The Langmuir waves are the spiky signal starting at about 0835 UT. The bottom panel shows the electron counting rate in three energy channels from the energetic particle experiment. The sharply peaked modulation in the counting rate with a period of about 3 minutes is produced by the azimuthal scanning of the detector and the spin of the spacecraft, and is indicative of a beamlike distribution of electrons streaming outward from the Sun along the solar wind magnetic field lines.	105
Figure 7.	A 150-minute frequency-time spectrogram from the wideband waveform receiver. The broadband signal from approximately 40 kHz to 80 kHz is the type III burst. The Langmuir waves are the intense, narrowband emissions first observed at approximately 0836 UT and 23 kHz. The sporadic narrowband emissions at approximately 46 to 50 kHz and 70 to 75 kHz are believed to be 2nd and 3rd harmonic distortion effects due to clipping in the receiver. The harmonics are easily seen from about 0936 UT to 0955 UT. The five intervals of "striped" spectrum (e.g., 0800:00 to 0804:20 UT) are periods when the wideband receiver is connected to the search coil magnetometers.	107
Figure 8.	A one-minute frequency-time spectrogram from the wideband receiver. The Langmuir waves are clearly visible at $f_{pe} \approx 25$ kHz. The intensity of the Langmuir waves shows extremely rapid temporal variations, down to the smallest time scale that can be resolved, which is the time between successive waveform blocks (66.67 ms). The Langmuir waves also show frequency spreading, sometimes by as much as 2 kHz. The frequency spreading is also highly variable, sometimes changing by a factor 5 or more between successive spectrums.	109
Figure 9.	A sampling of the Langmuir wave emission waveforms associated with the type III burst. The high-frequency, quasi-sinusoidal waveform evident in each panel is the Langmuir wave oscillation at $f \approx f_{pe}$, which is ~ 24 kHz during these intervals.	111
Figure 10.	A spectrum of the beat-type waveform in Figure 9c. The spectrum consists of two sharply defined peaks separated by about 400 Hz, which is the approximate beat frequency observed in the waveform. A low-frequency signal is also observed at ~ 400 Hz.	113

Figure 11.	An example of a "weak" waveform and its corresponding spectrum. This type of waveform contains no obvious Langmuir wave signal in the waveform (Panel b), but a signal is observed in the spectrum near the plasma frequency (Panel a).	115
Figure 12.	The number of waveform blocks as a function of peak electric field strength. The solid line gives the peak field strength for the waveforms measured directly (unclipped) or by extrapolation (moderately clipped). The dashed line gives the lower limit to the field strengths for severely clipped waveforms.	117
Figure 13.	The top panel is a high-resolution frequency-time spectrogram of the Langmuir waves. The bottom panel is the distribution of the field strengths shown in Figure 12 as a function of time.	119
Figure 14.	Examples of "constant over 8 ms" waveforms.	121
Figure 15.	The beat frequencies of the beat-type waveforms as a function of time. Although there is a great deal of scatter, a clear trend exists toward higher frequencies with increasing time. The solid line is the least-square linear fit to the data.	123
Figure 16.	The electron beam speeds determined by Equation 8 using the beat frequencies shown in Figure 15 and the corresponding value of θ determined from the Galileo magnetic field data (20-second averages). The predicted trend to smaller beam speeds with time is observed. The solid line is the theoretical beam speed calculated from $V_b = A/(t-t_0)$. . .	125
Figure 17.	A sketch of the electron foreshock region. Electrons streaming from the bow shock along the interplanetary magnetic field lines are convected downstream by the solar wind. The electrons originating from the tangent point with the highest energy define a region called the electron foreshock. The depth parameter D is defined as the distance along the solar wind flow from the tangent magnetic field line to the spacecraft. The depth parameter is positive for spacecraft locations downstream of the tangent field line, and negative for locations upstream. For a given depth parameter, only electrons with a velocity above a certain critical velocity can reach the spacecraft.	127
Figure 18.	A sketch of the electron and ion foreshock regions. Energetic ions also stream into the solar wind from the bow shock. Because the ions are slower than the electrons, the ion foreshock boundary is located downstream of the electron foreshock boundary. It should be noted that both ions and electron beams can be observed in the ion foreshock.	129

- Figure 19. A sketch of the frequency of maximum growth versus the ratio of the beam velocity to the thermal speed (V_b/V_e). For electron speeds on the order of the thermal speed ($0 < V_b/V_e < 2$), the predicted frequency of maximum growth is below the plasma frequency. For higher beam speeds ($V_b/V_e \sim 3$) the frequency of maximum growth is above the plasma frequency. For very large beam speeds ($V_b/V_e \gg 3$), the predicted frequency approaches the plasma frequency. 131
- Figure 20. A sketch of the trajectory of Galileo during the Venus gravity assist flyby. A model bow shock is included to provide an estimate of the location and shape of the bow shock. 133
- Figure 21. A frequency-time spectrogram of the electric and magnetic field intensities measured by the medium- and low-frequency spectrum analyzers. Four bow shock crossings and the plasma region the spacecraft was in are shown at the top of Figure 21. The Langmuir waves can be most easily seen after the last bow shock crossing, in the frequency band 10 to 50 kHz of the electric field spectrum. At least two types of oscillations can be seen, one consisting of a nearly steady line at a frequency of about 43 kHz, which is believed to be the electron plasma frequency f_{pe} and a second component that is shifted both downward and upward in frequency from f_{pe} 135
- Figure 22. A high-resolution frequency-time spectrum of the Langmuir waves. The Langmuir waves can be most easily seen as the bursty signals that start approximately 12 seconds into the spectrogram. The Langmuir waves show large upshifts and downshifts in frequency from the electron plasma frequency (~ 43 kHz). The upshifts and downshifts can be as large as 20 kHz. The Langmuir waves also show extremely rapid temporal variations, many with time scales smaller than the time between successive waveform blocks (66.67 ms). 137
- Figure 23. The top panel is a frequency-time spectrum of the low-resolution waveforms (Mode 3 data). The signals are composed of two components, a weak narrowband component near the plasma frequency, and a stronger, broader bandwidth component that shows large upshifts and downshifts in frequency. The middle panel shows the depth parameter (see Figure 17) as determined from the measured solar wind magnetic field and a model bow shock. The bottom panel is a plot of the maximum peak electric field amplitudes of the waveform blocks. 139
- Figure 24. A sampling of the Langmuir emissions electric field waveforms observed at Venus. The waveforms show considerable variations and are similar to the Langmuir waveforms observed in association with the type III burst (see Figure 9). 141

- Figure 25. A spectrum of the waveform from panel (d) of Figure 24. The spectrum consists of two distinct frequency components, one at ~ 45.5 kHz and the other at ~ 48.3 kHz. The frequency difference of these two signals agrees with the observed beat frequency (~ 2.8 kHz). 143
- Figure 26. The bottom panel is an example of a chaotic-type waveform with very little beat pattern. The top panel is the spectrum of the chaotic-type waveform shown in the bottom panel. The spectrum exhibits a narrowband signal at ~ 42.5 kHz (believed to be the plasma frequency), and a broader signal upshifted in frequency, centered at ~ 54 kHz. Chaotic-type waveforms are frequently observed at Venus during periods with large upshifts and downshifts in the Langmuir wave emission frequency. 145
- Figure 27. The number of waveform blocks as a function of the peak electric field strength. 147
- Figure 28. The spectrum of the waveform block from panel (b) of Figure 24. The spectrum contains two main peaks, one centered at ~ 46 kHz, which is near the plasma frequency, and another that is upshifted in frequency, and centered at ~ 53 kHz. Each of the two main signals is broad in frequency and contains a great deal of structure. There is also a series of weak signals located from a few hundred Hz to about 9 kHz. The low-frequency signals are suggestive of the low-frequency ion sound waves predicted by parametric decay. 149
- Figure 29. A sketch of the trajectory of Galileo during the two Earth gravity assist flybys. The model bow shock is included for reference only, and no attempt has been made to verify the correct distance and position of the bow shock. During the first Earth flyby (E1), Galileo exited the magnetosheath near the nose of the bow shock. During the second flyby (E2), Galileo exited the shock further downstream. The different trajectories allowed Galileo to obtain measurements in different parts of the foreshock. 151
- Figure 30. A frequency-time spectrogram from the spectrum analyzer receivers. The Langmuir waves can be seen immediately after the bow shock crossing (~ 2334 UT) at about 42 kHz in the medium frequency spectrum analyzer receiver (middle panel). Strong bursts of Langmuir waves can be seen at approximately 2258 UT, 0015 UT, 0025 UT, 0043 UT, and from 0118 to 0143 UT. The Langmuir waves show a great deal of structure, including large downshifts and upshifts in frequency, and are very broad

- in frequency. The narrowband signal at 40 kHz is an interference signal from the spacecraft, and not related to the Langmuir waves. 153
- Figure 31. A 24-hour frequency-time spectrogram from the spectrum analyzer receivers. The first two hours of this spectrogram corresponds to the last two hours of Figure 30. Two types of Langmuir wave emissions are observed. Bursty Langmuir waves can be seen in the first two hours of the spectrogram. At ~ 0330 UT, a second type of Langmuir wave emission appears. This second type of emission is observed almost continually for the next five hours, with sporadic emissions observed for the next seven hours. This emission is less intense than the bursty emission and the large scale structure of the emissions is found in a narrow range in frequency. 155
- Figure 32. A high-resolution frequency-time spectrogram from the wideband waveform receiver for the interval immediately after Galileo exited the bow shock. The Langmuir waves are the bursty signals that start at ~ 2235 UT in the frequency range 40 kHz to 55 kHz. The structure of the Langmuir waves includes large upshifts and downshifts from the electron plasma frequency (estimated to be ~ 41 kHz at 2235 UT, decreasing to ~ 35 kHz at the end of the spectrum). The spectrum of the upshifted and downshifted Langmuir waves also exhibit large broadening in frequency, sometimes as much as 30 kHz. The signals between 60 and 100 kHz at two and three times the emission frequency of the intense Langmuir waves are most likely harmonic distortion due to clipping of the waveforms. 157
- Figure 33. The top panel is a high-resolution frequency-time spectrum of the Langmuir waves from Figure 32. The bottom panel shows the depth parameter as determined by the Galileo magnetometer experiment. A correlation exists between the depth parameter and the shifts in the frequency of the Langmuir waves. 159
- Figure 34. A high-resolution frequency-time spectrogram from the wideband waveform receiver. The Langmuir wave emissions during this interval are more constant and narrowbanded in frequency than the emissions shown in Figure 32. The signals at two and three times the frequency of the main emission (0530 UT at ~ 42 kHz and ~ 64 kHz) are most likely instrumental effects caused by clipping in the receiver. The white strips (for example 0453 to 0508 UT) are intervals where no wideband data are available. Six intervals of magnetic field wideband data are also shown. 161
- Figure 35. A one-minute frequency-time spectrogram from the wideband waveform receiver of an interval with large downshifts in frequency. The spectrum consists of sporadic narrowband emissions near the plasma frequency (~ 39 kHz), and broadband upshifted and downshifted emissions. A

- large band of downshifted Langmuir waves is observed starting ~ 18 seconds into the spectrum, in the frequency range 10 kHz to 25 kHz. Upshifted emissions can be observed from about 28 to 35 seconds into the spectrum. 163
- Figure 36. A one-minute frequency-time spectrogram from the wideband waveform receiver. An intense signal is observed at 32 kHz, with a weaker, more sporadic signal at about 37 kHz. Approximately 23 seconds into the spectrogram, the two signals appear to shift up in frequency very rapidly. The abrupt shift is probably caused by a rapid increase in the electron plasma density. After this shift in emission frequency, the more intense band is located at ~ 37 kHz, and the upper band at ~ 45 kHz. The spiky emissions at approximately two times the main emission bands are probably instrument effects, produced when the Langmuir wave signals are strong enough to clip the waveform receiver. The weak emission line at ~ 75 kHz may be electromagnetic radiation at $2f_{pe}$ 165
- Figure 37. A one-minute frequency-time spectrogram from the wideband waveform receiver for the interval that follows Figure 36. The two bands of emission continues for the first 14 seconds of the spectrogram. Approximately 14 seconds into the spectrogram, the intensity of the Langmuir wave emission decreases. The weak emission bands at ~ 37 kHz and ~ 74 kHz may be electromagnetic radiation produced in the electron foreshock at f_{pe} and $2f_{pe}$ which is propagating into the solar wind. Approximately 27 seconds into the spectrogram, the intensity of the Langmuir waves increase greatly. The narrowband, very intense emission is characteristic of Langmuir waves near the foreshock boundary. 167
- Figure 38. A one-minute frequency-time spectrogram from the wideband waveform receiver from the beginning of Figure 34. The ~ 10 -second period of decreasing emission intensity is probably due to the spacecraft rotation (the spin period of Galileo is ~ 20 seconds). 169
- Figure 39. The top panel is a frequency-time spectrogram of the interval of abrupt shift in frequency shown in Figure 36. The middle four panels show the magnetic field components and the total magnetic field. The bottom panel is the depth parameter calculated by the magnetometer experiment. The downward shift in frequency of the Langmuir waves at $\sim 0008:30$ UT is correlated to the increase in the B_Z component and in the total magnetic field B_T . The increase in the Langmuir wave frequency at ~ 0011 UT corresponds to the decrease in the B_Z component and in the total magnetic field B_T 171
- Figure 40. A sampling of the Langmuir wave emission waveforms obtained during the first Earth flyby. The waveforms are very similar to the waveforms

- observed at Venus and in association with the type III burst. The high-frequency, quasi-sinusoidal waveforms evident in each of these plots are the Langmuir wave oscillations. 173
- Figure 41. An example of a beat-type waveform (bottom panel) and its spectrum (top panel). Two distinct frequency components are observed, one at ~ 37 kHz and the other at ~ 42 kHz. A weak low-frequency signal is also observed at ~ 5 kHz. The frequency difference of these two signals, and the frequency of the low-frequency signal, agrees with the beat frequency (~ 5 kHz) of the waveform. 175
- Figure 42. An example of the spectrum (top panel) of a lower frequency beat-type waveform (bottom panel). Two distinct frequency components are observed, one at ~ 37.1 kHz and the other at ~ 38.1 kHz. A weak low-frequency signal is also observed at ~ 1 kHz. The frequency difference of these two signals, and the frequency of the low-frequency signal, agrees with the beat frequency (~ 1 kHz) of the waveform. 177
- Figure 43. An example of a chaotic-type waveform (bottom panel) and its spectrum (top panel). A weak high-frequency beat pattern can be seen in the waveform. The spectrum consists of two broad signals centered at 21.5 and 27.5 kHz. The chaotic-type waveforms observed at the Earth are similar to the chaotic-type waveforms observed at Venus (Figures 24b and 26) and are common during periods of large upshifts or downshifts in the emission frequency of the Langmuir waves. 179
- Figure 44. The number of waveform blocks as a function of peak electric field strength. The solid line gives the peak field strength for the waveforms measured directly (unclipped) or by extrapolation (moderately clipped). The dashed line gives the lower limit to the field strengths for severely clipped waveforms. 181
- Figure 45. The top panel is a high-resolution frequency-time spectrum of the Langmuir waves. The middle panel is a plot of the depth parameter. The bottom panel is a plot of the maximum peak electric field amplitudes of the waveform blocks. The largest amplitudes tend to occur during intervals of small depth parameters (for example 2235, 2258, 2328, 0013, and 0025 UT). These intervals corresponds to times when the spacecraft is near the upstream foreshock boundary. 183
- Figure 46. A 4-hour frequency-time spectrogram of the electric field intensities obtained from the spectrum analyzer receivers as Galileo exited the bow shock during the second Earth flyby. Galileo was in the magnetosheath from approximately 1706 to 1813 UT (characterized by the low-frequency broadband noise observed during this time period). The Langmuir waves can be seen immediately after Galileo exited the bow shock at about 1813 UT in the middle panel

(medium-frequency spectrum analyzer). The Langmuir waves range in frequency from approximately 10 to 26 kHz, and show a great deal of structure. Broadband low-frequency signals (5 Hz to about 200 Hz) are also observed in the bottom panel (low-frequency spectrum analyzer) during the intervals of Langmuir wave activity. The low-frequency signal is believed to be related to ion beams in the foreshock region. 185

Figure 47. A high-resolution frequency-time spectrogram from the wideband waveform receiver. The bursty nature and the large spreading in frequency of the Langmuir waves can be easily seen in the first hour of the spectrogram. The sporadic signals from approximately 30 to 70 kHz during the first hour of the spectrogram are believed to be instrument distortion due to clipping in the receiver. An intense narrowband Langmuir wave emission is observed at approximately 1945 UT. This interval contains the largest Langmuir wave electric field strengths observed by Galileo. Most of the signals at $2f_{pe}$ (~ 37 kHz) and $3f_{pe}$ (~ 55 kHz) during this interval is due to clipping in the receiver. 187

Figure 48. An expanded high-resolution frequency-time spectrogram from the wideband waveform receiver from near the beginning of Figure 47. Note the frequency axis ranges from 2 to 52 kHz. The structure of the Langmuir waves is very complex, and shows a large range in emission frequency (~ 2 kHz to ~ 30 kHz). The frequency of the Langmuir wave emissions often appears to be modulated by a low-frequency wave with a period of ~ 15 seconds. This apparent modulation can be seen from about 1820 to 1821:30 UT. 189

Figure 49. A high-resolution frequency-time spectrogram from the wideband waveform receiver from the interval shown in Figure 48. Note the frequency axis now runs from 0 to 40 kHz. The Langmuir waves appear to consist of at least two types of emissions, a narrowband emission and a broader emission downshifted and upshifted in frequency from the narrowband emission. Both types of emissions ramp up and down in frequency with a period on the order of 16 seconds. This modulation is most easily seen in the first 30 seconds of the spectrogram. The emissions appear to peak in frequency at approximately 3, 19, and 35 seconds. This type of spectrum is suggestive of the Langmuir waves "mapping out" low-frequency density fluctuations. A possible source of density fluctuations is propagating MHD waves (magnetosonic mode) generated by the ion beams present in the ion foreshock. 191

Figure 50. The 20-second magnetic field GSE averages of the three components of the magnetic field (top three panels) and the total magnetic field (bottom panel) for the interval immediately after Galileo exited the bow shock. The magnetic field contains a great deal of structure

- suggestive of MHD waves during the interval of chaotic Langmuir wave emission (approximately 1813 to 1930 UT). 193
- Figure 51. A high-resolution frequency-time spectrogram from the wideband waveform receiver corresponding to the interval of intense Langmuir waves shown in Figure 47 at approximately 1945 UT. The intense narrowband emission is characteristic of Langmuir waves near the electron foreshock boundary. Most of the signals occurring at multiples of the Langmuir wave emission frequency ($f_{pe} \sim 19$ kHz) are caused by clipping in the waveform receiver. The weak emissions observed at twice the main emission frequency, with no corresponding emission at three times the main emission frequency, for example the weak signal from about 27 to 32 seconds into the plot at ~ 38 kHz, are probably electromagnetic $2f_{pe}$ emissions produced by nonlinear processes. 195
- Figure 52. An expanded plot of the GSE magnetic field components and total field for the interval spanning Figure 51. The vertical line at 1945 UT shows the approximate time the Langmuir wave emissions begin in Figure 51. As can be seen, there is a decrease in the B_x and B_T magnetic fields, and the B_y magnetic component reverses direction. A similar decrease in B_x and B_T at $\sim 1951:30$ UT corresponds to the start time of the second short burst of Langmuir waves observed in Figure 47. Unfortunately, depth parameter values are not available to determine the exact position in the foreshock of Galileo during the second Earth flyby. 197
- Figure 53. A high-resolution frequency-time spectrogram of the Mode 4 data. The Langmuir waves range in frequency from approximately 3 kHz to > 25 kHz. The emissions are very spiky, with extremely rapid temporal variations down to the smallest timescale that can be resolved, which is the time between successive waveform blocks (8.33 ms). The Langmuir waves also show large frequency spreading, sometimes by as much as 15 kHz. The wide range of structure is believed to be a product of the spacecraft location in the foreshock and the presence of density fluctuations associated with MHD waves. 199
- Figure 54. A high-resolution frequency-time spectrogram of the Mode 4 data. A narrowband signal is observed at what is believed to be the plasma frequency (~ 17 kHz). During the first ~ 4.5 seconds of the spectrum, the emission is weak and nearly continuous. These characteristics are suggestive of thermally excited Langmuir waves. At ~ 4.5 seconds, a more intense, broader in frequency, emission is observed, ending at ~ 5.7 seconds. This more intense emission is most likely due to Langmuir waves generated by electron beams propagating out from the bow shock. The intense, spiky emissions observed from ~ 5 kHz to ~ 16 kHz are suggestive of downshifted Langmuir waves. 201

- Figure 55. An example of a beat-type waveform (bottom panel) and its spectrum (top panel). Two distinct frequency components are observed, one at ~ 19.15 kHz and the other at ~ 19.4 kHz. A very weak low-frequency signal at ~ 0.25 kHz is also observed, although the weakness of the signal makes it difficult to determine if the signal is real. The frequency difference of these two signals and the frequency of the low-frequency signal agree with the observed beat frequency (~ 0.25 kHz) of the waveform. 203
- Figure 56. An example of a chaotic-type waveform (bottom panel) and its spectrum (top panel). The spectrum consists of a broad signal centered at ~ 14.5 kHz. The chaotic beat-type waveforms of this type are usually associated with periods of large upshifts and downshifts in frequency of the Langmuir waves. 205
- Figure 57. An example of a chaotic-type waveform (bottom panel) and its spectrum (top panel). The spectrum consists of two broadband signals, both exhibiting a great deal of structure. Similar chaotic-type waveforms have been observed at Venus (Figures 24b and 26) and during the first Earth flyby (Figure 43), and make up most of the waveforms observed during the second Earth flyby. 207
- Figure 58. The bottom panel is an example of a "constant over 8 ms" waveform. The top panel is the spectrum of the waveform. 209
- Figure 59. The number of waveform blocks as a function of peak electric field strength. The solid line gives the peak field strength for the waveforms measured directly (unclipped) or by extrapolation (moderately clipped). The dashed line gives the lower limit to the field strengths for severely clipped waveforms. 211

CHAPTER I

INTRODUCTION

The Galileo spacecraft was designed to perform a broadly based exploration of the Jupiter system, including instruments to study planetary surfaces, atmospheres, and space environments under a wide range of conditions. The Challenger accident in 1986, and the decision to use the lower energy Inertial Upper Stage instead of the higher energy Centaur upper stage, resulted in a round about trajectory to reach Jupiter. The trajectory, known as the Venus-Earth-Earth gravity assist (VEEGA) trajectory, involved a gravity assist flyby of Venus and two gravity assist flybys of Earth. The flybys allowed Venus and Earth to be studied with Galileo's state-of-the-art remote-sensing and space physics instruments.

The purpose of this thesis is to report and interpret new high-resolution observations of Langmuir waves obtained from a variety of plasma environments with the Galileo spacecraft. The Galileo plasma wave instrument detected a series of highly structured Langmuir waves, or electron plasma oscillations, in the foreshock of Venus on February 10, 1990; in the foreshock of Earth on December 8-9, 1990, and again on December 8, 1992; and in conjunction with a type III solar radio burst on December 10, 1990. The high sampling rate of the plasma wave instrument allows the fine structure of the Langmuir waves to be examined at much higher resolution than previous studies. The Langmuir wave observations share many of the same characteristics, including similar fine structure and electric field strengths. The most striking characteristic that these observations have in

common is the occurrence of beat-type waveforms which are suggestive of interference between two waves of similar frequency and amplitude.

The Langmuir waves detected by Galileo were generated by electron beams streaming through the solar wind by a process known as the two-stream instability [Tonks and Langmuir, 1929; Bohm and Gross, 1949a, 1949b]. The dispersion relation for Langmuir waves can be derived both from fluid theory and from the Vlasov Equation (see Nicholson [1983] for derivations for both cases), and is usually written as

$$\omega^2 = \omega_{pe}^2 + 3k^2V_e^2, \quad (1)$$

where ω is the frequency of the Langmuir wave, $\omega_{pe} = (n_e e^2 / \epsilon_0 m_e)^{1/2}$ is the plasma frequency, k is the wavenumber, V_e is the electron thermal velocity, m_e is the electron mass, and n_e is the electron number density. Usually $\omega_{pe}^2 \gg 3k^2V_e^2$, so the frequency of the Langmuir waves is approximately the plasma frequency ($\omega \approx \omega_{pe}$). When a beam is present, the growth rate can be shown to be proportional to $\partial f / \partial v$, where f is the electron distribution function. An electron beam propagating through a plasma (the characteristic bump on tail distribution) always has a region of positive $\partial f / \partial v$. The study of electron beams and their interaction with Langmuir waves has been an active area of research for many years. Nonlinear interactions are believed to be responsible for the generation of electromagnetic radiation at the plasma frequency f_{pe} ($f_{pe} = \omega_{pe} / 2\pi$) and at the second harmonic of the plasma frequency $2f_{pe}$ [Ginzburg and Zheleznyakov, 1958]. This radiation is observed in type II and III solar radio bursts [McLean and Labrum, 1985] and upstream of Earth's bow shock [Hoang et al., 1981]. The nonlinear processes that occur when

Langmuir waves reach large amplitudes are very important for understanding the propagation of beams in plasmas. In the absence of nonlinear processes, Langmuir waves grow to such large amplitudes that resonant wave-particle interactions quickly scatter the beam.

The observations obtained by Galileo will be compared to the various theoretical predictions and evidence supporting the nonlinear parametric decay interpretation will be presented. It will also be shown that large upshifts and downshifts occur in the emission frequency of Langmuir waves observed upstream of the bow shocks at Venus and Earth. These shifts in frequency are correlated with the downstream distance from the tangent field line, implying that the frequency shifts are controlled by the electron beam velocity.

CHAPTER II

DESCRIPTION OF INSTRUMENT AND DATA

The data described in this study are from the Galileo plasma wave, energetic particle, and magnetometer instruments. Solar wind plasma parameters were also obtained from the National Space Science Data Center (NSSDC). The Galileo plasma wave instrument consists of three sweep frequency spectrum analyzers and a wideband waveform receiver. An electric dipole antenna is used to detect electric fields, and two search coil magnetometers are used to detect magnetic fields. The electric antenna is mounted perpendicular to the spacecraft spin axis, and consists of two graphite epoxy elements with a root diameter of 2.0 cm, tapering to a diameter of 0.3 cm at the tip. The effective length L_{eff} of the antenna is 3.5 m. Two preamplifiers, one for each element, are located at the base of the elements. The preamplifiers provide low impedance signals to the main electronics package. A 250 M Ω resistance grounds each element to the spacecraft structure to limit differential charging effects. Two search coil magnetometers, one optimized for low frequencies (5 Hz to 3.3 kHz), and the other optimized for high frequencies (1 to 50 kHz), are mounted orthogonal to each other on the high gain antenna feed. Both search coils are perpendicular to the spacecraft spin axis, with the high-frequency sensor mounted perpendicular to the electric dipole antenna and the low-frequency sensor oriented parallel to the electric dipole antenna. Each search coil is connected to a preamplifier which provides low impedance signals to the main electric package.

Figure 1 shows a block diagram of the Galileo plasma wave instrument. The main electronics package consists of three spectrum analyzers and a high-resolution wideband waveform receiver. The low-frequency spectrum analyzer covers a frequency range from 5.62 Hz to 31.1 Hz in four logarithmically-spaced channels. The medium frequency spectrum analyzer covers a frequency range from 42.1 Hz to 160.8 kHz in 112 logarithmically space channels. The high-frequency spectrum analyzer covers a frequency range from 100.8 kHz to 5.65 MHz in 42 logarithmically space channels. Figure 2 shows the sampling scheme of the various spectrum analyzer channels. The time required to obtain a complete spectrum from one antenna is 18.67 seconds. For most of this study, the low- and medium-frequency spectrum analyzers were cycled between the electric and magnetic antennas, providing alternating electric and magnetic spectrums. This cycling between the antennas results in a sampling period of 37.33 seconds between complete electric field spectrums. The high-frequency analyzer is always connected to the electric antenna.

The wideband waveform receiver provides digital measurements of electric and magnetic field waveforms at sampling rates up to $201,600 \text{ sample s}^{-1}$. At this sampling rate, bandwidths of up to 80 kHz can be obtained with negligible aliasing (the Nyquist frequency for a sampling rate of $201,600 \text{ sample s}^{-1}$ is 100.8 kHz). The bandwidth of the antialiasing filter ahead of the analog-to-digital filter was 80 kHz for all of the measurements in this study. The wideband waveform receiver was operated in a duty cycle mode for all of the data used in this study. This duty cycle mode of operation provides regularly spaced blocks of waveform data separated by gaps of constant duration. The length of the waveform block depends on the specific mode of operation. Four different modes of operation were used in this study. These modes are referred to as Modes 1 through 4. In

the most commonly used mode, defined as Mode 1, a waveform block consists of 1576 contiguous samples, lasting 7.82 ms. One waveform block is captured every 66.67 ms, with a gap of 58.85 ms between successive waveforms. Figure 3a shows an example of a Mode 1 electric field waveform block. The second most commonly used mode, defined as Mode 2, consists of 216 contiguous samples, lasting 1.07 ms. Again, one waveform block is captured every 66.67 ms, with a gap of 65.60 ms between successive waveforms. Figure 3b shows an example of a block of Mode 2 electric field waveform data. During part of the Venus gravity assist flyby, a third mode, defined as Mode 3, was employed. This mode consists of 128 contiguous samples, lasting 0.63 ms. One waveform block was captured every 66.67 ms, with a gap of 66.04 ms between successive waveforms. Figure 3c shows an example of a block of Mode 3 electric field waveform data. The last mode used in this study, defined as Mode 4, utilized the tape recorder on Galileo. This mode provides almost continuous waveform data. The data consists of 1600 contiguous samples, lasting 7.94 ms, with a waveform block being captured every 8.33 ms, with a gap of 0.39 ms between successive waveforms. Examples of two contiguous electric field waveform blocks using this mode are shown in Figures 3d and 3e. Table 1 summarizes the four wideband waveform receiver modes used in this study. The waveform data are usually displayed by taking a Fourier transform of each of the waveform blocks, and then plotting the sequence of transform amplitudes in the form of a frequency-time spectrogram.

One of the most important parameters measured by the plasma wave instrument, especially for determining the role of nonlinear processes, is the electric field amplitude. The electric field amplitude is difficult to measure for short, bursty signals. The low-rate spectrum analyzers have an integration time constant of 50 ms, which is too long to provide

an accurate determination of the amplitude of millisecond bursts. The high-rate waveform measurements do not have this limitation. However, the waveform receiver has an automatic gain control. The automatic gain control (AGC) circuit is employed to control the amplitude of the signal into the analog-to-digital converter (four-bit digitization provides a dynamic range of only 24 dB). The time constant of the AGC is approximately 100 ms, and the AGC is sampled once every 2.67 s. As the gain of the receiver varies in time, absolute amplitude measurements can only be obtained at times when the AGC value is sampled. The AGC sampling rate limits the determination of the absolute field strengths measured by the wideband receiver to a 0.1-s interval every 2.67 seconds, which corresponds to approximately 7% of the available waveforms. Even then, there is another problem, which is that the waveforms may be strongly clipped, which prevents an accurate measurement.

To obtain quantitative information on the distribution of the field strengths of the Langmuir waves, the waveform blocks for which an AGC gain measurement is available were examined to determine if Langmuir wave emissions were present. The peak electric field amplitude that occurred during the waveform block was then determined. If the Langmuir wave was not clipped, as in Figures 3b and 3c, the peak amplitude can be read directly from the plot. If the waveform is moderately clipped, as in Figures 3d and 3e, the peak amplitude can be estimated by extrapolating the envelope of the waveform beyond the boundary of the plot. If the waveform is severely clipped, as in Figure 3a, the amplitude cannot be measured. In this case, the clipping level is recorded to give a lower limit to the electric field strength. For a detailed description of the Galileo plasma wave instrument, see Gurnett et al. [1992].

The energetic particle experiment (EPD) provides 4π angular coverage and spectral measurements for electrons from 15 keV to > 11 MeV and for $Z \geq 1$ ions from 20 keV to 55 MeV. The electron detectors used in this study consist of four energy channels ranging from 15 to 93 keV. Table 2 lists the channels and their energy ranges. The electron detectors are mounted on a platform and rotated by a stepping motor. The combination of spacecraft spin and the stepper motor rotation (nominally stepping to the next position after each spacecraft spin) provides 4π steradian coverage of the unit sphere. For the data discussed in this study, a sunshade prevented electron measurements within about 55° of the solar direction. For a detailed discussion of the energetic particle experiment, see Williams et al. [1992].

The Galileo magnetometer experiment consists of two boom-mounted, three-axis fluxgate magnetometer assemblies. The Galileo magnetometer data used in this study primarily consist of 20-second averages of the magnetic field components and the total field in GSE coordinates. For the studies of Langmuir waves observed upstream of Earth and Venus, model bow shocks were determined by the magnetometer team to determine the position of Galileo in the foreshock region. For a detailed discussion of the magnetometer instrument, see Kivelson et al. [1992].

CHAPTER III

LANGMUIR WAVES ASSOCIATED WITH A TYPE III RADIO BURST

Type III solar radio bursts are produced by energetic electrons from solar flares [Wild, 1950; Lin, 1970; Alvarez et al., 1972; Fainberg and Stone, 1974; Gurnett and Frank, 1975; Lin et al., 1981]. The energetic electrons emitted from a solar flare stream into the interplanetary medium along open magnetic field lines and produce the radio emission by a two-step process first proposed by Ginzburg and Zheleznyakov [1958]. First, the electron beam produces electrostatic oscillations (Langmuir waves) near the plasma frequency f_{pe} by a beam-plasma instability [Tonks and Langmuir, 1929; Bohm and Gross, 1949a, 1949b]. Second, the Langmuir waves are converted to electromagnetic radiation at both the fundamental f_{pe} and the harmonic $2f_{pe}$ by nonlinear processes. Gurnett and Anderson [1976, 1977] first detected the existence of Langmuir waves in association with type III radio bursts using data from the Helios spacecraft.

The radio emission at the plasma frequency f_{pe} (fundamental emission) is believed to be produced by a wave-wave interaction involving a beam-driven Langmuir wave L , and a low-frequency ion-sound wave S . The two most likely processes are coalescence $L + S \rightarrow T$ and the decay $L \rightarrow T + S$, where T is the transverse electromagnetic wave. Both of these processes must conserve energy ($\omega_L + \omega_S = \omega_T$ and $\omega_L = \omega_T + \omega_S$, respectively) and momentum ($k_L + k_S = k_T$ and $k_L = k_T + k_S$, respectively). Robinson et al. [1994] showed that decay $L \rightarrow T + S$ is the most likely process. The dispersion relations for the Langmuir wave, the transverse electromagnetic wave, and the ion sound wave can be written

$$\omega_L = \omega_{pe} + 3V_e^2 k_L^2 / 2\omega_{pe} , \quad (2)$$

$$\omega_T = (\omega_{pe}^2 + k_T^2 c^2)^{1/2} , \quad (3)$$

$$\omega_S = k_S V_S , \quad (4)$$

where $V_S^2 = \gamma k_B T_e / m_i$ is the ion speed, $\gamma = 1 + 3T_i / T_e$ is the ratio of the specific heats, m_i is the ion mass, k_B is Boltzmann constant, T_e and T_i are the electron and ion temperatures, and c is the speed of light. Since $k_L \gg k_T$, the conservation conditions show that the ion-sound wave propagates in the direction of the Langmuir wave and is of comparable wavelength ($k_S = k_L$).

The emission at $2f_{pe}$ (harmonic emission) is also believed to be produced by a wave-wave interaction. This interaction involves two Langmuir waves, the beam-driven Langmuir wave L and another Langmuir wave L' , such that $L + L' = T$, where T is the electromagnetic wave at $2f_{pe}$. Again, energy ($\omega_L + \omega_{L'} = \omega_T$) and momentum ($k_L + k_{L'} = k_T$) must be conserved, resulting in $\omega_T = 2\omega_{pe}$ (since $\omega_L = \omega_{L'}$) and $k_L = -k_{L'}$ (since $k_L \gg k_T$).

As the electron beam moves outward from the Sun, the Langmuir waves are produced at progressively lower frequencies due to the decrease in the density of the solar wind plasma with increasing distance from the Sun. At distances well beyond the solar corona, the electron density varies as $1/R^2$, resulting in the plasma frequency varying as $1/R$ ($f_{pe} \propto n_e^{1/2}$). Figure 4 illustrates the two-step mechanism involved in the generation of a type III solar radio burst. The decrease in the plasma frequency with distance from the Sun

produces the characteristic frequency-time spectrum in which the frequency decreases with increasing time.

Although the two-step mechanism discussed above is widely accepted, many questions concerning type III bursts still remain. For example, determining the thresholds, growth rates, and saturation levels of the processes responsible for the fundamental and harmonic emissions are areas of active research [Cairns, 1987a, b, 1988; Lin et al., 1986; Melrose, 1986, 1987, 1989, 1990; Melrose and Goldman, 1987; Robinson et al., 1992, 1993, 1994]. Another area of active research is the study of processes that allow the electron beam producing the Langmuir waves to propagate to large distances. Sturrock [1964] showed that for a spatially homogeneous beam, the beam-plasma instability would disrupt the beam by removing the free energy of the beam, and producing very intense Langmuir waves. This process occurs on time-scales corresponding to beam propagation distances of only a few thousand kilometers, much less than the distances (> 1 AU) that electron beams associated with type III radio bursts have been observed [Lin, 1970; Lin et al., 1981, 1986]. Several saturation mechanisms have been suggested to limit the growth of the Langmuir waves and thereby allow the beam to propagate with little or no disruption (for a review, see Goldman [1983] and Muschietti [1990]). Nonlinear mechanisms that have been proposed include quasi-linear diffusion [Grogard, 1975, 1982; Takakura and Shibahashi, 1976; Magelssen and Smith, 1977], scattering by long-wavelength ambient density fluctuations [Escande and de Genouillac, 1978; Muschietti et al., 1985; Melrose et al., 1986], parametric and modulational decay instabilities [Papadopoulos et al., 1974; Fried et al., 1976; Bardwell and Goldman, 1976; Goldstein et al., 1979; Smith et al., 1979; Freund and Papadopoulos, 1980], the related nonlinear three-wave decay [Melrose, 1982;

Melrose et al., 1986; Lin et al., 1986; Cairns and Robinson, 1992b], stochastic growth [Robinson, 1992; Robinson et al., 1992, 1993], and the strongly nonlinear process of soliton collapse [Zakharov, 1972; Galeev et al., 1975; Wong and Quon, 1975; Nicholson et al., 1978; Goldman et al., 1980; Shapiro and Shevchenko, 1984]. All of these mechanisms shift the Langmuir waves out of resonance with the beam, thereby preventing the dissipation of the beam from the growth of intense electric fields.

Various experimental studies have been carried out to characterize the Langmuir waves observed in association with the type III radio bursts [Gurnett and Anderson, 1976, 1977; Gurnett et al., 1978, 1980, 1993; Tokar and Gurnett, 1980; Lin et al., 1981, 1986; Robinson et al., 1992]. The Langmuir waves observed in these studies show many similar characteristics. The electric field of the Langmuir waves is polarized along the solar wind magnetic field, and is usually very spiky, with large amplitude variations on time scales extending down to a small fraction of a second. However, none of the earlier measurements had sufficient time resolution to resolve the detailed frequency spectrum and waveform of the small scale structure. The Galileo waveform data provide the first opportunity to study these effects.

Description of the Type III Event Detected by Galileo

Langmuir waves associated with a type III solar radio burst were detected by Galileo on December 10, 1990, two days after the first Earth flyby. During this event, Galileo was located on the sunward side of Earth at a geocentric radial distance of $189.5 R_E$ and a local time of 9.6 hours. The heliocentric radial distance was 0.98 AU. Figure 5 shows a four-hour frequency-time spectrogram from the spectrum analyzer for this event. The onset of the type III burst was first detected at approximately 0743 UT in the high-frequency

spectrum analyzer. The event shows an intense band of noise sweeping downward in frequency with increasing time, which is the characteristic signature of a type III solar radio burst. Several other weaker type III bursts can also be seen in the spectrogram at 0713 UT, 0720 UT, 0945 UT, and 0955 UT. The Langmuir waves are the narrowband emissions that can be seen at about 24 kHz starting at approximately 0835 UT and continuing sporadically until approximately 1020 UT.

A search of the solar flare reports listed by the *National Geophysical Data Center* [1991] revealed that the type III burst at 0743 UT is probably associated with a type 2F solar flare that occurred at 15°N latitude, 47°W longitude with an onset time of 0730 UT. Since the flare was on the west side of the Sun, the spacecraft was in a favorable position to encounter energetic electrons from the flare. The relationship between the energetic electrons and the Langmuir waves can be seen in Figure 6. The top two panels of Figure 6 show the electric field intensities from the spectrum analyzer. The top panel shows the electric field integrated over 45.6 to 49.5 kHz, which spans $2f_{pe}$. The characteristic shape of a type III radio burst can be seen in this panel. The middle panel shows the electric field intensities integrated over 21.6 to 25.1 kHz, which spans the electron plasma frequency f_{pe} . The Langmuir waves are the spiky signal starting at about 0835 UT. The bottom panel of Figure 6 shows the electron counting rate in three energy channels, 29-42, 45-55, and 55-93 keV, from the Galileo energetic particle experiment. As can be seen in Figure 6, the energetic electron detector on Galileo began detecting energetic electrons arriving from the direction of the Sun at approximately 0820 UT (a data gap limits the exact determination of the time when Galileo first encountered the electrons). The sharply peaked modulation in the counting rate with a period of about 3 minutes is produced by the azimuthal scanning of

the detector and the spin of the spacecraft, and is indicative of a beamlike distribution of electrons streaming outward from the Sun along the solar wind magnetic field lines. The onset of the Langmuir waves at approximately 0835 UT occurs approximately 15 minutes after the arrival of the solar flare electrons at Galileo. The termination of the Langmuir waves corresponds roughly with the transition of the electron distribution from an anisotropic to a nearly isotropic distribution. This relationship is consistent with previous studies [Lin et al., 1981] which show that Langmuir waves are driven by a region of positive slope in the energetic electron distribution.

Figure 7 shows a 150-minute high-resolution frequency-time spectrogram obtained from the wideband waveform receiver for this event. The broadband signal from approximately 40 kHz to 80 kHz is the type III burst. The frequency and width of the type III emission decreases with time, as can be seen in Figure 5. The Langmuir waves are the intense, narrowband emissions first observed at approximately 0836 UT and 23 kHz. The Langmuir waves continue sporadically for approximately 110 minutes, increasing in frequency to approximately 25 kHz. The frequency of the Langmuir waves is believed to be near the plasma frequency, and the slight increase in frequency during the event is probably due to an increase in the solar wind electron density. The sporadic narrowband emissions at approximately 46 to 50 kHz and 70 to 75 kHz are believed to be 2nd and 3rd harmonic distortion effects due to clipping in the receiver. The harmonics are easily seen from about 0936 UT to 0955 UT. The five intervals (0800:00 to 0804:20 UT, 0829:40 to 0834:40 UT, 0900:00 to 0905:00 UT, 0930:20 to 0935:20 UT, and 1000:40 to 1005:40 UT) of "striped" spectrum shown in Figure 7 are intervals when the wideband receiver is connected to the

search coil magnetometers. The "striped" bands at the harmonics of ~ 2.4 kHz are interference signals from the spacecraft.

The relative strength of the signals shown in Figure 7 are indicated by the color bar located to the right of the spectrogram. It should be remembered that the wideband receiver utilizes an automatic gain control to increase the dynamic range (see the Instrument and Data section). The vertical bands which sporadically appear in the spectrum (e.g., 0844 UT) are caused by the presence of a strong signal that changes the gain of the wideband receiver. For example, at 0844 UT, the strong Langmuir wave emission at 23 kHz caused the gain of the wideband receiver to decrease, which produces the apparent decrease in the intensity of the type III emission from 50 kHz to 80 kHz, and also the decrease in the low-frequency signal (1 to 6 kHz).

Figure 8 shows a one-minute, high-resolution frequency-time spectrogram from the wideband receiver. Note that the frequency scale now ranges from 0 to 40 kHz. The Langmuir waves are clearly visible at $f_{pe} \approx 25$ kHz. The intensity of the Langmuir waves shows extremely rapid temporal variations, down to the smallest time scale that can be resolved, which is the time between successive waveform blocks (66.67 ms). The Langmuir waves also show frequency spreading, sometimes by as much as 2 kHz. The frequency spreading is also highly variable, sometimes changing by a factor 5 or more between successive spectrums. The weak signals (e.g., 4.9 and 9.7 kHz) are interference signals from the spacecraft.

Numerous bursty emissions in the frequency range from about 3 to 10 kHz can also be observed in Figures 7 and 8. These emissions typically have durations of less than a second and are believed to be ion sound waves of the type discussed by Gurnett and

Anderson [1977], Gurnett and Frank [1978], Gurnett et al. [1979a], and Kurth et al. [1979]. Although various theories predict ion sound waves to be generated by Langmuir waves, and a previous study of type III bursts [Lin et al., 1986] found ion sound waves in association with Langmuir waves, the ion sound waves observed in Figures 7 and 8 do not appear to be related to the Langmuir waves. For example, the ion sound wave bursts at 46 and 59 s in Figure 8 occur during periods of no Langmuir wave activity. This observation is consistent with results of Gurnett et al. [1979a] using Helios measurements which showed that ion sound waves can sometimes occur in the solar wind independently of solar flare induced Langmuir wave emissions.

To further explore the fine structure of the Langmuir waves, individual 7.82-ms waveform blocks were analyzed. During this event, approximately 83,000 electric waveform blocks were obtained, of which approximately 30% have clearly identifiable Langmuir wave oscillations. The instrument was in Mode 1 (7.82-ms blocks) during the entire event. Figure 9 shows four waveforms that were selected to illustrate the range of structure that is observed. Each panel represents one waveform block lasting 7.82 ms. The high-frequency, quasi-sinusoidal waveform evident in each panel is the Langmuir wave oscillation at $f \approx f_{pe}$, which is approximately 24 kHz during these intervals. Figure 9a shows an example of an isolated wave packet with a duration of approximately 3 ms. Figure 9b shows an example of two closely spaced packets. Figure 9c shows a string of packets, which is suggestive of interference between two nearly monochromatic waves of comparable amplitudes. Evidence that a string of packets is caused by interference between two nearly monochromatic components can be obtained by examining the spectrum of the individual waveforms. Figure 10 shows the spectrum of the waveform in Figure 9c. As

can be seen, the spectrum consists of two sharply defined peaks separated by about 400 Hz, which is the approximate beat frequency observed in the waveform. A low-frequency signal is also observed at approximately 400 Hz. The beat frequencies of the waveforms obtained during the interval of the type III burst vary from about 150 to 650 Hz. Beat frequencies below 150 Hz almost certainly occur, but the 58.85-ms gap between waveform blocks makes it difficult to determine the extent to which beats occur in this frequency range. Figure 9d shows a waveform that is severely clipped. The clipping is a limitation of the AGC system. For signals with rapidly increasing amplitudes, the gain of the receiver cannot respond fast enough, resulting in a clipped waveform. Roughly 2% of the type III Langmuir oscillations display severe clipping of this type.

Figure 11b shows an example of a waveform block containing "weak" Langmuir wave structure. This type of waveform contains no obvious Langmuir wave signal in the waveform (Figure 11b), but a signal is observed in the spectrum near the plasma frequency (Figure 11a). The "weak" Langmuir waves have electric field strengths similar to the noise level of the receiver. Although the electric field strengths in most of the "weak" cases are small ($\sim 0.02 \text{ mV m}^{-1}$), the actual strength of the signal for a specific waveform block depends on the gain setting of the instrument. Although these "weak" Langmuir wave emissions may be beam driven, it is more likely they are thermally excited. For a discussion of thermally excited Langmuir waves in the solar wind, see Meyer-Vernet and Perche [1989].

Electric Field Amplitudes

The electric field strengths of the Langmuir waves were determined by the method discussed in the Instrument and Data section. During the roughly 2-hour interval Langmuir waves were observed, a total of 2015 waveform blocks contain Langmuir wave emissions for which AGC gain measurements are available. Figure 12 shows the distribution of the peak electric field strengths. The solid line gives the peak field strength for the waveforms measured directly (unclipped) or by extrapolation (moderately clipped). The dashed line gives the lower limit to the field strengths for severely clipped waveforms. The severely clipped waveforms represent only a small fraction ($\sim 2\%$) of the total waveforms. Most of the field strengths are in the range from 0.01 to 1.0 mV/m, with the largest field strength measured being 1.7 mV/m. The sharp cutoff in the number of events below 0.01 mV/m is caused by the background noise level (due to the receiver noise level and other low-frequency signals), which makes it difficult to measure field strengths below 0.01 mV/m. The amplitude distribution follows a power law $dN/(dE/E) \sim E^{-\alpha}$, where dN is the number of events in electric field interval dE . The power law index α is approximately 1 over much of the E field range, with a slight increase around 1 mV/m. Figure 13 compares the spectrum of the Langmuir waves (top panel) to the distribution of the field strengths shown in Figure 12 as a function of time. No obvious trends in the electric field strength are observed.

Fine Structure

The characteristics of the Langmuir wave fine structure observed during this event were also surveyed. Unfortunately, the 7.82-ms length of the waveform block and the 58.85-ms gap between waveform blocks limit the ability to determine the size and

characteristics of the fine structure. Structure sizes larger than approximately 7.82 ms cannot be resolved, and structure sizes smaller than 7.82 ms can only be resolved when captured within the 7.82 ms sampling period of the waveform block. The gap between consecutive waveforms limits the ability to examine the larger scale structure. Langmuir waves observed in two consecutive waveforms (66.67 ms apart) may be part of the same macrostructure, or may be unrelated to each other. With these limitations, a survey of the fine structure is presented in this study. The survey involves the 2015 waveform blocks which had associated AGC values. These waveforms are the same ones studied in the electric field amplitude survey. The limits imposed by the finite size of the waveform blocks lead to four basic types of waveforms. The first type is defined as waveforms containing at least one wave packet completely captured within the waveform block (e.g., Figure 9a, b and c). A little over 3% of the waveforms have structure of this type (referred to as "< 8 ms" structure). Most of the waveforms with structure "< 8 ms" consist of beat-type waveforms (e.g., Figures 9b and 9c). The second type consists of waveform containing structure, but complete wave packets are not captured in the 7.82-ms block (e.g., Figures 9d and 3a). This structure type is referred to as "> 8 ms" structure and consists of 19.5% of the waveform blocks. Many of the "> 8 ms" waveforms appear to be beat-type waveforms with periods greater than 8 ms (e.g., Figure 9d). Unfortunately, the gap between waveform blocks makes it difficult to determine the exact structure of these waveforms. The third type contains Langmuir waves which are basically constant over the 7.82 ms (e.g., Figures 14a and 14b). Approximately 37.3% of the waveforms consist of this "constant over 8 ms" emissions. The fourth type consist of signals that are too weak to resolve any structure. This type of waveform, which are called "weak", exhibits no obvious

narrowband signal in the waveform (Figure 11b), but a signal is observed in the spectrum near the plasma frequency (Figure 11a). Approximately 40% of the waveforms are of this type. It should also be noted that the determination of the structure type for Langmuir waves with field strengths near the noise level of the waveform block (Figures 14a, 11b) is subject to some interpretation between "weak," "constant over 8 ms," and "> 8 ms." A summary of the above results is shown in the first columns of Table 3. The middle columns of Table 3 show the results when the waveform blocks with "weak" Langmuir wave emissions are removed. The last columns of Table 3 show the distribution of waveform blocks with peak electric field amplitudes above 0.1 mV m^{-1} as determined in the electric field survey. As can be seen, the larger fields have a higher percentage of structure with shorter time scales. This relationship would be expected if the fine structure is related to a nonlinear process. Although large field strengths are associated with the short-time structure, no relationship has been observed between the smallest scale sizes and the largest field strengths.

Discussion

This chapter has used the high-resolution waveform measurements obtained by the Galileo plasma wave instrument to investigate the fine structure of Langmuir waves observed in association with a type III solar radio burst. Table 4 summarizes the plasma parameters and the characteristics of the Langmuir waves for the type III event. When possible, the values shown in Table 4 were obtained from the instruments on Galileo. Unfortunately, the Galileo plasma instrument was not operating during this interval, so direct in situ measurements of plasma parameters were not possible. Due to the lack of Galileo plasma data, most of the solar wind plasma parameters shown in Table 4 are

estimates obtained from the NSSDC IMP-8 data. Table 5 shows the NSSDC IMP-8 one-hour averages for day 344, 1990. The type III burst examined in this study occurred from approximately 0743 to 1030 UT. Unfortunately, this event corresponds to a data gap in the IMP-8 data. The values of the solar wind speed and ion temperature shown in Table 4 were estimated from the IMP-8 values observed before and after the data gap. The solar wind electron density was estimated using the observed frequency (assumed to be f_{pe}) of the Langmuir waves, and a typical value for the solar wind electron temperature is shown. The beam velocity of $\leq 7.1 \times 10^7 \text{ m s}^{-1}$ was estimated by Reiner et al. [1994] using the velocity dispersion in the high-energy electron onset times and the onset time of the Langmuir waves. This value agrees with the beam speeds of $(3-10) \times 10^7 \text{ m s}^{-1}$ observed in association with type III Langmuir waves by Lin et al. [1986].

The structure of the Langmuir waves observed in this study spans a broad range of time scales, from tens of minutes (see Figure 7) to milliseconds (see Figure 9). If we assume that these structures are convected past the spacecraft at the solar wind speed ($\sim 330 \text{ km s}^{-1}$), the time scales correspond to spatial scales ranging from a few hundred thousand kilometers to a few hundred meters. The smallest structure observed in the waveforms is on the order of 1 ms. This lower limit is probably related to the Debye length, which is given by $\lambda_D = 69(T_e/n_e)^{1/2} \text{ m}$, where T_e is in degrees Kelvin, and n_e is in m^{-3} . Using the values shown in Table 4, λ_D is found to be $\sim 9.3 \text{ m}$. Dividing by the solar wind speed, $100 \lambda_D$ is found to be equivalent to $\sim 2.8 \text{ ms}$. $100 \lambda_D$ is shown at the top of Figure 9 as a reference. The shortest scale lengths of the structure corresponds to a spatial scale of a few tens of Debye lengths. The small scale structures observed in the waveforms are strongly suggestive of a nonlinear process.

Soliton Collapse

Isolated wave packets, such as Figure 9a, are suggestive of the strong turbulent process of soliton collapse. Soliton collapse occurs when the Langmuir wave electric field becomes so large that the ponderomotive force and nonlinear self-focusing cause the wave packet to contract and intensify [Zakharov, 1972]. This nonlinear feedback process leads to the collapse of the electric wave field into small, very intense soliton-like packets. The shift in wavelength as the collapse occurs transfers energy to large k values in the Fourier spectrum. Collapse is arrested by transit-time damping when the wave packet decreases to scale sizes of $\sim 20\lambda_D$. Transit-time damping transfers energy into fast, non-thermal electrons [Papadopoulos, 1978; Shapiro and Shevchenko, 1984; Goldman, 1984; Robinson, 1991].

For soliton collapse to occur, the electric field amplitude must become large enough for the self-focusing and ponderomotive effects to overcome dispersion. The dimensionless energy density W , defined as the ratio of the electric field energy density to the plasma energy density, is used in many studies to characterize the strength of the nonlinear interaction. Writing W in terms of the local peak electric fields E_{peak} gives

$$W = \epsilon_0 E_{\text{peak}}^2 / 4n_e k_B T_e \quad (5)$$

Recent work by Robinson and Newman [1991] and Cairns and Robinson [1992a] have determined the electric field of a wave packet of scale size L_i required to balance the self-focusing and ponderomotive effects against dispersion. Using their formalism, the collapse threshold can be written

$$E_{\text{peak}}(L_i) \geq (200n_e k_B T_e / \epsilon_0)^{1/2} \lambda_D / L_i \quad \text{V m}^{-1} \quad (6)$$

This equation holds during the entire collapse, with L_i replaced by $L(t)$, implying that smaller scale wave packets require larger fields.

Cairns and Robinson [1992a] have also proposed an additional threshold due to density fluctuations in the solar wind δn_{sw} disrupting the density troughs δn of the collapsing Langmuir waves. Disruption of the collapsing Langmuir waves can occur when $\delta n_{\text{sw}} \geq \delta n$ and the disruption time scale is smaller than the collapse time scale. The resulting threshold for disruption due to density fluctuations can be written as

$$E_{\text{peak}}(L_i) \geq (200n_e k_B T_e V_S / \epsilon_0 V_e)^{1/2} (\lambda_D / L_i)^{1/2} \quad \text{V m}^{-1} \quad (7)$$

For $\delta n_{\text{sw}} \ll \delta n$, the density well of the collapsing Langmuir wave is not disrupted, and the threshold for collapse is governed only by Equation 6. It should be noted that if soliton collapse is responsible for the fine structure of the Langmuir waves, Equations 6 and 7 predict a good correlation between the smallest structure sizes and the largest electric fields.

Considerable effort has gone into determining if the Langmuir waves associated with type III radio bursts undergo soliton collapse. Experimental studies have found that the electric field of the Langmuir wave emissions is very spiky, with large amplitude variations on time scales extending down to a small fraction of a second [Gurnett and Anderson, 1976]. The spiky amplitude variations have been suggested as evidence of soliton collapse, although the measured amplitude of the Langmuir waves in these earlier studies have been smaller than the predicted thresholds for soliton collapse. However, none of the earlier

measurements had sufficient time resolution to resolve the electric field strength of the spiky structure. Recently, Kellogg et al. [1992] presented evidence of collapsing Langmuir wave packets at millisecond time scales using the fast envelope sampler on the Ulysses spacecraft. These data consist of narrow spikes of width about 1 ms near the top of a weaker burst of Langmuir waves. Although these spikes are suggestive of soliton collapse, the reported electric field amplitudes are below the necessary threshold given by Equations 6 and 7.

To determine if soliton collapse is the cause of the fine structure detected by Galileo, the peak electric field values shown in Figure 12 were compared to the predicted thresholds for soliton collapse determined from Equations 6 and 7. Using the plasma parameters from Table 4, the thresholds for soliton collapse found from Equation 6 are $E_{\text{peak}} \geq 17 \lambda_D L^{-1} \text{ V m}^{-1}$ and from Equation 7 to be $E_{\text{peak}} \geq 2.9 (\lambda_D L^{-1})^{1/2} \text{ V m}^{-1}$, where L is the scale length of the wavepacket. From these thresholds, it is easy to see that the smallest structure sizes should correspond to the largest electric fields. Typical scale lengths of the smallest scale structure are on the order of $L = 100 \lambda_D$ (see Figure 9). The thresholds for structure of this size are found to be 170 mV m^{-1} and 290 mV m^{-1} respectively. These threshold voltages are two orders of magnitude greater than the largest electric field amplitudes (1.7 mV m^{-1}) observed during this event (see Figure 12). There exists the possibility that some of the severely clipped waveforms could have electric field strengths larger than 1.7 mV m^{-1} . However, the severely clipped waveforms are rare ($\sim 2\%$ of the waveforms), and an examination of the slopes of the clipped waveforms has shown that it is very unlikely that the electric field strengths of these waveforms are more than 2 to 4 times the clipped value. The largest severely clipped electric field strengths are on the order of 0.5 mV m^{-1} (see Figure 12). The actual value of the electric field would have to be approximately 100 times

larger than the clipped value for the thresholds from Equation 6 and 7 to be exceeded, which appears to be very unlikely. It is also possible that some of the waveforms that do not have corresponding AGC values could have fields much larger than 1.7 mV m^{-1} . However, it is doubtful that any of the waveforms have fields have amplitudes as large as 290 mV m^{-1} .

Coupling between the plasma and the electric antenna could result in the electric field strengths measured by Galileo to be smaller than their true value. However, this effect is believed to be small. Previous studies employing a wide range of antenna lengths (few meters to hundred of meters) and types of antenna (monopole and dipole, thin wire and spheres) have measured very similar electric field strengths for the Langmuir waves. Although the exact characteristics of the antenna coupling to the plasma is difficult to determine, it is unlikely that the diversity in the types and lengths of antennas on previous studies would produce similar results if this coupling greatly affected the measurement of the Langmuir waves.

Further evidence against soliton collapse is the lack of correlation between the smallest scale sizes and the electric field intensity. The electric field strength of a wavepacket should increase as it collapses (see Equation 6 and 7). This increase of the electric field strength with decreased scale size predicts even larger fields for the smaller structure (≥ 567 and 529 mV m^{-1} , respectively, for $L = 30 \lambda_D$). Although this study did find that the waveforms with larger field strengths tended to contain more structure, suggestive of a nonlinear process, the smallest structure did not correspond to the largest fields as predicted by Equation 6 and 7.

Another approach is to substitute the observed electric field strengths into the threshold equations and solve for the minimum scale length L required for soliton collapse to occur. Using the maximum observed field strength of 1.7 mV m^{-1} , scale lengths of $10,000 \lambda_D$ (280 ms) and $2.93 \times 10^6 \lambda_D$ (81,200 ms) are needed to exceed the threshold for soliton collapse. These scale lengths are much larger than the typical scale size of the observed fine structure (see Figure 9). Although some waveforms (e.g., Figure 9d) contain larger scale structure, and the spectrum analyzer measurements suggest some large scale structure, it is very unlikely that the Langmuir waves exceed the thresholds from Equations 6 and 7.

Additional evidence that soliton collapse is not involved is given in the frequency spectrum. As a packet collapses, the plasma density in the cavity will be reduced. This decrease in the plasma frequency reduces the wave frequency and should cause an asymmetric downward shift in the frequency spectrum. No such downward shift is observed. Thus it appears that soliton collapse is unlikely to be responsible for generating the fine structure of the Langmuir waves associated with this type III event.

Parametric Decay

Beat-type waveforms of the type illustrated in Figures 9b and 9c are almost certainly caused by interference between two waves of similar amplitude but slightly different frequency. Evidence that the waveforms consist of two nearly monochromatic components can be obtained by examining the spectrum of the individual waveforms. Figure 10 shows the spectrum of the waveform in Figure 9c. As can be seen, the spectrum consists of two sharply defined emission lines separated by about 400 Hz, which is the approximate beat frequency observed in the waveform. The two emission lines usually have approximately the same amplitude. The most likely candidates for these two waves are the beam-generated

Langmuir wave L and the oppositely propagating Langmuir wave L' responsible for the harmonic emission at $2f_{pe}$. An obvious source for the backward propagating Langmuir wave L' is a three-wave parametric decay process in which the beam-driven Langmuir wave decays into the oppositely propagating Langmuir wave and an ion sound wave

[Papadopoulos et al., 1974; Fried et al., 1976; Bardwell and Goldman, 1976; Goldstein et al., 1979; Smith et al., 1979; Freund and Papadopoulos, 1980; Melrose, 1982; Melrose et al., 1986; Lin et al., 1986; Cairns, 1987b; Robinson et al., 1993, 1994]. Since the electron beam is propagating away from the Sun, the beam-generated Langmuir wave is expected to be Doppler shifted upward in frequency by the outward radial motion of the solar wind, and the oppositely propagating Langmuir wave is expected to be shifted downwards in frequency. Based on this expectation, the higher frequency emission marked L in Figure 10 is believed to be the beam-driven Langmuir wave and the lower frequency emission marked L' is believed to be the backward propagating Langmuir wave. As can be seen in Figure 10, a weak low-frequency emission marked S sometimes also occurs at the beat frequency (~ 400 Hz in this case). This emission is believed to be the ion sound wave. Although other processes, such as excitation by electron beams of different speeds, could produce two or more Langmuir waves of slightly different frequencies, parametric decay is the most likely explanation why the two waves also have nearly the same amplitudes.

The three-wave parametric decay process $L \rightarrow L' + S$ is a nonlinear process in which a beam-generated Langmuir wave L (sometimes called the pump wave) decays into a Langmuir wave L' and an ion sound waves S . The process conserves momentum, $k_L = k_{L'} + k_S$, and energy, $\omega_L = \omega_{L'} + \omega_S$. The S -wave frequency and wavevector thus corresponds to the beat between the L and L' waves. Using the appropriate conservation

laws and dispersion relations (Equation 2 and 4), Cairns [1987b] showed that $k_S = 2k_L \cos \theta_{LS} - k_0$ and that $k_{L,L'} \geq k_0/2$, where θ_{LS} is the angle between the L and S wavevectors, and $k_0 = 2\omega_p V_S / 3V_e^2$ is the maximum wavenumber difference between L and L'. Since the maximum growth rate of the beam-generated Langmuir wave occurs at $k_L = \omega_p / V_b$, where V_b is the beam velocity, it follows that parametric decay can only occur if $V_b \leq 3V_e^2 / V_S$. This threshold beam velocity provides a check of the parametric decay theory, since beat-type waveforms should not be observed for beam speeds greater than $3V_e^2 / V_S$. Cairns [1987b] also showed that the decay proceeds fastest when the Langmuir wave L' is propagating in a direction opposite to the beam-generated Langmuir wave and that the ion sound wave S is propagating in the same direction as the beam-generated Langmuir wave ($\theta_{LS} = 0^\circ$), resulting in $k_S \approx 2k_L - k_0$ and $k_L \geq 3k_0/2$. Using $k_L = \omega_p / V_b$, the highest growth rate for the parametric decay process is found to occur for beam speeds $V_b \leq V_e^2 / V_S$.

Using the above ideas, Cairns and Robinson [1992b] derived a relationship between the frequency of the ion sound wave and the speed of the electron beam V_b . Assuming that the electron beam is traveling parallel to the magnetic field, and that k_L is parallel to V_b , they find that

$$V_b = \left[\frac{V_S}{3V_e^2} + \frac{\omega_S'}{2\omega_{pe} |V_S \pm v_{sw}| \cos \theta} \right]^{-1} \quad (8)$$

where ω_S' is the frequency of the ion sound wave in the spacecraft frame of reference and θ is the angle between the magnetic field and the solar wind velocity V_{sw} . The $-$ sign in

front of the v_{sw} term is used for Langmuir waves L propagating upstream into the solar wind, as occurs upstream of planetary bow shocks. In this case the L' waves propagate downstream, and are Doppler shifted to higher frequencies. The + sign is used for downstream propagating L waves, as occurs for type III bursts, and sometimes upstream of planetary bow shocks. In this case the L' waves are Doppler shifted to lower frequencies. Since the frequency of the ion sound wave must be the same as the beat frequency, ω_s' also corresponds to the frequency difference between the two Langmuir waves.

In Equation 8 it is usually the case that the first term in the bracket is much smaller than the second term. Since V_s is also usually much less than V_{sw} , the beat frequency ω_s' is then given to a good approximation by

$$\omega_s' \approx \frac{2\omega_{pe} V_{sw} |\cos\theta|}{V_b} \quad (9)$$

This relationship shows that as the beam speed decreases, the beat frequency should increase. From simple time-of-flight arguments the speed of the electron beam is expected to vary inversely with the time from the onset of the event at the Sun. This inverse relationship has been verified by Lin et al. [1981, 1986] and was found to be of the form $V_b = A/(t-t_0)$, where A is the path length, t is the time of the measurement, and t_0 is the onset time of the electron beam. Equation 9 then shows that the beat frequency should vary linearly with t. To test this prediction, the measured beat frequencies $f_s = \omega_s'/2\pi$ of the beat-type waveforms (e.g., Figures 9b and 9c) are shown in Figure 15. The beat frequencies were obtained by examining each of the approximately 83,000 electric field

waveform blocks captured during the type III event. Approximately 25,000 of the 83,000 waveform blocks contain Langmuir wave emissions. Clearly identifiable beat envelopes are observed in 894 waveform blocks (approximately 3.6% of the waveform blocks containing Langmuir waves). The period of the beat $T = 1/f_s$ is determined to the nearest 0.1 ms for each of these 894 waveforms. It should be noted that many of the waveform blocks appear to contain beat-type waveforms of periods > 7.82 ms (e.g., Figure 9d), or beat-type waveforms that are cut off by the edge of the waveform block. Unfortunately, the 58.85 ms data gap between the waveform blocks makes the determination of the period of these waveform blocks impossible. Although there is considerable scatter, a clear trend can be seen toward a higher beat frequency with increasing time, as predicted by Equation 9. The solid line in Figure 15 is the least-square linear fit to the data points.

To see if the predicted beam velocity agrees with allowed beam velocities for parametric decay, Figure 16 shows the electron beam speeds computed from Equation 8 using the measured beat frequencies and the corresponding value of θ determined from the Galileo magnetic field data (20-second averages). The solar wind velocity is assumed to be in the $-x_{GSE}$ direction for the determination of θ . Unfortunately, no plasma data are available from either Galileo or IMP-8 for the exact time of the type III burst, so the solar wind parameters used in Equation 8 ($V_e \sim 1.4 \times 10^6$ m s⁻¹, $V_s \sim 4.1 \times 10^4$ m s⁻¹, and $V_{sw} \sim 330$ km m⁻¹) were interpolated from the NSSDC IMP-8 plasma data using measurements before and after the event. These interpolated values are probably not changing much during the interval of the type III since the values before and after the data gap are very similar (see Table 5). As can be seen, the beam speeds are below the upper limit of $3V_e^2/V_s = 14.3 \times 10^7$ m s⁻¹ for parametric decay to occur, and are in good

agreement with the beam speed $V_e^2/V_s = 4.8 \times 10^7 \text{ m s}^{-1}$ that produces the most rapid decay. The beam speeds also agree well the estimate of $V_b \leq 7.1 \times 10^7 \text{ m s}^{-1}$ by Reiner et al. [1994] using the velocity dispersion in the higher energy electrons onset times and the onset times of the Langmuir waves for this event. The solid line in Figure 16 shows the beam speed calculated from $V_b = A/(t-t_0)$. The path length $A = 1.7 \text{ AU}$ used in this equation is the value obtained by Reiner et al. [1994] for this same event. The onset time of the flare was taken to be $t_0 \sim 0730 \text{ UT}$ [National Geophysical Data Center, 1991]. As can be seen, the beam speeds agree well with the trend in the speeds determined from Equation 8. Unfortunately, the lowest energy channel of the Galileo energetic electron experiment is 15 keV ($\sim 7.4 \times 10^7 \text{ m s}^{-1}$), which is too high to allow direct comparisons between the predicted electron beam speeds and the actual speed.

The scatter evident in Figures 15 and 16 could be produced by a variety of factors. Equation 9 shows that the beat frequency depends on four factors: the beam speed, the solar wind speed, the plasma frequency, and $\cos \theta$. Fluctuations in the beam speed and $\cos \theta$ are believed to be the most likely cause of the scatter, since the solar wind speed and the plasma frequency are nearly constant. Variations in the beam speed could be due to fluctuations in the region of positive slope ($\partial f / \partial v_{\parallel} > 0$) for which Langmuir waves can be excited. For a spread in velocity $\Delta V_b/V_b$ of the beam, Langmuir waves can be produced for k_L values in the range $(1-\Delta V_b/V_b)\omega_p/V_b < k_L < \omega_p/V_b$. Substituting these limits into Equation 9 shows that the spread in the beat frequency is approximately $\Delta f_s/f_s \approx \Delta V_b/V_b$. Assuming beam spreads on the order of $\Delta V_b/V_b \sim 0.1-0.3$ [Lin et al., 1981, 1986], the beat frequency would be expected to vary by approximately 10% to 30%. This variation is comparable to the observed spread in the frequency (see Figure 15). Fluctuations in the

electron beam speed due to the interactions of the beam with ambient density fluctuations, as proposed in the stochastic growth model of Robinson [1992] and Robinson et al. [1992, 1993, 1994], could also account for some of the scatter. The stochastic growth model predicts that the electron beam at a given location is made up of multiple beamlets (characteristic time scale ~ 10 ms), each with its own speed and width in velocity space. Although the average of all the beamlets at a given point is consistent with the beam characteristic reported by Lin et al. [1981, 1986], the individual beamlets could produce very rapid and large variations in the beat frequency. Unfortunately, little is known about the velocity space structure of the electron beams.

Variations in $\cos \theta$ could be produced by the interaction of the Langmuir waves with density fluctuations in the solar wind. It is easily shown that small density fluctuations in the solar wind can cause substantial refraction of Langmuir waves, thereby causing large deviations in the propagation direction related to the beam direction (assumed to be the magnetic field direction). Since little is known about small-scale density fluctuations, the magnitude of the resulting variation in θ is difficult to estimate. Using data from the Helios spacecraft Gurnett and Anderson [1977] found that the propagation direction of Langmuir waves was usually aligned within 20° of the magnetic field direction, which would produce approximately 10% variations in the beat frequency. Larger shifts in the Langmuir wave propagation direction are possible, but large variations in the propagation direction would bring the wave out of resonance with the electron beam, resulting in rapid damping.

Parametric decay also predicts that a low-frequency wave is produced. A previous study [Lin et al., 1986] has reported ion sound waves in association with type III related Langmuir wave events using data from the ISEE-3 spacecraft. Although no ion sound

waves can be seen in Figures 7 and 8 that are obviously correlated with the Langmuir waves, an examination of the spectrums of the individual waveform blocks often show weak, low-frequency signals at the beat frequency. The spectrum of the waveform in Figure 9c is shown in Figure 10. The main signal near the plasma frequency (~ 24 kHz) consists of two peaks of comparable amplitude, separated by approximately 400 Hz. A weak signal can be seen at 400 Hz, which is the approximate beat frequency observed in the waveform. Many of the spectrums of the beat-type waveforms contain similar weak low-frequency structure at or near the beat frequency. These low-frequency signals are suggestive of the low-frequency ion sound waves predicted by parametric decay. The Galileo electric antenna, 6.6 m tip-to-tip, is considerably shorter than the 90 m tip-to-tip antenna used by Lin et al. [1986] which may explain the why these low-frequency waves are so weak. Also, if the ion temperatures are of the same order as the electron temperature, the low-frequency waves will be strongly damped out. Unfortunately, the electron and ion temperatures are not known for this interval, so the damping cannot be evaluated.

CHAPTER IV

LANGMUIR WAVES UPSTREAM OF THE BOW SHOCK AT VENUS

Langmuir waves have been observed in the solar wind upstream of the bow shock of Venus [Scarf et al., 1980; Hospodarsky et al., 1994], Earth [Scarf et al., 1971; Fredricks et al., 1971; Filbert and Kellogg, 1979; Fuselier et al., 1985], Jupiter [Scarf et al., 1979; Gurnett et al., 1979b; Gurnett et al., 1981a; Canu et al., 1993; Thiessen et al., 1993], Saturn [Gurnett et al., 1981; Scarf et al., 1982], Uranus [Gurnett et al., 1986], and Neptune [Gurnett et al., 1989]. These waves are believed to be produced by energetic electrons escaping into the solar wind from the bow shock. As the electrons stream along the interplanetary magnetic field lines, the solar wind convects the guiding centers of the particles downstream due to the $\mathbf{v}_{sw} \times \mathbf{B}$ electric field as shown in Figure 17. The electrons originating from the tangent point with the highest energy define a region called the electron foreshock. Due to time-of-flight effects, only the electrons above a certain critical velocity can reach the spacecraft, thereby forming a beam [Filbert and Kellogg, 1979]. The existence of a beam provides the region of positive slope, $\partial f / \partial v > 0$, necessary for generating the Langmuir waves. Electrons below this critical velocity are convected downstream before they can reach the spacecraft. Energetic ions also stream into the solar wind from the bow shock. Because the ions are slower than the electrons, the ion foreshock boundary is located downstream of the electron foreshock boundary. It should be noted that both ions and electron beams can be observed in the ion foreshock. Figure 18 shows a sketch of a typical planetary foreshock.

One method of characterizing the location of a spacecraft in relation to the foreshock is via a characteristic distance D , called the depth parameter (also known as the DIFF parameter). The depth parameter is defined as the distance along the solar wind flow from the tangent magnetic field line to the spacecraft, as shown in Figure 17. The depth parameter is positive for spacecraft locations downstream of the electron foreshock, and negative for locations upstream of the foreshock. For a given depth parameter, only electrons with a velocity above a certain critical velocity can reach the spacecraft. The critical velocity can be determined from the equation $v_c = d v_{sw}/D$ [Filbert and Kellogg, 1979] where v_c is the critical velocity, d is the distance along the tangent field line from the tangent point to the spacecraft, v_{sw} is the solar wind velocity, and D is the depth parameter.

Langmuir waves observed in association with planetary bow shocks exhibit a great deal of structure and variability. The type of structure observed is related to the position of the spacecraft in the foreshock. The Langmuir waves near the tangent field line usually occur in a narrow band in frequency ($\Delta f/f$ of a few percent) near the plasma frequency and are usually very intense ($E \sim 10 \text{ mV m}^{-1}$ at Earth). As a spacecraft moves deeper into the foreshock region (increasing depth parameter), the Langmuir waves become weaker and more irregular. The spectrum of the Langmuir waves also spreads both upward and downward in frequency, and the bandwidth increases ($\Delta f/f \sim 0.5$) [Etcheto and Faucheux, 1984; Fuselier et al., 1985; Lacombe et al., 1985]. At Earth, the downshifts and upshifts in the emission frequency are found to be correlated with the depth parameter. This correlation is believed to be related to the speed of the electron beams producing the Langmuir waves [Etcheto and Faucheux, 1984; Fuselier et al., 1985; Lacombe et al., 1985]. Beam speeds on the order of the thermal velocity (expected at large depth parameters) are

believed responsible for the downshifted emissions. Beam speeds of a few times the thermal speed (expected at moderate depth parameter) are believed to produce the upshifted emissions.

Fuselier et al. [1985] showed that for a cold tenuous Maxwellian electron beam, the frequency of maximum growth depends on the speed of the beam. Figure 19 shows a plot of the frequency of maximum growth versus the ratio of the beam velocity to the thermal speed (V_b/V_e). For electron speeds on the order of the thermal speed ($0 < V_b/V_e < 2$), the predicted frequency of maximum growth is below the plasma frequency. For higher beam speeds ($V_b/V_e \sim 3$) the frequency of maximum growth is above the plasma frequency. For very large beam speeds ($V_b/V_e \gg 3$), the predicted frequency approaches the plasma frequency. More recent work by Cairns [1987c, 1989], Cairns and Fung [1988], and Dum [1990a, b and c] have shown that the relationship between the frequency of maximum growth and the beam velocity depends on n_b/n_e , T_b/T_e , and the shape of the distribution function (e.g., Maxwellian or Lorentz). In the ion foreshock, the Langmuir waves often exhibit highly structured emissions. This structure is believed to be related to the low electron beam speeds and also to the presence of MHD waves associated with the ions beams.

The Langmuir wave emissions observed upstream of planetary bow shocks are also very bursty in nature and show considerable fine structure. At Jupiter the electric field waveforms of Langmuir waves show structure on the order of milliseconds (tens of Debye lengths) [Gurnett et al., 1981a]. At Venus, Hospodarsky et al. [1994] reported structures as small as 0.15 ms (~ 10 Debye lengths). Considerable effort has gone into explaining the fine structure of the Langmuir waves observed upstream of planetary bow shocks. Many of

the theories and models developed to explain the Langmuir waves associated with type III radio bursts have also been used to attempt to account for the characteristic of the Langmuir waves observed upstream of planetary bow shocks. Some of the mechanisms that have been proposed include parametric and modulational decay instabilities [Papadopoulos et al., 1974; Fried et al., 1976; Bardwell and Goldman, 1976; Goldstein et al., 1979; Smith et al., 1979; Freund and Papadopoulos, 1980; Lin et al., 1986; Cairns and Robinson, 1992b; Robinson et al., 1993, 1994] and strongly nonlinear processes, such as soliton collapse [Zakharov, 1972; Galeev et al., 1975; Nicholson et al., 1978; Goldman, 1984; Shapiro and Shevchenko, 1984; Robinson and Newman, 1991].

Langmuir waves observed upstream of the bow shock of Venus were first reported by Scarf et al. [1980] using data from an electric field detector flown on the Pioneer Venus Orbiter. More recent studies by Crawford et al. [1990, 1991, 1993a, 1993b] have shown that the characteristics of the Langmuir waves are very similar to the Langmuir waves observed upstream of Earth's bow shock. The Langmuir waves are polarized with the wave electric field parallel to the static magnetic field and are detected only when the spacecraft is magnetically connected to the bow shock. The peak electric field intensities (10 mV m^{-1}) are similar to Langmuir wave intensities observed upstream of Earth's bow shock. The Galileo gravity assist flyby of Venus provided an opportunity to study these Langmuir waves at much higher resolution than was possible for these earlier studies.

Galileo Observations from the Venus Flyby

The Langmuir waves presented here were detected by the Galileo plasma wave instrument on February 10, 1990. For a review of the initial Galileo Venus observations, see Kivelson et al. [1991], Gurnett et al. [1991], Williams et al. [1991], and Frank et al.

[1991]. Figure 20 shows a sketch of the trajectory of Galileo during the gravity assist flyby of Venus. A model bow shock is also shown in Figure 20. This model bow shock is included only to provide an estimate of the location and shape of the bow shock. The Galileo magnetometer data showed that Galileo skimmed along the edge of the bow shock, entering and exiting the magnetosheath many times [Kivelson et al., 1991]. Figure 21 shows the frequency-time spectrograms of the electric and magnetic field intensities obtained from the medium- and low-frequency receivers, which provide low-rate measurements in 116 channels from 5 Hz to 160 kHz. Four bow shock crossings determined by the magnetometer experiment [Kivelson et al., 1991] are shown by arrows at the top of Figure 21, along with the corresponding plasma regions. The slight offset of the arrows from the increase in the electric and magnetic field noise levels in the spectrogram (a characteristic of magnetosheath crossings) is due to the sweep time of the receivers and the size of the pixels. The multiple shock crossings are caused by the bow shock moving back and forth over the spacecraft [Kivelson et al., 1991]. The Langmuir waves can be seen in the upper panel (electric field spectrum) starting at about 0450 UT, in the 10- to 50-kHz frequency band. A weak Langmuir wave signal can also be seen between the shocks, from about 0440 to 0447 UT, also in the 10- to 50-kHz frequency band. At least two types of oscillations can be seen, one consisting of a nearly steady line at a frequency of about 43 kHz, which is believed to be the electron plasma frequency f_{pe} and a second component that is shifted both downward and upward in frequency from f_{pe} . The identification of 43 kHz as the electron plasma frequency is in good agreement with the Galileo plasma instrument, which measured an electron density of $\sim 22 \text{ cm}^{-3}$ ($f_{pe} \sim 42 \text{ kHz}$) for the time interval from 0448 to 0638 UT [Frank et al., 1991]. The 43-kHz component is most easily observed after the last

shock crossing, starting at approximately 0450 UT and continuing sporadically until approximately 0525 UT. A very weak 43-kHz signal can also be seen between the two magnetosheath crossings, from about 0441 to 0444 UT. The upshifts and downshifts in frequency are most easily observed from approximately 0450 to 0502 UT, from 0505 to 0512 UT, and at 0524 UT. The Langmuir waves are believed to be produced by electrons streaming from the bow shock into the solar wind along the magnetic field lines. Magnetic field-aligned electron fluxes propagating upstream from the bow shock to the spacecraft at energies above ~ 100 eV have been reported by the Galileo plasma instrument [Frank et al., 1991].

The structure of the Langmuir waves can be observed in much greater detail using data from the wideband waveform receiver. During the Venus flyby, most of the data (approximately 28 minutes) consist of blocks of 128 contiguous samples lasting 0.63 ms (Mode 3). Two blocks of the higher resolution Mode 1 data, each approximately 78 seconds long, were also recorded, one near the beginning of the measurement interval (04:33 UT) and the other at the end (05:23 UT). One waveform block is captured every 66.67 ms, for both cases, with a gap of 66.04 and 58.85 ms, respectively, between successive waveforms (see the Instrument and Data section for more detail).

Figure 22 shows a 50-second spectrogram produced from the higher resolution waveforms (Mode 1). The Langmuir waves can be most easily seen as the bursty signals that start approximately 12 seconds into the spectrogram. A weak signal at approximately 43 kHz can also be observed a few seconds before the onset of the much stronger emission. The Langmuir waves show large upshifts and downshifts in frequency from the electron plasma frequency, which was estimated to be approximately 43 kHz during this interval.

The upshifts and downshifts can be as large as 20 kHz. The Langmuir waves also show extremely rapid temporal variations, many with time scales smaller than the time between successive waveform blocks (66.67 ms).

The top panel of Figure 23 shows a frequency-time spectrogram of the low-resolution waveforms (Mode 3). This spectrogram shows the entire low-resolution data set. Note that the time scale is now in minutes, and the total interval displayed is 30 minutes, from 0435 to 0505 UT. The signals are composed of two components, a weak narrowband component near the plasma frequency, and a stronger broader bandwidth component that shows large upshifts and downshifts in frequency. The middle panel of Figure 23 shows the depth parameter (see Figure 17) as determined from the measured solar wind magnetic field and a model bow shock [Kivelson et al., 1991]. Note that the depth and up distance defined in the caption of Figure 5 from Kivelson et al. [1991] is incorrect. Depth is defined as positive when the spacecraft is antisunward of the upstream foreshock boundary, and up distance is negative in the antisunward direction from the tangent point.

The uncertainty in the depth parameter was estimated by varying the terminator shock distance. Using as an upper limit the range of $0.1 R_V$ as a function of θ_{bn} found by Zhang et al. [1991] for the terminator crossing distances, the eccentricity and semi-latus rectum of the shock model was modified in order to maintain a fixed sub-polar distance of the shock. The shock model terminator distance ranged from 2.309 to $2.409 R_V$, corresponding to eccentricities of 0.925 to 0.995 . The referenced shock has a terminator distance of $2.359 R_V$, eccentricity of 0.96 , sub-polar distance of $1.425 R_V$, and focus offset of $0.4 R_V$. These changes in the shock shape have the largest effect on the depth parameter for large distances downstream of the sub-solar point. The projected field line encounters

the shock around $x = -5 R_V$ when the depth is near zero in Figure 23, and the uncertainty in the depth parameter is largest here. Furthermore, in determining the range, this analysis assumes that θ_{bn} varies from 0° to 90° , but since the field is nearly tangent to the shock surface, $\theta_{bn} \sim 90^\circ$ for depth ~ 0 . Thus the errors bars give an upper limit to the range in depth.

As can be seen from Figure 23, the magnitude of the depth parameter and the shifts in the frequency of the Langmuir waves are correlated. The correlation is especially evident after 0450 UT. As the depth parameter increases from approximately 0450 to 0453 UT, the Langmuir waves shift downward in frequency. From approximately 0453 to 0500 UT, the Langmuir waves shift upward in frequency as the magnitude of the depth parameter decreases. From approximately 0500 to 0503 UT, the depth parameter is small ($\sim 1 R_V$) and the Langmuir waves shift upward in frequency. The correlation before 0450 UT is not as good. During this interval, the uncertainties in the depth parameter and the multiple crossings of the bow shock make it difficult to compare the depth parameter and the Langmuir waves. The correlation of the depth parameter with the downshifts and upshifts in frequency observed at Venus is very similar to the correlation observed in earlier studies at Earth [Fuselier et al., 1985]. This correlation is believed to be related to the speed of the electron beams producing the Langmuir waves [Etcheto and Faucheux, 1984; Fuselier et al., 1985; Lacombe et al., 1985]. Beam speeds on the order of the thermal velocity (expected at large depth parameters) are believed responsible for the downshifted emissions. Beam speeds of a few times the thermal speed (expected at moderate depth parameter) are believed to produce the upshifted emissions (see Figure 19). The large upshifts in frequencies observed at Venus cannot be explained using Figure 19. More recent work by Cairns

[1987c, 1989], Cairns and Fung [1988], and Dum [1990a, b and c] have shown that the relationship between the frequency of maximum growth and the beam velocity can vary depending on the plasma and beam parameters. The primary parameters that affects the relationship are the beam density n_b , the beam temperature T_b , and the shape of the distribution function of the beam (e.g., Maxwellian or Lorentz). For example, Dum [1990c] showed that a very cold Maxwellian beam ($n_b/n_e = 0.05$) can produce Langmuir waves at frequencies much above the plasma frequency ($\sim 1.5 f_{pe}$). Further work is required to determine if the plasma and beam parameters at Venus can account for the large upshifts in frequency.

The origin of the narrowband emission near the plasma frequency from approximately 0441 to 0446 UT and 0452 to 0459 UT is not as well understood. The low intensity and steadiness of the emission during these intervals are suggestive of thermally excited Langmuir waves. Meyer-Vernet and Perche [1989] present analytical expressions and numerical results of the thermally excited Langmuir waves for a range of plasma conditions and ratios of the effective antenna length to the Debye length (L_{eff}/λ_D). Their spectrum of thermally excited Langmuir waves (their Figure 8) has the same basic shape as the observed narrowband emission (assuming a bi-Maxwellian plasma with a ratio of the temperature of the hot component to the cold component = 100, and $L_{eff}/\lambda_D = 1$). However, their predicted electric field intensities are smaller than the observed electric field intensities by approximately a factor of ten. Also, four intervals (0439-0441 UT, 0447-0448 UT, 0449-0450 UT, and 0502-0503 UT) exist in Figure 23 where the narrowband emission disappears as the depth parameter goes to zero, which corresponds to Galileo leaving the foreshock. The first two intervals correspond to times when Galileo entered the

magnetosheath [Kivelson et al., 1991]. The absence of a signal during these intervals can be explained by the decrease in the gain of the wideband receiver due to the strong broadband low-frequency signals that are present in this region (see Figure 21). During the last two intervals, Galileo is believed to be upstream of the tangent field line and no longer in the foreshock region. Although the depth parameter is still positive for the last interval, the characteristics of the electric and magnetic field spectrum from Figure 21 suggests that Galileo briefly exited the foreshock. This disappearance of the narrowband signal as Galileo exits the foreshock is not expected. The model of the thermally excited Langmuir emissions assumes only a bi-Maxwellian plasma and does not take into account the presence of an electron beam. It is possible that the presence of a weak electron beam enhances the thermal emission. The discrepancy between the observed emission intensities and the theory could possibly be removed by redoing the analysis of Meyer-Vernet and Perche [1989] for the specific conditions encountered by Galileo during this interval. In particular, a detailed analysis of the Galileo antenna configuration (the Galileo antenna is not a simple linear wire dipole antenna) and using the actual L_{eff}/λ_D value of ~ 0.4 would improve the model. Also, using the actual plasma parameters and electron distribution functions found in the foreshock region and in the solar wind at Venus would provide a much better model to determine if the observed emissions are thermally excited Langmuir emissions.

An alternative explanation of the origin of the narrowband emissions has been proposed by Onsager and Holzworth [1990]. They suggest that long-wavelength, weakly damped Langmuir waves generated at the upstream foreshock boundary are convected downstream by the solar wind. Their measurements at Earth's foreshock using the AMPTE spacecraft have features (their Figure 1) that are very similar to those seen in the top panel

of Figure 23. However, the electric field intensity of the emission at the plasma frequency was usually larger than the electric field intensity of the downshifted emissions. The opposite was observed at Venus. The electric field intensity of the downshifted emissions observed upstream of Venus was usually larger than the intensity of the emission at the plasma frequency.

A similar model of downstream waves based on convection from the upstream foreshock boundary has been proposed by Robinson and Newman [1991]. In their model, wave packets are formed near the foreshock boundary by nonlinear strong-turbulence effects. These wave packets convect downstream with the solar wind while collapsing to short scale lengths and high electric field intensities, much higher than the electric fields observed at Venus. This model was developed to account for the distribution of the most intense plasma waves observed at Earth's electron foreshock, and does not predict the weak emissions that are observed at Venus.

A fourth possible explanation for the narrowband emissions is that high-speed electron beams are present at the same time as the slow-speed electron beams. The high-speed beam could produce the emission near the plasma frequency, and the slow beam could produce the downshifted emissions. However, high-speed beams usually produce more intense, bursty Langmuir waves than the observed weak narrowband emission. Further work is required to determine the exact process, or processes, that produce the narrowband emission near the plasma frequency.

To study the fine structure of the Langmuir waves, the individual waveform blocks were examined. Approximately 28,000 waveform blocks were captured by the wideband waveform receiver at Venus, of which approximately 2360 were Mode 1 (7.82-ms blocks),

and 25,800 were Mode 3 (0.63-ms blocks). Figure 24 shows four of the Mode 1 waveform blocks. As can be seen, the waveforms show considerable variations and are similar to the Langmuir waveforms observed in association with the type III burst (Figure 9). The high-frequency quasi-sinusoidal oscillations are Langmuir waves. The most striking feature in the waveforms is the beat-type waveforms. Panel (a) and (d) show a string of wave packets that are suggestive of interference between two nearly monochromatic waves of comparable amplitude. Further evidence of the interference hypothesis can be obtained from the spectrum of the beat-type waveforms. Figure 25 shows the spectrum of the waveform from panel (d). Two distinct frequency components, one at approximately 45.5 kHz and the other at approximately 48.3 kHz are observed. The frequency difference of these two signals agrees with the observed beat frequency (~ 2.8 kHz). The frequency of the beat pattern varies throughout the data set, from approximately 0.15 to 7 kHz. Beat frequencies below 0.15 kHz may occur, but the gaps between waveform blocks prevent any determination of lower frequency characteristics. Panel (c) suggests a beat-like waveform of a lower frequency, or possibly an isolated wavepacket. The limited length of the waveform blocks and the 58.85-ms data gap between blocks prevent the determination of the exact characteristics of waveforms of this type.

Panel (b) of Figure 24 shows a more chaotic waveform. It should be noted that "chaotic" in this context refers to the disorganized state of the waveform, and not to the theories of Chaos. A weak beat pattern can often be observed in this type of waveform, but it is not as evident as cases similar to panels (a) and (d). The bottom panel of Figure 26 shows an example of a chaotic-type waveform with very little beat pattern. The spectrum of the waveform is shown in the top panel of Figure 26. The spectrum exhibits a narrowband

signal at ~ 42.5 kHz (believed to be the plasma frequency), and a broader signal upshifted in frequency, centered at approximately 54 kHz. Chaotic-type waveforms were not observed during the type III event, but are frequently observed at Venus during periods with large upshifts and downshifts in the Langmuir wave emission frequency.

Electric Field Amplitudes

During the Venus flyby, AGC values were available for 1770 waveform blocks, and of these, 601 had distinguishable Langmuir wave emissions. Each of the 601 waveform blocks were examined to determine the peak electric field amplitude using the method discussed in the Instrument and Data section. Approximately 9% of the 601 waveforms that have corresponding AGC values were clipped in some manner, but none of these waveforms were so severely clipped that the peak amplitude could not be estimated by extrapolating the waveform envelope beyond the plot. The results of this survey are shown in Figure 27. As can be seen, the largest peak electric field amplitude was a little over 1 mV/m, which corresponds to an energy density ratio of approximately 10^{-8} . The majority of the amplitudes ranged between 0.003 and 0.1 mV/m (energy density ratios of 10^{-13} to 10^{-11}). These results are in good agreement with the Pioneer Venus electric field measurements reported by Crawford et al. [1990]. The flattening of the distribution at approximately 0.05 mV/m, and the sharp drop off in the number of events below 0.01 mV/m is probably caused by the background noise level (due to the receiver noise level and other low-level signals), which makes it difficult to measure weak field strengths, especially for the low-resolution waveforms (Mode 3).

The distribution of the electric field amplitudes depends partially on the location of Galileo in the foreshock. The bottom panel of Figure 23 shows the variation over time of

the peak electric field strength of the Langmuir waves shown in Figure 27. The largest amplitudes tend to occur during periods of small depth parameters (for example 04:38.5, 04:47 to 04:51 and 05:02 UT). These intervals correspond to times when the spacecraft is near the upstream foreshock boundary. This correlation agrees with results obtained at Venus [Crawford et al., 1990, 1991] and at Earth [Filbert and Kellogg, 1979; Etcheto and Faucheux, 1984; Fuselier et al., 1985; Lacombe et al., 1985] which showed that the largest electric field amplitudes are observed near the upstream foreshock boundary.

Fine Structure

The characteristics of the Langmuir wave fine structure observed upstream of the bow shock of Venus were also surveyed. Unfortunately, most of the data obtained at Venus is the lower-resolution Mode 3 data. The 0.63-ms length of the waveform block and the 66.04-ms gap between waveform blocks in the Mode-3 data greatly limit the ability to determine the size and characteristics of the fine structure for this mode. Because of these limitations, only a survey of the higher-resolution Mode 1 data obtained at 05:23 UT are presented in this study. The 78-second interval of the Mode 1 data contains 1198 waveform blocks, of which 576 contain distinguishable Langmuir wave emissions. Figure 22 shows a frequency-time spectrogram of the first 50 seconds of this interval. The same four basic types of waveforms used in the type III fine structure survey discussed earlier are used to categorize the waveforms obtained at Venus. The first type is defined as waveforms containing at least one wave packet completely contained within the waveform block (e.g., Figure 24a, c and d). Approximately 15 % of the waveforms have structure of this type (referred to as "< 8 ms" structure). The waveforms with structure "< 8 ms" were further categorized between beat-type waveforms (e.g., Figures 24b and d) and "others" (e.g.,

Figure 24c). The second type consists of waveforms containing structure, but complete wave packets are not captured in the 7.82-ms block (e.g., Figures 9d and 3a). This structure type is referred to as "> 8 ms" structure and consists of 24.7% of the waveform blocks. Some of the "> 8 ms" waveforms appear to be beat-type waveforms with periods greater than 8 ms (e.g., Figure 9d). Unfortunately, the gap between waveform blocks makes it difficult to determine the exact structure of these waveforms. The third type contains Langmuir waves that are basically constant over the 7.82 ms (e.g., Figures 14a and 14b). Approximately 3.5% of the waveforms consist of this "constant over 8 ms" emissions. The large decrease in this type of waveform compared to the type III survey (see Table 3) is probably due to the higher intensity of background signals present at Venus. The background signals produce a great deal of variation in the waveforms. Approximately 15.1% of the waveforms consist of the fourth type, referred to as "weak" structure. This waveform type exhibits no obvious Langmuir wave signal in the waveform (Figure 11b), but a signal is observed in the spectrum near the plasma frequency (Figure 11a). One additional type of waveform (chaotic-type waveforms) is observed at Venus which was not observed during the type III event. Approximately 42% of the waveforms in this survey are of this type. The chaotic-type waveforms were further divided into "chaotic: beats" (Figure 24b) and "chaotic: no beats" (Figure 26). It should also be noted that the determination of the structure type for Langmuir waves is subject to some interpretation, especially between the "< 8 ms: beats" and the "chaotic: beats" types. A summary of the above results is shown in the first columns of Table 6. The last columns of Table 6 show the results when the waveform blocks with "weak" Langmuir wave emissions are removed.

Discussion

This chapter has used the very high-resolution waveform measurements captured by the Galileo plasma wave experiment to describe the fine structure of Langmuir waves in the solar wind upstream of the bow shock of Venus. Table 7 summarizes the plasma parameters and observed characteristics of the Langmuir waves for the Venus observations. The values shown in Table 7 (except for the solar wind ion temperature) were obtained from the instruments on Galileo. The ion temperature was estimated from the Pioneer Venus data provided by the NSSDC.

The Langmuir waves observed upstream of Venus contain both long-time scale structure (downshifts and upshifts in frequency) and short-time scale structure (beat-type wave packets). The shortest time scales consist mainly of highly coherent beat-type waveforms, with beat frequencies ranging from approximately 0.15 to 7 kHz. Little structure is observed at time scales less than about 0.15 ms. If we assume that the structures are convected by the spacecraft at the solar wind speed (~ 450 km/s), this time scale would correspond to a spatial scale of ~ 65 meters. This spatial cutoff is probably related to the Debye length. Using the solar wind parameters from Table 7, λ_D is found to be 8.2 m. Dividing λ_D by the solar wind speed, $100 \lambda_D$ gives 1.82 ms which is shown at the top of Figure 24. The short scale cutoff of 0.15 ms corresponds to a spatial scale of approximately 8 Debye lengths. The very fine structure of the waveforms observed upstream of Venus is very similar to the structure observed in association with the type III radio burst, and is suggestive of a similar nonlinear process.

Soliton Collapse

To determine if the fine structure of the Langmuir waves observed at Venus is caused by the strong nonlinear process of soliton collapse, the threshold voltage for collapse is found using Equations 6 and 7. Using the parameters shown in Table 7, the thresholds for soliton collapse are found to be $E_{\text{peak}} \geq 46.1 \lambda_D L^{-1} \text{ V m}^{-1}$ and $9.0 (\lambda_D L^{-1})^{1/2} \text{ V m}^{-1}$. Typical scale sizes of the smallest structure (see Figure 24) is on the order of $L = 100 \lambda_D$. This scale size yields thresholds of 461 mV m^{-1} and 900 mV m^{-1} respectively. These thresholds are over four hundred times larger than any of the measured values. If an electric field of 1 mV/m , which is the largest field that was measured, is assumed in Equation 6, a scale length $\geq 46,000 \lambda_D$ (842 ms) is needed for collapse to occur. The threshold determined from Equation 7 is much larger. Again using $E_{\text{peak}} = 1 \text{ mV m}^{-1}$, the threshold is $\geq 81 \times 10^6 \lambda_D$ ($1.47 \times 10^6 \text{ ms}$). These scale lengths are much larger than the observed fine structure (see Figure 24). It is possible that some of the waveform blocks that do not have corresponding AGC values could have a much higher amplitude than 1 mV/m , but it is doubtful that any have amplitudes as large as 461 mV m^{-1} . Furthermore, the field strength should increase with smaller structure ($E_{\text{peak}} \geq 4.61 \text{ V m}^{-1}$ and 2.85 V m^{-1} for $L = 10 \lambda$). Amplitudes of this magnitude would severely clip and distort the waveform receiver, and no severe distortion of this type was observed. Also, no correlation between the smallest structure sizes and largest fields is observed. Thus it appears that soliton collapse is not responsible for generating the fine structure of the Langmuir waves.

Parametric Decay

The beat-type waveforms (Figures 24a and d) are strongly suggestive of two waves of comparable amplitude, but slightly different frequency interfering with each other. One

possible source of the two waves is two Langmuir waves being excited by electron beams of different velocities. Variations of the electron beam velocities have been proposed to explain the downshifts and upshifts in frequency [Fuselier et al., 1985; Cairns, 1987c, 1989; Cairns and Fung, 1988; Fitzenreiter et al., 1990]. However, this explanation does not account for the many cases where the two waves are of comparable amplitudes. Random superposition of wave packets from waves excited by different velocity beams would not be expected to have the same amplitude. Different electron beam velocities probably account for much of the fine structure that is observed, especially the more chaotic beat-like waveforms (Figures 24b and 26). However, it is unlikely that it accounts for all of the beat-like waveforms.

Parametric decay is a more likely explanation of the beat-type waveforms. Evidence of parametric decay is given by the predicted electron beam velocities obtained from Equation 8. Using the parameters from Table 7, beat frequencies ranging from 200 to 7000 Hz, and $\theta \sim 55^\circ$ determined from the magnetometer data [Kivelson et al., 1991] for the interval of the high-resolution waveforms (Figure 22), Equation 8 predicts beam speeds of 61.5×10^6 to 2.1×10^6 m s⁻¹. These predicted beam speeds agree very well with the magnetic field aligned electron fluxes of 100 to 1000 eV (6×10^6 to 20×10^6 m/s) measured by the plasma instrument [Frank et al., 1991].

Parametric decay predicts that a low-frequency wave, probably an ion sound wave, should be observed. Even though there is no evidence of low-frequency waves related to Langmuir waves in Figure 22, an examination of the individual spectra of beat-type waveforms often shows a weak low-frequency signal. Figure 28 shows the spectrum of the waveform in panel (b) of Figure 24. As can be seen, there are two main peaks, one

centered at approximately 46 kHz, which is near the plasma frequency, and another that is upshifted in frequency, and centered at approximately 53 kHz. Each of the two main signals is broad in frequency and contains a great deal of structure. There is also a series of weak signals located from a few hundred Hz to about 9 kHz. The broadband signal located from approximately 6 to 8 kHz is the approximate frequency difference of the two main signals, and is in good agreement with the beat frequency observed in the waveform (~ 7 kHz). The low-frequency signals, especially the signals located at the observed beat frequencies, are strongly suggestive of the low-frequency ion sound waves predicted above. These signals are often very weak and do not appear in every beat-type waveform spectrum, which may explain why they are not observed in Figure 22. Also, since $T_i \sim T_e$ during this interval, the ion-sound waves should be quickly damped, limiting the ability of Galileo to observe the waves.

CHAPTER V

LANGMUIR WAVES UPSTREAM OF THE BOW SHOCK AT EARTH

High-frequency waves associated with nonthermal (few keV) electrons streaming into the solar wind from Earth's bow shock were first reported by Scarf et al. [1971] and Fredricks et al. [1971]. Later studies, including Gurnett and Frank [1975], Rodriguez and Gurnett [1975, 1976], Filbert and Kellogg [1979], and Anderson et al. [1981], showed that these waves were in fact Langmuir waves. These waves are electrostatic, polarized with the wave electric field parallel to the static magnetic field, and are observed only when the spacecraft is magnetically connected to the bow shock. Etcheto and Faucheux [1984] and Fuselier et al. [1985] found that the Langmuir waves exhibit considerable structure, both large scale structure (upshifts and downshifts in frequency) and short scale (bursty) structure. The Langmuir waves are usually most intense near the electron foreshock boundary, and become weaker and contain more large-scale structure with increasing distance downstream from the upstream foreshock boundary (increasing depth parameter). The range of field intensities reported in these earlier studies are hundreds of $\mu\text{V m}^{-1}$ to about 10 mV m^{-1} . The measurement of the peak electric field intensities of the Langmuir waves, especially the short bursty structures, has been an area of debate for many years. The two Galileo gravity assist flybys provided an opportunity to study these Langmuir waves at much higher resolution than was possible for these earlier studies.

Galileo Observations at Earth

The Langmuir wave measurements presented here were obtained by the Galileo plasma wave experiment on December 8 to 9, 1990, and December 8, 1992. Figure 29 shows the trajectory of Galileo during the two gravity assist flybys of Earth. The model bow shock included in Figure 29 is for reference only, and no attempt has been made to verify the correct distance and position of the bow shock. During the first Earth flyby (E1 in Figure 29), Galileo exited the magnetosheath near the nose of the bow shock. During the second flyby (labelled E2 in Figure 29), Galileo exited the shock further downstream. The different trajectories allowed Galileo to obtain measurements in different parts of the foreshock.

Data from the First Earth Flyby

Figures 30 and 31 show frequency-time spectrograms of the electric field intensities obtained from the spectrum analyzer receivers as Galileo exited the bow shock during the first Earth flyby. Figure 30 shows a four-hour spectrogram, starting at 2200 UT on December 8, 1990. The bow shock crossing occurs at approximately 2234 UT, and is indicated by the broadband noise observed from approximately 5 Hz to 5 kHz. The Langmuir waves can be seen immediately after the bow shock crossing (~ 2334 UT) at about 42 kHz in the medium frequency spectrum analyzer receiver (middle panel of Figure 30). The Langmuir waves during this interval are very bursty in nature. Strong bursts of Langmuir waves can be seen at approximately 2258 UT, 0015 UT, 0025 UT, 0043 UT, and from 0118 to 0143 UT. The Langmuir waves show a great deal of structure, including large downshifts and upshifts in frequency, and are very broad in frequency. The narrowband signal at 40 kHz observed throughout most of Figure 30 is an interference

signal from the spacecraft, and not related to the Langmuir waves. A few weak type III bursts are observed in the upper panel of Figure 30 (high-frequency spectrum analyzer), but are not related to the Langmuir waves.

Figure 31 shows a 24-hour spectrogram starting at 0000 UT, December 9, 1990. The first two hours of Figure 31 corresponds to the last two hours of Figure 30. Two types of Langmuir wave emissions can be observed in Figure 31. The bursty Langmuir waves discussed above can be seen in the first two hours of the spectrogram. At approximately 0330 UT, a second type of Langmuir wave emission appears. This second type of emission is observed almost continually for the next five hours, with sporadic emissions observed for the next seven hours. This emission is less intense than the bursty emissions and the large scale structure of the emissions is found in a narrow range in frequency. The frequency of the emission also decreases during this interval. The decrease in frequency is probably due to a decrease in the solar wind electron plasma density. This hypothesis is confirmed with an examination of the IMP-8 solar wind plasma density data. Table 8 shows the IMP-8 data provided by the NSSDC for the interval in which Langmuir waves are observed during the first Earth flyby. As can be seen, the solar wind plasma density (n_i) starts to decrease at approximately 0200 UT, December 9. The values of the plasma densities measured by IMP-8 over the interval Langmuir waves are observed agrees very well with the densities predicted from the observed frequency of the Langmuir waves.

The structure of the Langmuir waves can be more easily seen in the wideband data. Figure 32 shows a 123-minute spectrogram of wideband waveform data for the interval immediately after Galileo exited the bow shock. This period correspond to approximately the first two-hour interval of Figure 30. The Langmuir waves are the bursty signals that

start at approximately 2235 UT in the frequency range 40 kHz to 55 kHz. The spectrums presented in Figure 32 consist of data captured in two different modes (Mode 1 and Mode 2) of the wideband receiver. The majority of the spectrogram consists of the lower resolution Mode 2 data, with two intervals from approximately 2336 to 0008 UT and 0010 to 0013 UT of the higher resolution Mode 1 data. The improvement in frequency resolution of the Mode 1 data compared to the Mode 2 data can be most easily observed during the four intervals the wideband receiver was attached to the search coil antennas (2228-2234 UT, 2259-2304 UT, 2330-2235 UT, and 0100-0105 UT). The interference lines at 0100-0105 UT (Mode 1) are much narrower in frequency than the interference lines observed during the three earlier magnetic field spectrums (Mode 2). The signals between 60 and 100 kHz at two and three times the emission frequency of the intense Langmuir waves are most likely harmonic distortion due to clipping of the waveforms.

The structure of the Langmuir waves includes large upshifts and downshifts from the electron plasma frequency (estimated to be approximately 41 kHz at 2235 UT, decreasing to approximately 35 kHz at the end of the spectrum). Examples of these shifts in frequency can be seen from 2235-2237 (upshift) and 2238-2250 (downshift). The upshifts in frequency can be as large as 15 kHz (2236 UT), and the shift in frequency of the downshifts can be as large as 30 kHz (2238 UT to 2250 UT). The spectrum of the upshifted and downshifted Langmuir waves also exhibit large broadening in frequency, sometimes as much as 30 kHz.

The downshifts and upshifts in frequency are expected to be correlated with the position of the spacecraft in the foreshock region as was found at Venus (see Figure 23). The top panel of Figure 33 shows an expanded 30-minute spectrogram for an interval from Figure 32. Note that the frequency scale now goes from 9 to 60 kHz. The bottom panel

shows the depth parameter as determined by the Galileo magnetometer experiment [Kivelson and Khurana, personal communication]. The depth parameter was computed using a program that varies the shape and size of the shock according to the solar wind dynamic pressure and the magnetosonic Mach number as determined by the IMP-8 spacecraft as a function of time. The depth parameter is calculated from this model using the Galileo magnetic field measurements. Due to the fact that no electron temperature data are available, $T_e = T_i$ was assumed. As many of the parameters used in the calculation have to propagate from the upstream position of IMP-8 to the bow shock, some uncertainties in the time values associated with the depth parameter occur [Kivelson and Khurana, personal communication]. These uncertainties have been estimated to be on the order of a few minutes. Furthermore, the Galileo magnetometer experiment was in a calibration mode for the interval 22:00 (Dec 8) UT to 01:30 (Dec 9) UT. This calibration mode severely limited the resolution of the magnetic field data during this interval, making the determination of the depth parameter subject to further errors.

As can be seen in Figure 33, a correlation exists between the depth parameter and the shifts in frequency, but the correlation is not as good as the one observed at Venus (Figure 23). Many of the depth parameter variations corresponds to changes in the structure of the Langmuir wave spectrum. For example, during the interval when the emission is upshifted in frequency (2234:30 to 2237:30 UT), the depth parameter is $\sim 1.5 R_E$. At approximately 2237:30 UT, the depth parameter rapidly increases, and the Langmuir waves emission frequency shifts downward in frequency. During the next ten minutes, the depth parameter and the spectrum of the Langmuir waves vary a great deal. At approximately 2248:30 UT, the depth parameter increases to beyond $10 R_E$ and a corresponding decrease

in the Langmuir wave activity is observed. Although the correlation between the shifts in the Langmuir wave emission frequency and the depth parameter is not perfect, the differences can probably be explained by uncertainties in the calculated depth parameter.

Figure 34 shows an approximately five-hour wideband spectrogram starting at about 0338 UT, December 9, 1990. This spectrogram shows a portion of the Langmuir waves observed in Figure 31. The Langmuir wave emissions during this interval are more constant and narrowbanded in frequency. Although the emissions in Figure 34 show upshifts and downshifts in frequency and spectral broadening, the shifts ($\Delta f/f_{pe} \sim 0.2$) are much smaller than those observed in Figure 32 ($\Delta f/f_{pe} \sim 0.6$). The signals at two and three times the frequency of the main emission (0530 UT at ~ 42 kHz and ~ 64 kHz) are most likely instrumental effects caused by clipping in the receiver. The white strips (for example 0453 to 0508 UT) are intervals where no wideband data are available. There is also no wideband data available for the interval between Figures 32 and 34. Six intervals of magnetic field wideband data are also shown in Figure 34 (0405, 0508, 0535, 0606, 0737, and 0807 UT).

The extremely rapid temporal variations of the Langmuir waves can be more easily seen in Figures 35 to 38. Figure 35 shows a one-minute spectrogram of an interval with large downshifts in frequency from Figure 32 (~ 2351 UT). The spectrum consists of sporadic narrowband emissions near the plasma frequency (~ 39 kHz), and broadband upshifted and downshifted emissions. These emissions are similar to those observed at Venus (see the top panel of Figure 23). A large band of downshifted Langmuir waves is observed starting approximately 18 seconds into the spectrum, in the frequency range 10 kHz to 25 kHz. Upshifted emissions can be observed from about 28 to 35 seconds into Figure 35.

Figure 36 shows a high-resolution, one-minute spectrogram of several interesting Langmuir wave emissions observed at Earth. At the start of the spectrum, an intense band is observed at 32 kHz, with a weaker, more sporadic band at about 37 kHz. This two-banded spectrum is similar to the spectrum observed at Jupiter by Voyager 1 (see panel c of Plate 1 from Gurnett et al. [1981]). Approximately 23 seconds into the spectrogram, the two bands appear to shift up in frequency very rapidly. After this shift in emission frequency, the more intense band is now at approximately 37 kHz, and the upper band at about 45 kHz. A weak narrowband signal at the same frequency as the intense band appears in the upper band during the first 23 seconds of the spectrogram. One possible explanation of this weak narrowband emission may be that it is electromagnetic radiation produced at f_{pe} which has propagated from the region producing the higher frequency band. The lack of a similar weak signal associated with the 32 kHz emission could be due to the electromagnetic wave being quickly damped in the higher density plasma ($f < f_{pe}$). The spiky emissions at approximately two times the main emission bands are probably instrument effects, produced when the Langmuir wave signals are bursty and strong enough to clip the waveform receiver. The weak emission line at approximately 75 kHz may be electromagnetic radiation at $2f_{pe}$ [Hoang et al., 1981; Cairns and Melrose, 1985].

The abrupt shift in frequency of the emission approximately 23 seconds into Figure 36 is probably caused by a rapid increase in the electron plasma density. The frequency-time spectrogram in the top panel of Figure 39 shows that the shift in frequency observed in Figure 36 is part of a larger structure. This structure begins at approximately 0008:30 UT, where the frequency of the Langmuir waves suddenly decreases to ~ 30 kHz. It should be noted that the intervals 0008:00 to 0010:30 UT and 0013:20 to 0026:00 consist of lower

frequency resolution Mode 2 data. The increase in the frequency of the Langmuir waves at approximately 0011 UT corresponds to the shift in frequency shown in Figure 36. The downward shift in frequency of the Langmuir waves at approximately 0008:30 UT is correlated to the increase in the B_Z component and in the total magnetic field B_T shown in the middle four panels of Figure 39. The increase in the Langmuir wave frequency at approximately 0011 UT corresponds to the decrease in the B_Z component and in the total magnetic field B_T . No correlation is observed between the abrupt shifts in frequency and the depth parameter (bottom panel of Figure 39) during this interval. The abrupt cutoffs of the Langmuir emissions at about 0014:30 and 0016:00 UT, and the return of the emission at about 0015:00 and 0023:00 UT correlate very well with the depth parameter becoming negative (Galileo exiting and reentering the foreshock region). The weak signal at approximately 38 kHz during these periods may be thermally excited Langmuir waves or possible electromagnetic radiation produced at f_{pe} .

Figure 37 shows the one-minute interval that follows Figure 36. The two bands of emission continues for the first 14 seconds of the spectrogram. Approximately 14 seconds into the spectrogram, the intensity of the Langmuir wave emission decreases and the gain of the receiver increases. The gain increase is indicated by the increase in the intensity of the low-frequency signals (an examination of the AGC values for this interval confirms that the gain of the receiver has increased). The reduction in the wave intensity is probably due to a rotation of the solar wind magnetic field or a fluctuation of the bow shock position that caused Galileo to exit the electron foreshock region. The weak emission band at approximately 37 kHz may be electromagnetic radiation produced in the electron foreshock at f_{pe} which is propagating out of the foreshock region into the solar wind. Further

evidence for this hypothesis is the weak emission at $2f_{pe}$ (~ 74 kHz). This emission is probably electromagnetic radiation at $2f_{pe}$ produced by a similar process as discussed in association with the type III burst. Instrument effects due to clipping of the waveforms may account for some of the $2f_{pe}$ emission, but an examination of the waveforms during this interval reveals very little clipping. Although the signal at f_{pe} could be produced by thermally excited Langmuir waves, or by fluctuations in the solar wind magnetic field direction causing Galileo to briefly reentering the electron foreshock, neither of these two methods predicts the $2f_{pe}$ emission. Approximately 27 seconds into the spectrogram, the intensity of the Langmuir waves increase greatly, and the gain of the receiver decreases. It is believed that the magnetic field has rotated and Galileo has reentered the foreshock region. The narrowband Langmuir waves observed during this interval are the most intense emissions observed during the first Earth flyby. The narrowband, very intense emission is characteristic of Langmuir waves near the foreshock boundary [Etcheto and Faucheux, 1984; Fuselier et al., 1985]. Again, the signals at ~ 74 kHz (two times the frequency of the main band emission) are due to clipping in the receiver, although a weak electromagnetic $2f_{pe}$ emission may also be present.

Figure 38 shows a 1-minute spectrogram from the beginning of Figure 34. The Langmuir waves appear broader in frequency during this interval, with some upshifts and downshifts in frequency, although not as large as the shifts observed in Figure 35. The emissions during this interval are also less intense than the emissions shown in Figure 37. The approximate 10-second period of decreasing emission intensity is probably due to the spacecraft rotation (the spin period of Galileo is ~ 20 seconds).

To characterize the fine structure of the Langmuir waves, a large number of individual waveform blocks was studied. Approximately 460,000 waveform blocks were captured by the wideband waveform receiver at Earth during the 18 hours after Galileo exited the bow shock. Approximately 390,000 waveforms were "Mode 1" (7.82-ms blocks) and approximately 70,000 were "Mode 2" (1.07-ms blocks). Figure 40 shows four waveform blocks containing Langmuir wave emissions from the high-resolution data (Mode 1). As can be seen, the waveforms are very similar to the waveforms observed at Venus and in association with the type III burst. The high-frequency, quasi-sinusoidal waveforms evident in each of these plots are the Langmuir wave oscillations. Again the most striking feature is the beat-type waveforms. Panels (b) and (d) of Figure 40 show a string of wave packets that are suggestive of interference between two nearly monochromatic waves of comparable amplitude. Further evidence of the interference hypothesis can be obtained from the spectrum of the beat-type waveforms. Figures 41 and 42 show the waveform and spectrum of beat-type waveforms. Figure 41 shows the spectrum (top panel) of a beat-type waveform (bottom panel). Two distinct frequency components are observed, one at approximately 37 kHz and the other at approximately 42 kHz. A weak low-frequency signal is also observed at approximately 5 kHz. The frequency difference of these two signals, and the frequency of the low-frequency signal, agrees with the beat frequency (~ 5 kHz) of the waveform. Figure 42 shows the spectrum (top panel) of a lower frequency beat-type waveform (bottom panel). Again, two distinct frequency components are observed, one at approximately 37.1 kHz and the other at approximately 38.1 kHz. A weak low-frequency signal is also observed at approximately 1 kHz. The frequency difference of these two signals, and the frequency of the low-frequency signal, agrees with the beat frequency (~ 1

kHz) of the waveform. The frequency of the beat pattern varies throughout the data set, from approximately 0.15 to 7 kHz. Figure 40a suggests a beat-type waveform of a lower frequency or possibly an isolated wavepacket. The limited length of the waveform blocks and the 58.85-ms data gap between blocks prevent the determination of the exact characteristics of this waveform. Beat frequencies below 0.15 kHz probably occur, but the gaps between waveform blocks prevent any determination of lower frequency characteristics. Panel (c) of Figure 40 shows an isolated packet with a duration of ~ 2 ms. Isolated packets of this type are rare and are suggestive of soliton collapse.

Figure 43 shows an example of a chaotic-type waveform (bottom panel) and its spectrum (top panel) obtained during the first Earth flyby. A weak high-frequency beat pattern can be seen in the waveform. The spectrum consists of two broad signals centered at 21,500 and 27,500 Hz. The chaotic-type waveforms observed at the Earth are similar to the chaotic-type waveforms observed at Venus (Figures 24b and 26) and are common during periods of large upshifts or downshifts in the emission frequency of the Langmuir waves. The spectrum of the chaotic waveforms are usually broad in frequency, and can contain a very complex mixture of signals.

Electric Field Amplitudes

Langmuir waves were detected by Galileo for approximately 16 hours after exiting the bow shock during the first Earth flyby. During this interval, AGC values are available for over 30,000 waveform blocks. Approximately 8250 of the 30,000 waveform blocks with corresponding AGC have been examined, and of these, 3919 have distinguishable Langmuir wave emissions. This survey of electric field amplitudes includes the entire interval shown in Figure 32. The interval shown in Figure 32 contains the most intense

Langmuir waves observed during the Earth 1 flyby, as determined from the spectrum analyzer measurements and an examination of the AGC values. This interval contains 6508 waveform blocks with corresponding AGC values, of which 4501 are the low-resolution (Mode 2) blocks, and 2007 are the high-resolution (Mode 1) blocks. Langmuir wave emissions were observed in 2873 of the waveform blocks during the interval shown in Figure 32. The remainder of the 3919 waveform blocks (1046 total) which make up this survey are obtained during the interval shown in Figure 34. Each of the 3919 waveform blocks were examined to determine the peak electric field amplitude using the method discussed in the Instrument and Data Section. Twenty-six of the 3919 waveforms were so severely clipped that the peak amplitude could not be estimated by extrapolating the waveform envelope beyond the plot. The results of this survey are shown in Figure 44. Two lines are shown in the plot. The solid line gives the peak electric field strengths for the waveforms that can be measured directly, or by extrapolating the waveform envelope beyond the plot. The dashed line gives the lower limit of the field strengths for the severely clipped waveforms. The severely clipped waveforms represent only a small fraction ($\sim 0.7\%$) of the total number of waveforms. The largest peak electric field amplitude was 13.8 mV m^{-1} , which corresponds to an energy density ratio of approximately 10^{-5} . The amplitudes ranged between about 0.005 and 14 mV m^{-1} . These results are in good agreement with earlier studies [Filbert and Kellogg, 1979; Etcheto and Faucheux, 1984]. The flattening of the distribution at approximately 0.1 mV m^{-1} , and the sharp drop off in the number of events below 0.003 mV/m is probably caused by the background noise level (due to the receiver noise level and other low-level signals), which makes it difficult to measure weak field strengths, especially for the lower-resolution waveforms (Mode 2). The

distribution of the electric field intensities also depends on the location of the spacecraft in the foreshock. During periods the spacecraft is near the upstream foreshock boundary (small depth parameter), the Langmuir waves are usually very intense and exhibit a different distribution of electric field intensities than those observed during intervals of large down shifts in frequency (large depth parameter).

This variation in the distribution of intensities can be seen in Figure 45. The top panel of Figure 45 shows the spectrum of the Langmuir waves shown in Figure 32. The middle panel shows the depth parameter as determined by the Galileo magnetometer experiment and the bottom panel shows the variation of the peak electric field strength over time. As can be seen, the largest amplitudes tend to occur during intervals of small depth parameters (for example 2235, 2258, 2328, 0013, and 0025 UT). These intervals corresponds to times when the spacecraft is near the upstream foreshock boundary. This correlation agrees with results obtained at Venus [Crawford et al., 1990, 1991; Hospodarsky et al., 1994] and at Earth [Filbert and Kellogg, 1979; Etcheto and Faucheux, 1984; Fuselier et al., 1985; Lacombe et al., 1985], which showed that the largest electric field amplitudes were observed near the foreshock boundary.

Data from the Second Earth Flyby

Figure 46 shows a four-hour frequency-time spectrogram of the electric field intensities obtained from the spectrum analyzer receivers as Galileo exited the bow shock during the second Earth flyby on December 8, 1992. It should be remembered that the Galileo exited the magnetosheath further downstream during the second Earth flyby (see Figure 29), allowing a different region of the foreshock to be sampled. Galileo was in the magnetosheath from approximately 1706 to 1813 UT (characterized by the low-frequency

broadband noise observed during this time period). The Langmuir waves can be seen immediately after Galileo exited the bow shock at about 1813 UT in the middle panel of Figure 46 (medium-frequency spectrum analyzer). The Langmuir waves range in frequency from approximately 10 to 26 kHz, and show a great deal of structure. The Langmuir waves are easily observed for approximately 1.5 hours after exiting the bow shock, with only a few sporadic emissions from approximately 1930 to 2035 UT. The interval the Langmuir waves are observed during the Earth 2 flyby is much shorter (~ 2.5 hours) than the interval the Langmuir waves are observed during the first Earth flyby (~ 16 hours). Broadband low-frequency signals (5 Hz to about 200 Hz) are also observed during the intervals of Langmuir wave activity. The low-frequency signal can be easily seen from approximately 1815 to 1830 UT, 1837 to 1940 UT, and 2040 to 2048 UT in the bottom panel of Figure 46 (low-frequency spectrum analyzer). The low-frequency signal is believed to be related to ion beams in the foreshock region, implying that Galileo is in the ion foreshock. The broadband signal at approximately 2030 to 2100 UT in the frequency band 50 to 100 kHz is believed to be auroral kilometric radiation (AKR).

Figure 47 shows a 140-minute high-resolution wideband spectrogram of the Langmuir waves observed during the Earth 2 flyby. The bursty nature and the large spreading in frequency of the Langmuir waves can be easily seen in the first hour of the spectrogram. The sporadic signals from approximately 30 to 70 kHz during the first hour of the spectrogram are believed to be instrument distortion due to clipping in the receiver. The large spread in frequency is due to the large spread in the frequency of the Langmuir wave emissions as the distortion occurs at harmonics of the frequency of the clipped signal. An intense narrowband Langmuir wave emission is observed at approximately 1945 UT.

This interval contains the largest Langmuir wave electric field strengths observed by Galileo. Again, most of the signals at $2f_{pe}$ (~ 37 kHz) and $3f_{pe}$ (~ 55 kHz) during this interval is due to clipping in the receiver.

Figure 48 shows a 5-minute expanded high-resolution frequency-time spectrogram from near the beginning of Figure 47. Note the frequency axis for Figure 48 ranges from 2 to 52 kHz. The structure of the Langmuir waves is very complex, and shows a large range in emission frequency (~ 2 kHz to ~ 30 kHz). The frequency of the Langmuir wave emissions often appears to be modulated by a low-frequency wave with a period of approximately 15 seconds. This apparent modulation can be seen from about 1820 to 1821:30 UT. The frequency of the emission has the rough shape of a sawtooth waveform with a period of ~ 15 seconds. Figure 49 shows a 1-minute high-resolution spectrogram of this interval. Note the frequency axis now runs from 0 to 40 kHz. The Langmuir waves appear to consist of at least two types of emissions, a narrowband emission and a broader emission downshifted and upshifted in frequency from the narrowband emission. Both types of emissions ramp up and down in frequency with a period on the order of 15 seconds. This modulation is most easily seen in the first 30 seconds of the spectrogram. The emissions appear to peak in frequency at approximately 3, 19, and 35 seconds. This type of spectrum is suggestive of the Langmuir waves "mapping out" low-frequency density fluctuations. A possible source of density fluctuations is propagating MHD waves (magnetosonic mode) generated by the ion beams present in the ion foreshock [Fredericks et al., 1972; Leckband, 1992]. Evidence for MHD waves occurring during this interval is shown in Figure 50. Figure 50 shows 20-second GSE averages of the three components of the magnetic field (top three panels) and the total magnetic field (bottom panel) for the

interval immediately after Galileo exited the bow shock. As can be seen, the magnetic field contains a great deal of structure suggestive of MHD waves during the interval of chaotic Langmuir wave emission (approximately 1813 to 1930 UT).

Figure 51 shows a one-minute high-resolution spectrogram corresponding to the interval of intense Langmuir waves shown in Figure 47 at approximately 1945 UT. The intense narrowband emission is characteristic of Langmuir waves near the electron foreshock boundary. The most likely cause of the high intensities of the Langmuir wave emission is a rotation of the solar wind magnetic field that causes Galileo to reenter the electron foreshock region. An examination of the magnetometer data confirms this hypothesis. Figure 52 shows about 20 minutes of Galileo magnetometer data for the interval spanning Figure 51. The vertical line at 1945 UT shows the approximate time the Langmuir wave emissions begin in Figure 51. As can be seen, there is a decrease in the B_x and B_T magnetic fields, and the B_y magnetic component reverses direction. A similar decrease in B_x and B_T at approximately 1951:30 UT corresponds to the start time of the second short burst of Langmuir waves observed in Figure 47. Unfortunately, depth parameter values are not available to determine the exact position in the foreshock of Galileo during the second Earth flyby. The largest Langmuir wave electric field strengths observed by Galileo occur during this interval at approximately 37 seconds into the spectrogram.

Most of the signals occurring in Figure 51 at multiples of the Langmuir wave emission frequency ($f_{pe} \sim 19$ kHz) are caused by clipping in the waveform receiver. The weak emissions observed at twice the main emission frequency, with no corresponding emission at three times the main emission frequency, for example the weak signal from about 27 to 32 seconds into the plot at about 38 kHz, are probably electromagnetic $2f_{pe}$

emissions. Similar $2f_{pe}$ emissions have been observed at Earth [Gurnett 1975; Gurnett and Frank, 1975; Hoang et al., 1981] and are produced by nonlinear processes.

During the second Earth flyby, nine intervals of the almost continuous Mode 4 waveform data were obtained by utilizing the tape recorder on Galileo. These intervals are approximately 15 seconds long and are separated by approximately 15 minutes of Mode 1 data. Five of the Mode 4 data intervals (1826:35, 1841:45, 1856:55, 1912:05, 1927:15 UT) contain Langmuir wave emissions. Figures 53 and 54 show spectrograms of two of the Mode 4 data intervals. It should be noted that the length of the time axis is now approximately 7.5 seconds and the frequency axis has been cutoff at 30 kHz. The Mode 4 waveform data consist of 1600 contiguous samples lasting 7.94 ms, with a waveform block being captured every 8.33 ms, with a gap of 0.39 ms between successive waveforms. The spectrograms shown in Figures 53 and 54 are obtained by taking a Fourier transform of each of the waveform blocks, and then plotting the sequence of transform amplitudes in the form of a frequency-time spectrogram. These spectrograms are produced from the same number (910) of waveform blocks as the one-minute Mode 1 spectrograms (Figures 49 and 51), resulting in the highest time resolution data obtained by the Galileo plasma wave instrument.

Figure 53 shows the wide range of structure associated with the Langmuir waves observed during the second Earth flyby. The Langmuir waves range in frequency from approximately 3 kHz to > 25 kHz. The emissions are very spiky, with extremely rapid temporal variations down to the smallest timescale that can be resolved, which is the time between successive waveform blocks (8.33 ms). The Langmuir waves also show large frequency spreading, sometimes by as much as 15 kHz. As discussed above, this wide

range of structure is believed to be a product of the spacecraft location (far from the tangent field line implying slow electron beam speeds induced downshifts), and the presence of density fluctuations associated with MHD waves.

Figure 54 also shows a variety of Langmuir wave structure observed during the second Earth flyby. A narrowband signal is observed at what is believed to be the plasma frequency (~ 17 kHz). Two types of emissions appear to make up the narrowband emission. During the first ~ 4.5 seconds of the spectrum, the emission is weak and nearly continuous. These characteristics are suggestive of thermally excited Langmuir waves as discussed in association with Venus. At approximately 4.5 seconds, a more intense, broader in frequency, emission is observed, ending at approximately 5.7 seconds. This more intense emission is most likely due to Langmuir waves generated by electron beams propagating out from the bow shock. The intense, spiky emissions observed from ~ 5 kHz to ~ 16 kHz are suggestive of downshifted Langmuir waves. The narrowband emissions appear to be slightly modulated in frequency, with a slight rise in emission frequency at 2 seconds, then decreasing to approximately 16 kHz at 5.5 seconds. The emission frequency then increases to approximately 17 kHz at the end of the spectrum. The downshifted emission also appear to be modulated with approximately the same period. This modulation is suggestive of Galileo encountering a small density wave.

To examine the fine structure of the Langmuir waves, the individual waveform blocks were studied. Approximately 128,000 waveform blocks were captured by the wideband waveform receiver during the ~ 2.25 hours after Galileo exited the bow shock. Approximately 120,000 waveforms were Mode 1 (7.82-ms blocks, 58.85-ms data gap) and approximately 8000 were Mode 4 (7.94-ms blocks, 0.39-ms data gap). Figures 55, 56, 57

and 58 show examples of Mode 1 waveform blocks (bottom panel) and their spectrum (top panel). As can be seen, the waveforms are very similar to the waveforms observed at during the first Earth flyby, the Venus flyby, and in association with the type III burst. The most striking feature is the beat-type waveforms. The bottom panel of Figure 55 shows two wave packets that are suggestive of a beat between two nearly monochromatic waves of comparable amplitude. Further evidence of the beat hypothesis can be obtained from the spectrum of the beat-type waveforms (top panel). Two distinct frequency components, one at approximately 19.15 kHz and the other at approximately 19.4 kHz, are observed. A very weak low-frequency signal at approximately 0.25 kHz is also observed, although the weakness of the signal makes it difficult to determine if the signal is real. The frequency difference of these two signals and the frequency of the low-frequency signal agree with the observed beat frequency (~ 0.25 kHz) of the waveform. The frequency of the beat pattern varies throughout the data set, from approximately 0.15 to 5 kHz. Beat frequencies below 0.15 kHz probably occur, but the gaps between waveform blocks prevent any determination of lower frequency characteristics.

Figure 56 shows the spectrum (top panel) of a more chaotic beat-type waveform (bottom panel). The spectrum shown in Figure 56 is much broader than the spectrum in Figure 55. The chaotic beat-type waveforms of this type are usually associated with periods of large upshifts and downshifts in frequency of the Langmuir waves. An even more chaotic waveform is shown in the bottom panel of Figure 57. The spectrum shown in the top panel of Figure 57 consists of two broadband signals, both exhibiting a great deal of structure. Chaotic-type waveforms similar to Figures 56 and 57 have been observed at

Venus (Figures 24b and 26) and during the first Earth flyby (Figure 43), and make up most of the waveforms observed during the second Earth flyby.

Figure 58 shows a more "constant" waveform. The emission frequency and amplitude are basically steady during the 8-ms period of the waveform block. A low-frequency oscillation (~ 200 Hz) also appears to be present, producing the variation in the average value of the electric field. The spectrum shows a narrowband signal at what is believed to be the plasma frequency (~ 18.4 kHz). The limited length of the waveform blocks and the 58.85-ms data gap between blocks prevents the determination of the exact characteristics of this waveform.

Electric Field Amplitudes.

Langmuir waves were detected by Galileo for ~ 2.25 hours after exiting the bow shock during the second Earth flyby. AGC values are available for over 9000 waveform blocks during this interval. Approximately 1000 of the waveform blocks with corresponding AGC have been examined, and of these, 512 have distinguishable Langmuir wave emissions. This survey of electric field amplitudes includes the five Mode 4 intervals containing Langmuir waves discussed above, and the interval of intense Langmuir waves shown in Figure 51 (Mode 1 data). The interval shown in Figure 51 contains the most intense Langmuir waves observed during the Earth 2 flyby, as determined from the spectrum analyzer measurements and an examination of the AGC values. Each of the waveform blocks were examined to determine the peak electric field amplitude using the method discussed in the Instrument and Data Section. 14 of the 512 waveforms were so severely clipped that the peak amplitude could not be estimated by extrapolating the waveform envelope beyond the plot. The results of this survey are shown in Figure 59. Two lines are

shown in the plot. The solid line gives the peak electric field strengths for the waveforms that can be measured directly, or by extrapolating the waveform envelope beyond the plot. The dashed line gives the lower limit of the field strengths for the severely clipped waveforms. The severely clipped waveforms represent only a small fraction ($\sim 3\%$) of the total number of waveforms. The largest peak electric field amplitude was 35.5 mV m^{-1} , which corresponds to an energy density ratio of approximately 10^{-4} . The amplitudes ranged between about 0.005 and 35 mV m^{-1} . These results are in good agreement with the peak electric field amplitudes obtained during the first Earth flyby. The flattening of the distribution at approximately 0.3 mV m^{-1} and the sharp drop off in the number of events below 0.01 mV/m are probably caused by the background noise level (due to the receiver noise level and other low-level signals), which makes it difficult to measure weak field strengths. The distribution of the electric field intensities also depends on the type of emission being observed. The interval of the intense Langmuir waves shown in Figure 51 contains a higher percentage of the larger electric field amplitudes ($> 0.1 \text{ mV m}^{-1}$) than the Langmuir waves observed during intervals of large variation in emission frequency (first hour of Figure 47).

Discussion

This chapter has used the high-resolution waveform measurements obtained by the Galileo plasma wave instrument to describe the structure of the Langmuir waves observed in the solar wind upstream of Earth's bow shock. Tables 9 and 10 summarize the plasma parameters and characteristics of the Langmuir waves observed during the Earth 1 and Earth 2 flybys, respectively. When possible, the values were obtained from instruments on Galileo. However, the Galileo plasma instrument was not operating during the first Earth

flyby so the plasma parameters had to be obtained from other spacecraft, such as IMP-8. Due to the changes (see Table 8) of the solar wind parameters during the ~ 16 hours Langmuir waves were observed during the first Earth flyby, a range of values are given for many of the parameters shown in Table 9. Table 11 shows the NSSDC IMP-8 one-hour averages for day 343-344, 1992. The Langmuir waves observed during the Earth 2 flyby occur from approximately 1815 to 2045 (see Figure 46). Unfortunately, the interval the Langmuir waves were observed during the second Earth flyby corresponds to a data gap in the IMP-8 data. The solar wind speed and ion temperature shown in Table 10 were estimated from the IMP-8 values obtained at 2200 UT. The electron density was estimated from the observed frequency of the "main" Langmuir wave emission in Figure 51. The large variation in the frequency of the Langmuir wave emissions, especially during the 90 minutes following the bow shock crossing, makes the determination of the electron density during this period very difficult.

The Langmuir waves observed at both Earth flybys contain both long-time scale structure (the downshifts and upshifts in frequency) and short-time scale structure (beat-type wave packets). The shortest time scales consist mainly of highly coherent beat-type waveforms, with beat frequencies ranging from approximately 0.15 to 7 kHz for the first Earth flyby and 0.15 to 5 kHz for second Earth flyby. The largest beat frequencies are usually observed during periods of large upshifts or downshifts in the frequency of the Langmuir waves, and are usually found in the "chaotic" type waveforms. Little structure is observed at time scales less than about 0.15 and 0.2 ms, respectively. If we assume that the structures are convected by the spacecraft at the solar wind speed (~ 380 and ~ 680 km/s), these time scales would correspond to a spatial scales of ~ 57 and ~ 136 meters,

respectively. This spatial cutoff is probably related to the Debye length. Using the solar wind parameters shown in Tables 9 and 10, λ_D is found to be ~ 10 m for the first Earth flyby and ~ 12.6 m for the second Earth flyby. Dividing λ_D by the solar wind speed, $100 \lambda_D$ is found to be ~ 2.6 ms and ~ 1.9 . The short scale cutoff of 0.15 and 0.2 ms corresponds to a spatial scale of approximately 6 Debye lengths for Earth 1 and approximately 10 Debye lengths for Earth 2. These values for the short scale cutoff are similar to the value obtained at Venus ($\sim 8 \lambda_D$), but much smaller than the value obtained at the type III ($\sim 30 \lambda_D$). The very fine structure of the waveforms is suggestive of a nonlinear process.

Soliton Collapse

The few cases of isolated wavepackets (e.g., Figure 40c) are suggestive of a strong nonlinear process, such as soliton collapse. To determine if the fine structure of the Langmuir waves observed near the Earth is caused by a strong nonlinear process, the threshold voltages for collapse are found using Equation 6 and 7. Using the parameters from Table 9, the thresholds for soliton collapse for the first Earth flyby are found from Equation 6 to be $E_{\text{peak}} \geq (14.5 - 30.6) \lambda_D L^{-1} \text{ V m}^{-1}$ and from Equation 7 to be $E_{\text{peak}} \geq (2.46 - 6.12) (\lambda_D L^{-1})^{1/2} \text{ V m}^{-1}$. The spread in the threshold values are due to the variations of n_e and V_S during the flyby. A typical scale size of the smallest structure is approximately $L = 100 \lambda_D$ (see Figure 40). Using $L = 100 \lambda_D$, the thresholds are found to be (145 to 306) mV m $^{-1}$ and (246 to 612) mV m $^{-1}$, respectively. For the first Earth flyby, these thresholds are ten to sixty times larger than the largest measured value. If an electric field of 14 mV/m is assumed, which is approximately the largest electric field that was measured during the first Earth flyby, scale lengths of approximately $1036 \lambda_D$ (27 ms) and

$30,876 \lambda_D$ (802 ms) are needed in the most favorable cases for collapse to occur. This scale length is much larger than most of the fine structure observed during the first Earth flyby.

Using the parameters from Table 10, the thresholds for soliton collapse are found for the second Earth flyby from Equation 6 to be $E_{\text{peak}} \geq 14.5 \lambda_D L^{-1} \text{ V m}^{-1}$ and from Equation 7 to be $E_{\text{peak}} \geq 2.83 (\lambda_D L^{-1})^{1/2} \text{ V m}^{-1}$. Again using a scale size of $L = 100 \lambda_D$, the thresholds are found to be 145 and 283 mV m^{-1} , respectively. For the second Earth flyby, the calculated thresholds are four to eight times larger than the largest measured value. If an electric field of 36 mV/m is assumed, which is the largest measured field during the second Earth flyby, a scale length of approximately $400 \lambda_D$ (6.7 ms) and $6180 \lambda_D$ (117 ms) is needed for collapse to occur. Although the maximum electric fields observed during the Earth flybys are much closer to the necessary threshold for soliton collapse than the observations associated with the type III burst and at Venus, the amplitudes are still too small for soliton collapse to be occurring. Furthermore, the field strength should increase with smaller structure. Assuming $L = 10 \lambda_D$, the thresholds are $E_{\text{peak}} \geq (1.45\text{-}3.06) \text{ V m}^{-1}$ and $(0.78\text{-}1.94) \text{ mV m}^{-1}$ for the first Earth flyby, and $E_{\text{peak}} \geq 1.45 \text{ mV m}^{-1}$ and 0.89 mV m^{-1} for the second Earth flyby. Amplitudes of this magnitude would severely clip and distort the waveform receiver, and no severe distortion of this type was observed. Also, no correlation between the smallest structure sizes and the largest field strengths is observed during the Earth flybys. Thus it appears that soliton collapse is not responsible for generating the fine structure of the Langmuir waves upstream of Earth's bow shock.

Parametric Decay

The beat-type waveforms (e.g., Figures 41, 42, and 55) are strongly suggestive of two waves of comparable amplitude, but slightly different frequency interfering with each other. Evidence that the waveforms consist of two nearly monochromatic components can be obtained by examining the spectrum of the individual waveforms. Figure 41 shows the spectrum (top panel) of a beat-type waveform (bottom panel) from the first Earth flyby. As can be seen, the spectrum consists of two sharply defined emission lines, one at approximately 37 kHz and the other at approximately 42 kHz. A weak low-frequency signal is also observed at approximately 4.8 kHz. The frequency difference of these two signals, and the frequency of the low-frequency signal, agrees with the observed beat frequency (~ 4.8 kHz) of the waveform. Figure 42 shows the spectrum (top panel) of a lower frequency beat-type waveform (bottom panel). Again, two distinct frequency components, one at approximately 37.1 kHz and the other at approximately 38.1 kHz are observed. A weak low-frequency signal is also observed at approximately 1 kHz. The spectrums of the beat-type waveforms obtained during the second Earth flyby also show two sharply defined emission lines separated by the beat frequency. Figure 55 shows the spectrum (top panel) of a beat-type waveform (bottom panel) from the second Earth flyby. Two distinct frequency components, one at approximately 19.15 kHz and the other at approximately 19.4 kHz are observed.

One possible explanation of the beat-type waveforms is that two Langmuir waves are being excited by electron beams of different velocities. Variations of the electron beam velocities are believed to be responsible for the downshifts and upshifts in the Langmuir wave emission frequency [Fuselier et al., 1985; Cairns, 1987c, 1989; Fitzenreiter et al.,

1990]. However, this explanation does not account for the fact that in most cases the two waves have comparable amplitudes. Random superposition of wave packets excited by different velocity beams would not be expected to have the same amplitude. Different electron beam velocities probably account for much of the fine structure that is observed upstream of the Earth, especially the chaotic-type waveforms (Figures 43, 55, and 56). However, it is unlikely that it accounts for the beat-type waveforms.

The three wave parametric decay process is the most likely explanation for the beat-type waveforms. Evidence of parametric decay is given by the predicted electron beam velocities obtained from Equation 8. For the first Earth flyby, using the average values from Table 9 ($f_{pe} = 31,000$ Hz, $V_{sw} = 3.8 \times 10^5$ m s⁻¹, $V_e = 1.5 \times 10^6$ m s⁻¹, $V_S = 5.2 \times 10^4$ m s⁻¹), beat frequencies ranging from 200 to 5000 Hz, and $\theta \sim 45^\circ$, Equation 8 predicts beam speeds of 56×10^6 to 2.6×10^6 m s⁻¹. For the second Earth flyby, using the values from Table 10 ($f_{pe} = 20,000$ Hz, $V_{sw} = 6.8 \times 10^5$ m s⁻¹, $V_e = 1.5 \times 10^6$ m s⁻¹, $V_S = 5.7 \times 10^4$ m s⁻¹), beat frequencies ranging from 200 to 5000 Hz, and $\theta \sim 45^\circ$, Equation 8 predicts beam speeds of 56.4×10^6 to 3.3×10^6 m s⁻¹. These predicted beam speeds agree very well with the beam speeds of 6×10^6 to 23×10^6 m s⁻¹ associated with Langmuir waves reported by Anderson et al. [1981] using data from the ISEE-1 spacecraft.

Parametric decay also predicts that a low-frequency wave is produced. Previous studies [Anderson et al., 1981; Onsager and Holzworth, 1990] have observed ion sound waves in association with Langmuir wave upstream of the bow shock of the Earth. An examination of the spectrums of the individual beat-type waveforms often show weak, low-frequency signals at the beat frequency. The spectrums of the beat-type waveforms shown in Figures 41, 42, and 55 all contain low frequency signals at the beat frequency. These

low-frequency signals are strongly suggestive of the low-frequency ion sound waves predicted by the parametric decay theory. The Galileo electric antenna, 6.6 m tip-to-tip, is considerably shorter than the antenna used by Anderson et al. [1981] (215 m tip-to-tip) and by Onsager and Holzworth [1990] (47 m tip-to-tip), which may explain the why these low-frequency waves are so weak. Also, if the ion temperatures are of the same order as the electron temperature, the low-frequency waves will be strongly damped out. Unfortunately, the electron temperature is not known for this interval, so the damping cannot be evaluated.

CHAPTER VI

CONCLUSIONS

This thesis has examined the characteristics and fine structure of Langmuir waves observed by the wideband plasma wave instrument on the Galileo spacecraft under a variety of conditions. This study included Langmuir waves observed in association with a type III solar radio burst and Langmuir waves observed upstream of the bow shocks of Venus and Earth. Although the Langmuir waves are produced under substantially different conditions, they share many similar characteristics. The most striking similarity is the occurrence of beat-like structures with beat frequencies ranging from approximately 150 to 650 Hz for the type III event, and from approximately 150 to 7000 Hz in the regions upstream of the bow shocks at Earth and Venus. The beat-type waveforms observed near the tangent field lines of the Earth and Venus are usually very similar to the beat-type waveforms observed in association with the type III burst. However, Langmuir waves observed further downstream from the foreshock boundary (large depth parameter) usually exhibited a more chaotic-type waveform. Chaotic-type waveforms of this type are not observed at the type III burst. The smallest observed fine structure of the Langmuir waves corresponds to spatial scales of $\sim 30 \lambda_D$ for the type III burst, and $\sim 10 \lambda_D$ for Earth and Venus. The electric field strengths of the Langmuir waves in all three regions ranged from approximately 0.005 to 10 mV m⁻¹.

A survey of the peak electric field strengths of the Langmuir waves was performed for the three regions where Langmuir waves were observed to determine the importance of a strong turbulent process in explaining the fine structure. The peak field strengths were

generally in the range from 1 to 30 mv m^{-1} , which in all cases are too small for a strong nonlinear process to be important. Also, the predicted relationship between the structure size and the electric field strength that should exist during the collapse process was not observed. Thus it appears that soliton collapse is not responsible for generating the fine structure of the Langmuir waves observed in this study.

The beat-type waveforms are found to be consistent with the predictions of a three-wave parametric decay process. The evidence for parametric decay consist of the following.

- (1) Parametric decay explains why the two waves responsible for the beat-type waveforms have similar amplitudes.
- (2) The beam speeds determined from the theory agree well with the beam speeds observed by Galileo at Venus, by earlier studies at Earth, and from simple time-of-flight estimates during a type III burst.
- (3) The beam speeds are below the upper velocity limit required for parametric decay and are in the proper range for the most rapid parametric decay.
- (4) Low-frequency waves suggestive of the ion sound wave predicted by the parametric decay theory are observed in conjunction with many of the beat-type waveforms.
- (5) The evolution in the beat frequency during the type III burst agrees with the temporal evolution predicted by the parametric decay theory.

Although a similar trend should also occur upstream of the bow shocks of Venus and Earth, the large downshifts and upshifts in the frequency of the Langmuir waves makes it very difficult to resolve the evolution of the beat frequency produced by parametric decay from that produced by slow electron beams. These results strongly indicate that three-wave parametric decay is the mechanism responsible for the beat-type Langmuir wave emissions observed in association with type III radio emissions and upstream of the bow shocks of Venus and Earth.

The Langmuir wave observations at Earth and Venus are found to contain large upshifts and downshifts in the emission frequency. These shifts in frequency are found to be correlated to the downstream distance from the tangent field line. Near the upper edge of the foreshock boundary, the Langmuir waves are found in a narrow band near the plasma frequency. For moderate distances from the tangent field line (a few R_V or R_E), the Langmuir waves are found to shift up in frequency. For larger distances, the Langmuir waves shift down in frequency. This correlation implies that the shifts in frequency are controlled by the velocity of the electron beam producing the Langmuir waves. Langmuir waves observed upstream of Earth's bow shock during the second gravity assist flyby on December 8, 1992, also showed large frequency variations which appear to be produced by fluctuations in the electron plasma density. The likely source of the variations is MHD wave-induced density fluctuations. Further work is needed to verify the correlation between the variations in the frequency of the Langmuir wave and the MHD waves observed by the magnetometer experiment.

Future missions (e.g., the Cluster mission) should provide further tests of these results. The four Cluster spacecraft, to be launched in 1995, should encounter both Langmuir waves associated with type III solar radio bursts and Langmuir waves upstream of the Earth's bow shock. Each of the Cluster spacecraft contain improved wideband waveform receivers. The two main improvements are the use of programmable digital gain amplifiers and eight-bit analog-to-digital (A/D) converters. The digital gain amplifiers allows the gain setting of the instrument to be known at all times, which will allow the electric field strength to be determined for entire data set. The eight-bit digitization will provide a dynamic range of 48 dB, compared to the 24 dB for Galileo, thereby increasing

the resolution of the measurements. Furthermore, multiple measurements of the same Langmuir wave structure by the four Cluster spacecraft should allow detailed analysis of the flow speed, structure size, and evolution of the Langmuir waves. This, and other future missions should improve our understanding of the nonlinear characteristics of these waves.

Table 1. Wideband Waveform Receiver Modes

Mode	# of Samples	Length of Waveform Blocks (ms)	Gap Between Waveform Blocks (ms)	FFT Resolution (Hz)
1	1576	7.82	58.85	128
2	216	1.07	65.60	933
3	128	0.63	66.04	1575
4	1600	7.94	0.39	126

Table 2. Energetic Particle Experiment

Channel Name	Energy Range (keV)
E0	15 - 29
E1	29 - 42
E2	42 - 55
E3	55 - 93

Table 3. Characteristics of the Langmuir Wave Emissions: Type III

	All		No Weak		$E > 0.1 \frac{\text{mV}}{\text{m}}$ (peak)	
	#	%	#	%	#	%
Weak (FFT)	805	40.0	---	---	---	---
Constant over 8 ms	751	37.3	751	62.1	27	13.3
> 8ms	393	19.5	393	32.5	136	67.0
< 8ms: beat	60	3.0	60	5.0	38	18.7
< 8ms: other	6	0.3	6	0.5	2	1.0
Total	2015		1210		203	

Table 4. Plasma Parameters and Langmuir Wave Characteristics: Type III

Quantity	Symbol	Value	Unit	Source
Solar wind electron density	n_e	7.1×10^6	m^{-3}	(a)
Solar wind speed	v_{sw}	3.3×10^5	$m s^{-1}$	(b)
Electron temperature	T_e	1.3×10^5	K	(c)
Ion temperature	T_i	1.9×10^4	K	(b)
Electron thermal speed	V_e	1.4×10^6	$m s^{-1}$	(d)
Ion sound speed	V_s	4.1×10^4	$m s^{-1}$	(d)
Debye length	λ_D	9.3	m	(d)
Electron plasma frequency	ω_{pe}	1.5×10^5	s^{-1}	(a)
Electron plasma frequency	f_{pe}	24×10^3	Hz	(a)
Solar wind magnetic field	B_{sw}	14	nT	(e)
Electron cyclotron frequency	Ω_e	2.8×10^3	s^{-1}	(d)
Electron cyclotron frequency	f_e	446	Hz	(d)
Beam velocity	V_b	$< 7 \times 10^7$	$m s^{-1}$	(f)
Maximum Langmuir field	E_{max}	1.7×10^{-3}	$V_{peak} m^{-1}$	(a)
Typical Langmuir field	E_{typ}	10^{-5}	$V_{peak} m^{-1}$	(a)
Maximum energy density ratio	W	5.0×10^{-7}	---	(d)

(a) determined from plasma wave observations

(b) estimate from IMP-8

(c) typical value

(d) derived from the given values

(e) Galileo magnetometer

(f) estimate from Reiner et al. [1994]

Table 5. IMP-8 Solar Wind Parameters: Type III

Day	Hr	B nT	B _{Lat} Deg.	B _{Long} Deg.	T _i °K	n _i cm ⁻³	v _{sw} km/s	v _{Long} Deg.	v _{Lat} Deg.	σ °K	σ cm ⁻³	σ_v km
344	0	7.2	4.0	346.0	17426.	8.8	332.	4.1	1.0	2278.	0.6	2.9
344	1	7.6	5.0	339.0	18213.	9.0	332.	1.3	1.6	5821.	0.5	2.1
344	2	ND	ND	ND	ND	ND	ND	ND	ND	ND	ND	ND
344	3	ND	ND	ND	ND	ND	ND	ND	ND	ND	ND	ND
344	4	ND	ND	ND	ND	ND	ND	ND	ND	ND	ND	ND
344	5	ND	ND	ND	ND	ND	ND	ND	ND	ND	ND	ND
344	6	ND	ND	ND	ND	ND	ND	ND	ND	ND	ND	ND
344	7	ND	ND	ND	ND	ND	ND	ND	ND	ND	ND	ND
344	8	ND	ND	ND	ND	ND	ND	ND	ND	ND	ND	ND
344	9	ND	ND	ND	ND	ND	ND	ND	ND	ND	ND	ND
344	10	ND	ND	ND	ND	ND	ND	ND	ND	ND	ND	ND
344	11	ND	ND	ND	ND	ND	ND	ND	ND	ND	ND	ND
344	12	ND	ND	ND	ND	ND	ND	ND	ND	ND	ND	ND
344	13	8.5	35.0	21.0	ND	ND	ND	ND	ND	ND	ND	ND
344	14	8.8	26.0	360.0	19637.	9.5	329.	0.6	2.4	4828.	0.5	3.1
344	15	8.6	13.0	358.0	24032.	9.2	324.	0.6	1.6	8405.	1.8	4.3
344	16	8.6	-12.0	358.0	28407.	8.4	321.	-0.4	-1.7	9062.	1.0	7.7
344	17	7.2	-13.0	11.0	30747.	6.7	316.	1.1	-2.9	9889.	1.2	10.
344	18	7.2	-10.0	14.0	36022.	6.3	312.	0.8	-0.3	16297	0.9	4.0
344	19	7.1	5.0	7.0	22215.	6.2	306.	-1.8	-0.6	13968	0.5	2.5
344	20	8.0	16.0	7.0	19637.	6.5	306.	-1.7	-0.4	10850	0.8	2.3
344	21	7.6	24.0	21.0	20055.	6.4	312.	-1.1	2.5	8953.	0.6	11.
344	22	7.2	20.0	34.0	29956.	6.4	315.	0.7	2.9	18748	1.1	9.2
344	23	ND	ND	ND	ND	ND	ND	ND	ND	ND	ND	ND

ND = No Data

Table 6. Characteristics of the Langmuir Wave Emissions: Venus

	All		No Weak	
	#	%	#	%
Weak (FFT)	87	15.1	---	---
Constant over 8 ms	20	3.5	20	4.1
> 8ms	142	24.7	142	29.0
< 8ms: beats	68	11.8	68	13.9
< 8ms: other	17	3.0	17	3.5
Chaotic: beats	190	33.0	190	38.9
Chaotic: other	52	9.0	52	10.6
Total	576		489	

Table 7. Plasma Parameters and Langmuir Wave Characteristics: Venus

Quantity	Symbol	Value	Unit	Source
Solar wind density	n_e	22×10^6	m^{-3}	(a)
Solar wind speed	v_{sw}	4.5×10^5	m s^{-1}	(a)
Electron temperature	T_e	3.1×10^5	K	(a)
Ion temperature	T_i	$\sim 1.8 \times 10^5$	K	(b)
Electron thermal speed	V_e	2.2×10^6	m s^{-1}	(c)
Ion sound speed	V_s	8.4×10^4	m s^{-1}	(c)
Debye length	λ_D	8.2	m	(c)
Electron plasma frequency	ω_{pe}	$\sim 2.76 \times 10^5$	s^{-1}	(d)
Electron plasma frequency	f_{pe}	$\sim 43 \times 10^3$	Hz	(d)
Solar wind magnetic field	B_{sw}	~ 14	nT	(e)
Electron cyclotron frequency	Ω_e	$\sim 2.8 \times 10^3$	s^{-1}	(e)
Electron cyclotron frequency	f_e	~ 446	Hz	(e)
Beam velocity	V_b	$(6-20) \times 10^6$	m s^{-1}	(a)
Maximum Langmuir field	E_{max}	1.0×10^{-3}	$V_{peak} \text{ m}^{-1}$	(d)
Typical Langmuir field	E_{typ}	10^{-5}	$V_{peak} \text{ m}^{-1}$	(d)
Maximum energy density ratio	W	2.4×10^{-8}	---	(c)

(a) from Frank et al. [1991]

(b) estimate from Pioneer Venus

(c) derived from the given values

(d) determined from plasma wave observations

(e) Kivelson et al. [1991]

Table 8. IMP-8 Solar Wind Parameters: Earth 1

Day	Hr	B nT	B _{Lat} Deg.	B _{Long} Deg.	T _i °K	n _i cm ⁻³	v _{sw} km/s	v _{Long} Deg.	v _{Lat} Deg.	σ _T °K	σ _n cm ⁻³	σ _v km/s
342	20	7.9	-9.0	131.0	119108	22.6	410.	-2.1	-6.7	41379.	1.8	10.4
342	21	7.8	38.0	166.0	112503	22.4	400.	-0.1	-7.5	37262.	1.6	7.9
342	22	7.5	9.0	114.0	98900.	21.0	396.	-2.5	-5.9	34950.	1.9	9.8
342	23	7.2	24.0	132.0	94414.	19.5	393.	-2.5	-7.0	32732.	2.8	9.7
343	0	6.6	34.0	123.0	63382.	20.4	395.	-2.2	-5.2	9864.	4.6	8.6
343	1	6.4	50.0	168.0	64175.	19.2	393.	-0.7	-3.5	12216.	2.9	4.4
343	2	5.9	12.0	281.0	74550.	16.0	393.	2.4	-1.9	9176.	1.9	5.0
343	3	5.8	-18.0	319.0	54648.	11.3	401.	2.5	0.4	20711.	2.5	4.1
343	4	8.2	-21.0	334.0	38082.	7.1	406.	0.2	3.5	14690.	1.3	8.1
343	5	8.2	-8.0	325.0	25446.	5.6	392.	0.4	2.7	4112.	0.5	9.7
343	6	8.3	-7.0	330.0	25927.	5.3	386.	1.1	1.0	15896.	0.7	5.3
343	7	8.6	-6.0	337.0	28918.	5.1	377.	2.4	0.4	3418.	0.3	6.0
343	8	9.0	-11.0	348.0	25446.	5.6	370.	4.3	-1.2	2402.	0.7	7.4
343	9	8.6	-14.0	353.0	27650.	6.2	374.	3.6	-2.8	4625.	1.0	4.6
343	10	8.6	-16.0	0.0	27650.	6.8	376.	3.2	-0.1	3617.	1.0	3.5
343	11	ND	ND	ND	ND	ND	ND	ND	ND	ND	ND	ND
343	12	8.2	-16.0	18.0	31819.	8.0	382.	2.9	0.6	9506.	1.0	5.5
343	13	6.9	-9.0	16.0	56858.	9.1	364.	2.4	-0.4	27237.	1.7	12.8
343	14	8.4	-15.0	347.0	39897.	8.1	349.	3.8	-1.3	19967.	1.0	4.3
343	15	7.7	-15.0	358.0	48306.	8.7	360.	4.6	1.3	13988.	1.7	21.5
343	16	9.1	-3.0	20.0	30482.	5.9	386.	1.2	2.4	21714.	1.1	12.3
343	17	8.6	4.0	34.0	32363.	8.0	367.	-1.0	0.7	6587.	1.2	16.0
343	18	8.2	20.0	96.0	30482.	10.0	396.	1.3	1.4	8085.	1.3	13.2
343	19	8.0	14.0	30.0	27400.	10.6	364.	-1.4	1.0	9891.	2.5	8.5
343	20	8.1	9.0	42.0	24264.	10.6	360.	-2.6	1.1	3857.	1.3	9.3
343	21	7.9	14.0	18.0	28918.	11.3	344.	-1.4	1.6	6111.	0.9	4.3
343	22	7.2	3.0	353.0	30218.	10.7	341.	2.9	2.1	28356.	2.8	4.3
343	23	7.0	6.0	337.0	22662.	9.7	334.	4.7	0.1	5909.	0.8	2.8

ND = No Data

Table 9. Plasma Parameters and Langmuir Wave Characteristics: Earth 1

Quantity	Symbol	Value	Unit	Source
Solar wind density	n_e	$4.5\text{-}20 \times 10^6$	m^{-3}	(a)
Solar wind speed	v_{sw}	$3.6\text{-}4.0 \times 10^5$	m s^{-1}	(b)
Electron temperature	T_e	1.5×10^5	K	(c)
Ion temperature	T_i	$25 - 95 \times 10^3$	K	(b)
Electron thermal speed	V_e	1.5×10^6	m s^{-1}	(d)
Ion sound speed	V_s	$4.3 - 6 \times 10^4$	m s^{-1}	(d)
Debye length	λ_D	6 - 13	m	(d)
Electron plasma frequency	ω_{pe}	$1.2\text{-}2.5 \times 10^5$	s^{-1}	(a)
Electron plasma frequency	f_{pe}	$19 - 40 \times 10^3$	Hz	(a)
Solar wind magnetic field	B_{sw}	6 - 9	nT	(b,e)
Electron cyclotron frequency	Ω_e	$1.2\text{-}1.8 \times 10^3$	s^{-1}	(d)
Electron cyclotron frequency	f_e	190 - 290	Hz	(d)
Maximum Langmuir field	E_{max}	13.8×10^{-3}	$V_{peak} \text{ m}^{-1}$	(a)
Typical Langmuir field	E_{typ}	10^{-5}	$V_{peak} \text{ m}^{-1}$	(a)
Maximum energy density ratio	W	4.5×10^{-5}	—	(a)

(a) determined from plasma wave observations

(b) IMP-8

(c) typical value

(d) derived from the given values

(e) Galileo magnetometer

Table 10. Plasma Parameters and Langmuir Wave Characteristics: Earth 2

Quantity	Symbol	Value	Unit	Source
Solar wind density	n_e	$\sim 4.5 \times 10^6$	m^{-3}	(a)
Solar wind speed	v_{sw}	$\sim 6.8 \times 10^5$	m s^{-1}	(b)
Electron temperature	T_e	1.5×10^5	K	(c)
Ion temperature	T_i	$\sim 8 \times 10^4$	K	(b)
Electron thermal speed	V_e	1.5×10^6	m s^{-1}	(d)
Ion sound speed	V_s	5.7×10^4	m s^{-1}	(d)
Debye length	λ_D	12.6	m	(d)
Electron plasma frequency	ω_{pe}	$\sim 1.26 \times 10^5$	s^{-1}	(a)
Electron plasma frequency	f_{pe}	$\sim 20 \times 10^3$	Hz	(a)
Solar wind magnetic field	B_{sw}	~ 10	nT	(e)
Electron cyclotron frequency	Ω_e	2×10^3	s^{-1}	(d)
Electron cyclotron frequency	f_e	320	Hz	(d)
Maximum Langmuir field	E_{max}	36×10^{-3}	$V_{peak} \text{ m}^{-1}$	(a)
Typical Langmuir field	E_{typ}	10^{-5}	$V_{peak} \text{ m}^{-1}$	(a)
Maximum energy density ratio	W	3×10^{-4}	—	(d)

(a) determined from plasma wave observations

(b) Estimate from IMP-8

(c) typical value

(d) derived from the given values

(e) Galileo magnetometer

Table 11. IMP-8 Solar Wind Parameters: Earth 2

Day	Hr	B nT	B _{Lat} Deg.	B _{Long} Deg.	T _i °K	n _i cm ⁻³	v _{sw} km/s	v _{Long} Deg.	V _{Lat} Deg.	σ _T °K	σ _{n,3} cm ⁻³	σ _v km/s
343	6	8.1	16.0	329.0	152693.	4.7	697.	0.4	2.4	90253.	0.7	14.8
343	7	8.1	54.0	348.0	258009.	5.2	734.	1.5	1.9	169436.	1.1	33.4
343	8	7.9	20.0	334.0	137134.	4.9	701.	2.1	0.8	118309.	0.6	22.9
343	9	7.6	-25.0	299.0	163801.	4.7	715.	0.3	-1.6	65471.	0.4	33.6
343	10	ND	ND	ND	163801.	4.8	733.	-1.4	-2.0	70030.	0.2	27.1
343	11	ND	ND	ND	ND	ND	ND	ND	ND	ND	ND	ND
343	12	ND	ND	ND	207977.	5.3	722.	6.7	-1.3	ND	ND	ND
343	13	ND	ND	ND	ND	ND	ND	ND	ND	ND	ND	ND
343	14	ND	ND	ND	ND	ND	ND	ND	ND	ND	ND	ND
343	15	ND	ND	ND	ND	ND	ND	ND	ND	ND	ND	ND
343	16	ND	ND	ND	ND	ND	ND	ND	ND	ND	ND	ND
343	17	ND	ND	ND	ND	ND	ND	ND	ND	ND	ND	ND
343	18	ND	ND	ND	ND	ND	ND	ND	ND	ND	ND	ND
343	19	ND	ND	ND	ND	ND	ND	ND	ND	ND	ND	ND
343	20	ND	ND	ND	ND	ND	ND	ND	ND	ND	ND	ND
343	21	ND	ND	ND	ND	ND	ND	ND	ND	ND	ND	ND
343	22	6.3	ND	33.0	81187.	3.9	681.	3.2	2.0	6549.	0.4	3.3
343	23	6.6	-1.0	351.0	76290.	4.0	657.	-1.3	1.2	24256.	0.4	12.8
344	0	ND	ND	ND	33466.	3.1	666.	-2.9	ND	ND	ND	ND
344	1	ND	ND	ND	ND	ND	ND	ND	ND	ND	ND	ND
344	2	ND	ND	ND	ND	ND	ND	ND	ND	ND	ND	ND
344	3	ND	ND	ND	ND	ND	ND	ND	ND	ND	ND	ND
344	4	ND	ND	ND	ND	ND	ND	ND	ND	ND	ND	ND
344	5	ND	ND	ND	ND	ND	ND	ND	ND	ND	ND	ND
344	6	6.3	-3.0	269.0	ND	ND	ND	ND	ND	ND	ND	ND
344	7	6.1	-1.0	298.0	131757.	4.7	674.	-2.2	1.6	47557.	0.2	13.9
344	8	ND	ND	ND	78941.	4.7	686.	0.1	4.3	ND	ND	ND
344	9	ND	ND	ND	167824.	4.5	697.	-0.5	-0.5	55638.	0.4	9.2

ND = No Data

Figure 1. A block diagram of the Galileo plasma wave instrument. The main electronics package consists of three spectrum analyzers and a high-resolution wideband waveform receiver. An electric dipole antenna is used to detect electric fields and two search coil magnetometers are used to detect magnetic fields.

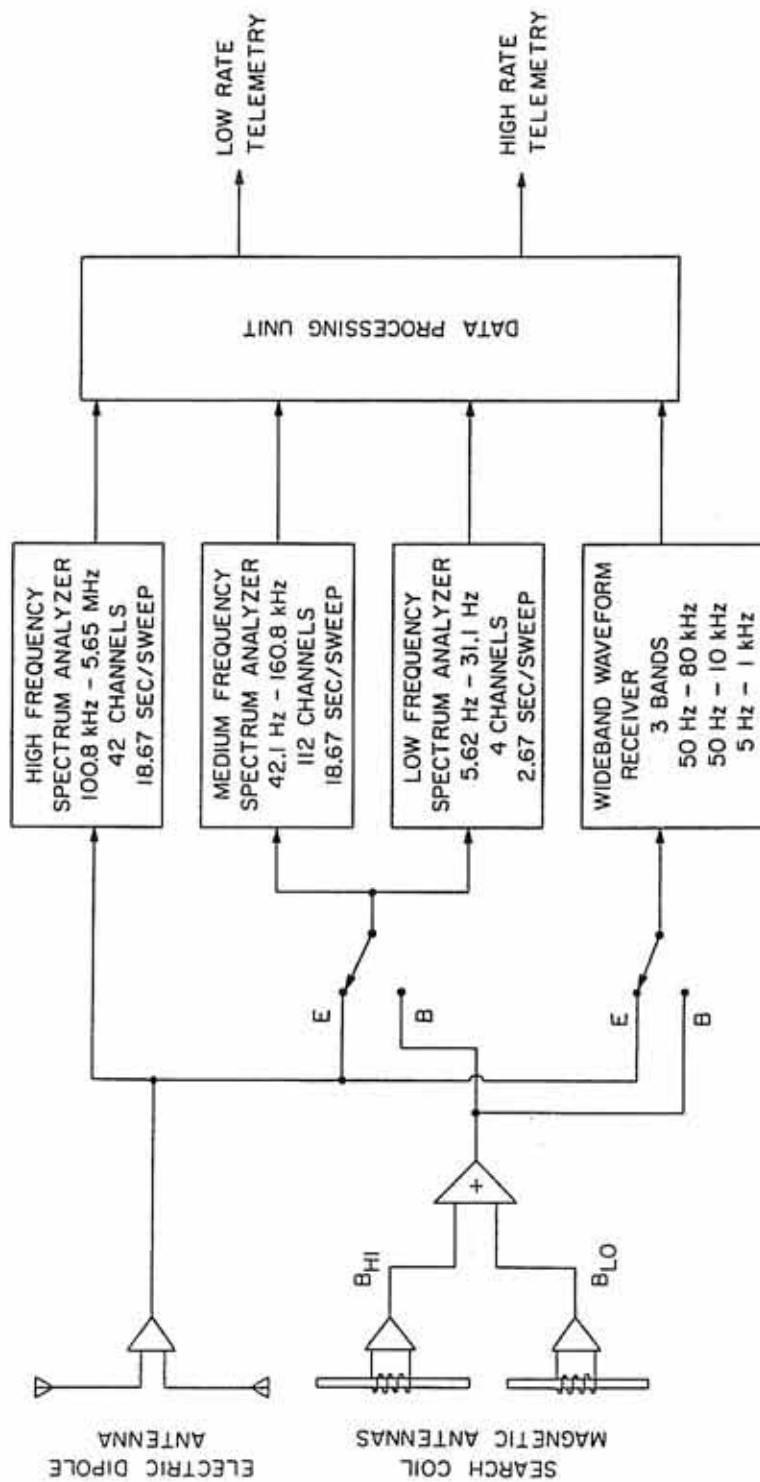


Figure 2. A diagram showing the scheme for sampling the spectrum analyzer receivers. The time required to obtain a complete spectrum from one antenna is 18.67 seconds. For most of this study, the low- and medium-frequency spectrum analyzers were cycled between the electric and magnetic antennas, providing alternating electric and magnetic spectrums. This cycling between the antennas results in a sampling period of 37.33 seconds between complete electric field spectrums. The high-frequency analyzer is always connected to the electric antenna.

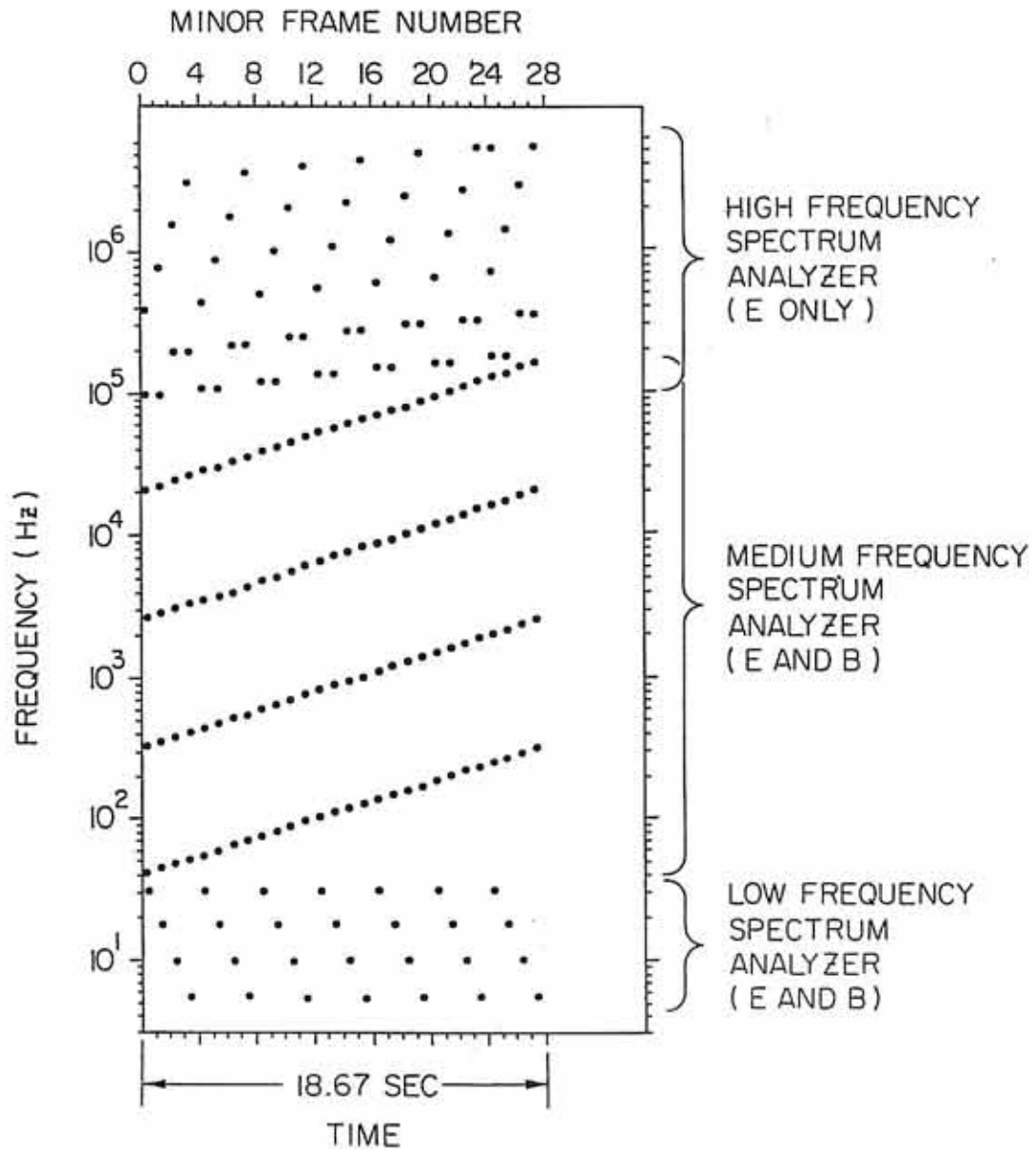


Figure 3. Representative waveforms for the four modes of the wideband waveform receiver. Table 1 summarizes the characteristics of the four wideband waveform receiver modes used in this study.

C-G94-263

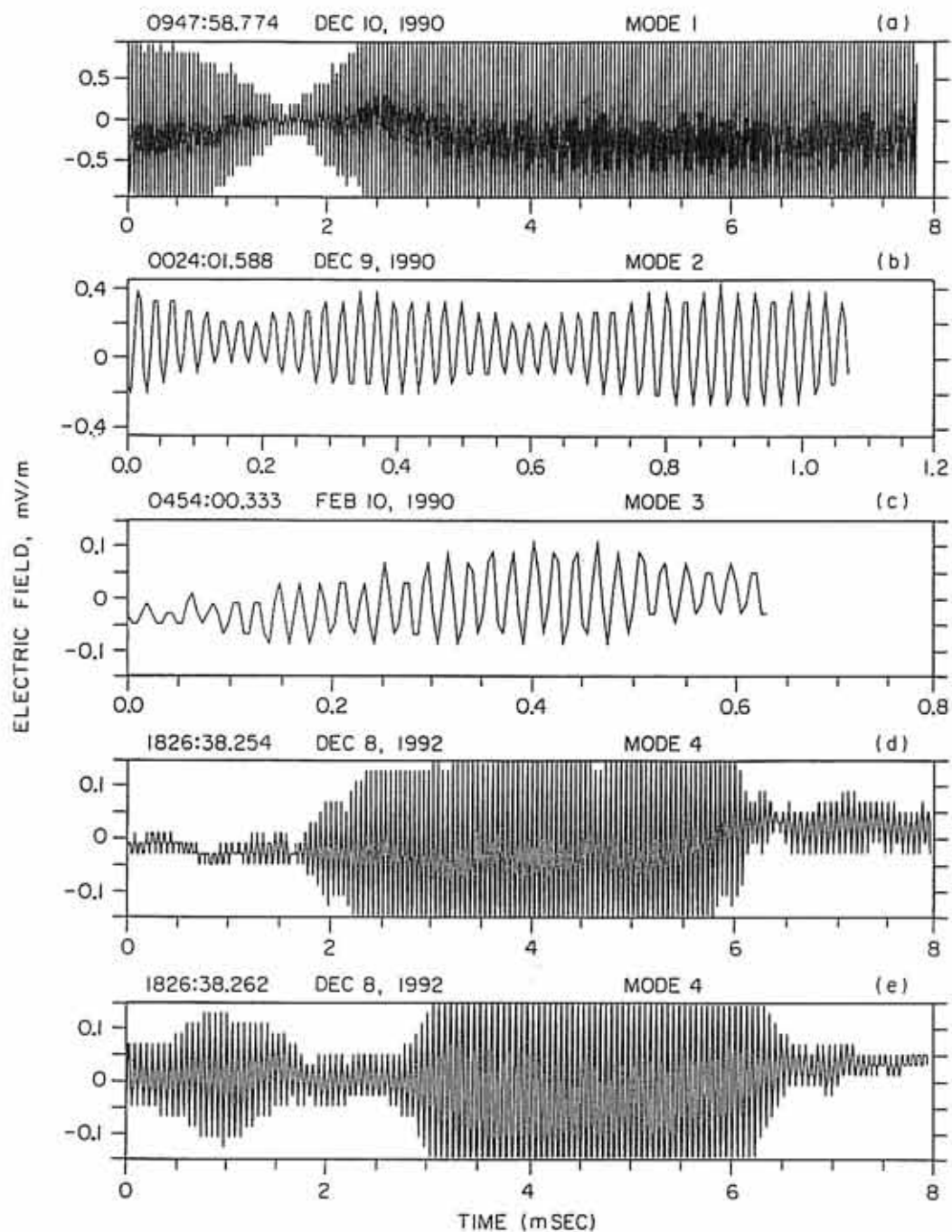


Figure 4. A sketch of the two-step mechanism involved in the generation of a type III solar radio burst. First, the electron beam produces Langmuir waves near the plasma frequency f_{pe} by a beam-plasma instability. Second, the Langmuir waves are converted to electromagnetic radiation at both the fundamental f_{pe} and the harmonic $2f_{pe}$ by nonlinear processes. As the electron beam moves outward from the Sun, the Langmuir waves are produced at progressively lower frequencies due to the decrease in the density of the solar wind plasma with increasing distance from the Sun. The decrease in the plasma frequency with distance from the Sun produces the characteristic frequency-time spectrum in which the frequency decreases with increasing time.

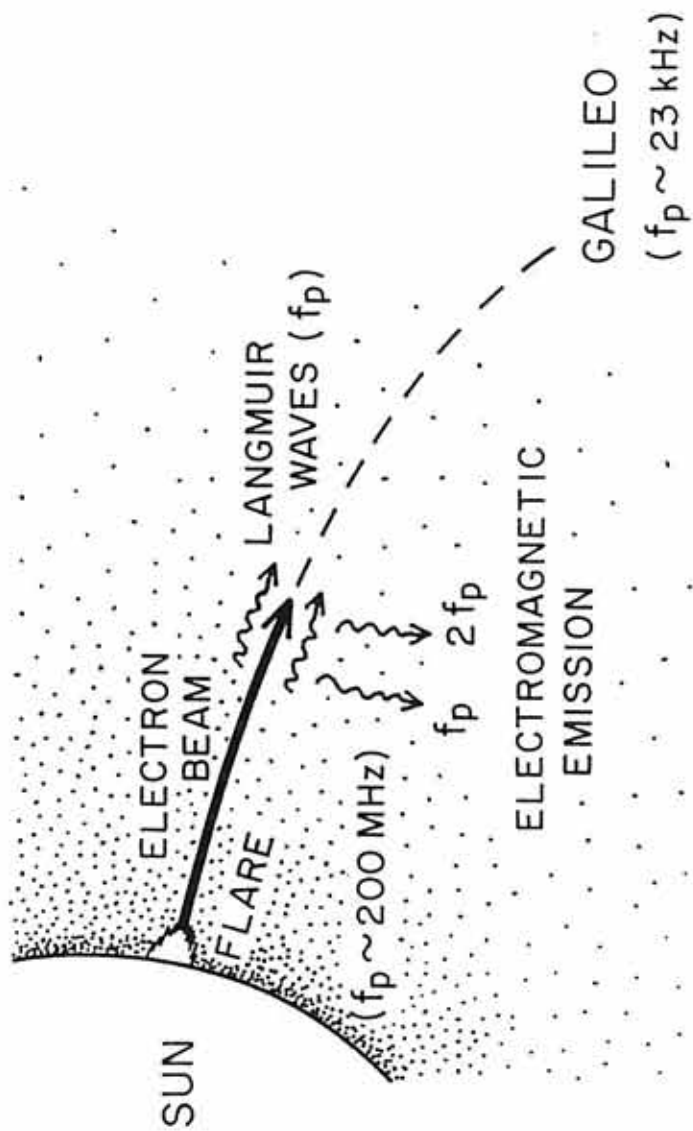


Figure 5. A four-hour frequency-time spectrogram from the spectrum analyzer for this event. The onset of the type III burst was first detected at ~ 0743 UT in the high-frequency spectrum analyzer. The event shows an intense band of noise sweeping downward in frequency with increasing time, which is the characteristic signature of a type III solar radio burst. Several other weaker type III bursts can also be seen in the spectrogram at 0713 UT, 0720 UT, 0945 UT, and 0955 UT. The Langmuir waves are the narrowband emissions that can be seen at about 24 kHz starting at ~ 0835 UT and continuing sporadically until ~ 1020 UT.

Galileo PWS

University of Iowa

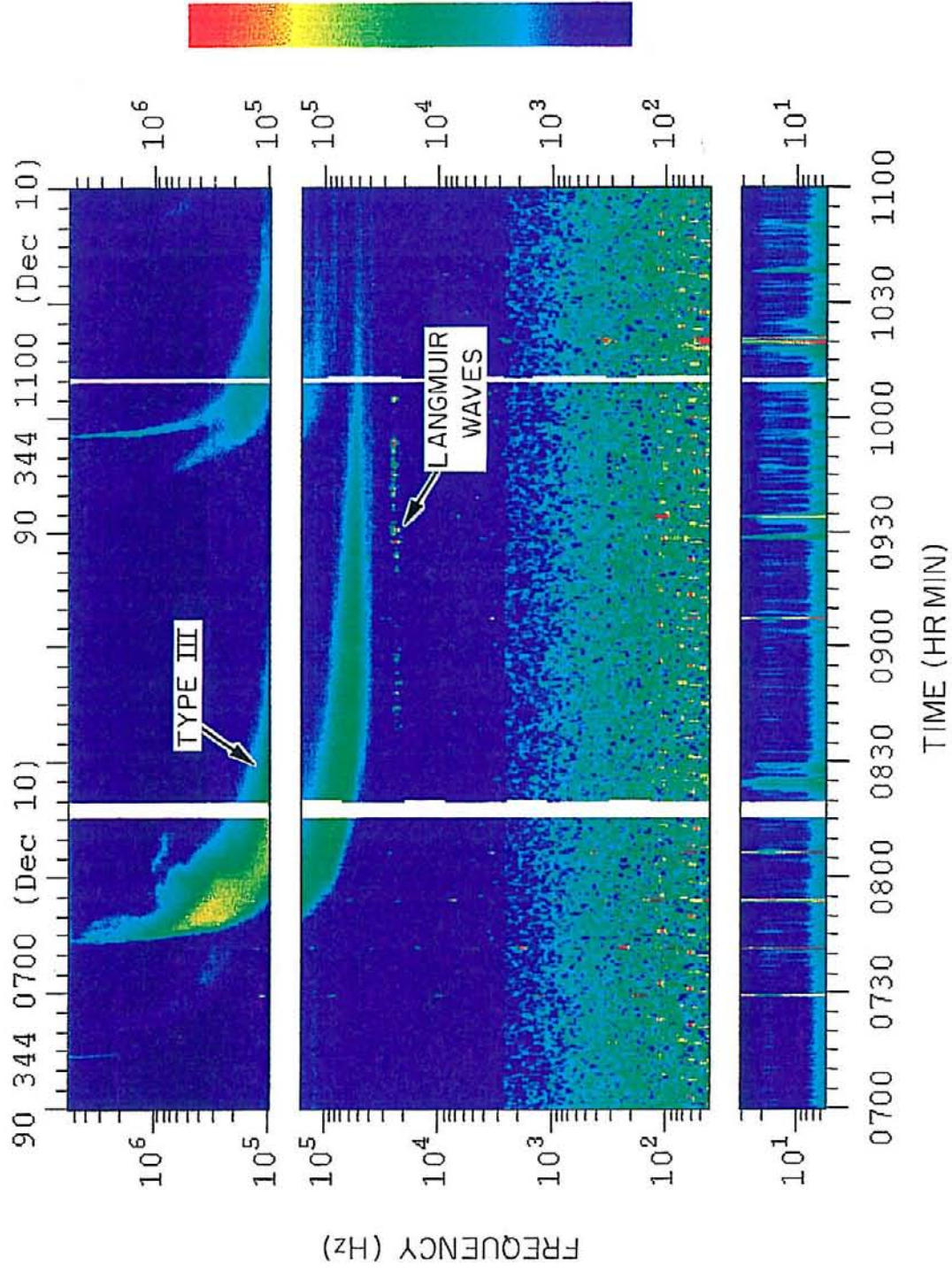


Figure 6. Channel plots from the medium-frequency spectrum analyzer receiver and the energetic particle instrument. The top panel shows the electric field intensities from 45.6 to 49.5 kHz, which spans $2f_{pe}$. The middle panel shows the electric field intensities from 21.6 to 25.1 kHz, which spans the electron plasma frequency f_{pe} . The Langmuir waves are the spiky signal starting at about 0835 UT. The bottom panel shows the electron counting rate in three energy channels from the energetic particle experiment. The sharply peaked modulation in the counting rate with a period of about 3 minutes is produced by the azimuthal scanning of the detector and the spin of the spacecraft, and is indicative of a beamlike distribution of electrons streaming outward from the Sun along the solar wind magnetic field lines.

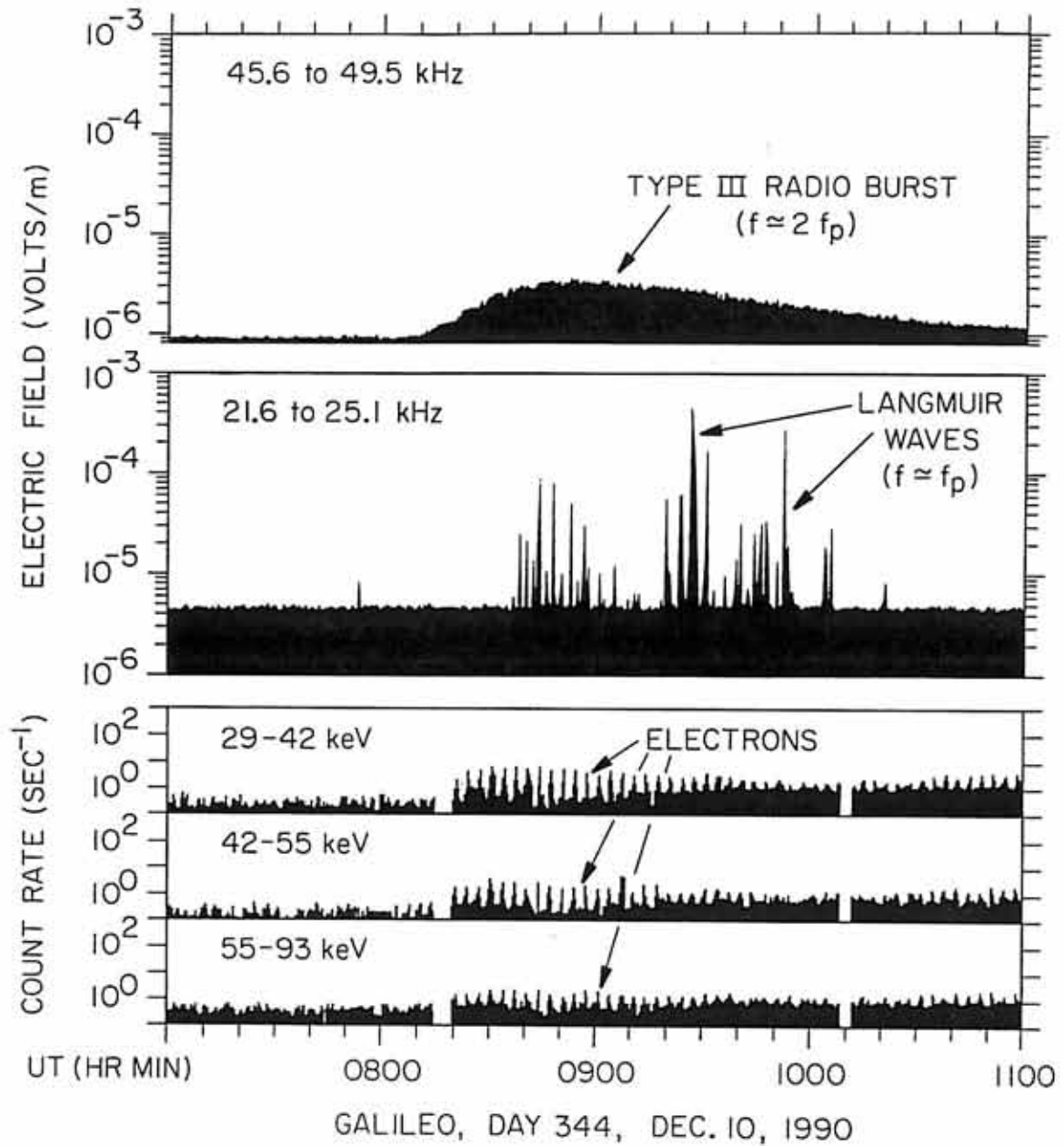


Figure 7. A 150-minute frequency-time spectrogram from the wideband waveform receiver. The broadband signal from approximately 40 kHz to 80 kHz is the type III burst. The Langmuir waves are the intense, narrowband emissions first observed at approximately 0836 UT and 23 kHz. The sporadic narrowband emissions at approximately 46 to 50 kHz and 70 to 75 kHz are believed to be 2nd and 3rd harmonic distortion effects due to clipping in the receiver. The harmonics are easily seen from about 0936 UT to 0955 UT. The five intervals of "striped" spectrum (e.g., 0800:00 to 0804:20 UT) are periods when the wideband receiver is connected to the search coil magnetometers.

GALILEO

START - 1990 344 07:59 (10 December)

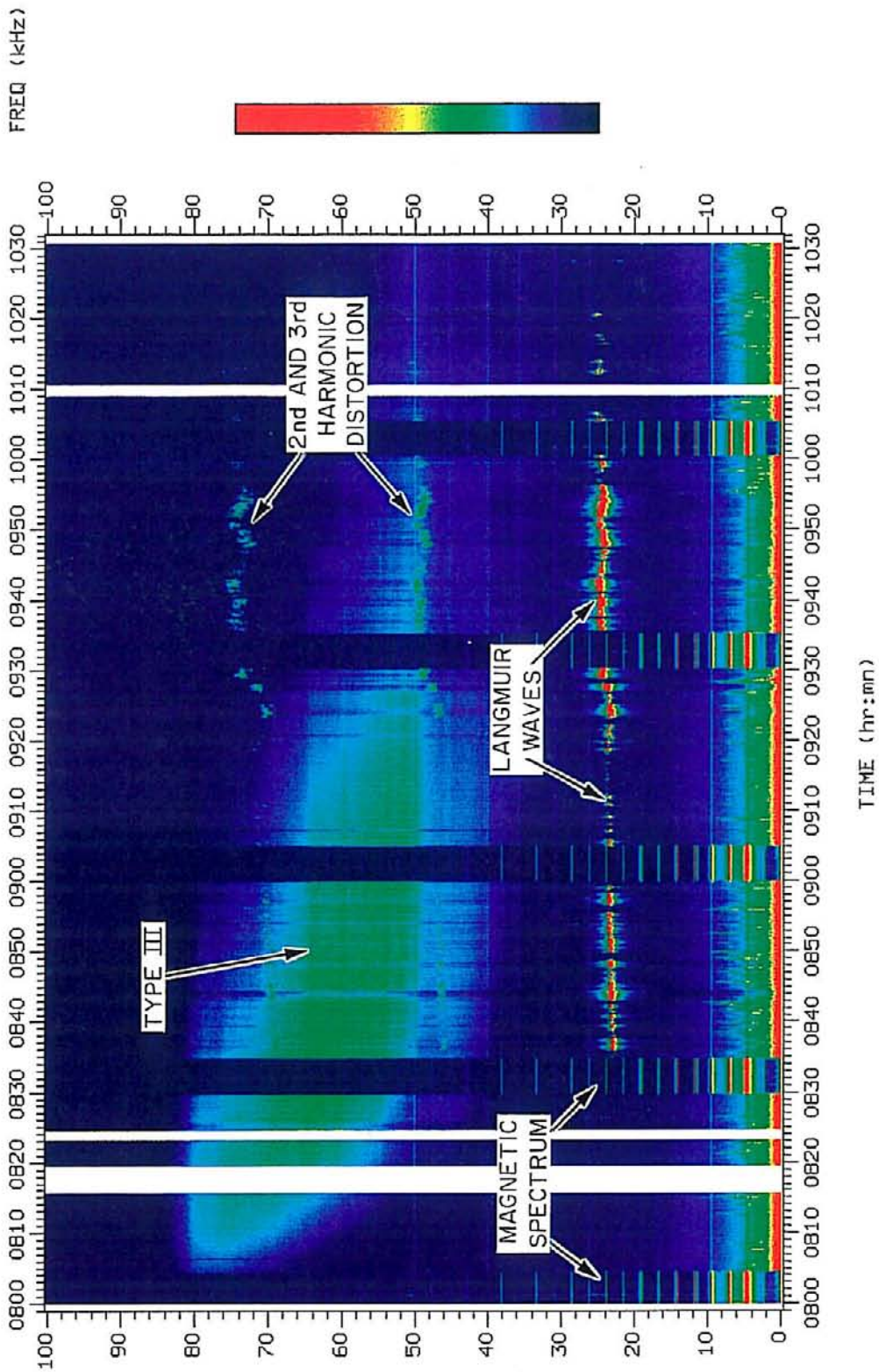
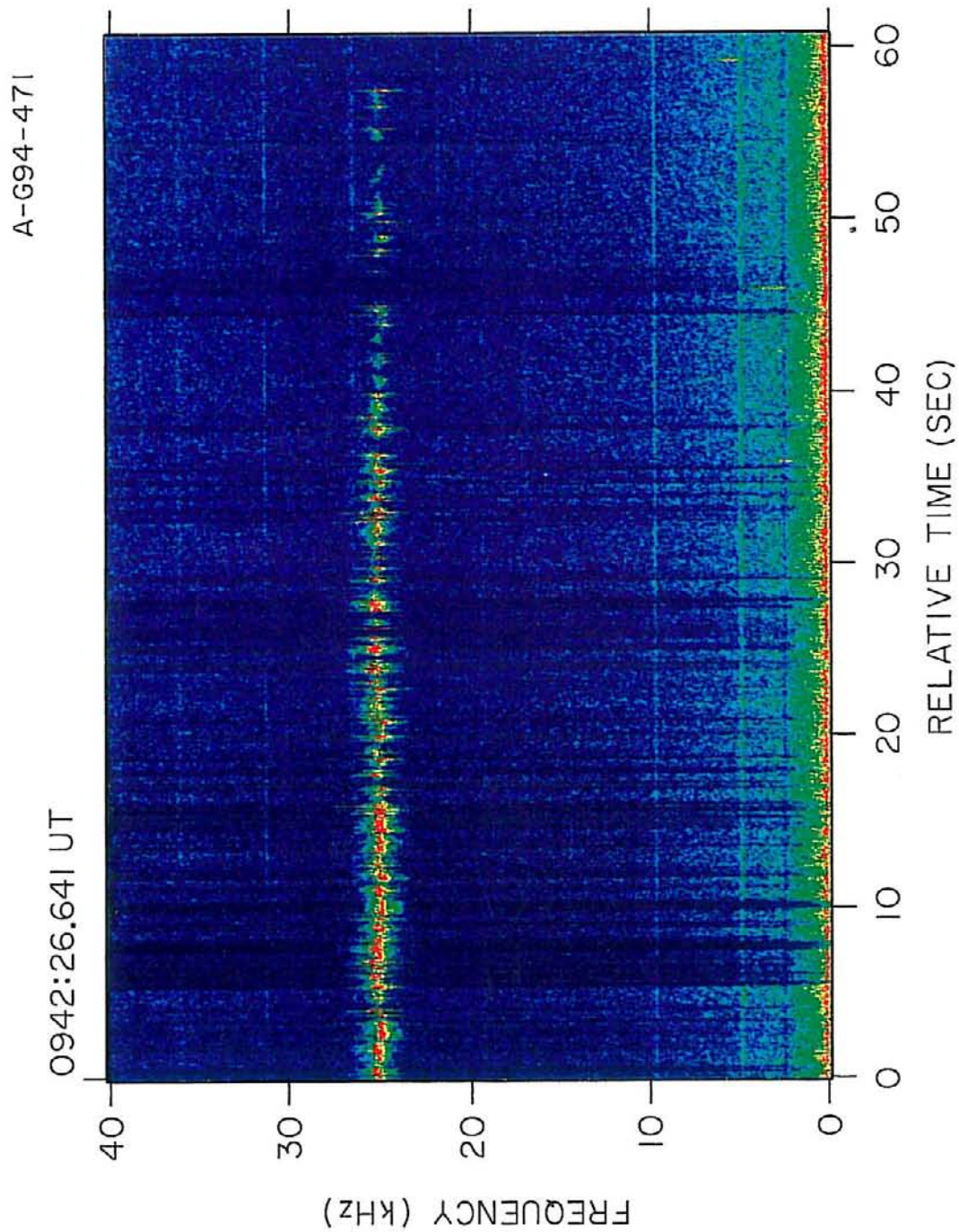


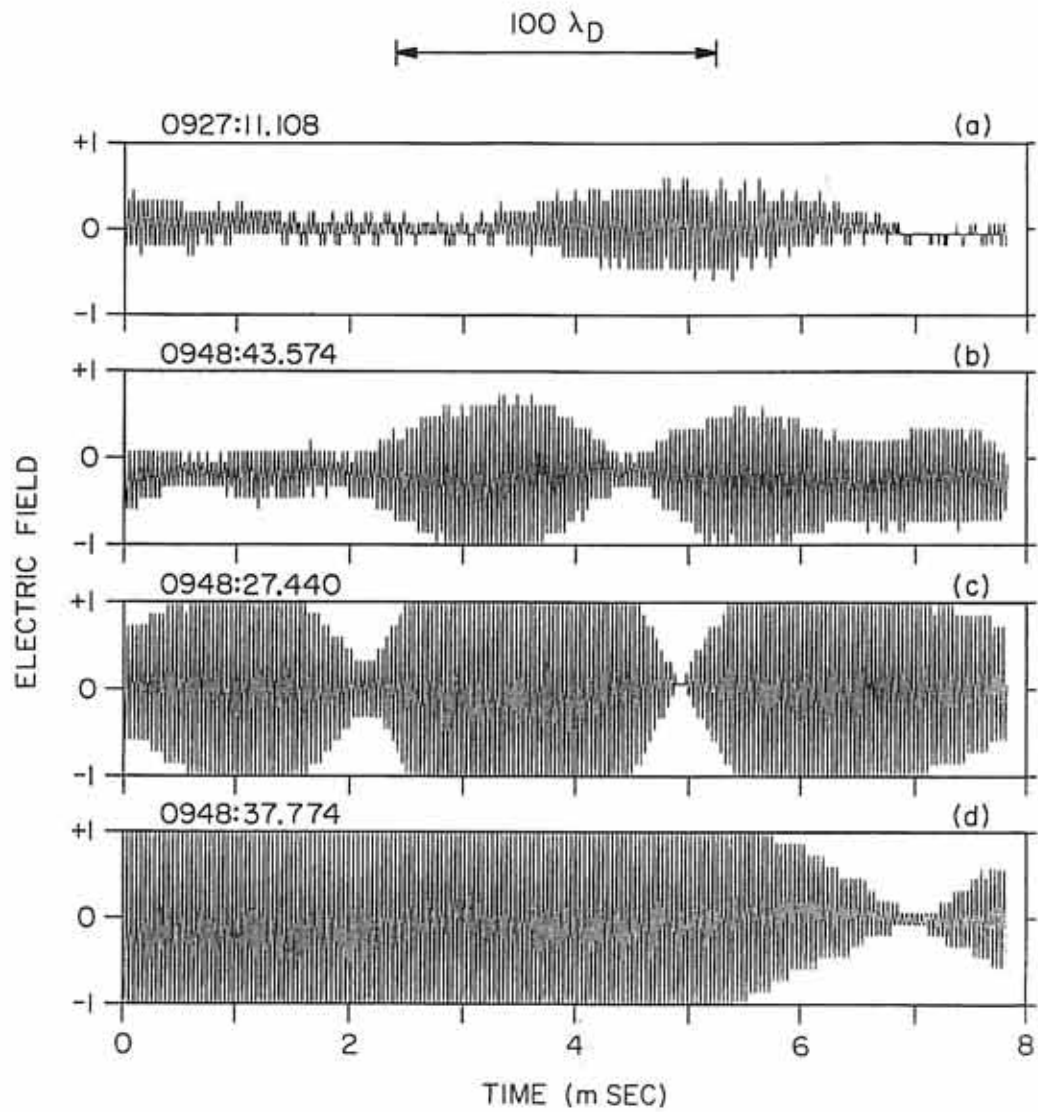
Figure 8. A one-minute frequency-time spectrogram from the wideband receiver. The Langmuir waves are clearly visible at $f_{pe} \approx 25$ kHz. The intensity of the Langmuir waves shows extremely rapid temporal variations, down to the smallest time scale that can be resolved, which is the time between successive waveform blocks (66.67 ms). The Langmuir waves also show frequency spreading, sometimes by as much as 2 kHz. The frequency spreading is also highly variable, sometimes changing by a factor 5 or more between successive spectrums.



GALILEO - TYPE III, DEC 10, 1990

Figure 9. A sampling of the Langmuir wave emission waveforms associated with the type III burst. The high-frequency, quasi-sinusoidal waveform evident in each panel is the Langmuir wave oscillation at $f \approx f_{pe}$, which is ~ 24 kHz during these intervals.

C-G91-431-5



GALILEO-TYPE III, DAY 344, DEC. 10, 1990

Figure 10. A spectrum of the beat-type waveform in Figure 9c. The spectrum consists of two sharply defined peaks separated by about 400 Hz, which is the approximate beat frequency observed in the waveform. A low-frequency signal is also observed at ~ 400 Hz.

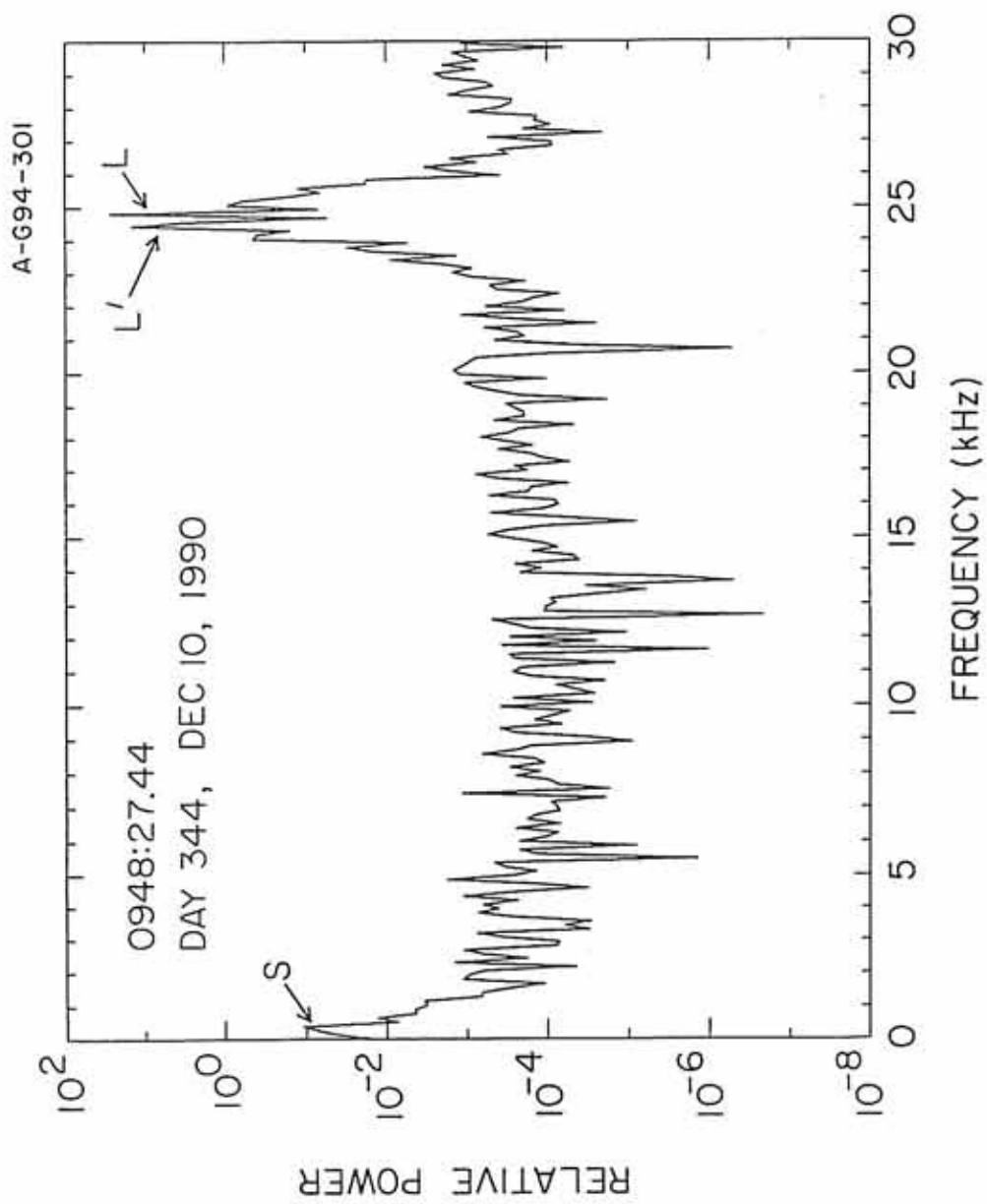
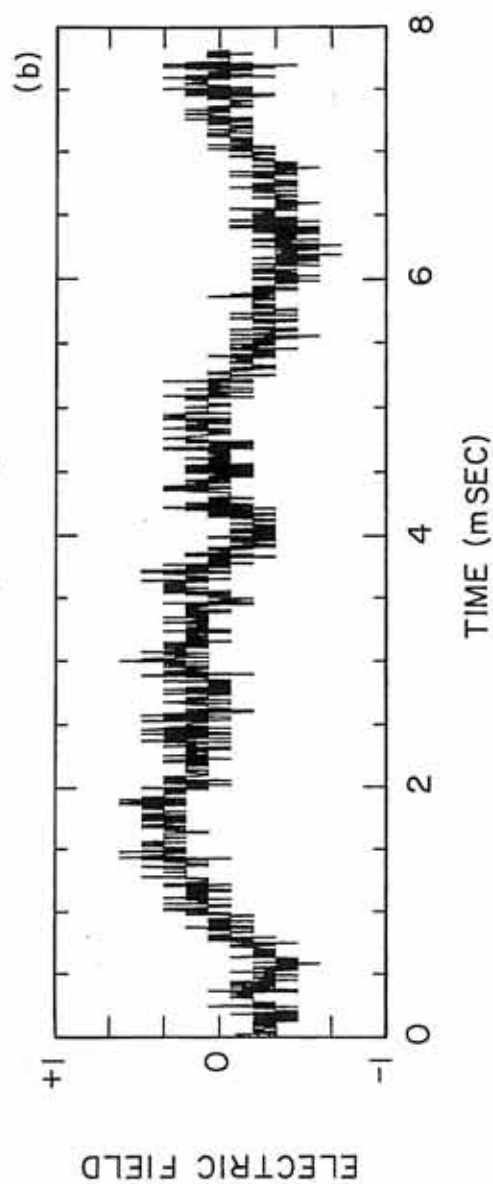
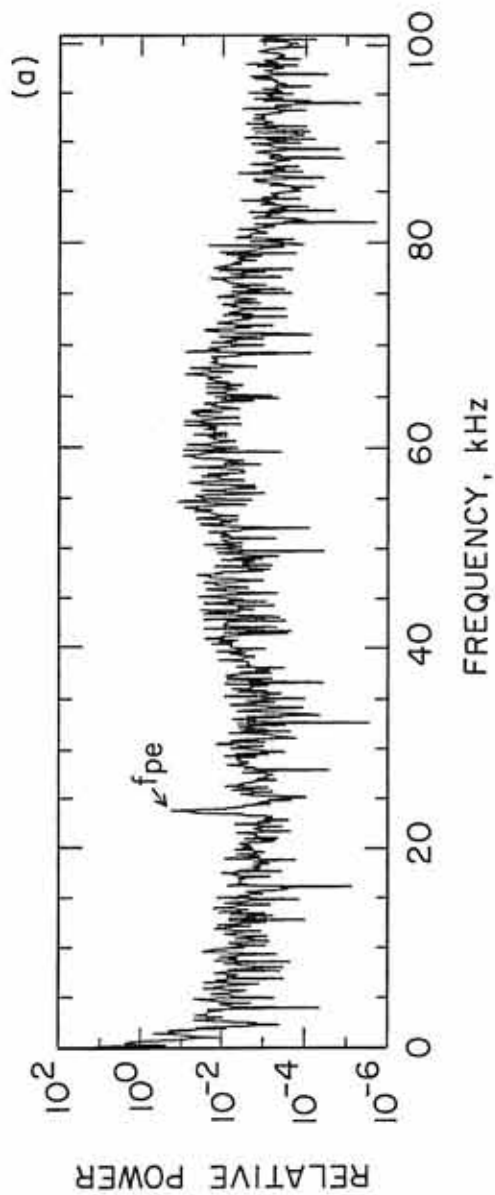


Figure 11. An example of a "weak" waveform and its corresponding spectrum. This type of waveform contains no obvious Langmuir wave signal in the waveform (Panel b), but a signal is observed in the spectrum near the plasma frequency (Panel a).

A-G94-281



GALILEO, 0852:57.443, DAY 344, DEC 10, 1990

Figure 12. The number of waveform blocks as a function of peak electric field strength. The solid line gives the peak field strength for the waveforms measured directly (unclipped) or by extrapolation (moderately clipped). The dashed line gives the lower limit to the field strengths for severely clipped waveforms.

A-G92-307

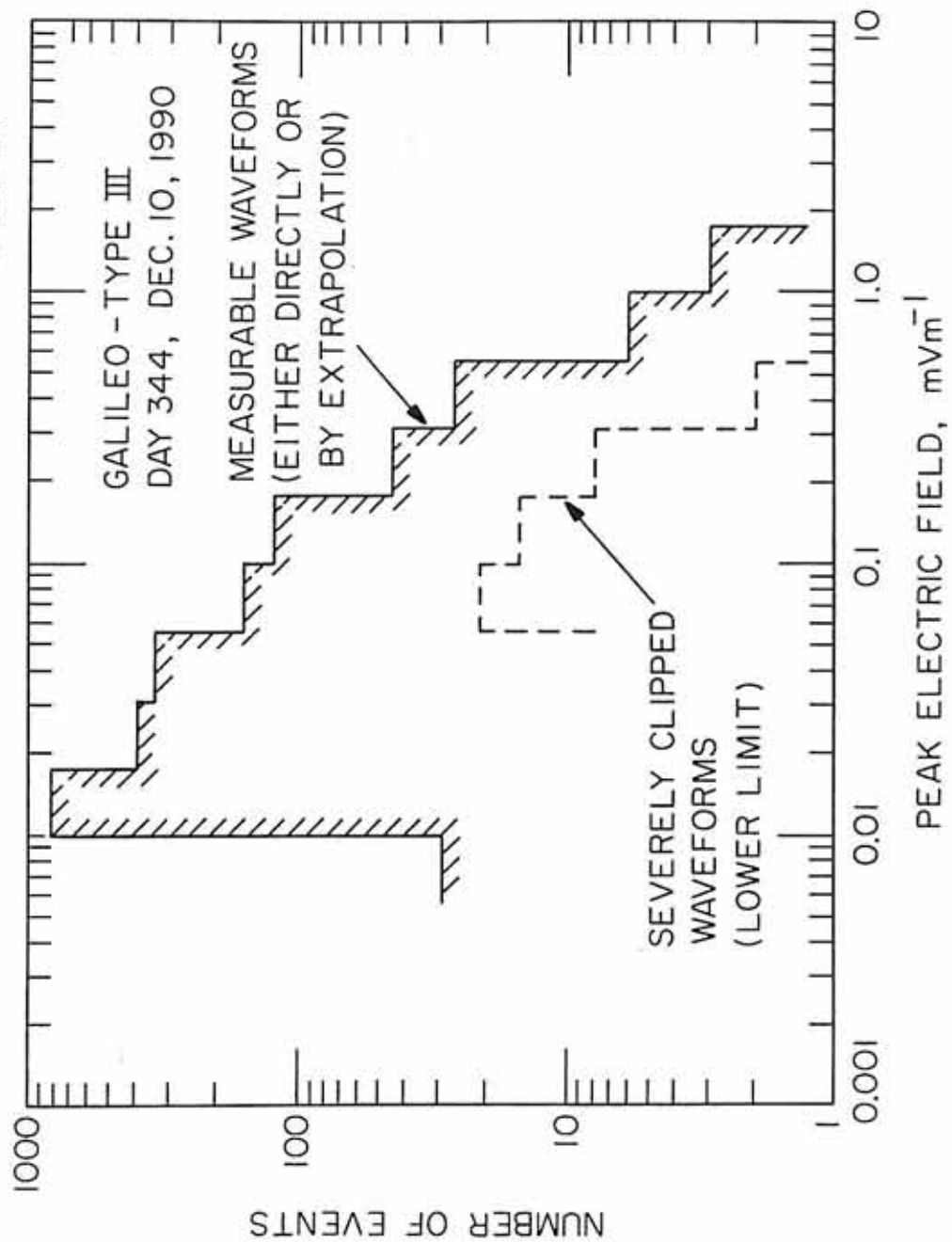
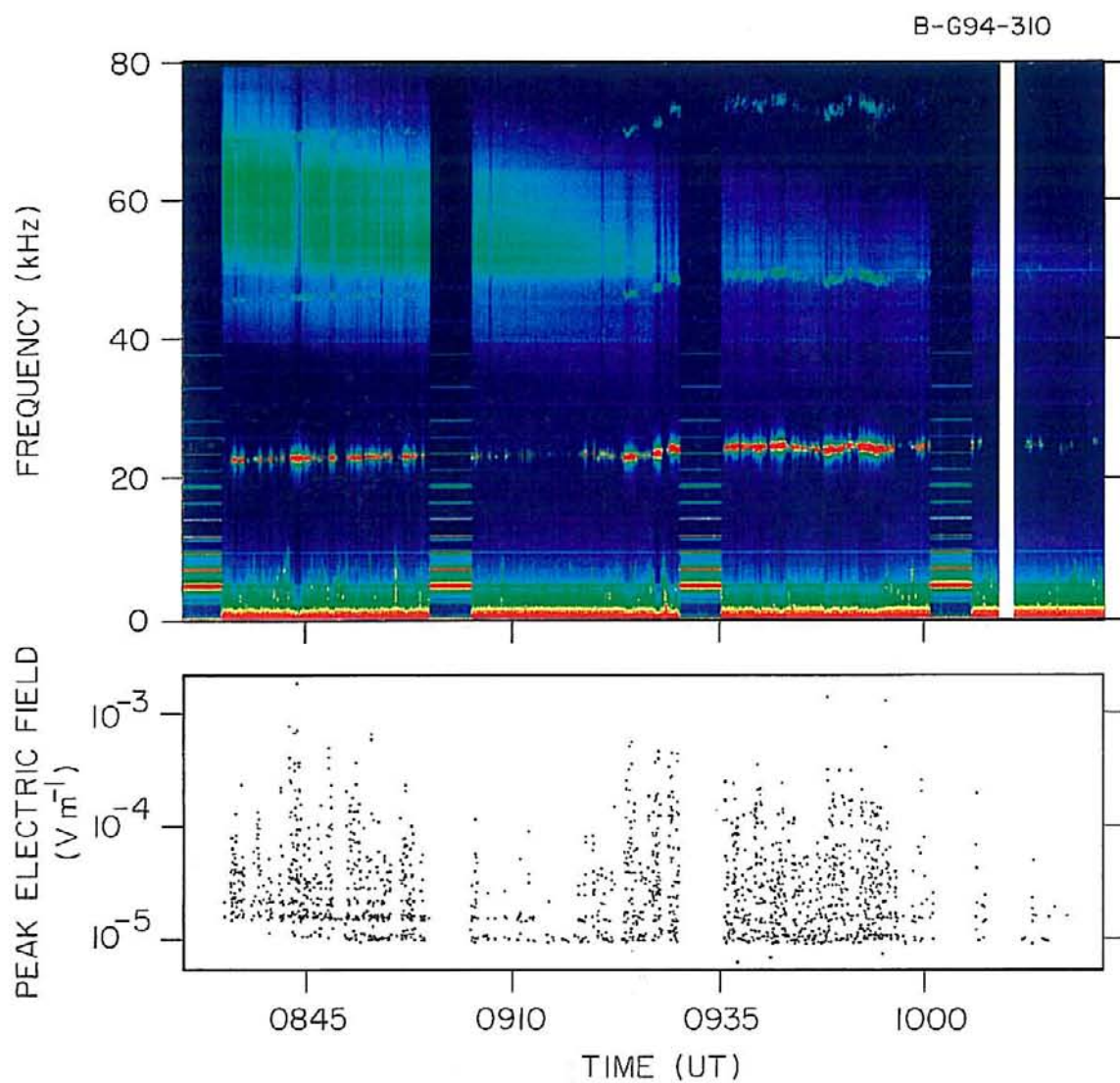


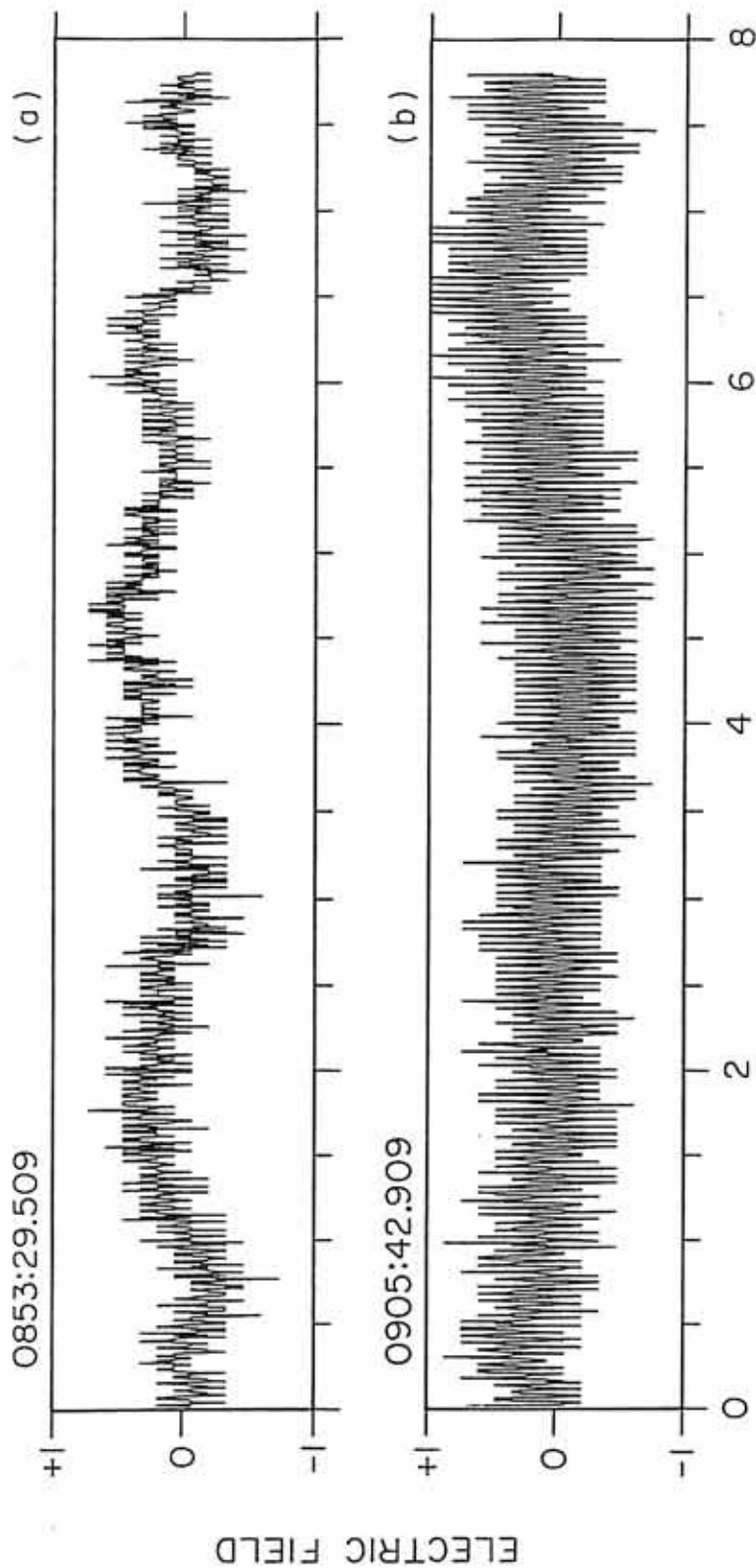
Figure 13. The top panel is a high-resolution frequency-time spectrogram of the Langmuir waves. The bottom panel is the distribution of the field strengths shown in Figure 12 as a function of time.



GALILEO - TYPE III, DAY 344, DEC 10, 1990

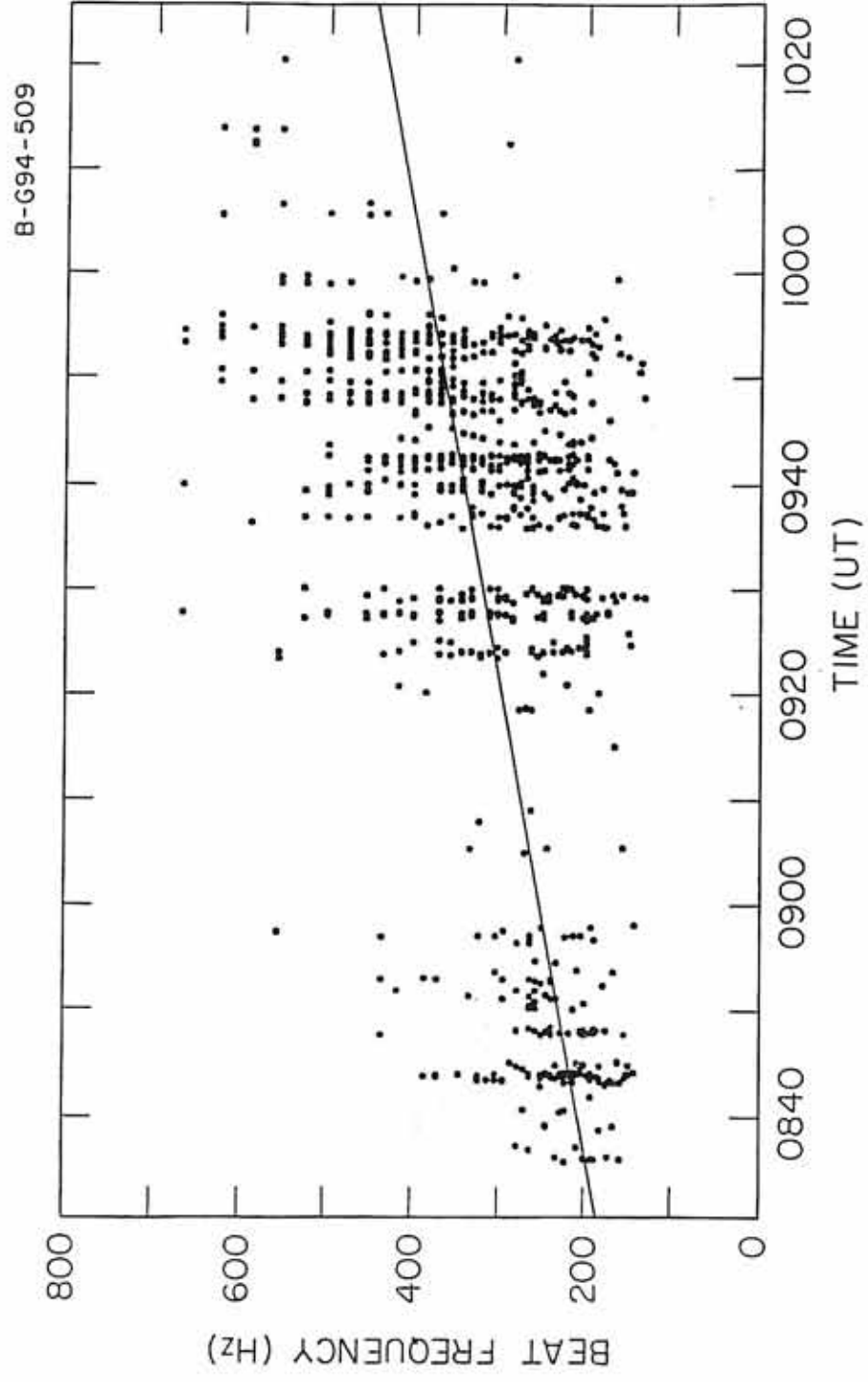
Figure 14. Examples of "constant over 8 ms" waveforms.

B-G94-282



GALILEO DAY 344, 1990

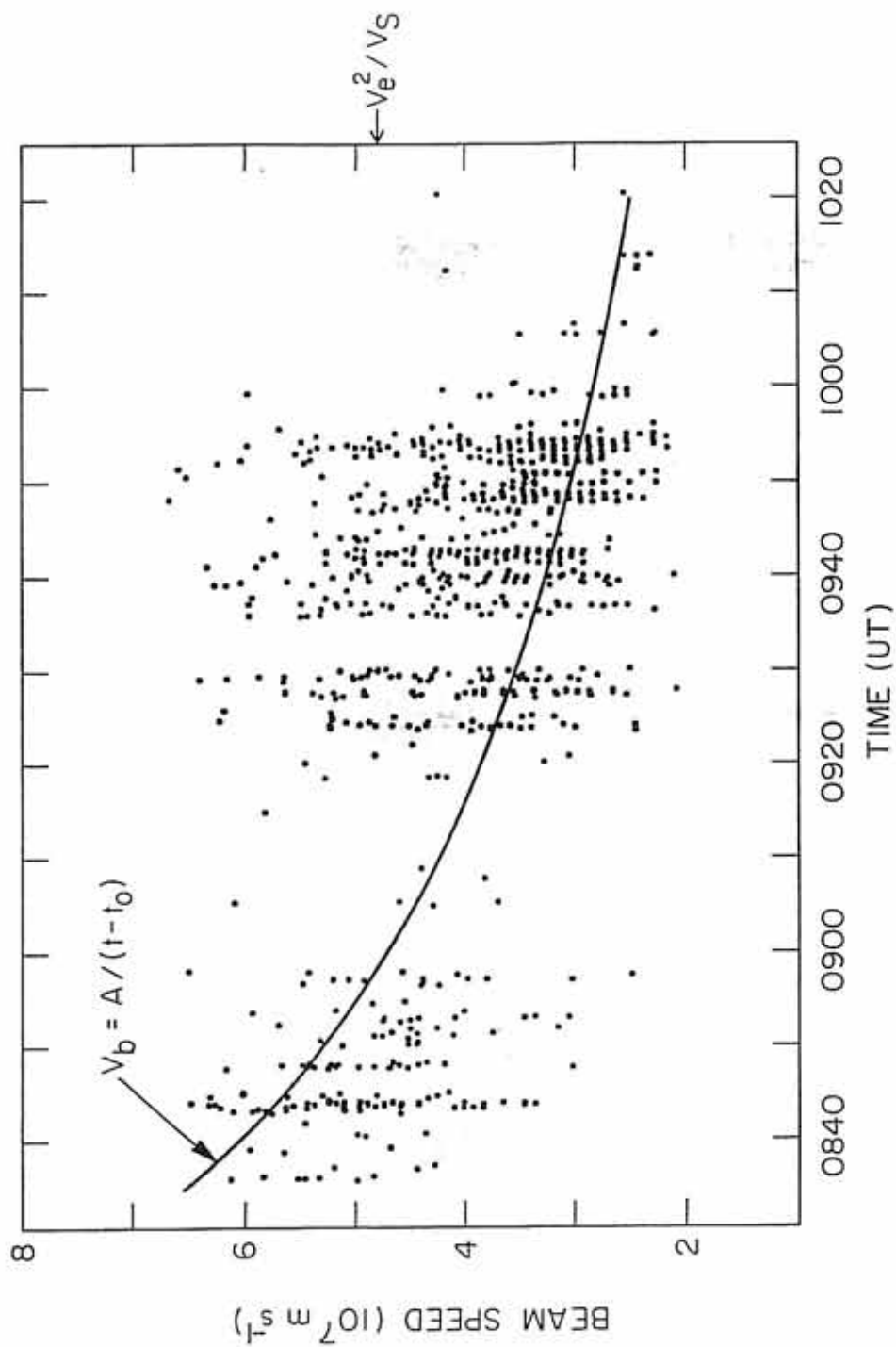
Figure 15. The beat frequencies of the beat-type waveforms as a function of time. Although there is a great deal of scatter, a clear trend exists toward higher frequencies with increasing time. The solid line is the least-square linear fit to the data.



GALILEO, DAY 344, DEC 10, 1990

Figure 16. The electron beam speeds determined by Equation 8 using the beat frequencies shown in Figure 15 and the corresponding value of θ determined from the Galileo magnetic field data (20-second averages). The predicted trend to smaller beam speeds with time is observed. The solid line is the theoretical beam speed calculated from $V_b = A/(t-t_0)$.

B-G94-465



GALILEO, DAY 344, DEC 10, 1990

Figure 17. A sketch of the electron foreshock region. Electrons streaming from the bow shock along the interplanetary magnetic field lines are convected downstream by the solar wind. The electrons originating from the tangent point with the highest energy define a region called the electron foreshock. The depth parameter D is defined as the distance along the solar wind flow from the tangent magnetic field line to the spacecraft. The depth parameter is positive for spacecraft locations downstream of the tangent field line, and negative for locations upstream. For a given depth parameter, only electrons with a velocity above a certain critical velocity can reach the spacecraft.

A-G93-62-2

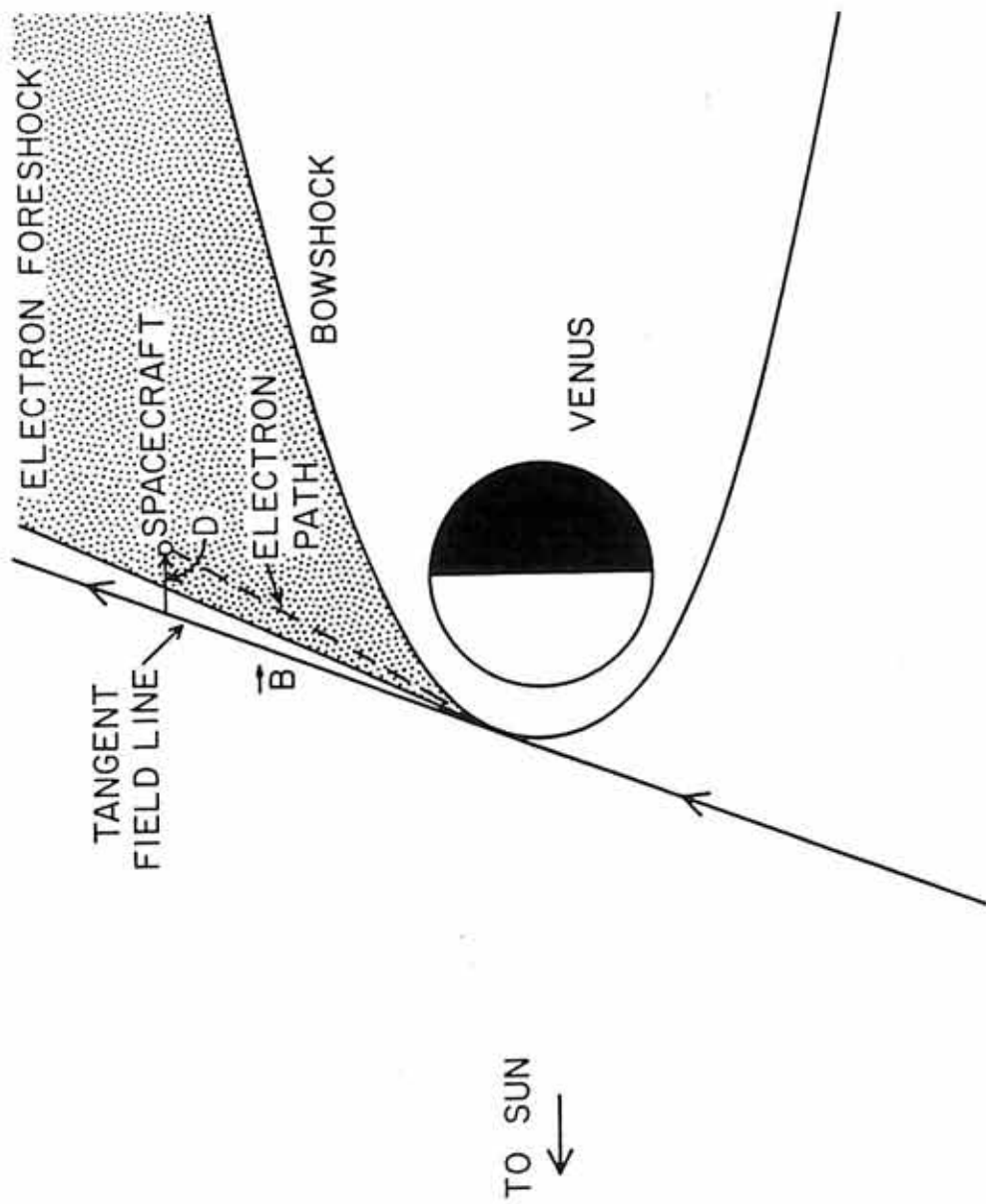


Figure 18. A sketch of the electron and ion foreshock regions. Energetic ions also stream into the solar wind from the bow shock. Because the ions are slower than the electrons, the ion foreshock boundary is located downstream of the electron foreshock boundary. It should be noted that both ions and electron beams can be observed in the ion foreshock.

A-G84-579

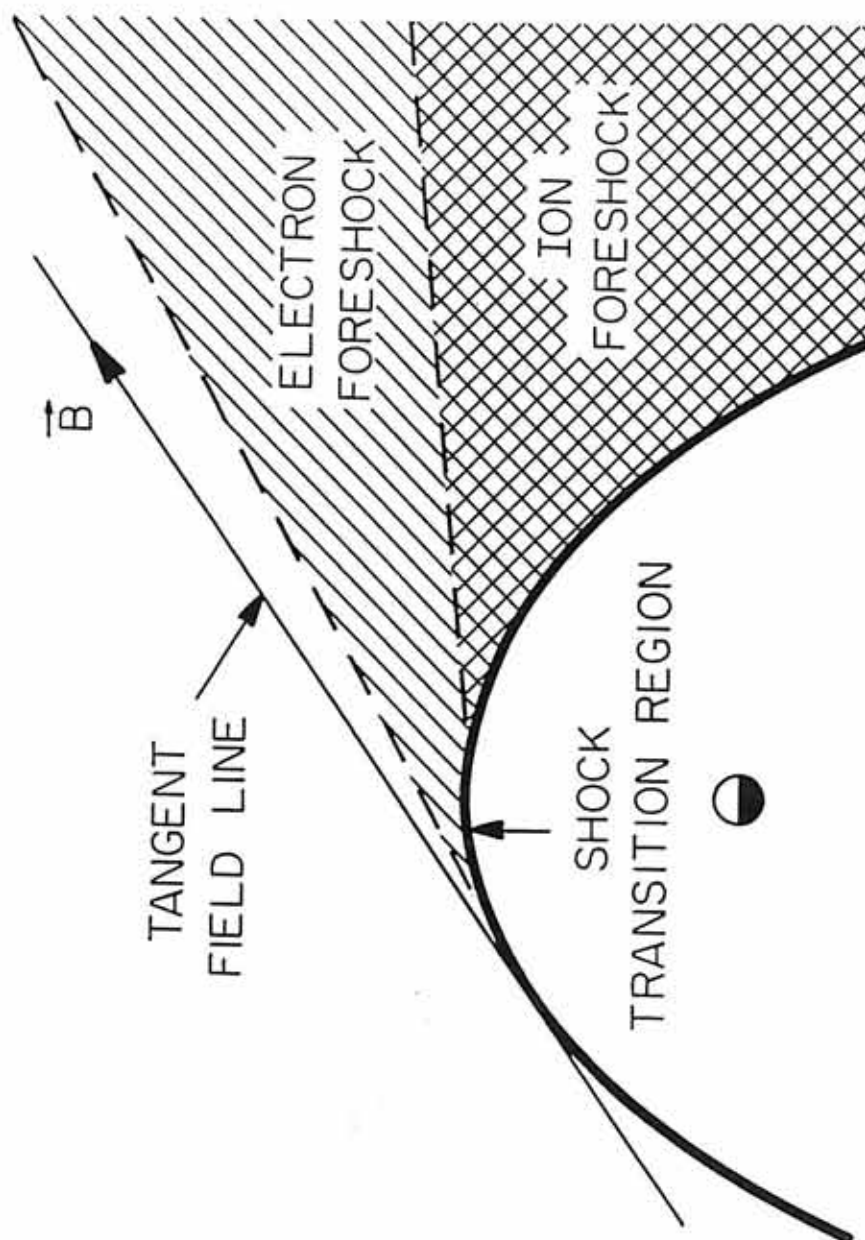


Figure 19. A sketch of the frequency of maximum growth versus the ratio of the beam velocity to the thermal speed (V_b/V_e). For electron speeds on the order of the thermal speed ($0 < V_b/V_e < 2$), the predicted frequency of maximum growth is below the plasma frequency. For higher beam speeds ($V_b/V_e \sim 3$) the frequency of maximum growth is above the plasma frequency. For very large beam speeds ($V_b/V_e \gg 3$), the predicted frequency approaches the plasma frequency.

A-G92-50

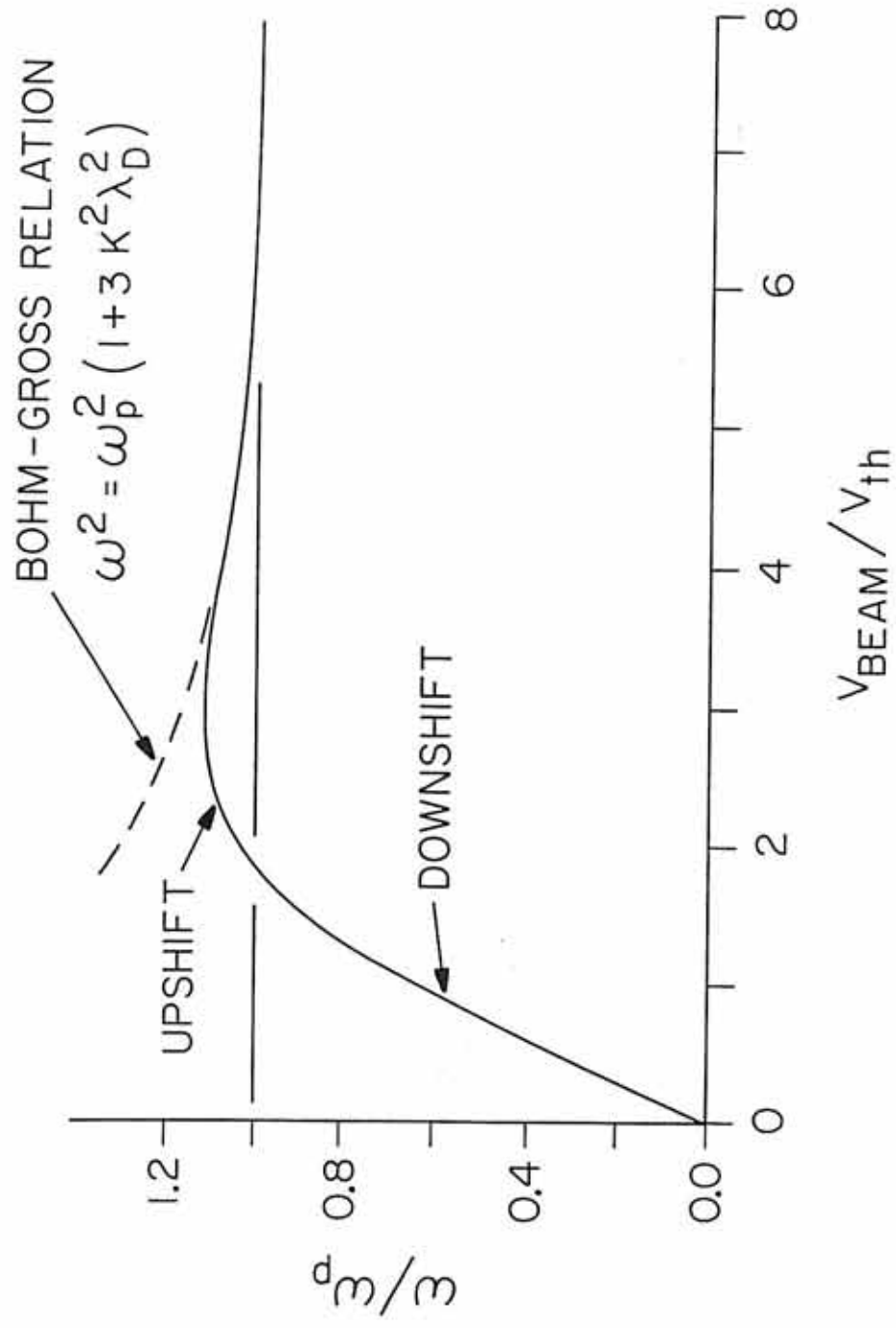


Figure 20. A sketch of the trajectory of Galileo during the Venus gravity assist flyby. A model bow shock is included to provide an estimate of the location and shape of the bow shock.

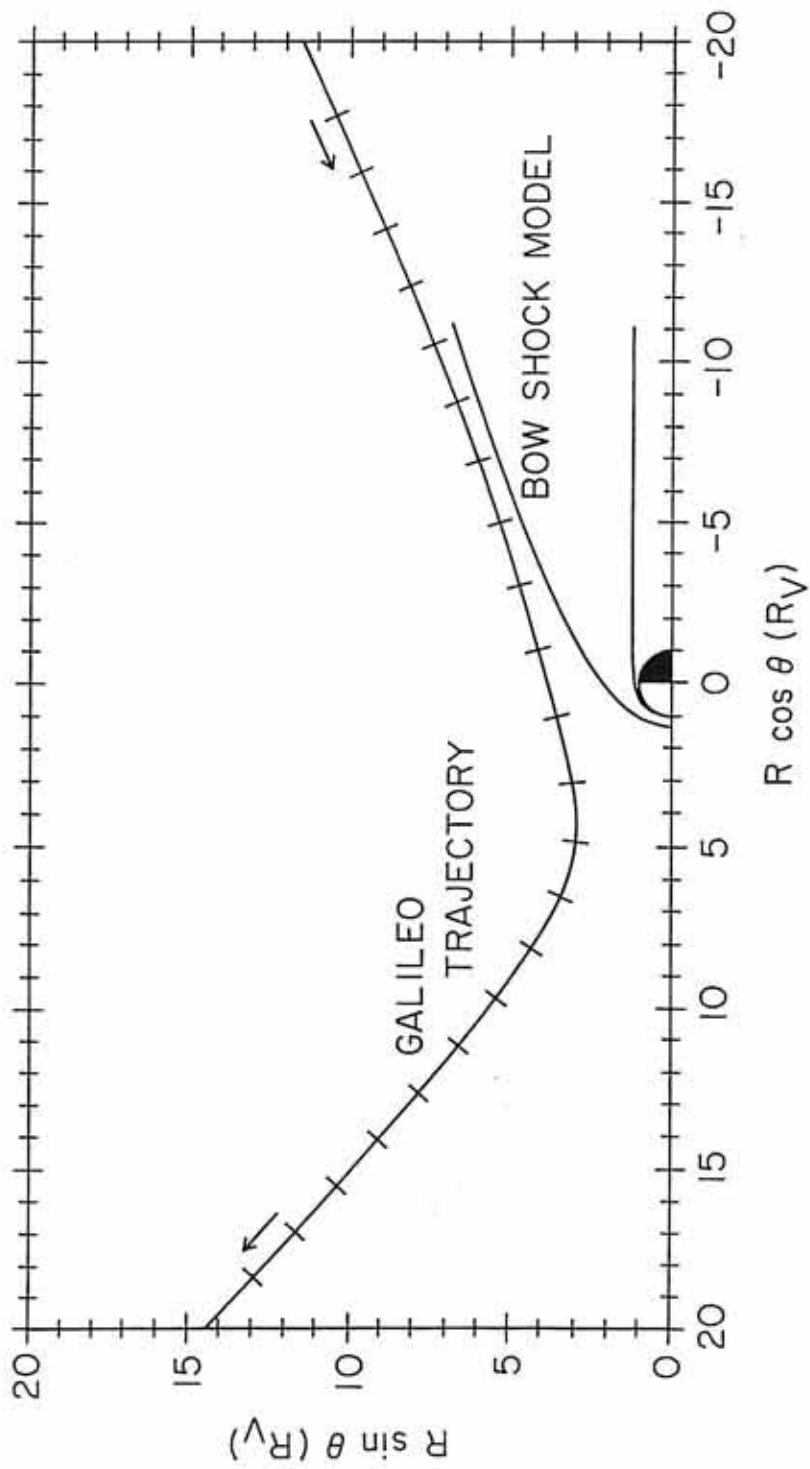


Figure 21. A frequency-time spectrogram of the electric and magnetic field intensities measured by the medium- and low-frequency spectrum analyzers. Four bow shock crossings and the plasma region the spacecraft was in are shown at the top of Figure 21. The Langmuir waves can be most easily seen after the last bow shock crossing, in the frequency band 10 to 50 kHz of the electric field spectrum. At least two types of oscillations can be seen, one consisting of a nearly steady line at a frequency of about 43 kHz, which is believed to be the electron plasma frequency f_{pe} and a second component that is shifted both downward and upward in frequency from f_{pe} .

B-G9I-145

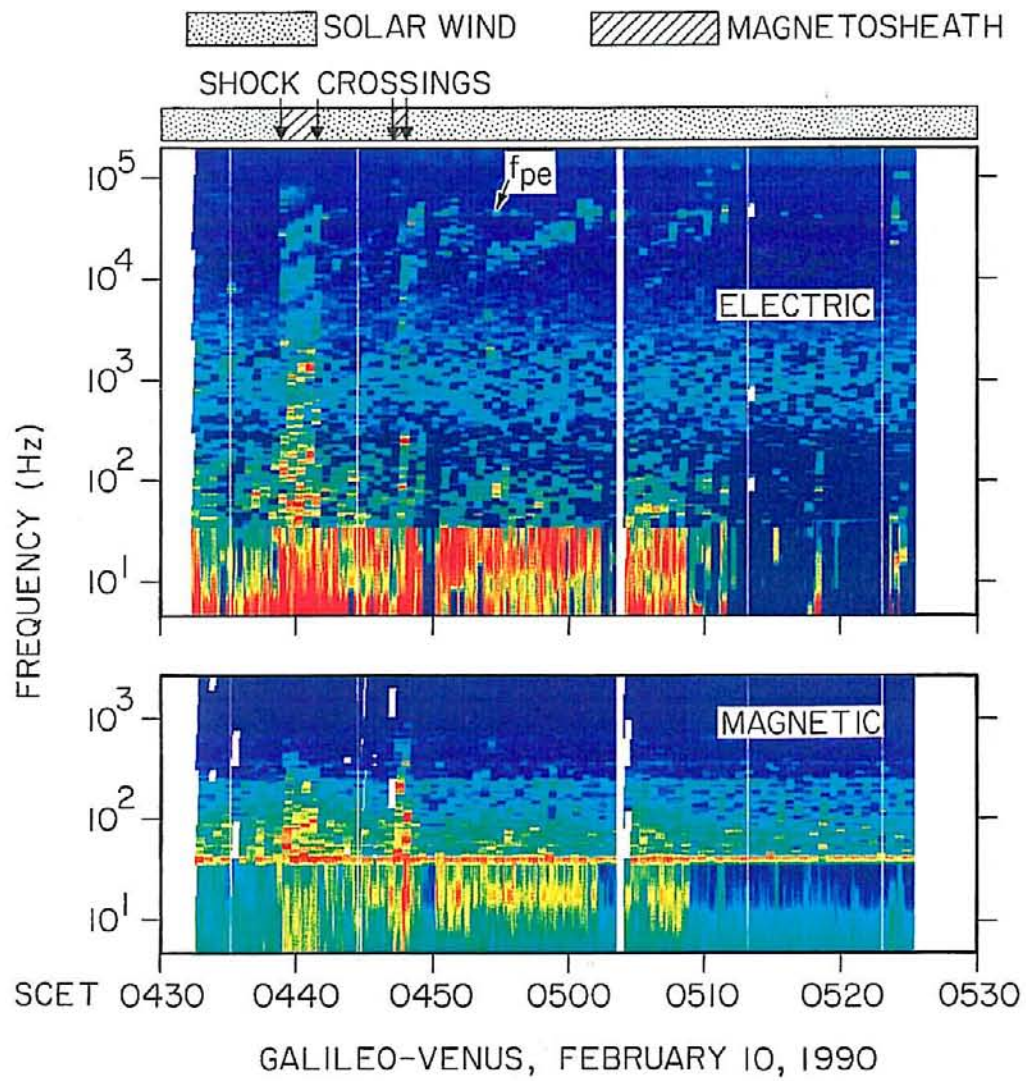
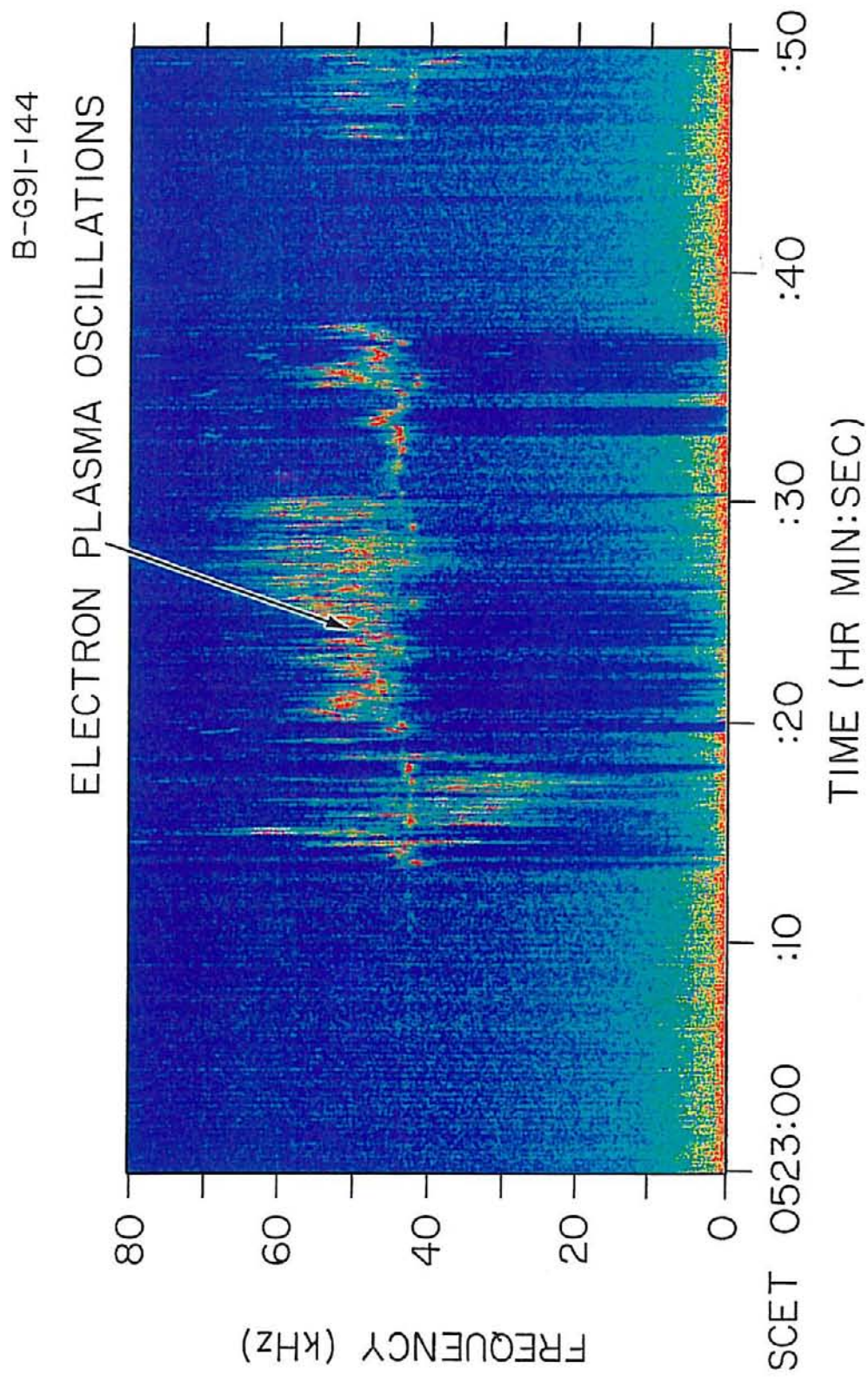


Figure 22. A high-resolution frequency-time spectrum of the Langmuir waves. The Langmuir waves can be most easily seen as the bursty signals that start approximately 12 seconds into the spectrogram. The Langmuir waves show large upshifts and downshifts in frequency from the electron plasma frequency (~ 43 kHz). The upshifts and downshifts can be as large as 20 kHz. The Langmuir waves also show extremely rapid temporal variations, many with time scales smaller than the time between successive waveform blocks (66.67 ms).



GALILEO-VENUS, FEBRUARY 10, 1990

Figure 23. The top panel is a frequency-time spectrum of the low-resolution waveforms (Mode 3 data). The signals are composed of two components, a weak narrowband component near the plasma frequency, and a stronger, broader bandwidth component that shows large upshifts and downshifts in frequency. The middle panel shows the depth parameter (see Figure 17) as determined from the measured solar wind magnetic field and a model bow shock. The bottom panel is a plot of the maximum peak electric field amplitudes of the waveform blocks.

B-G93-93-1

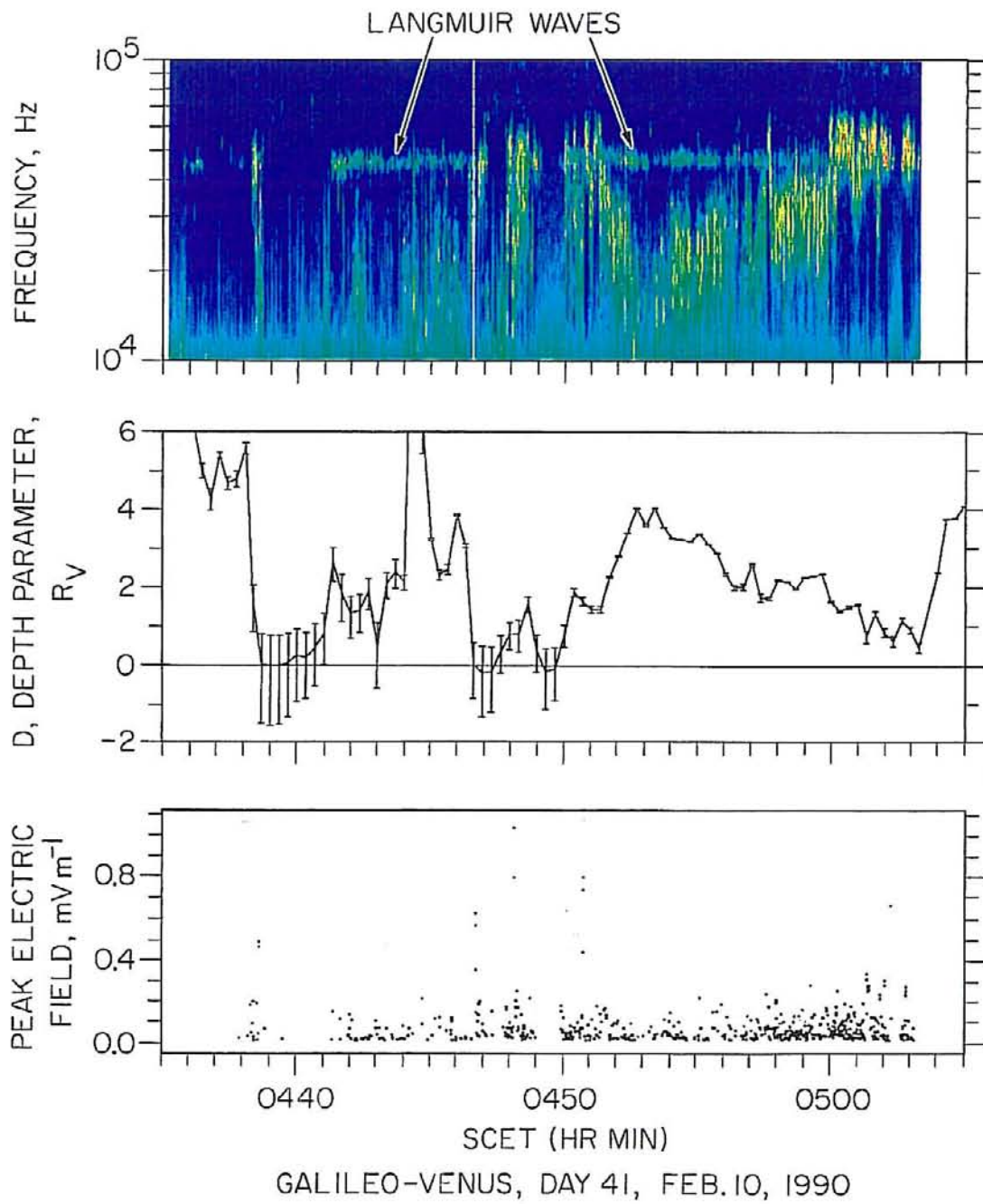
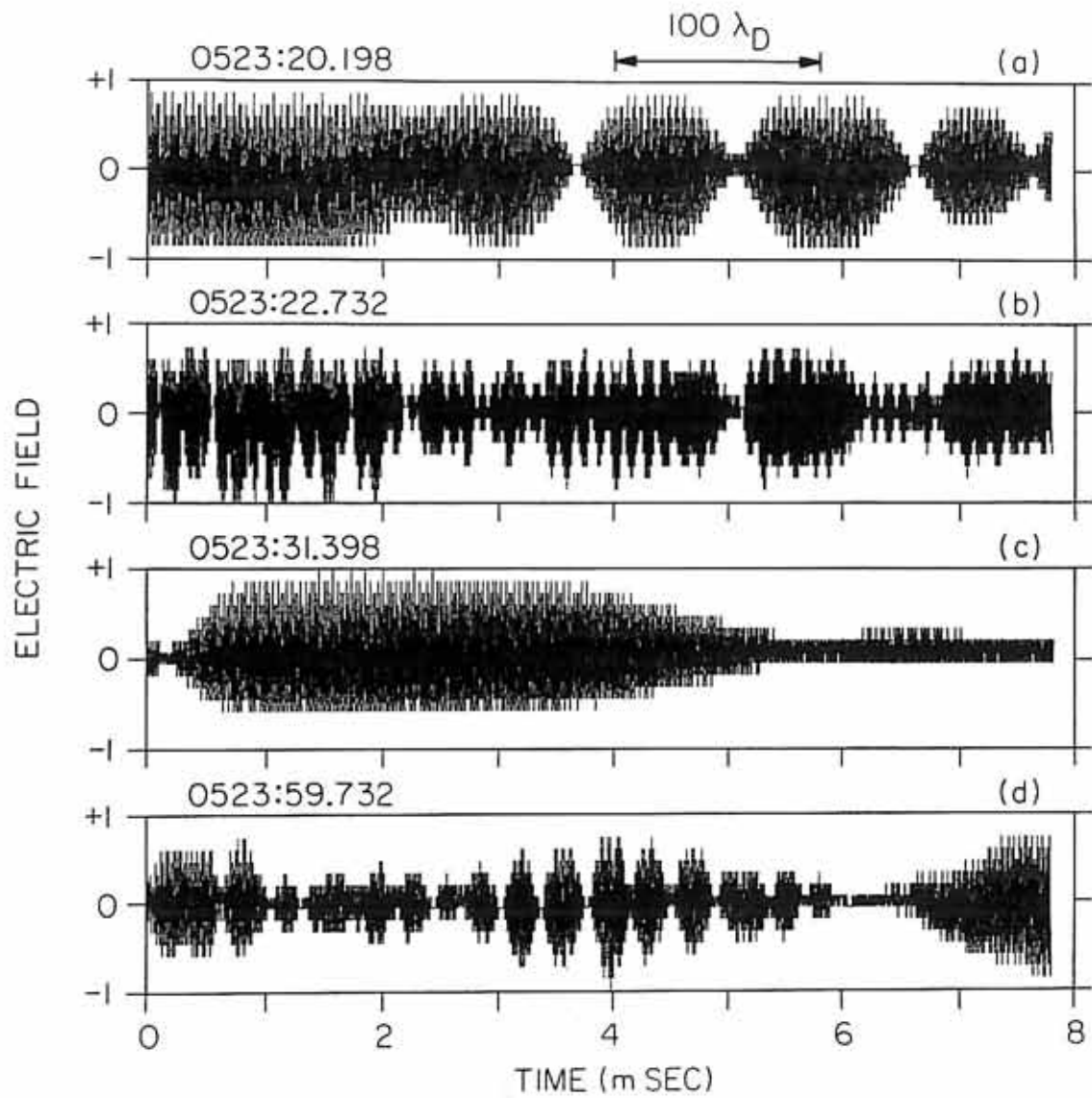


Figure 24. A sampling of the Langmuir emissions electric field waveforms observed at Venus. The waveforms show considerable variations and are similar to the Langmuir waveforms observed in association with the type III burst (see Figure 9).

C-G93-138-2



GALILEO-VENUS, DAY 41, FEB. 10, 1990

Figure 25. A spectrum of the waveform from panel (d) of Figure 24. The spectrum consists of two distinct frequency components, one at ~ 45.5 kHz and the other at ~ 48.3 kHz. The frequency difference of these two signals agrees with the observed beat frequency (~ 2.8 kHz).

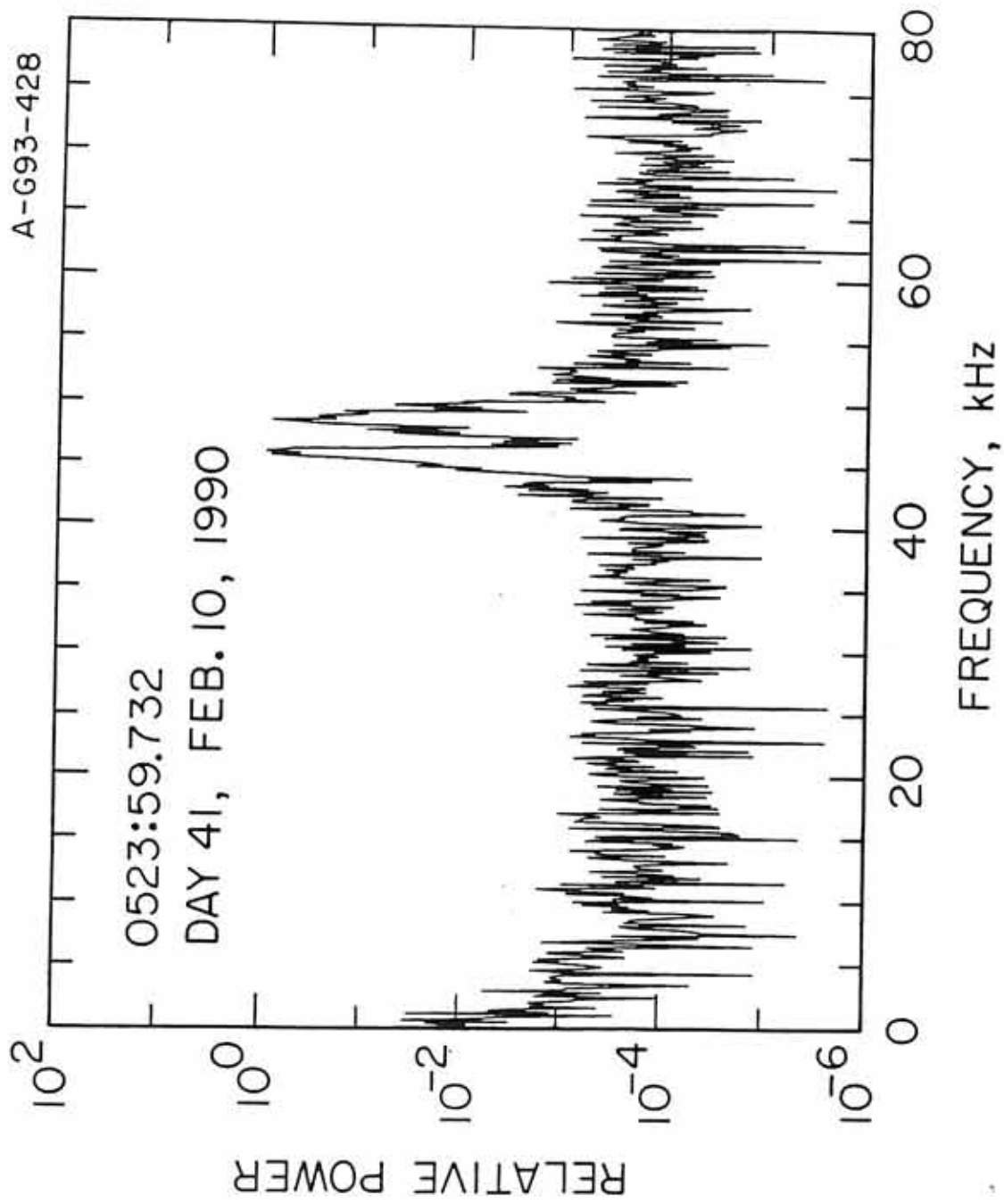
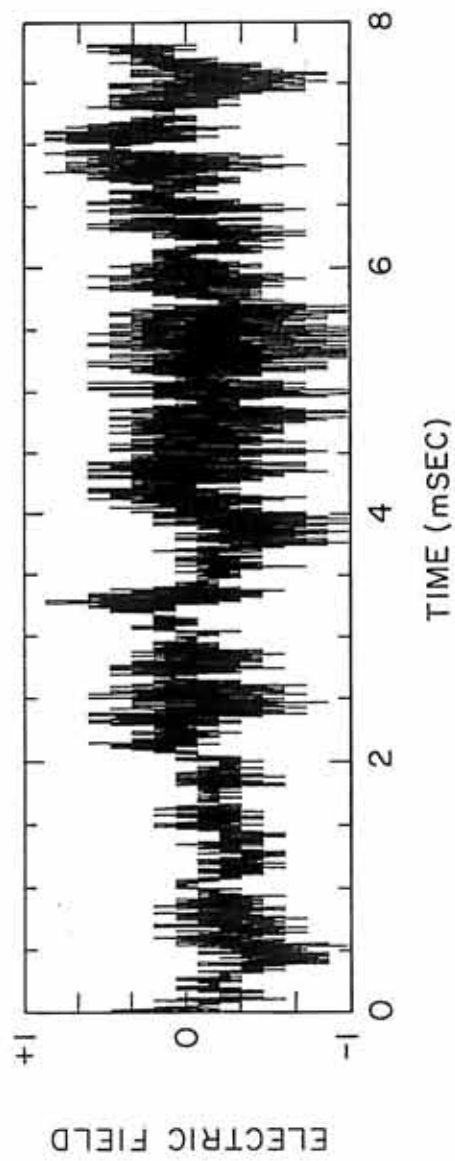
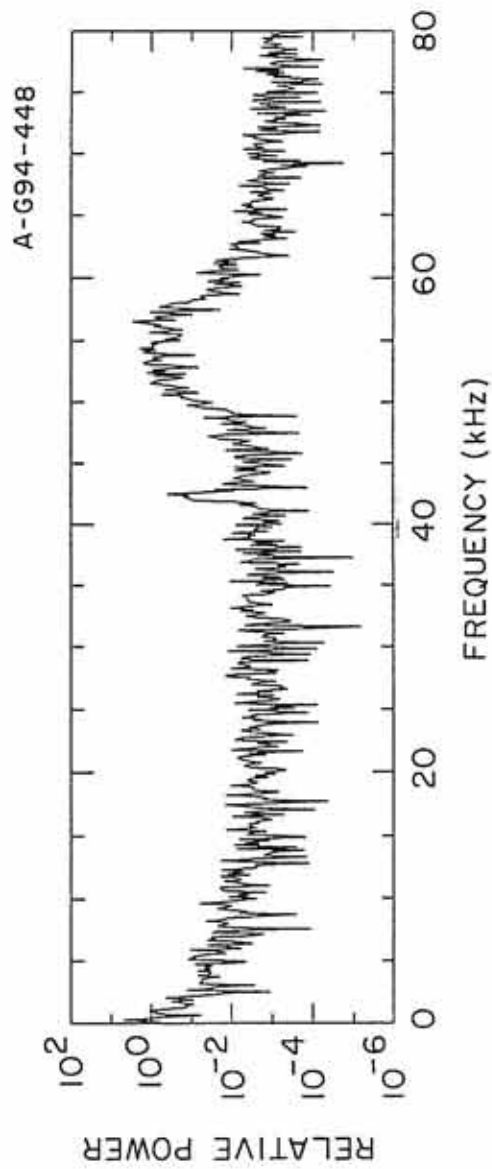


Figure 26. The bottom panel is an example of a chaotic-type waveform with very little beat pattern. The top panel is the spectrum of the chaotic-type waveform shown in the bottom panel. The spectrum exhibits a narrowband signal at ~ 42.5 kHz (believed to be the plasma frequency), and a broader signal upshifted in frequency, centered at ~ 54 kHz. Chaotic-type waveforms are frequently observed at Venus during periods with large upshifts and downshifts in the Langmuir wave emission frequency.



GALILEO, 0523:27.265, DAY 41, FEB 10, 1990

Figure 27. The number of waveform blocks as a function of the peak electric field strength.

A-G92-484-1

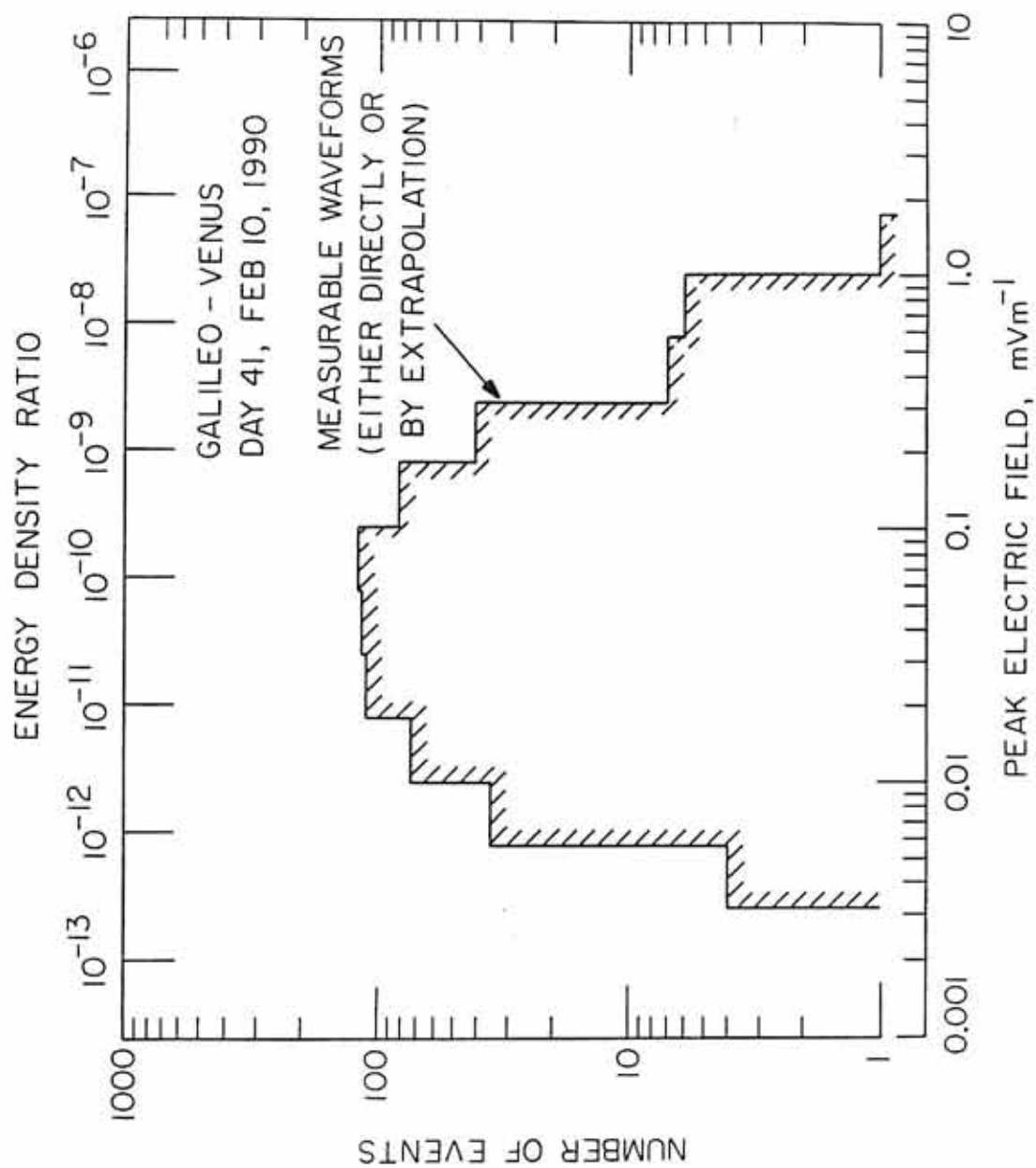


Figure 28. The spectrum of the waveform block from panel (b) of Figure 24. The spectrum contains two main peaks, one centered at ~ 46 kHz, which is near the plasma frequency, and another that is upshifted in frequency, and centered at ~ 53 kHz. Each of the two main signals is broad in frequency and contains a great deal of structure. There is also a series of weak signals located from a few hundred Hz to about 9 kHz. The low-frequency signals are suggestive of the low-frequency ion sound waves predicted by parametric decay.

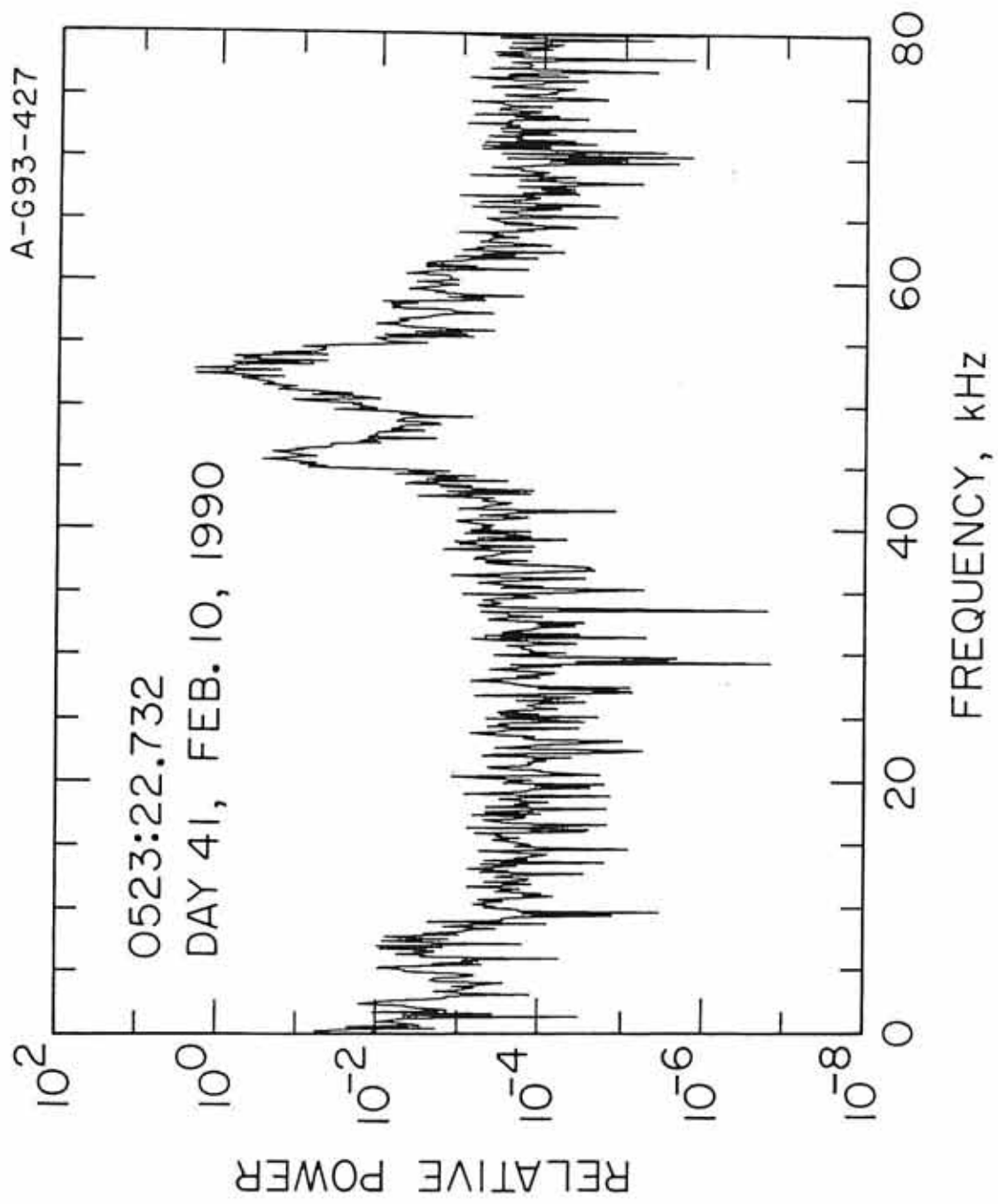


Figure 29. A sketch of the trajectory of Galileo during the two Earth gravity assist flybys. The model bow shock is included for reference only, and no attempt has been made to verify the correct distance and position of the bow shock. During the first Earth flyby (E1), Galileo exited the magnetosheath near the nose of the bow shock. During the second flyby (E2), Galileo exited the shock further downstream. The different trajectories allowed Galileo to obtain measurements in different parts of the foreshock.

A-G94-270

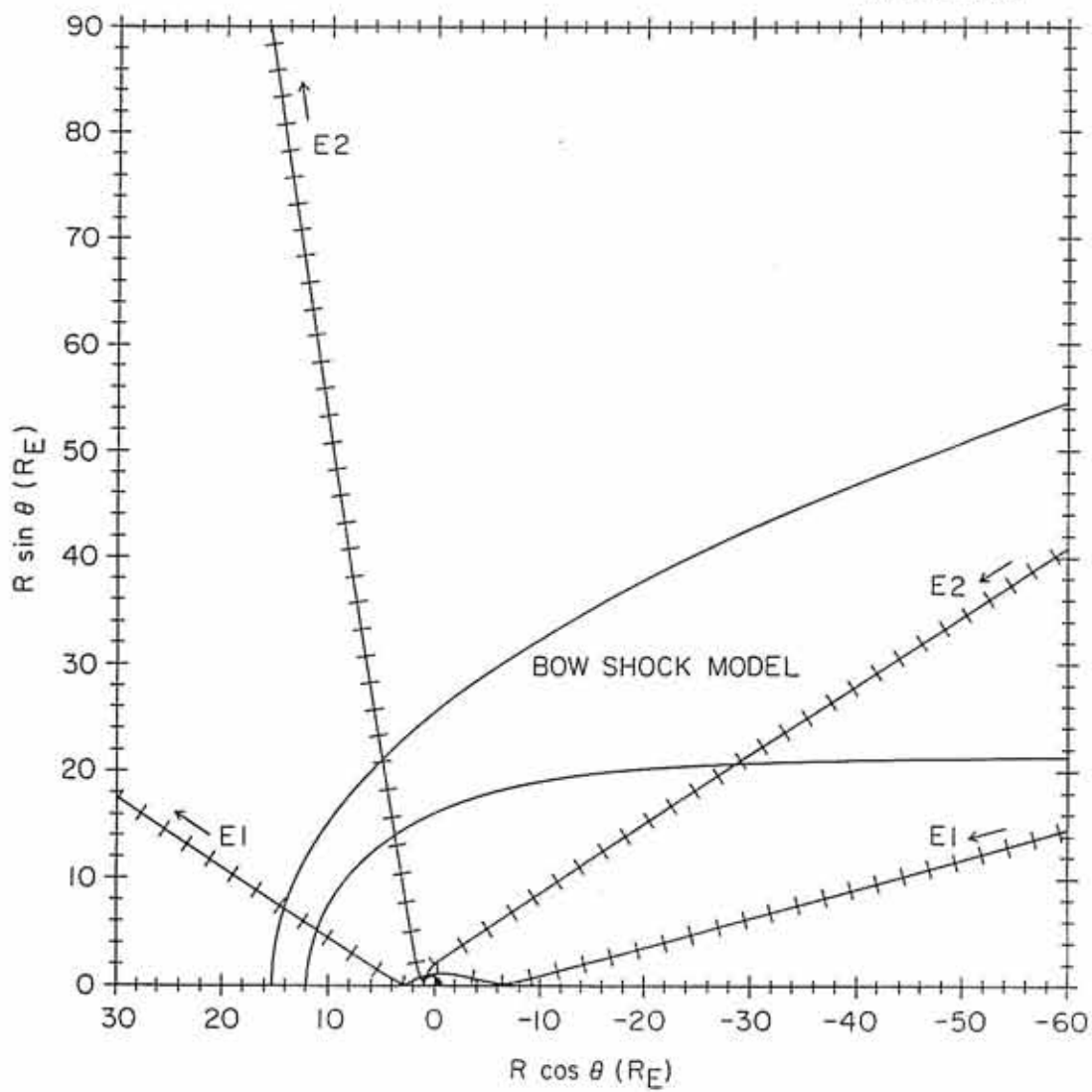


Figure 30. A frequency-time spectrogram from the spectrum analyzer receivers. The Langmuir waves can be seen immediately after the bow shock crossing (~ 2334 UT) at about 42 kHz in the medium frequency spectrum analyzer receiver (middle panel). Strong bursts of Langmuir waves can be seen at approximately 2258 UT, 0015 UT, 0025 UT, 0043 UT, and from 0118 to 0143 UT. The Langmuir waves show a great deal of structure, including large downshifts and upshifts in frequency, and are very broad in frequency. The narrowband signal at 40 kHz is an interference signal from the spacecraft, and not related to the Langmuir waves.

Galileo PWS University of Iowa

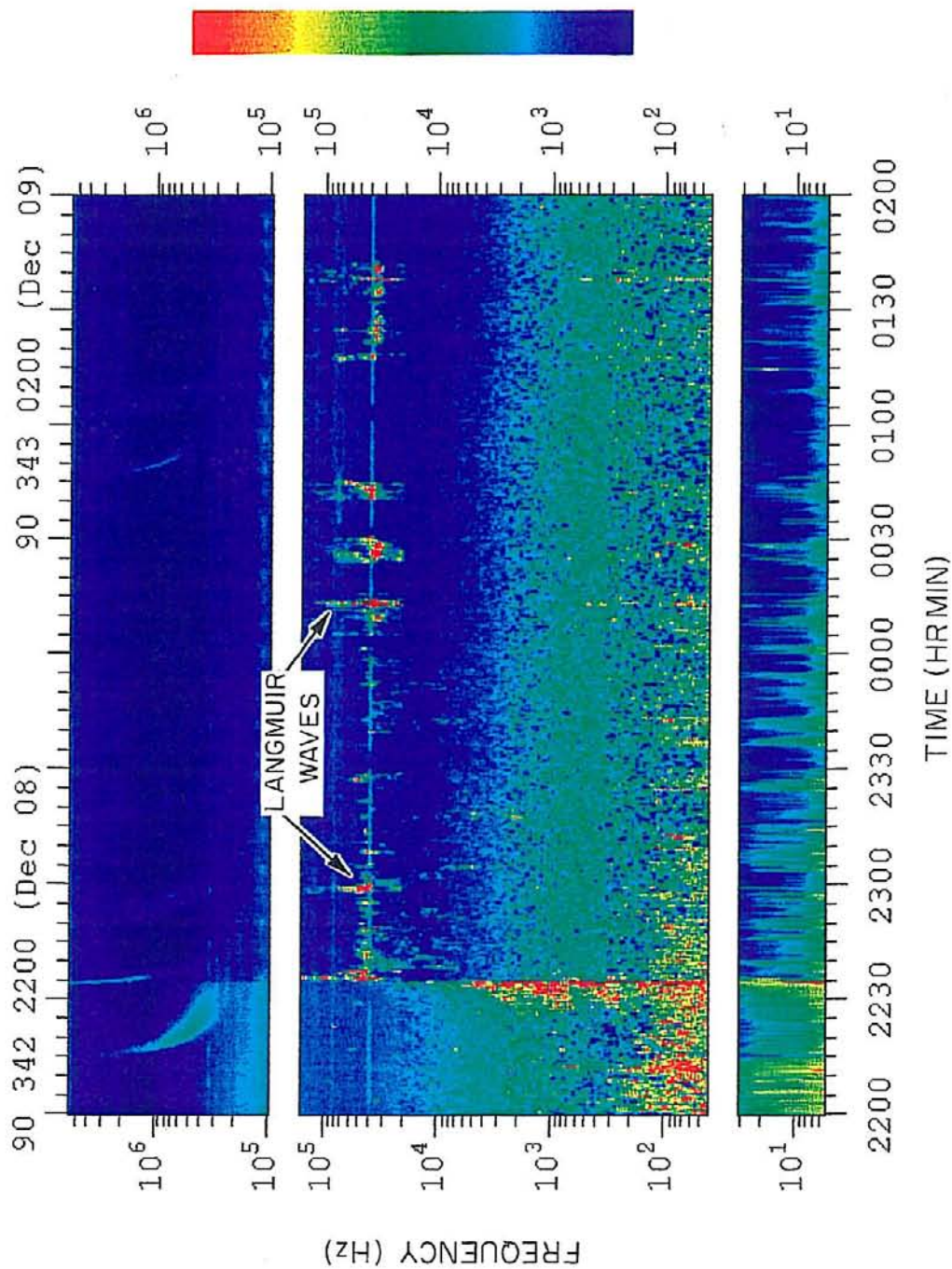


Figure 31. A 24-hour frequency-time spectrogram from the spectrum analyzer receivers. The first two hours of this spectrogram corresponds to the last two hours of Figure 30. Two types of Langmuir wave emissions are observed. Bursty Langmuir waves can be seen in the first two hours of the spectrogram. At ~ 0330 UT, a second type of Langmuir wave emission appears. This second type of emission is observed almost continually for the next five hours, with sporadic emissions observed for the next seven hours. This emission is less intense than the bursty emission and the large scale structure of the emissions is found in a narrow range in frequency.

Galileo PWS University of Iowa

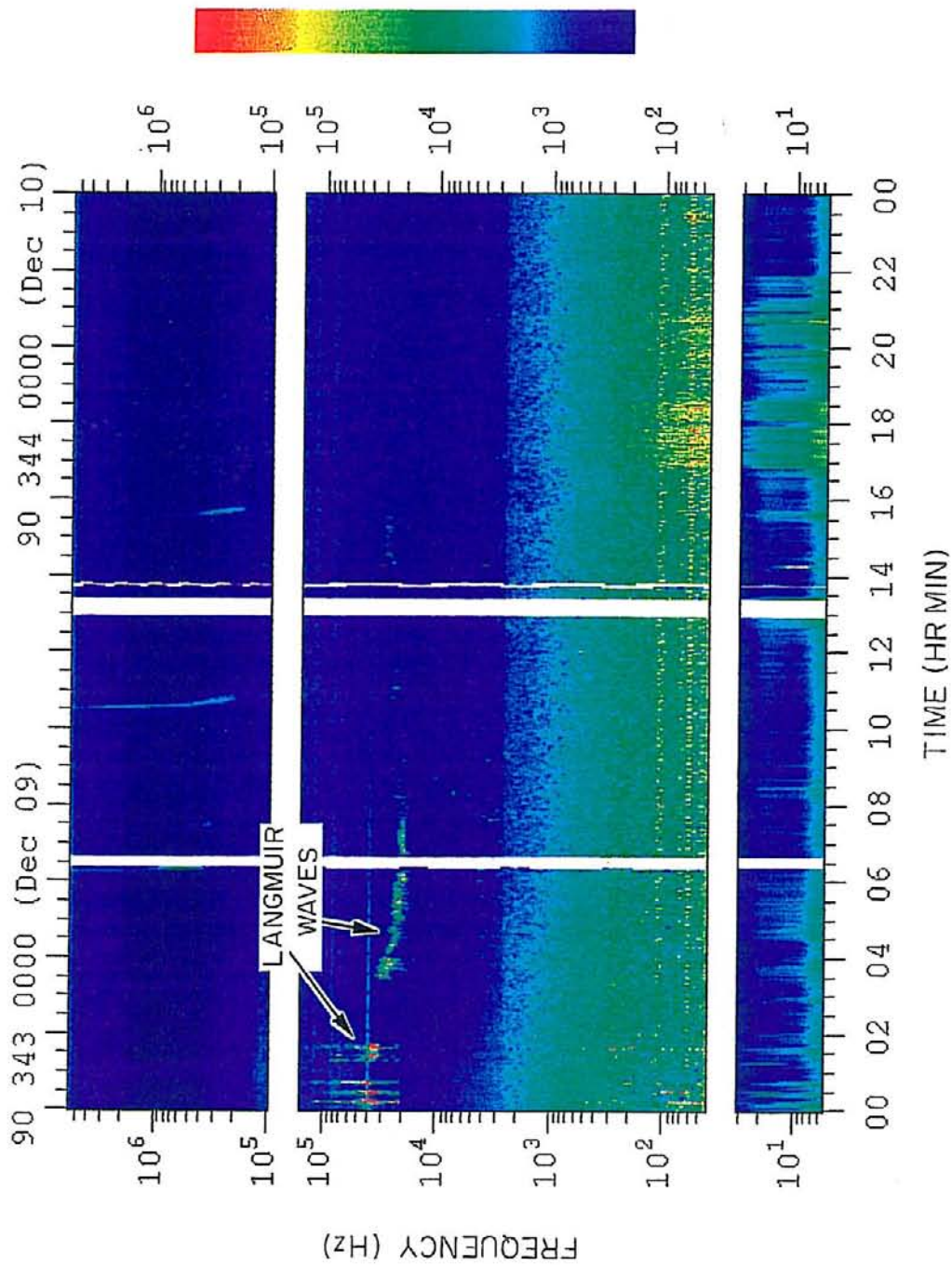


Figure 32. A high-resolution frequency-time spectrogram from the wideband waveform receiver for the interval immediately after Galileo exited the bow shock. The Langmuir waves are the bursty signals that start at ~ 2235 UT in the frequency range 40 kHz to 55 kHz. The structure of the Langmuir waves includes large upshifts and downshifts from the electron plasma frequency (estimated to be ~ 41 kHz at 2235 UT, decreasing to ~ 35 kHz at the end of the spectrum). The spectrum of the upshifted and downshifted Langmuir waves also exhibit large broadening in frequency, sometimes as much as 30 kHz. The signals between 60 and 100 kHz at two and three times the emission frequency of the intense Langmuir waves are most likely harmonic distortion due to clipping of the waveforms.

GALILEO

START - 1990 342 22:24 (8 December)

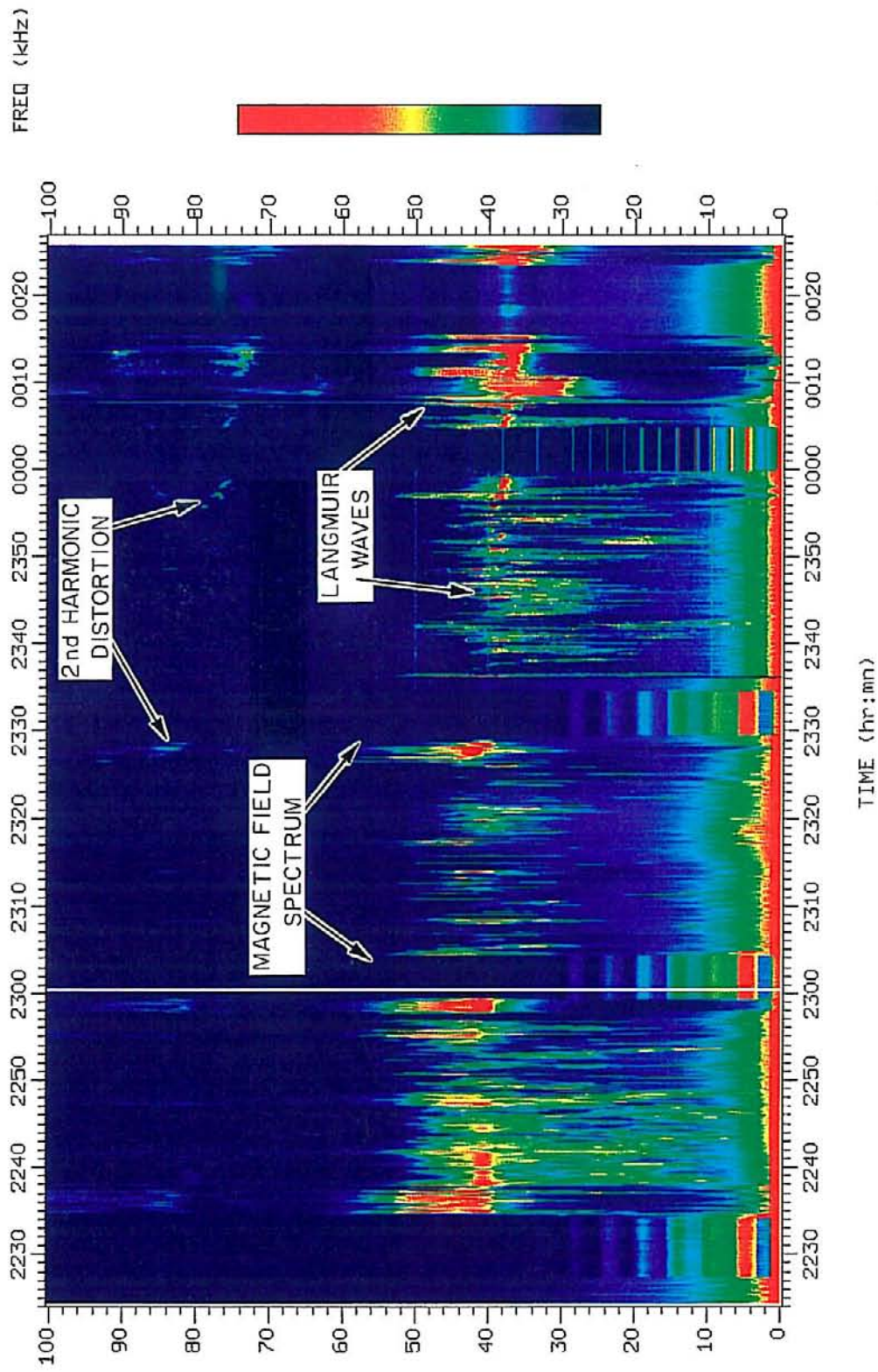
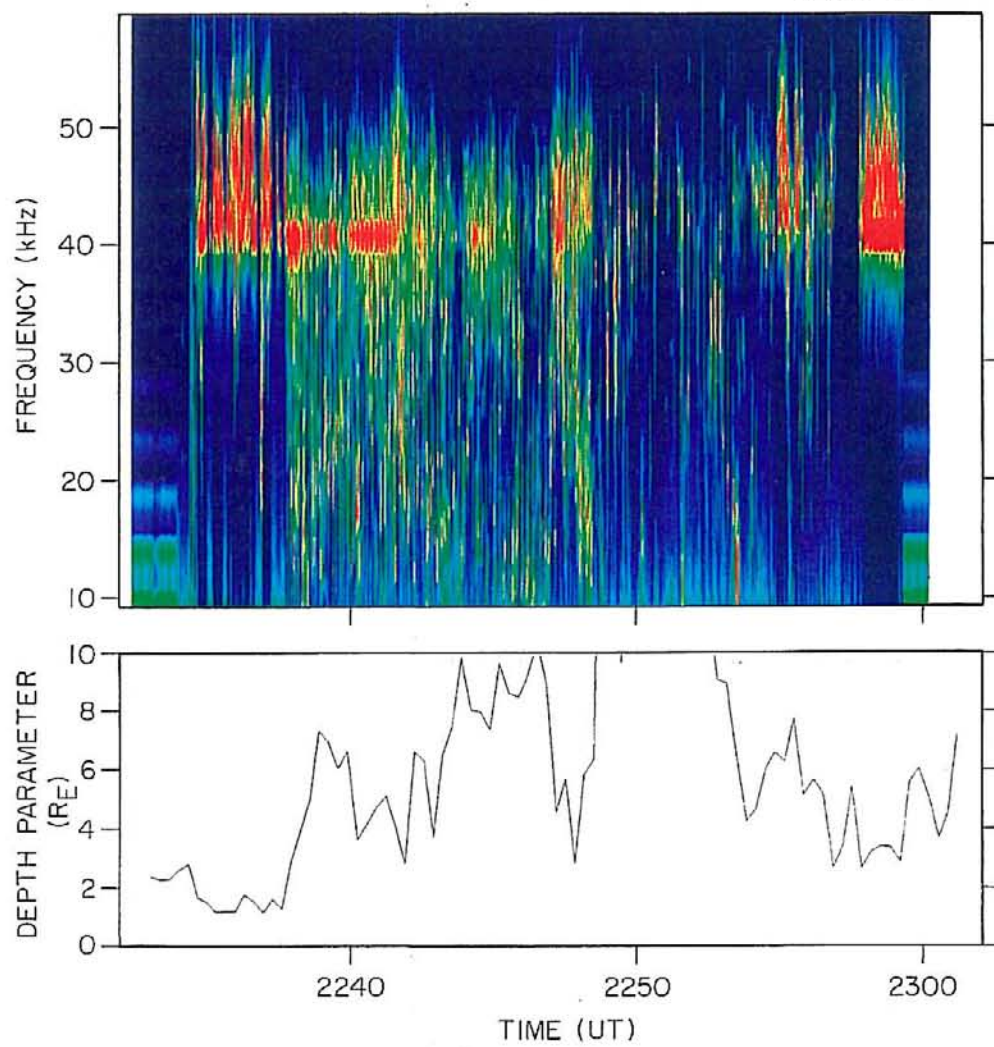


Figure 33. The top panel is a high-resolution frequency-time spectrum of the Langmuir waves from Figure 32. The bottom panel shows the depth parameter as determined by the Galileo magnetometer experiment. A correlation exists between the depth parameter and the shifts in the frequency of the Langmuir waves.

B-G94-309



GALILEO-EARTH I, DAY 342, DEC 8, 1990

Figure 34. A high-resolution frequency-time spectrogram from the wideband waveform receiver. The Langmuir wave emissions during this interval are more constant and narrowbanded in frequency than the emissions shown in Figure 32. The signals at two and three times the frequency of the main emission (0530 UT at ~ 42 kHz and ~ 64 kHz) are most likely instrumental effects caused by clipping in the receiver. The white strips (for example 0453 to 0508 UT) are intervals where no wideband data are available. Six intervals of magnetic field wideband data are also shown.

GALILEO

START - 1990 343 03:37 (9 December)

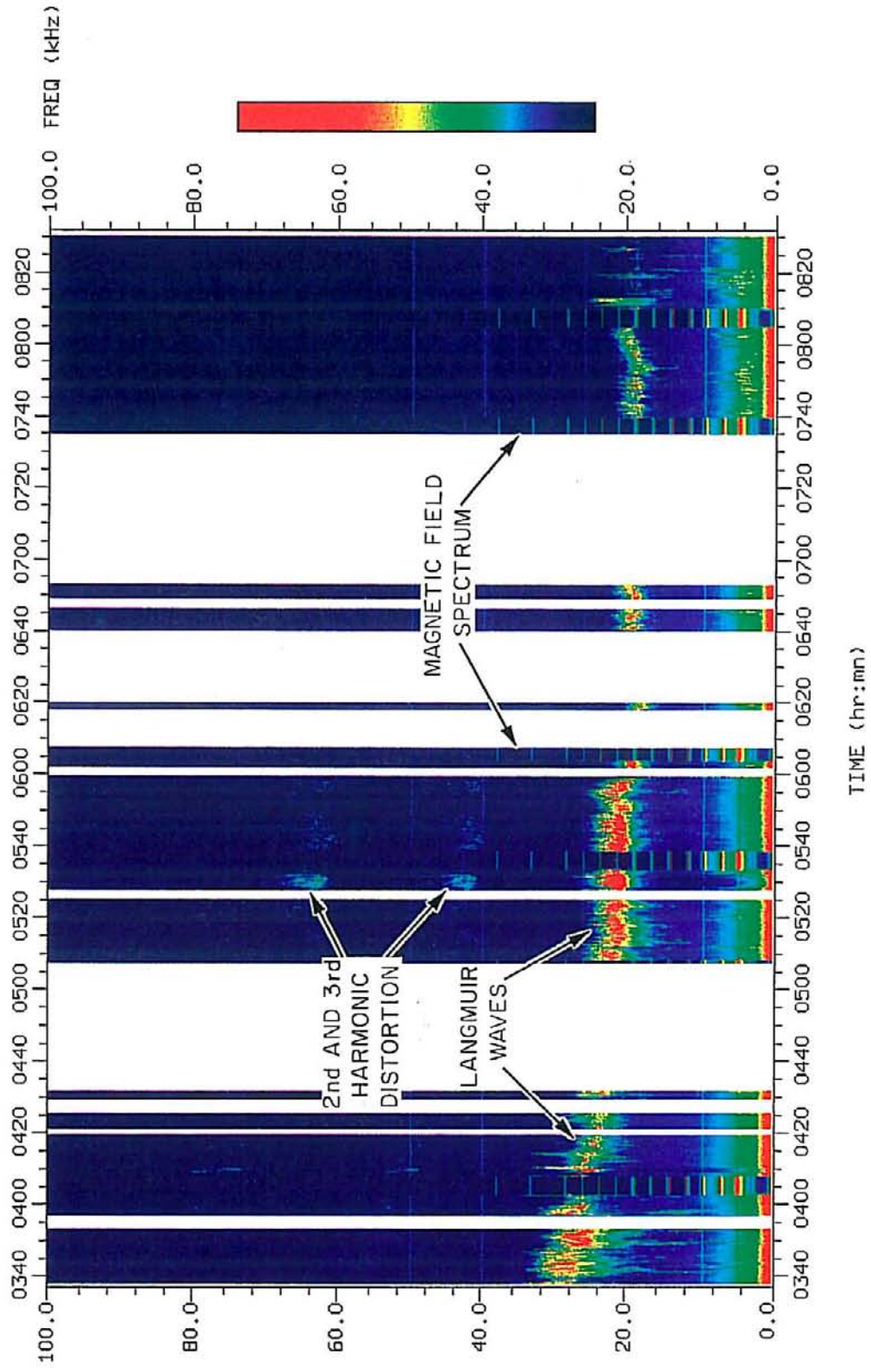
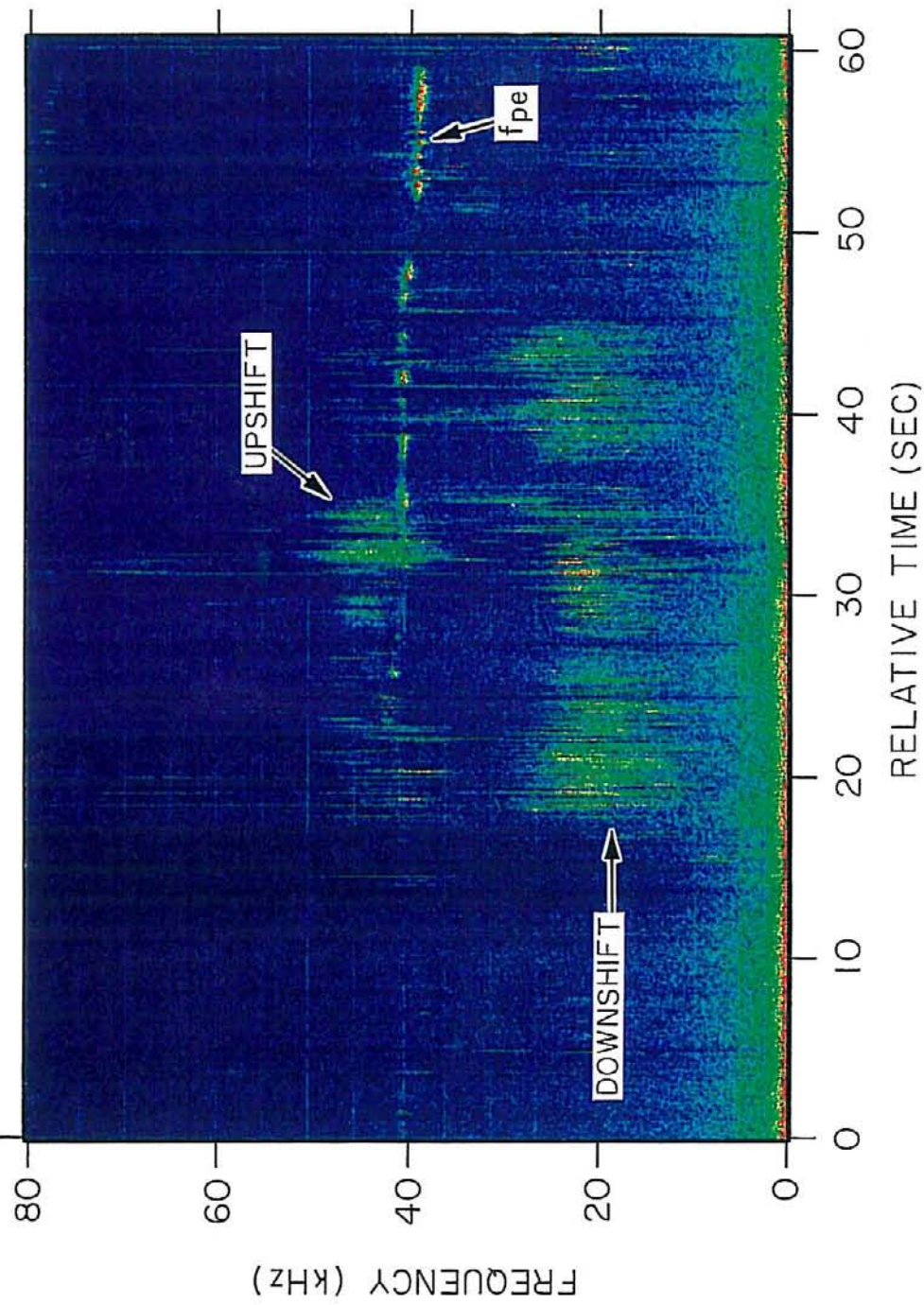


Figure 35. A one-minute frequency-time spectrogram from the wideband waveform receiver of an interval with large downshifts in frequency. The spectrum consists of sporadic narrowband emissions near the plasma frequency (~ 39 kHz), and broadband upshifted and downshifted emissions. A large band of downshifted Langmuir waves is observed starting ~ 18 seconds into the spectrum, in the frequency range 10 kHz to 25 kHz. Upshifted emissions can be observed from about 28 to 35 seconds into the spectrum.

A-G94-472

2351:20.723 UT

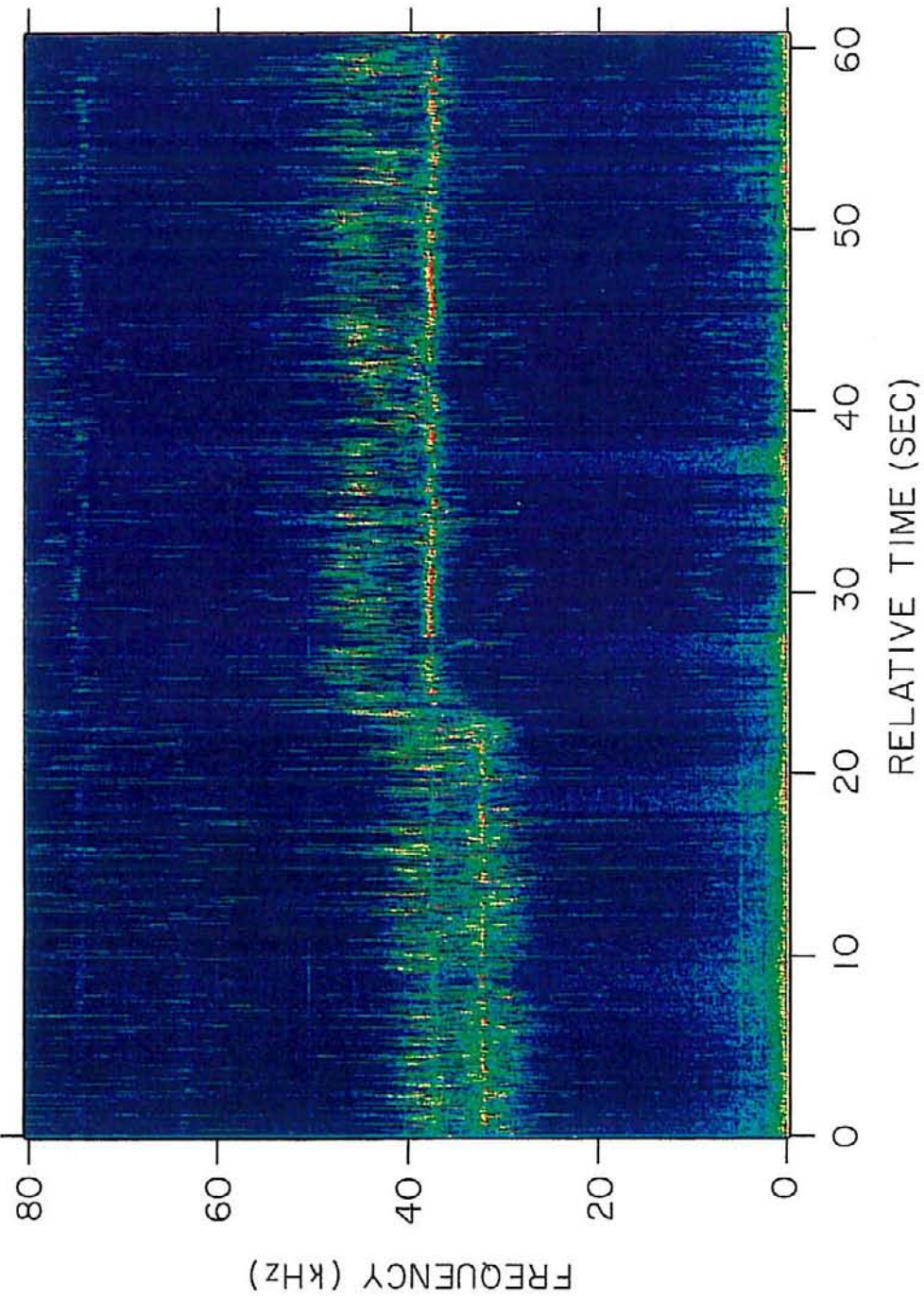


GALILEO - EARTH I, DEC 8, 1990

Figure 36. A one-minute frequency-time spectrogram from the wideband waveform receiver. An intense signal is observed at 32 kHz, with a weaker, more sporadic signal at about 37 kHz. Approximately 23 seconds into the spectrogram, the two signals appear to shift up in frequency very rapidly. The abrupt shift is probably caused by a rapid increase in the electron plasma density. After this shift in emission frequency, the more intense band is located at ~ 37 kHz, and the upper band at ~ 45 kHz. The spiky emissions at approximately two times the main emission bands are probably instrument effects, produced when the Langmuir wave signals are strong enough to clip the waveform receiver. The weak emission line at ~ 75 kHz may be electromagnetic radiation at $2f_{pe}$.

A-G94-470

0010:33.389 UT

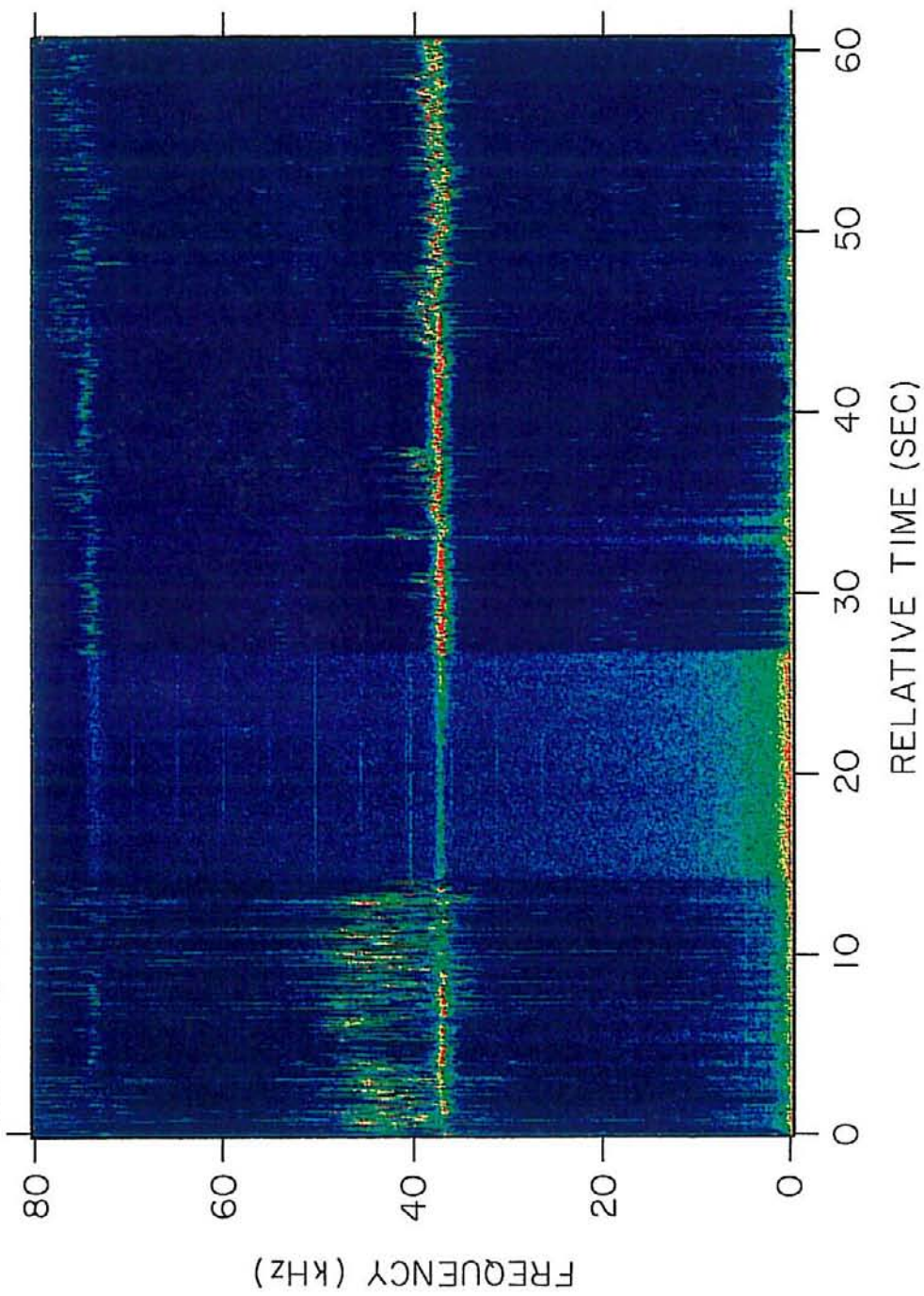


GALILEO-EARTH I, DEC 9, 1990

Figure 37. A one-minute frequency-time spectrogram from the wideband waveform receiver for the interval that follows Figure 36. The two bands of emission continues for the first 14 seconds of the spectrogram. Approximately 14 seconds into the spectrogram, the intensity of the Langmuir wave emission decreases. The weak emission bands at ~ 37 kHz and ~ 74 kHz may be electromagnetic radiation produced in the electron foreshock at f_{pe} and $2f_{pe}$ which is propagating into the solar wind. Approximately 27 seconds into the spectrogram, the intensity of the Langmuir waves increase greatly. The narrowband, very intense emission is characteristic of Langmuir waves near the foreshock boundary.

A-G94-469

0011:34.055 UT

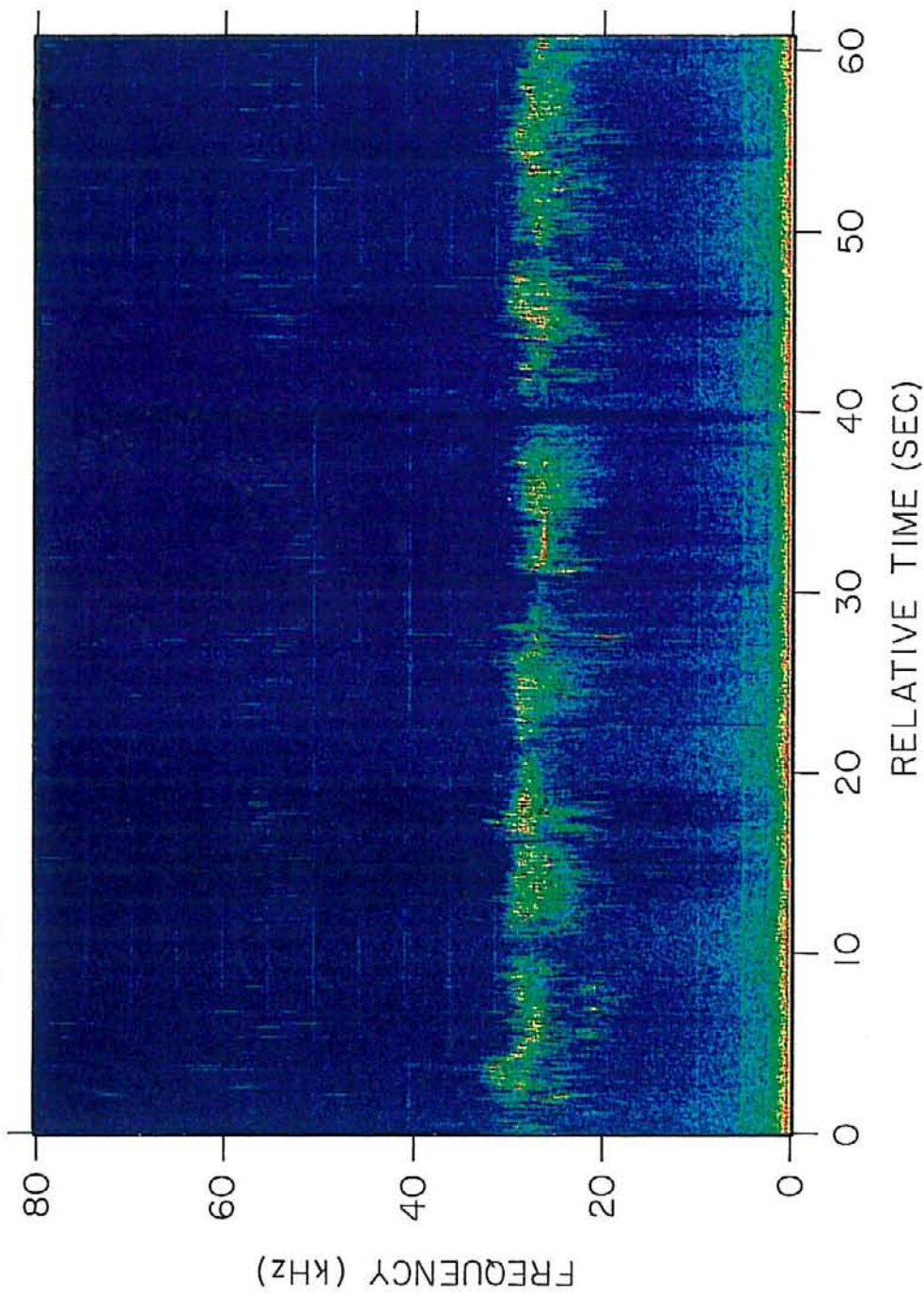


GALILEO-EARTH I, DEC 9, 1990

Figure 38. A one-minute frequency-time spectrogram from the wideband waveform receiver from the beginning of Figure 34. The ~ 10 -second period of decreasing emission intensity is probably due to the spacecraft rotation (the spin period of Galileo is ~ 20 seconds).

A-G94-468

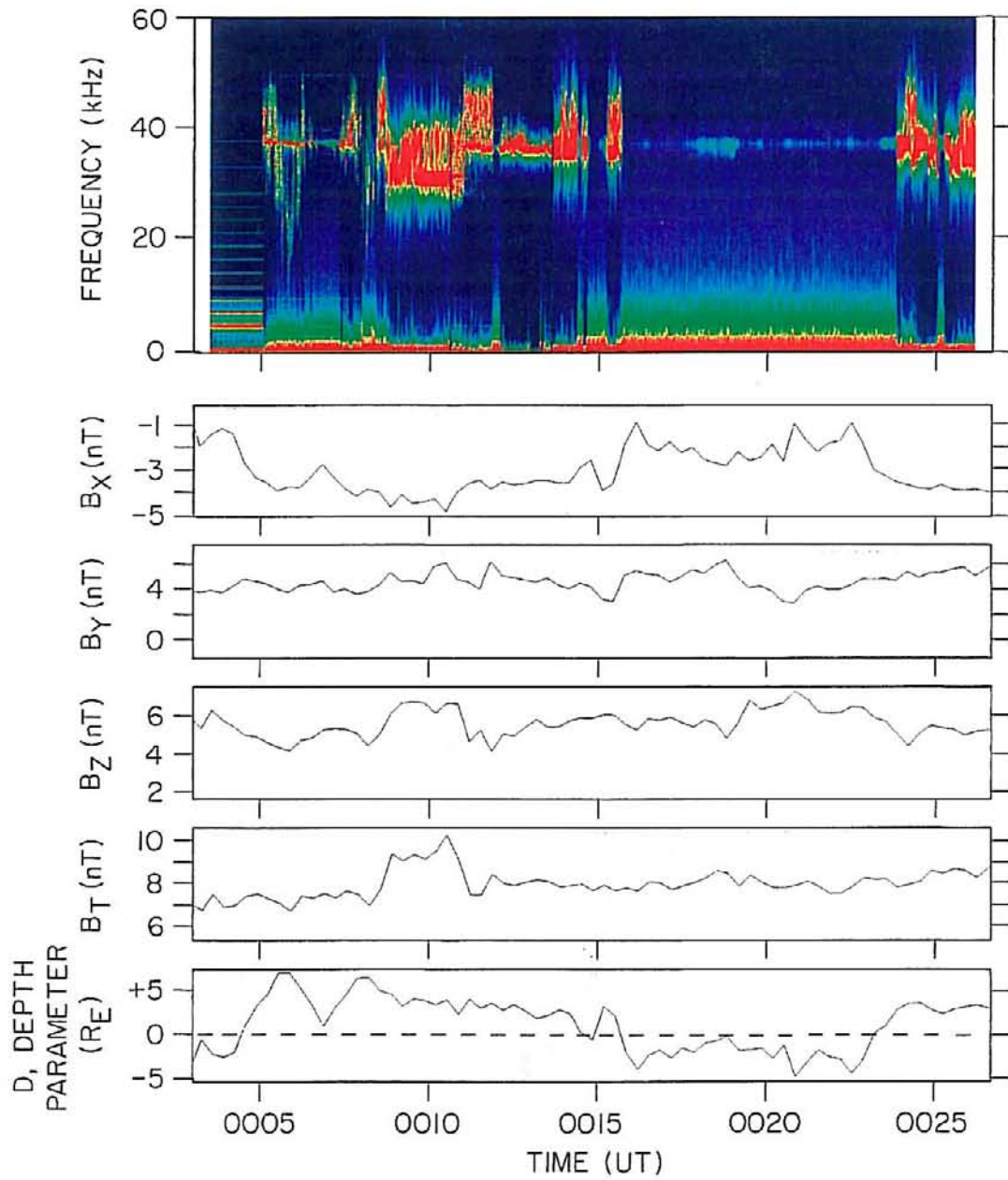
0350:58.713 UT



GALILEO-EARTH I, DEC 9, 1990

Figure 39. The top panel is a frequency-time spectrogram of the interval of abrupt shift in frequency shown in Figure 36. The middle four panels show the magnetic field components and the total magnetic field. The bottom panel is the depth parameter calculated by the magnetometer experiment. The downward shift in frequency of the Langmuir waves at $\sim 0008:30$ UT is correlated to the increase in the B_Z component and in the total magnetic field B_T . The increase in the Langmuir wave frequency at ~ 0011 UT corresponds to the decrease in the B_Z component and in the total magnetic field B_T .

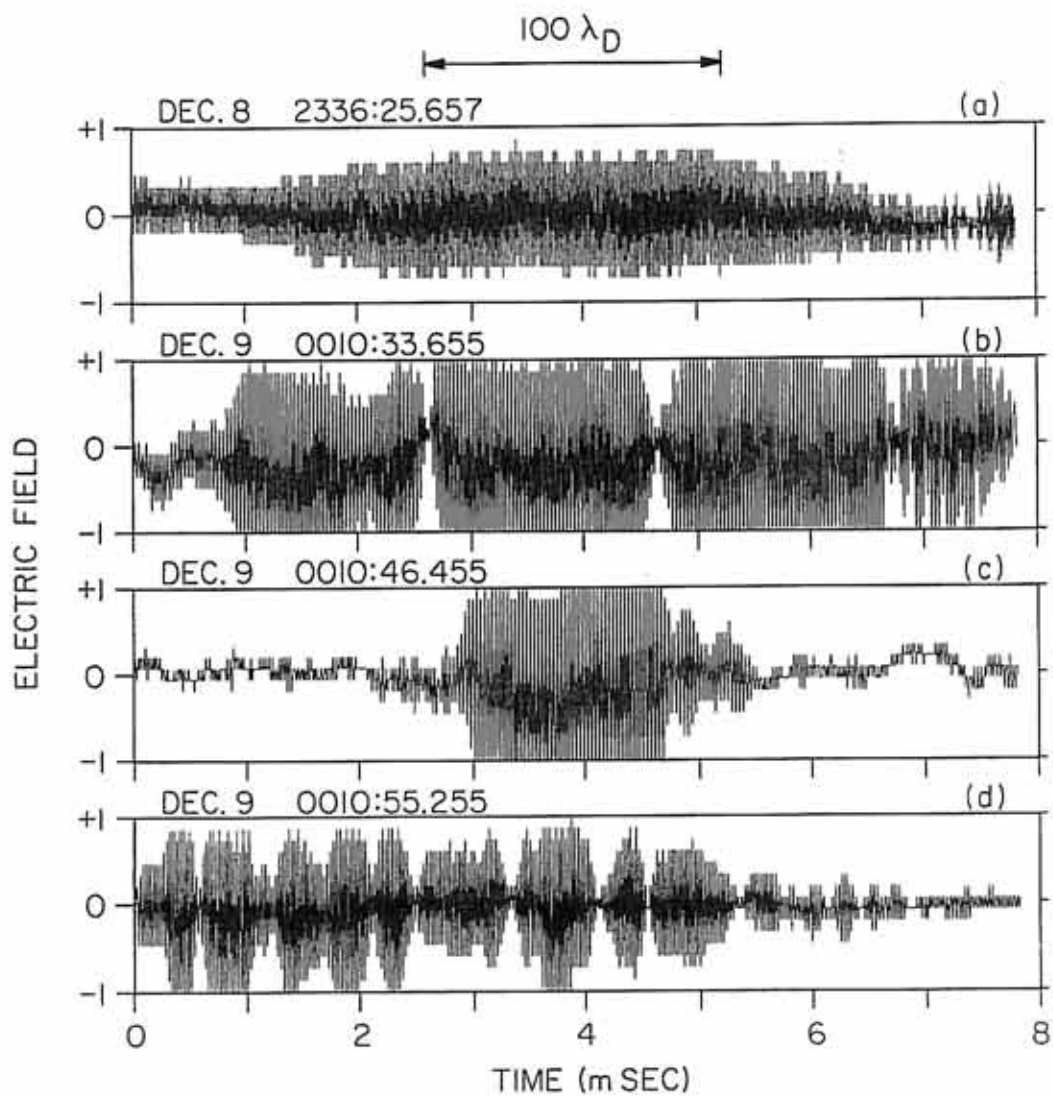
B-G94-45I



GALILEO-EARTH I, DAY 343, DEC 9, 1990

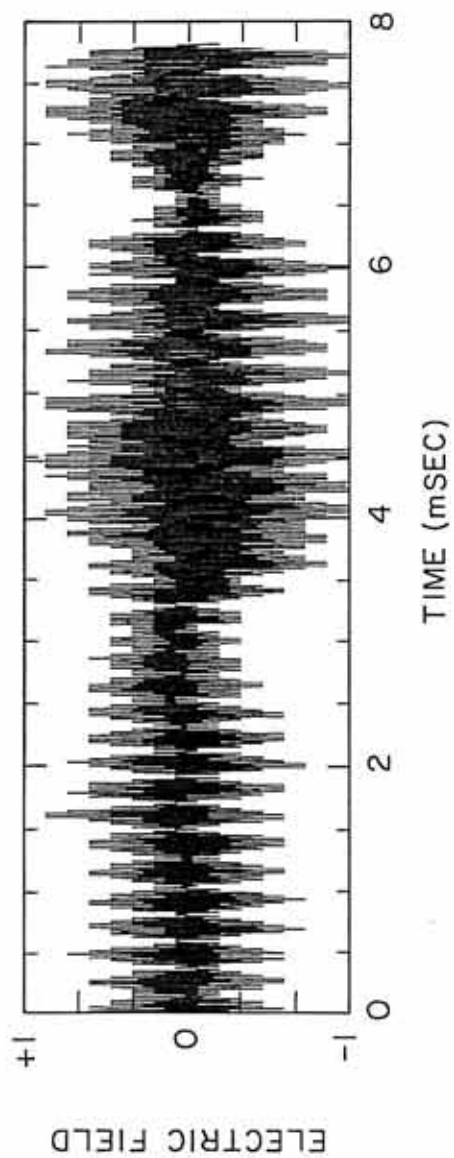
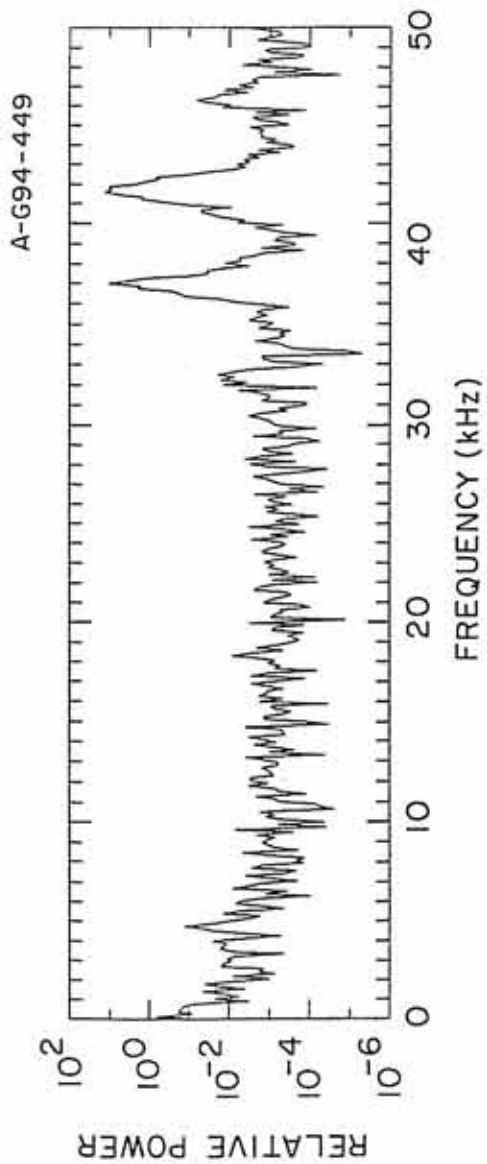
Figure 40. A sampling of the Langmuir wave emission waveforms obtained during the first Earth flyby. The waveforms are very similar to the waveforms observed at Venus and in association with the type III burst. The high-frequency, quasi-sinusoidal waveforms evident in each of these plots are the Langmuir wave oscillations.

C-G92-13-1



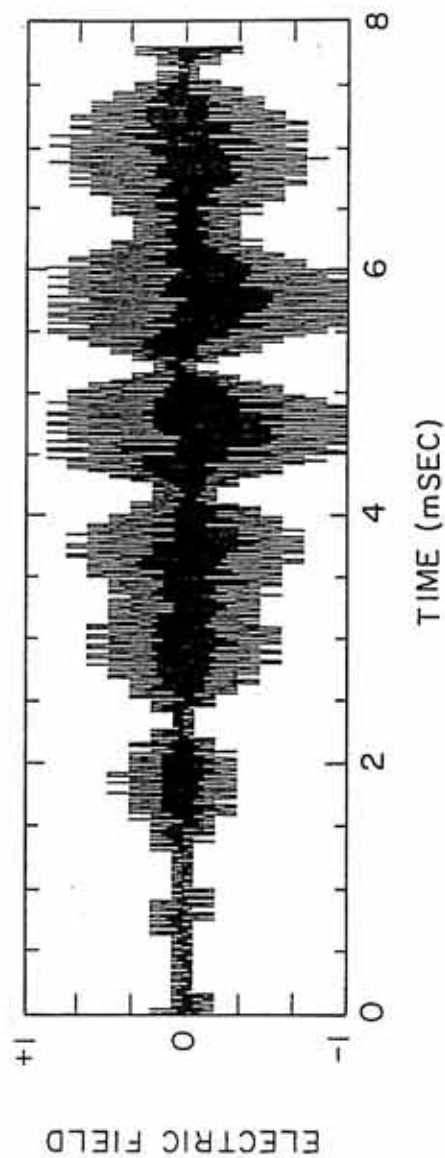
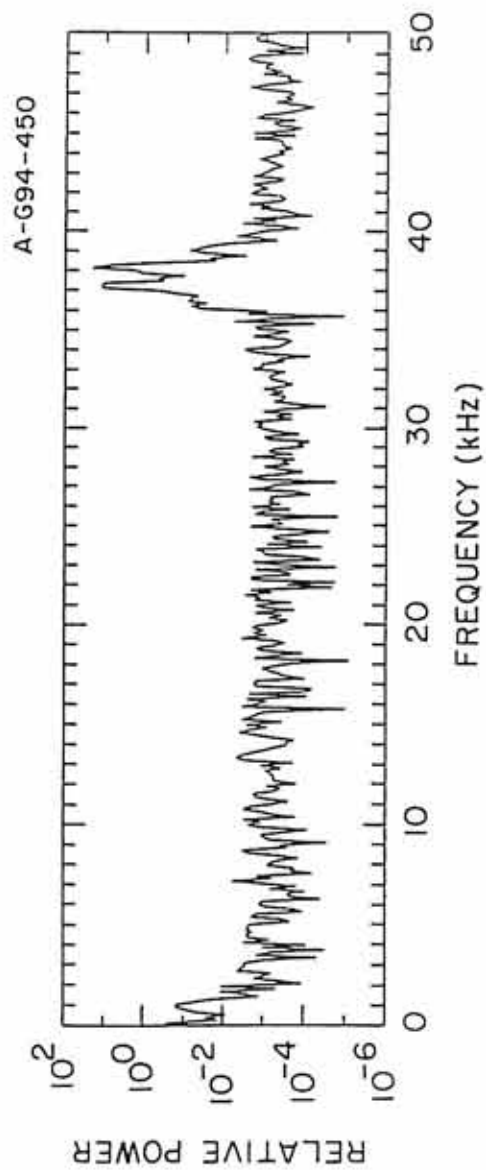
GALILEO-EARTH 1, DAYS 342-343, DEC. 8-9, 1990

Figure 41. An example of a beat-type waveform (bottom panel) and its spectrum (top panel). Two distinct frequency components are observed, one at ~ 37 kHz and the other at ~ 42 kHz. A weak low-frequency signal is also observed at ~ 5 kHz. The frequency difference of these two signals, and the frequency of the low-frequency signal, agrees with the beat frequency (~ 5 kHz) of the waveform.



GALILEO, 0012:07.189, DAY 343, DEC 9, 1990

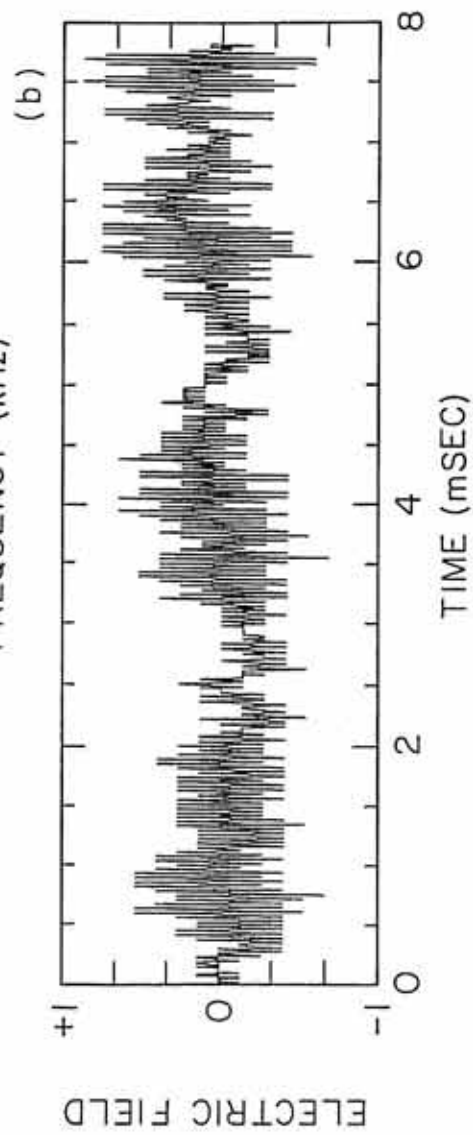
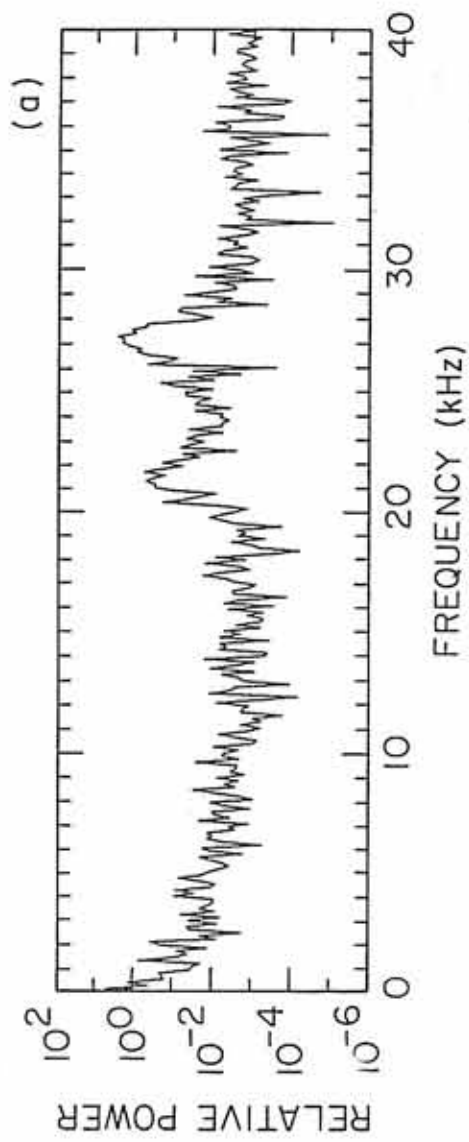
Figure 42. An example of the spectrum (top panel) of a lower frequency beat-type waveform (bottom panel). Two distinct frequency components are observed, one at ~ 37.1 kHz and the other at ~ 38.1 kHz. A weak low-frequency signal is also observed at ~ 1 kHz. The frequency difference of these two signals, and the frequency of the low-frequency signal, agrees with the beat frequency (~ 1 kHz) of the waveform.



GALILEO, 0012:18.522, DAY 343, DEC 9, 1990

Figure 43. An example of a chaotic-type waveform (bottom panel) and its spectrum (top panel). A weak high-frequency beat pattern can be seen in the waveform. The spectrum consists of two broad signals centered at 21.5 and 27.5 kHz. The chaotic-type waveforms observed at the Earth are similar to the chaotic-type waveforms observed at Venus (Figures 24b and 26) and are common during periods of large upshifts or downshifts in the emission frequency of the Langmuir waves.

A-G94-522



GALILEO, 0357:05.713, DAY 343, DEC 9, 1990

Figure 44. The number of waveform blocks as a function of peak electric field strength. The solid line gives the peak field strength for the waveforms measured directly (unclipped) or by extrapolation (moderately clipped). The dashed line gives the lower limit to the field strengths for severely clipped waveforms.

B-G94-305

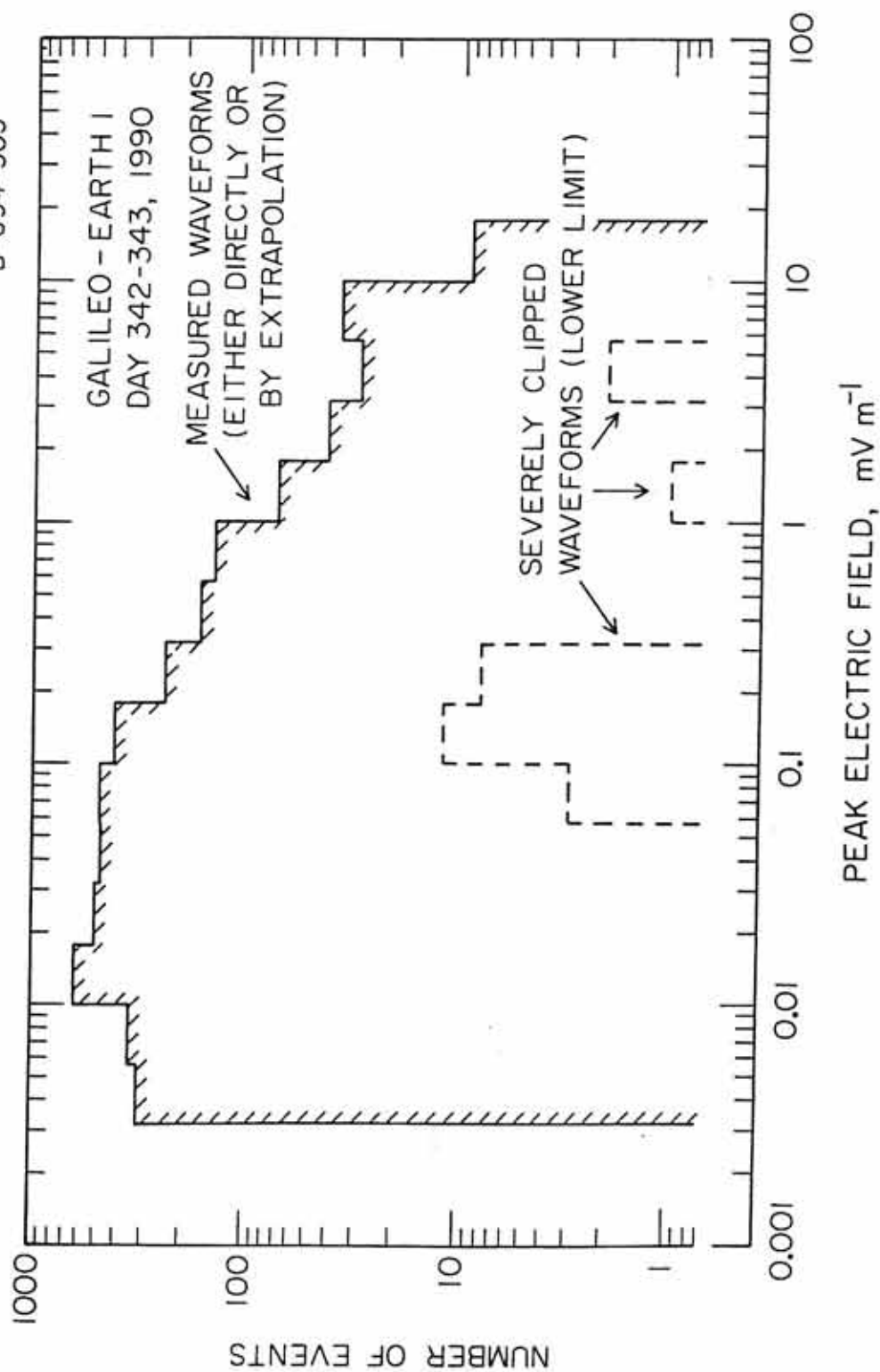
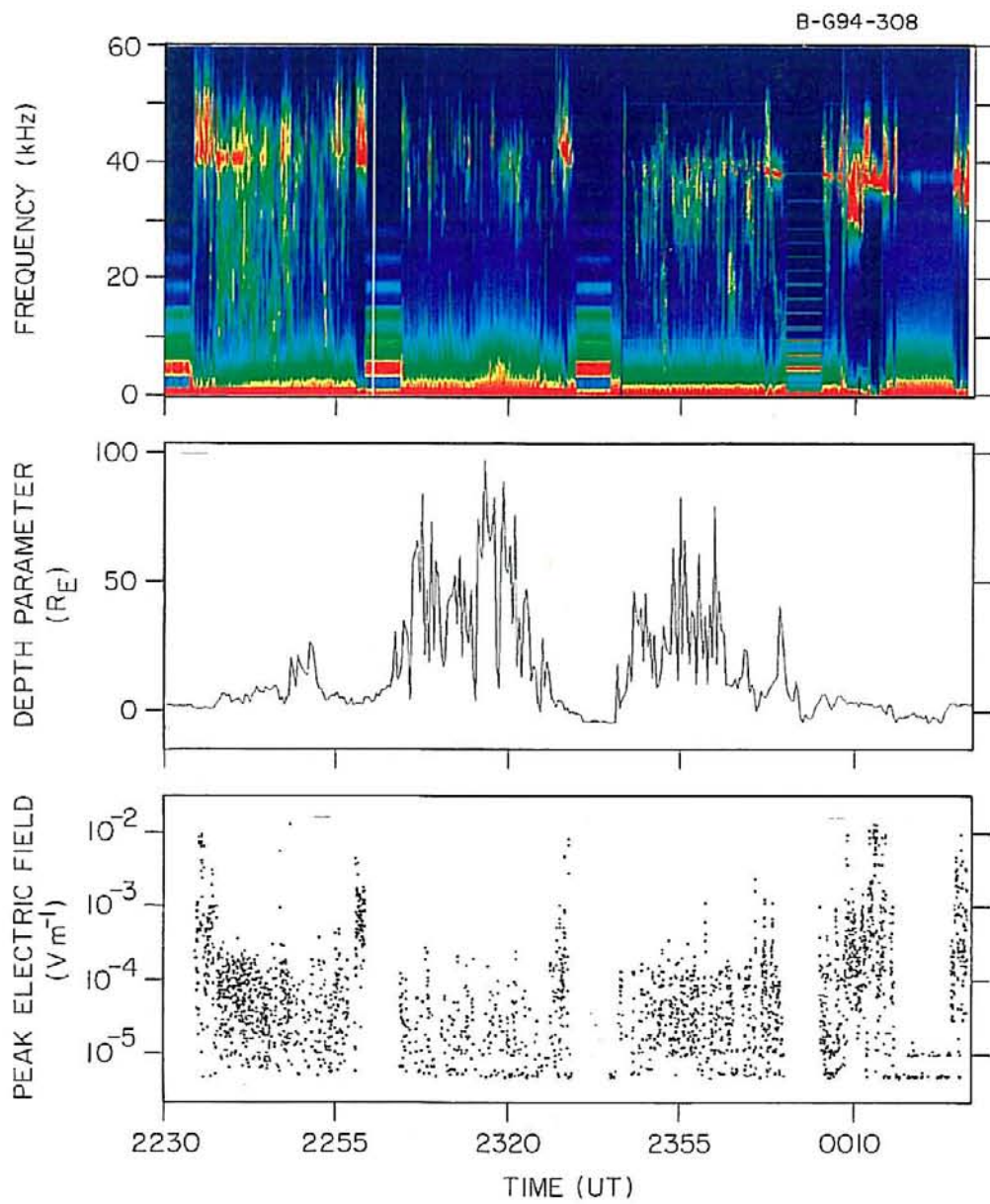


Figure 45. The top panel is a high-resolution frequency-time spectrum of the Langmuir waves. The middle panel is a plot of the depth parameter. The bottom panel is a plot of the maximum peak electric field amplitudes of the waveform blocks. The largest amplitudes tend to occur during intervals of small depth parameters (for example 2235, 2258, 2328, 0013, and 0025 UT). These intervals corresponds to times when the spacecraft is near the upstream foreshock boundary.



GALILEO - EARTH I, DAY 342-343, 1990

Figure 46. A 4-hour frequency-time spectrogram of the electric field intensities obtained from the spectrum analyzer receivers as Galileo exited the bow shock during the second Earth flyby. Galileo was in the magnetosheath from approximately 1706 to 1813 UT (characterized by the low-frequency broadband noise observed during this time period). The Langmuir waves can be seen immediately after Galileo exited the bow shock at about 1813 UT in the middle panel (medium-frequency spectrum analyzer). The Langmuir waves range in frequency from approximately 10 to 26 kHz, and show a great deal of structure. Broadband low-frequency signals (5 Hz to about 200 Hz) are also observed in the bottom panel (low-frequency spectrum analyzer) during the intervals of Langmuir wave activity. The low-frequency signal is believed to be related to ion beams in the foreshock region.

Galileo PWS University of Iowa

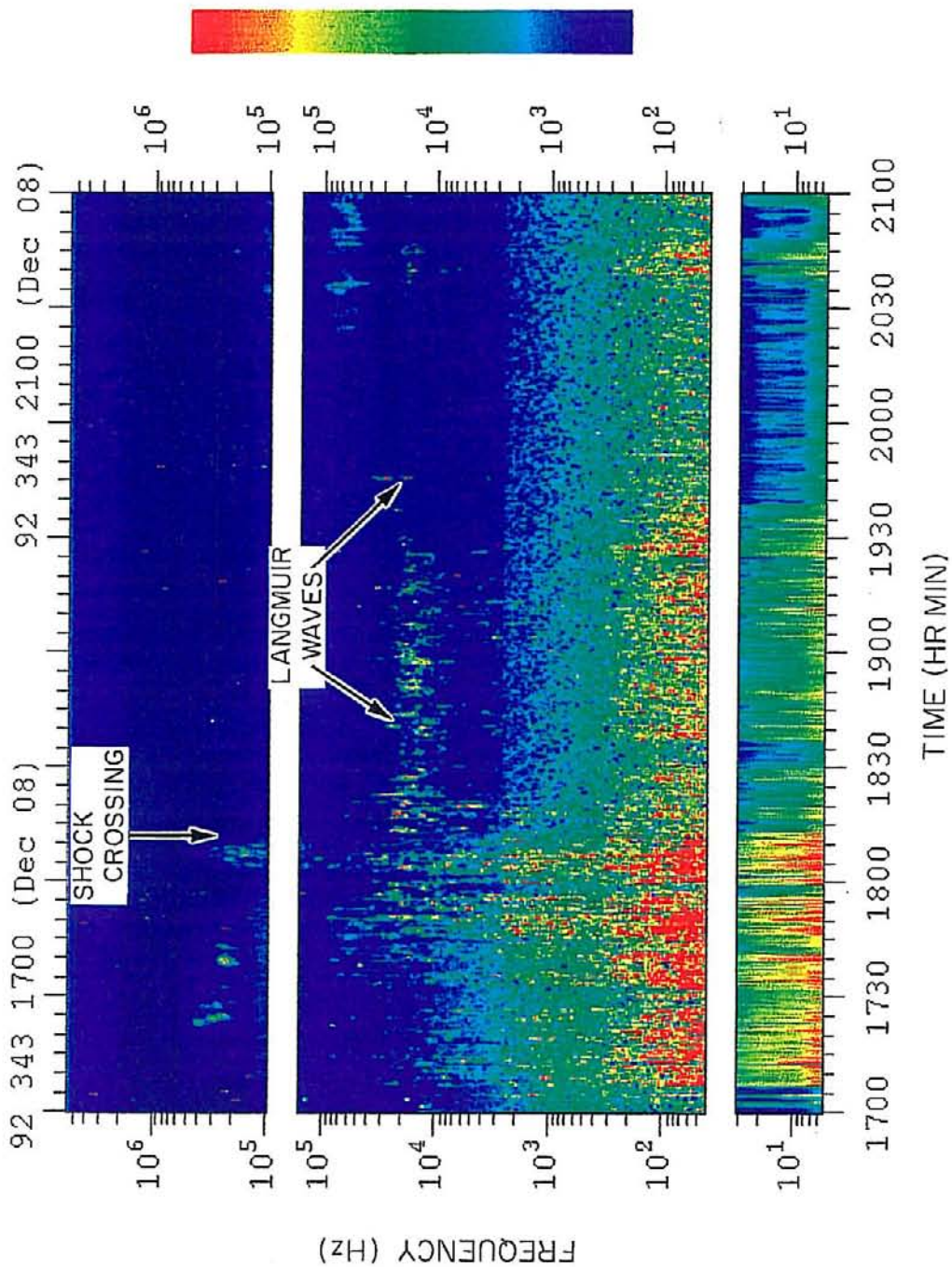


Figure 47. A high-resolution frequency-time spectrogram from the wideband waveform receiver. The bursty nature and the large spreading in frequency of the Langmuir waves can be easily seen in the first hour of the spectrogram. The sporadic signals from approximately 30 to 70 kHz during the first hour of the spectrogram are believed to be instrument distortion due to clipping in the receiver. An intense narrowband Langmuir wave emission is observed at approximately 1945 UT. This interval contains the largest Langmuir wave electric field strengths observed by Galileo. Most of the signals at $2f_{pe}$ (~ 37 kHz) and $3f_{pe}$ (~ 55 kHz) during this interval is due to clipping in the receiver.

GALILEO

START - 1992 343 18:11 (8 December)

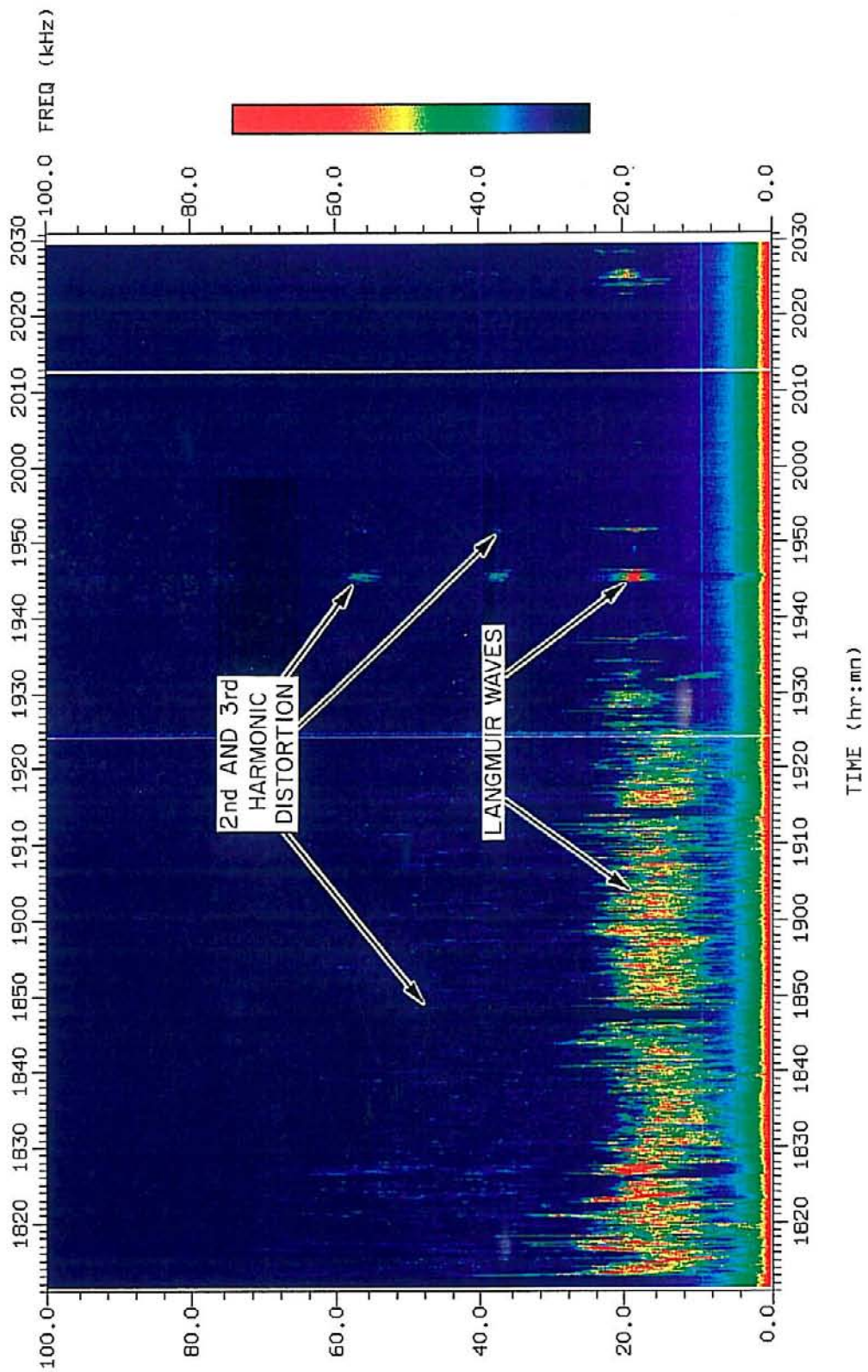


Figure 48. An expanded high-resolution frequency-time spectrogram from the wideband waveform receiver from near the beginning of Figure 47. Note the frequency axis ranges from 2 to 52 kHz. The structure of the Langmuir waves is very complex, and shows a large range in emission frequency (~ 2 kHz to ~ 30 kHz). The frequency of the Langmuir wave emissions often appears to be modulated by a low-frequency wave with a period of ~ 15 seconds. This apparent modulation can be seen from about 1820 to 1821:30 UT.

GALILEO

START - 1992 343 18:18 (8 December)

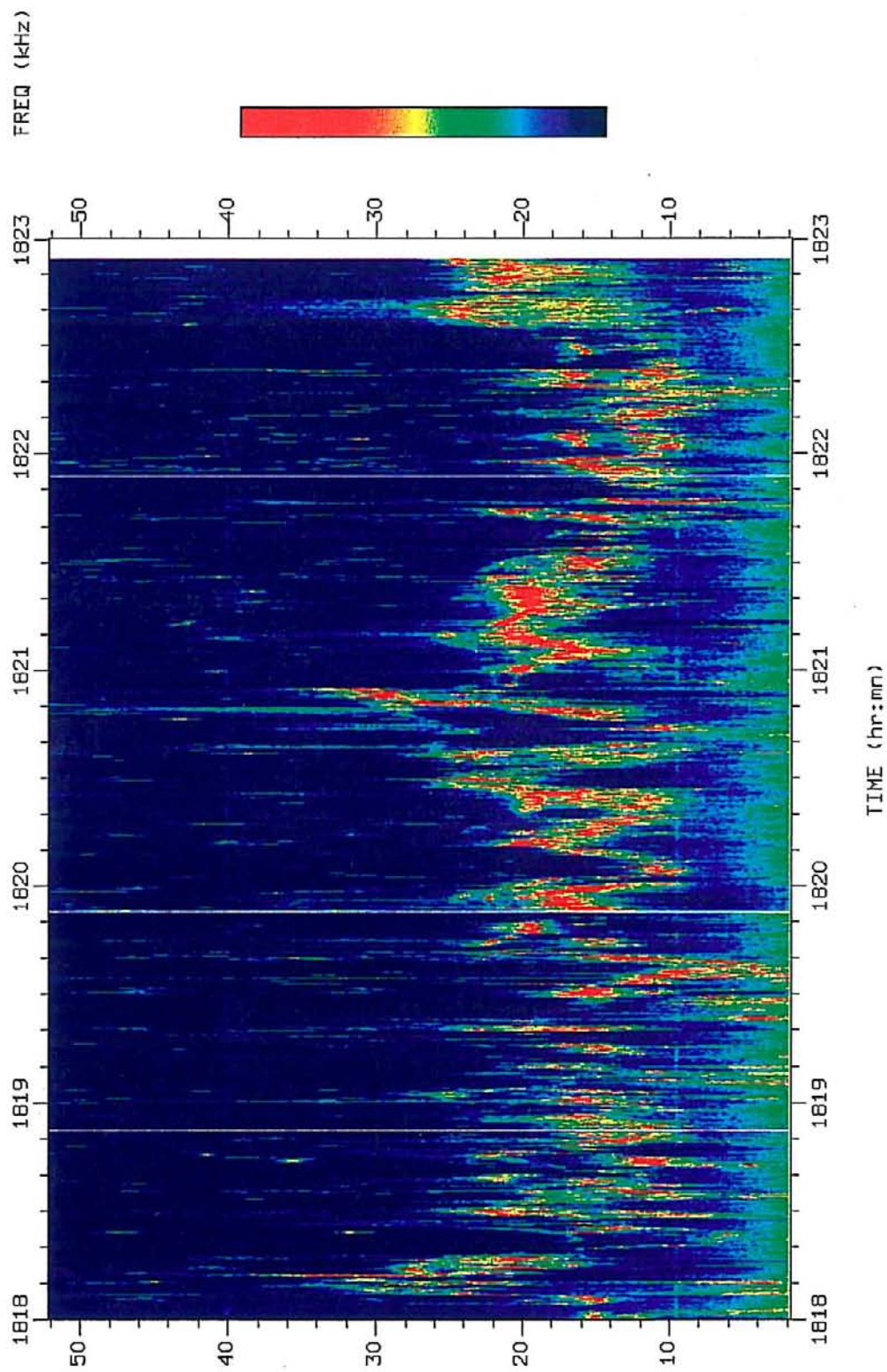
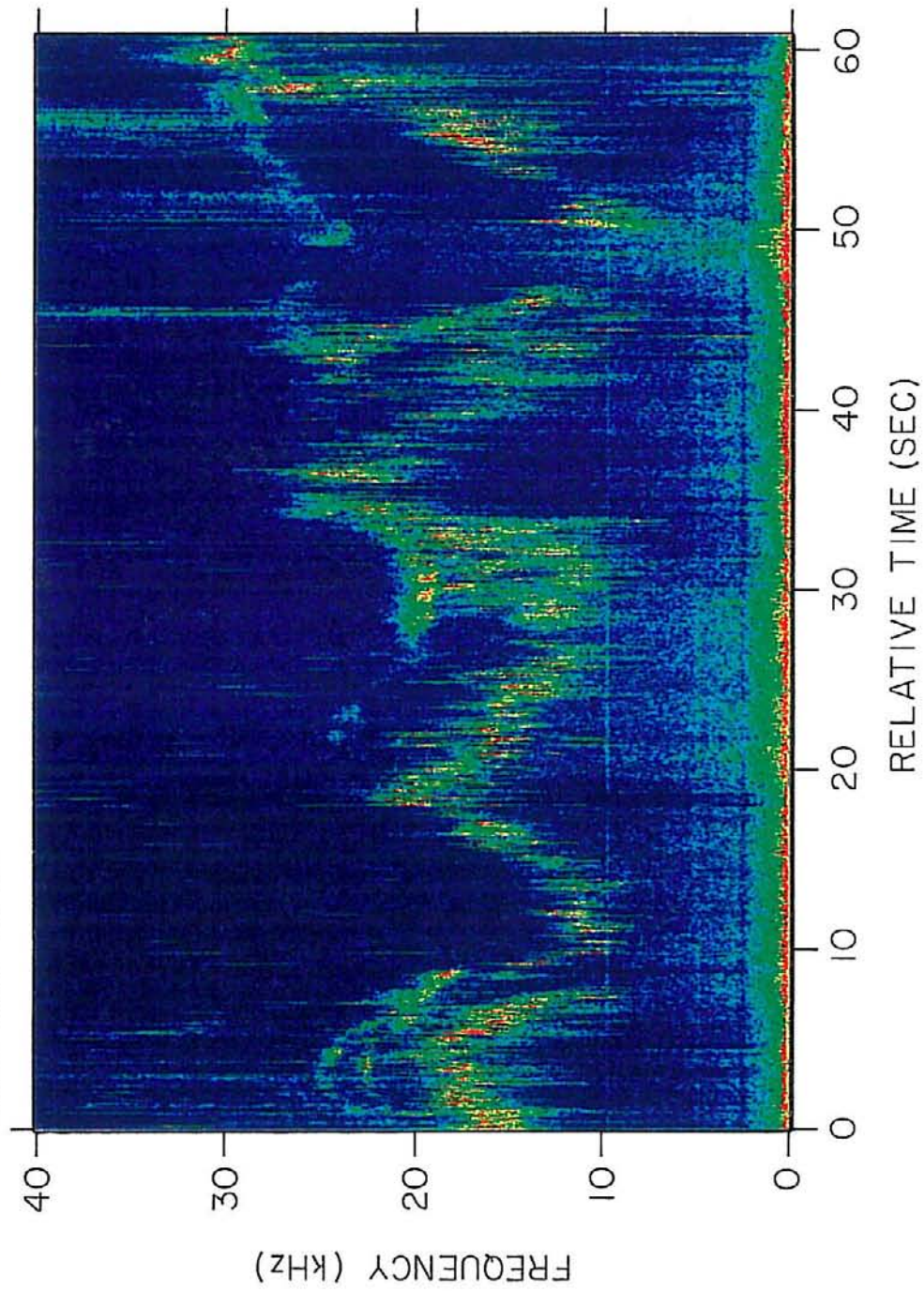


Figure 49. A high-resolution frequency-time spectrogram from the wideband waveform receiver from the interval shown in Figure 48. Note the frequency axis now runs from 0 to 40 kHz. The Langmuir waves appear to consist of at least two types of emissions, a narrowband emission and a broader emission downshifted and upshifted in frequency from the narrowband emission. Both types of emissions ramp up and down in frequency with a period on the order of 16 seconds. This modulation is most easily seen in the first 30 seconds of the spectrogram. The emissions appear to peak in frequency at approximately 3, 19, and 35 seconds. This type of spectrum is suggestive of the Langmuir waves "mapping out" low-frequency density fluctuations. A possible source of density fluctuations is propagating MHD waves (magnetosonic mode) generated by the ion beams present in the ion foreshock.

A-G94-467

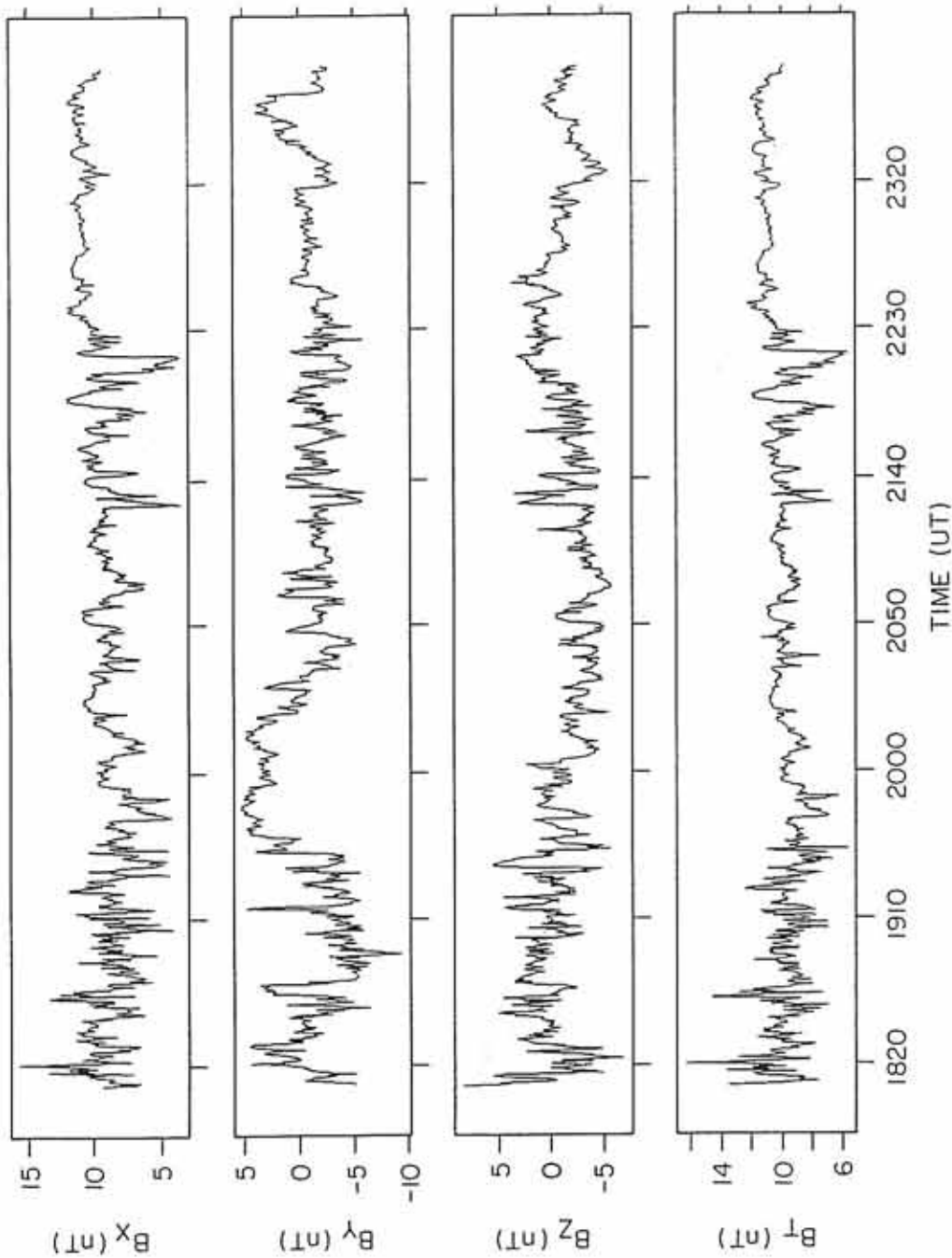
1819:53.346 UT



GALILEO - EARTH 2, DEC 8, 1992

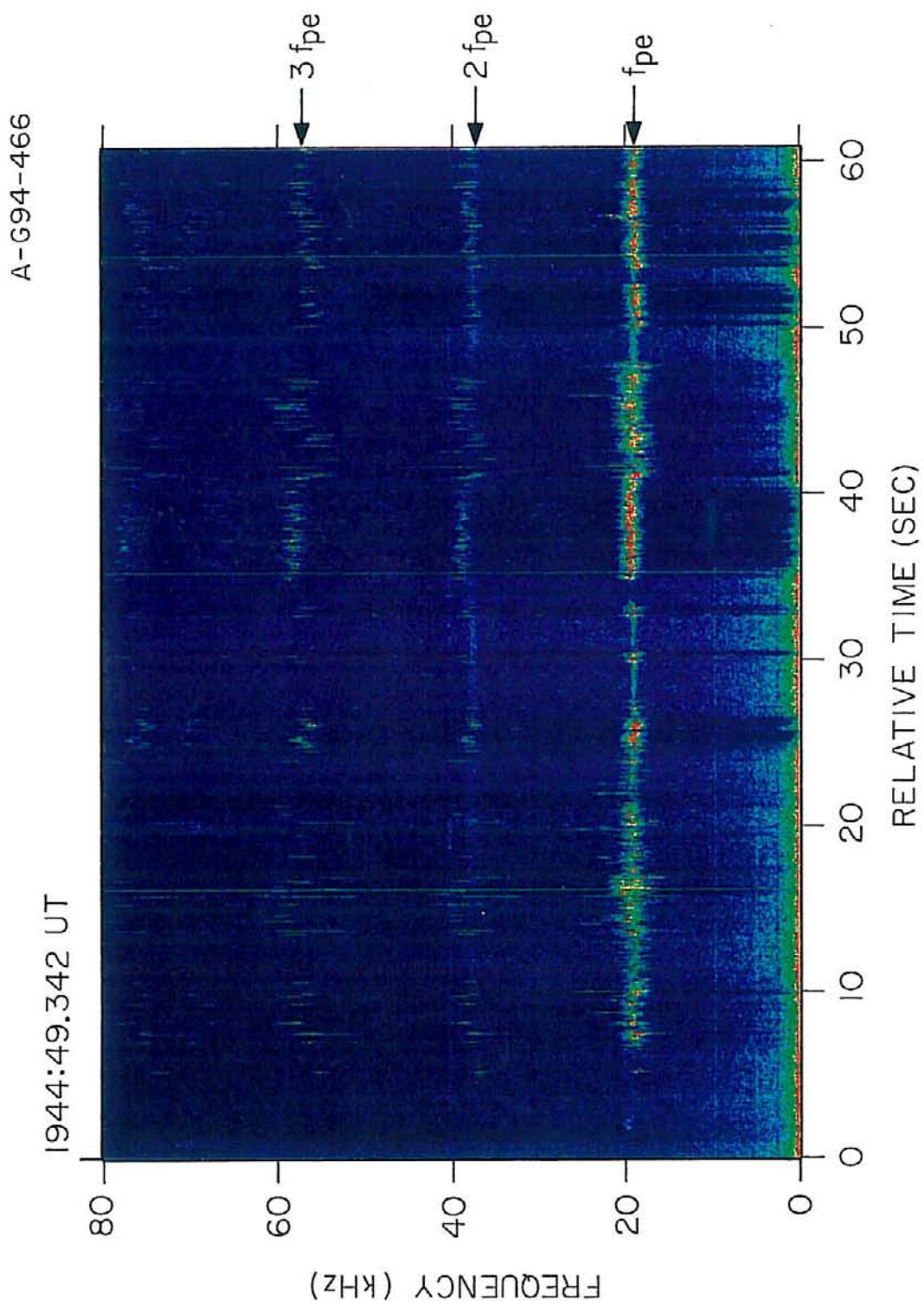
Figure 50. The 20-second magnetic field GSE averages of the three components of the magnetic field (top three panels) and the total magnetic field (bottom panel) for the interval immediately after Galileo exited the bow shock. The magnetic field contains a great deal of structure suggestive of MHD waves during the interval of chaotic Langmuir wave emission (approximately 1813 to 1930 UT).

B-G94-306



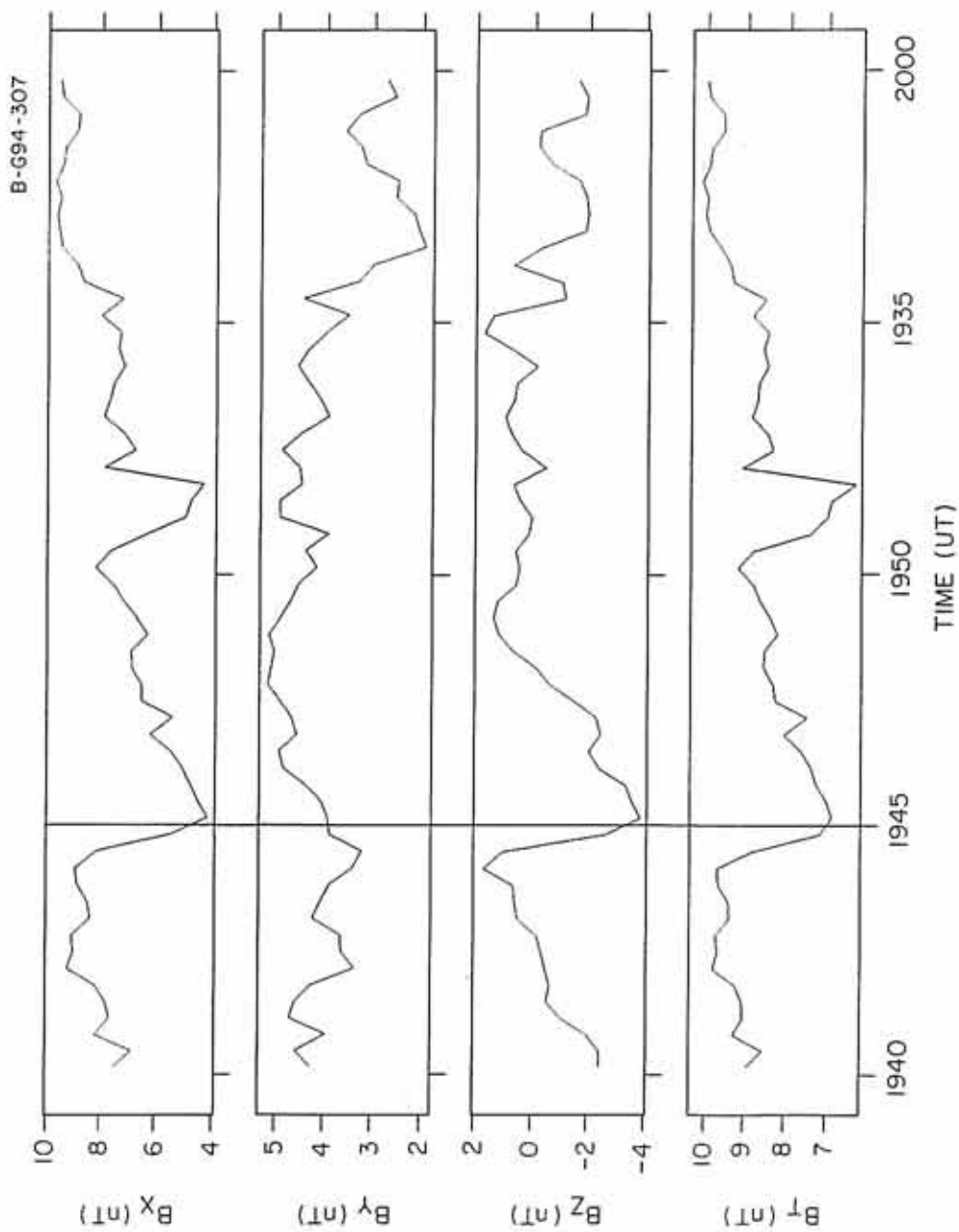
GALILEO-EARTH 2, DAY 343, DEC 8, 1992

Figure 51. A high-resolution frequency-time spectrogram from the wideband waveform receiver corresponding to the interval of intense Langmuir waves shown in Figure 47 at approximately 1945 UT. The intense narrowband emission is characteristic of Langmuir waves near the electron foreshock boundary. Most of the signals occurring at multiples of the Langmuir wave emission frequency ($f_{pe} \sim 19$ kHz) are caused by clipping in the waveform receiver. The weak emissions observed at twice the main emission frequency, with no corresponding emission at three times the main emission frequency, for example the weak signal from about 27 to 32 seconds into the plot at ~ 38 kHz, are probably electromagnetic $2f_{pe}$ emissions produced by nonlinear processes.



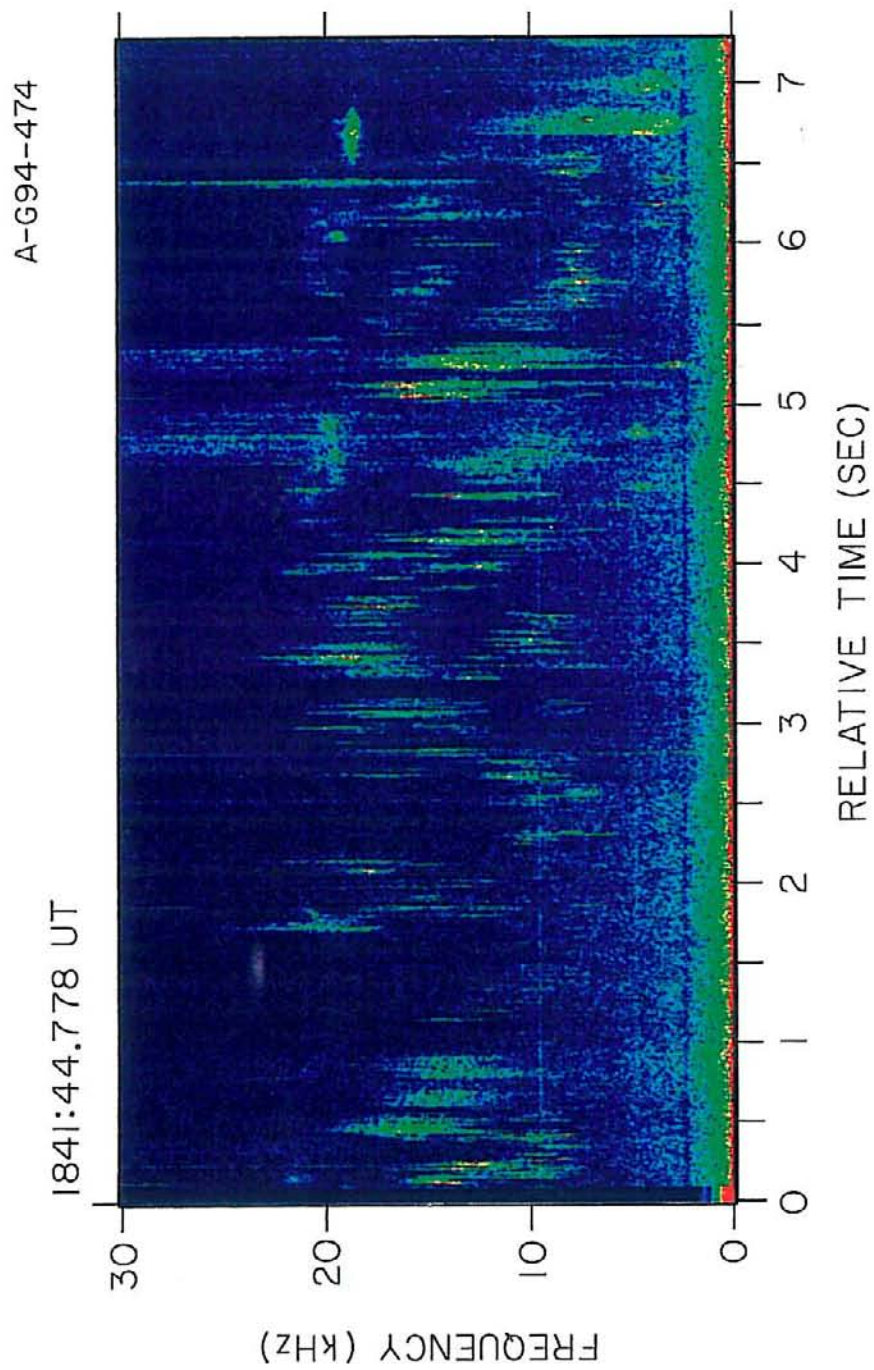
GALILEO - EARTH 2, DEC 8, 1992

Figure 52. An expanded plot of the GSE magnetic field components and total field for the interval spanning Figure 51. The vertical line at 1945 UT shows the approximate time the Langmuir wave emissions begin in Figure 51. As can be seen, there is a decrease in the B_x and B_T magnetic fields, and the B_y magnetic component reverses direction. A similar decrease in B_x and B_T at $\sim 1951:30$ UT corresponds to the start time of the second short burst of Langmuir waves observed in Figure 47. Unfortunately, depth parameter values are not available to determine the exact position in the foreshock of Galileo during the second Earth flyby.



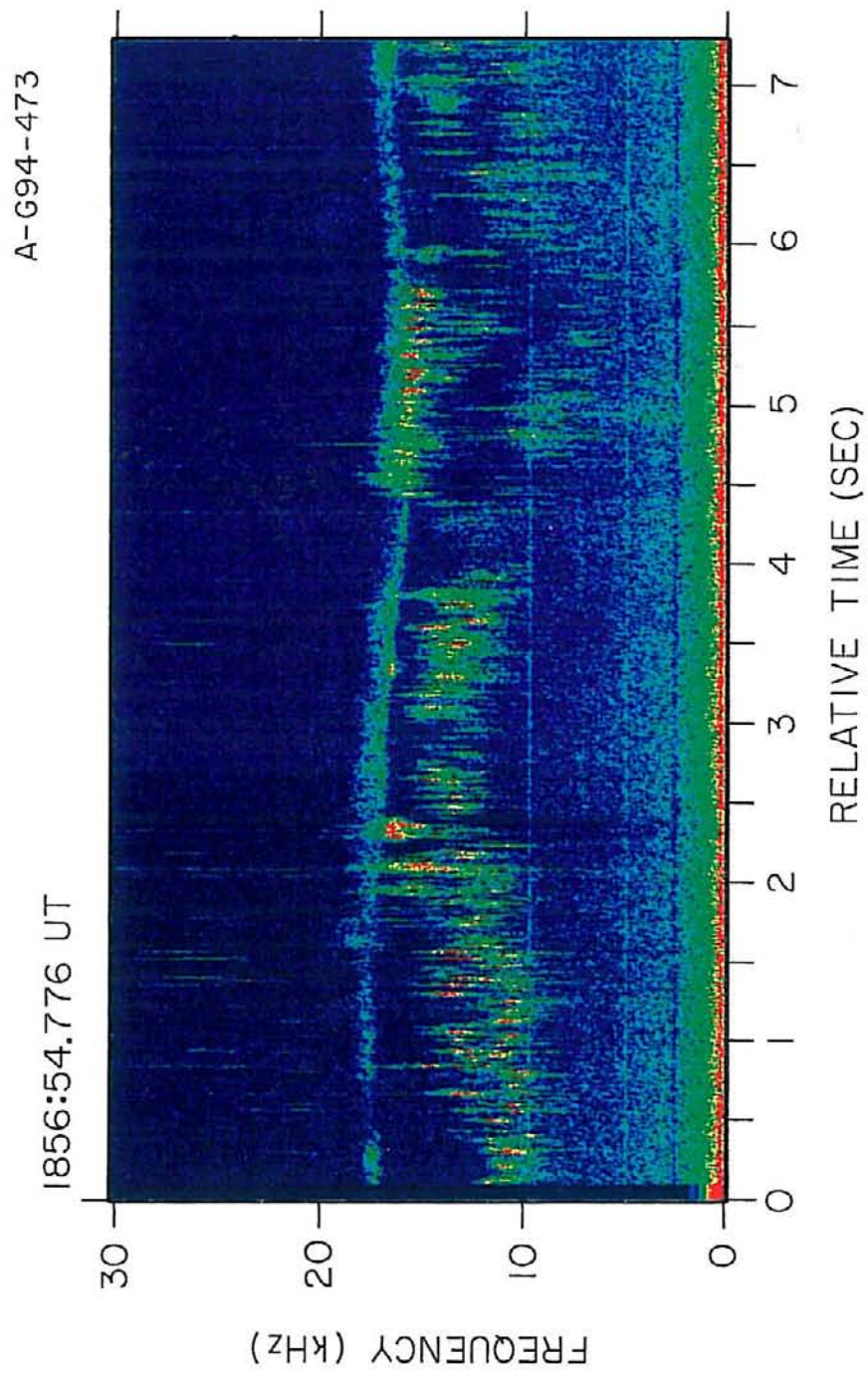
GALILEO-EARTH 2, DAY 343, DEC 8, 1992

Figure 53. A high-resolution frequency-time spectrogram of the Mode 4 data. The Langmuir waves range in frequency from approximately 3 kHz to > 25 kHz. The emissions are very spiky, with extremely rapid temporal variations down to the smallest timescale that can be resolved, which is the time between successive waveform blocks (8.33 ms). The Langmuir waves also show large frequency spreading, sometimes by as much as 15 kHz. The wide range of structure is believed to be a product of the spacecraft location in the foreshock and the presence of density fluctuations associated with MHD waves.



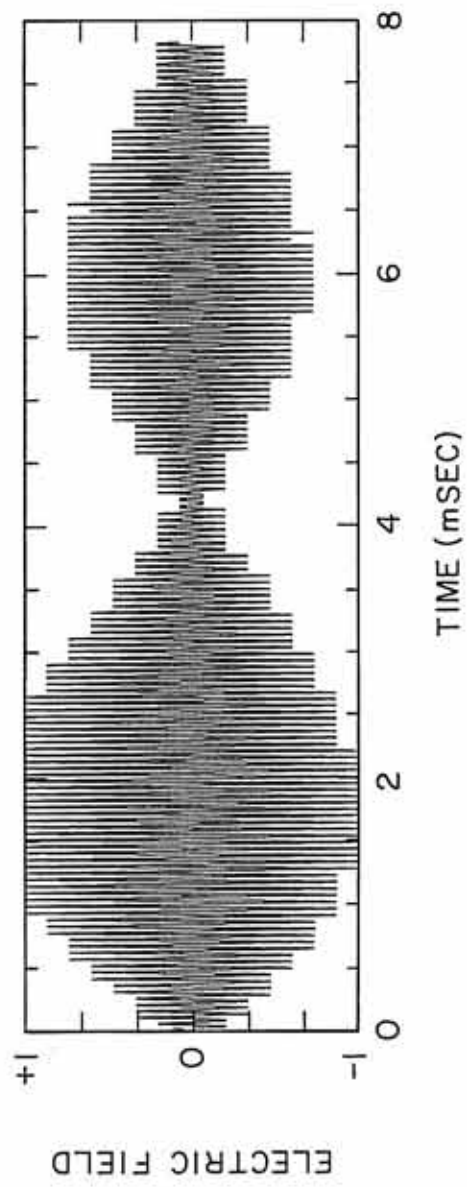
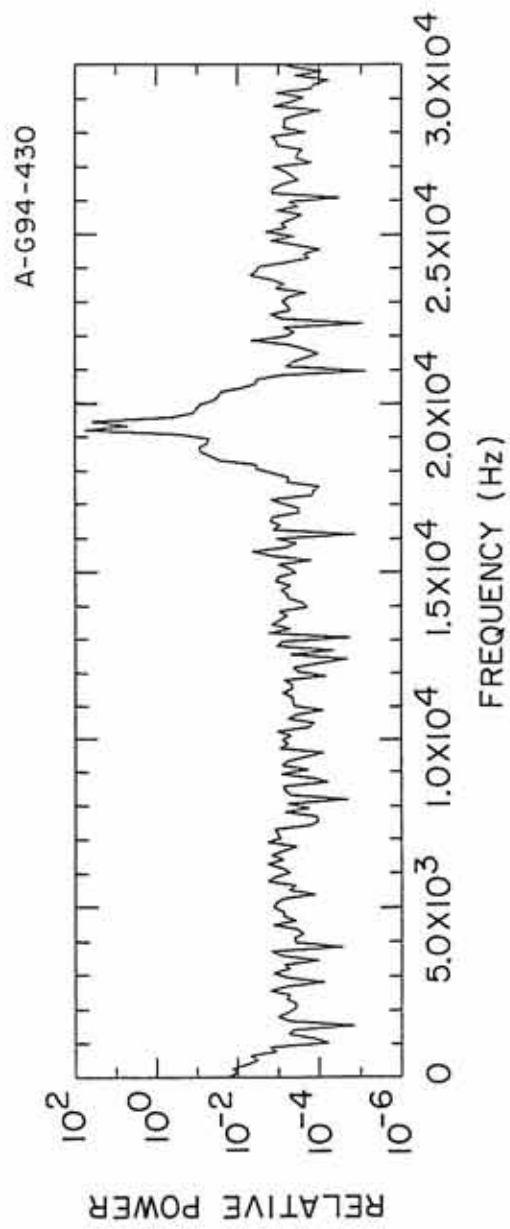
GALILEO - EARTH 2, DEC 8, 1992

Figure 54. A high-resolution frequency-time spectrogram of the Mode 4 data. A narrowband signal is observed at what is believed to be the plasma frequency (~ 17 kHz). During the first ~ 4.5 seconds of the spectrum, the emission is weak and nearly continuous. These characteristics are suggestive of thermally excited Langmuir waves. At ~ 4.5 seconds, a more intense, broader in frequency, emission is observed, ending at ~ 5.7 seconds. This more intense emission is most likely due to Langmuir waves generated by electron beams propagating out from the bow shock. The intense, spiky emissions observed from ~ 5 kHz to ~ 16 kHz are suggestive of downshifted Langmuir waves.



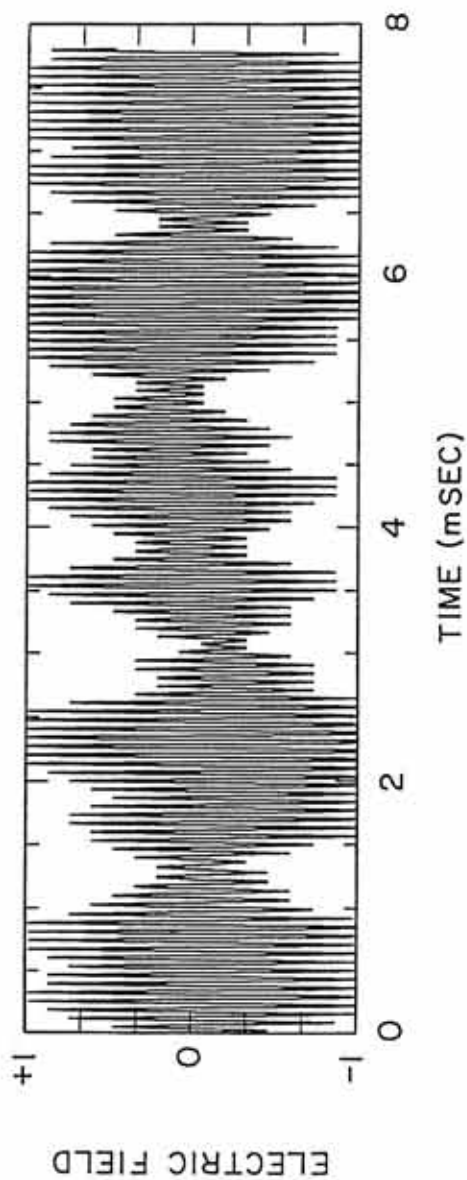
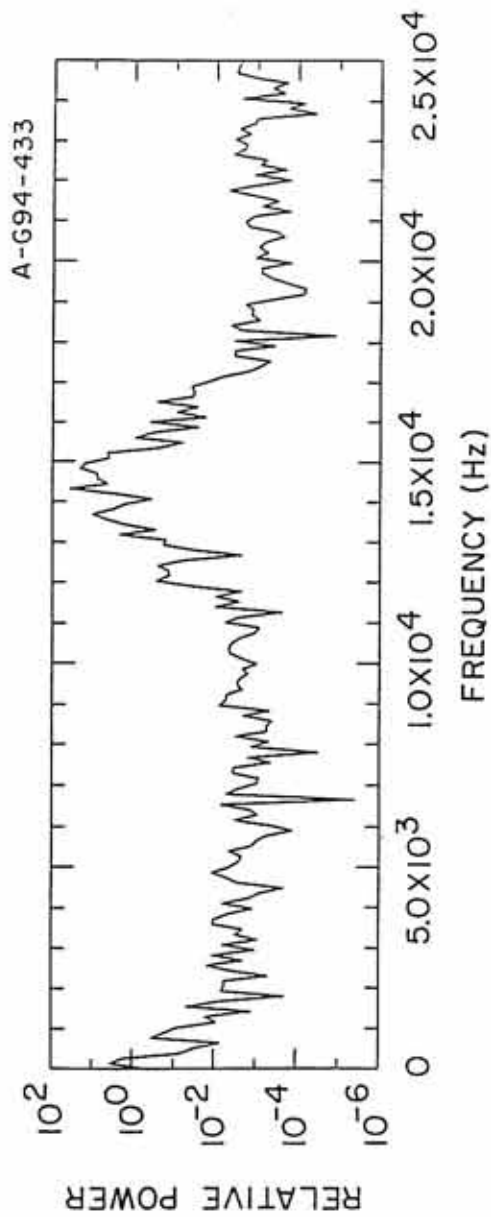
GALILEO-EARTH 2, DEC 8, 1992

Figure 55. An example of a beat-type waveform (bottom panel) and its spectrum (top panel). Two distinct frequency components are observed, one at ~ 19.15 kHz and the other at ~ 19.4 kHz. A very weak low-frequency signal at ~ 0.25 kHz is also observed, although the weakness of the signal makes it difficult to determine if the signal is real. The frequency difference of these two signals and the frequency of the low-frequency signal agree with the observed beat frequency (~ 0.25 kHz) of the waveform.



GALILEO, 1945:25.542, DAY 343, DEC 8, 1992

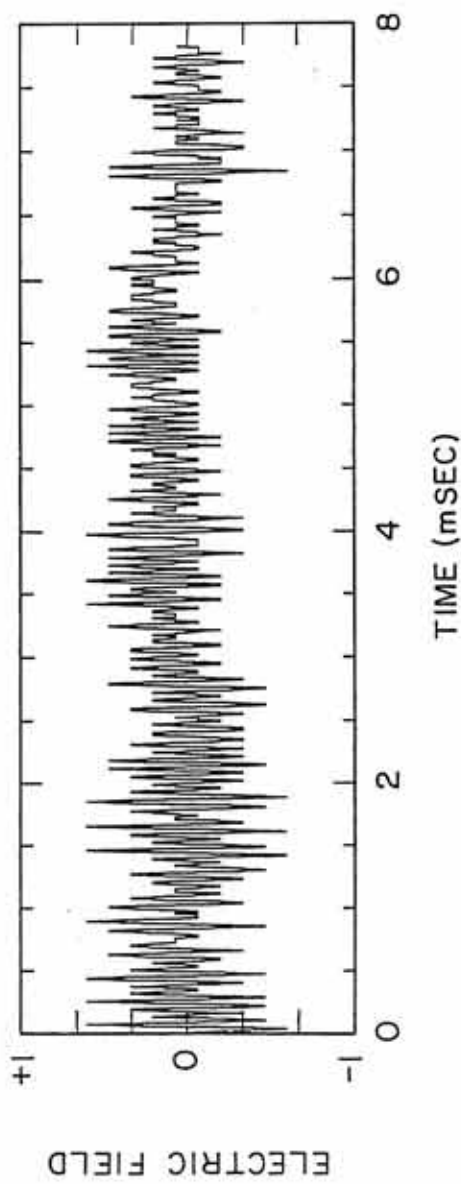
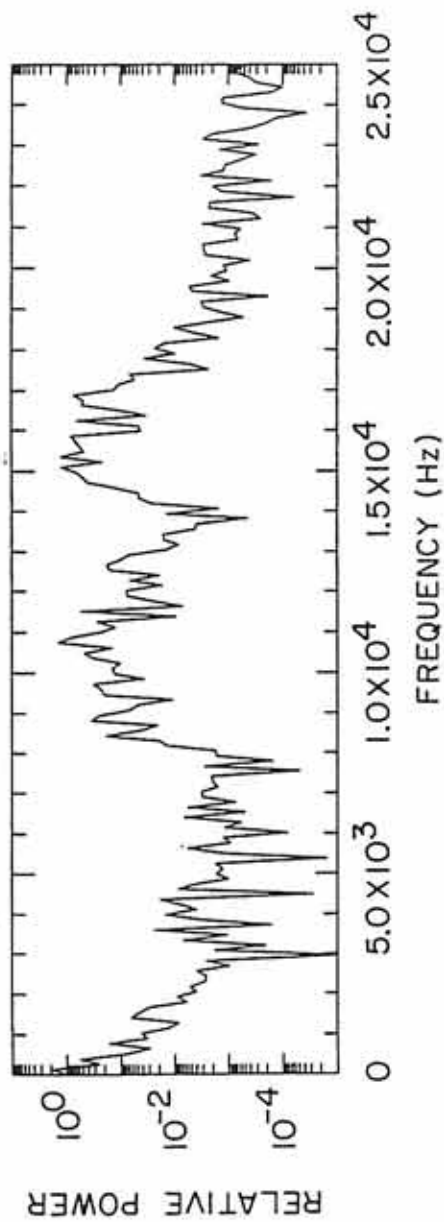
Figure 56. An example of a chaotic-type waveform (bottom panel) and its spectrum (top panel). The spectrum consists of a broad signal centered at ~ 14.5 kHz. The chaotic beat-type waveforms of this type are usually associated with periods of large upshifts and downshifts in frequency of the Langmuir waves.



GALILEO, 1815:29.279, DAY 343, DEC 8, 1992

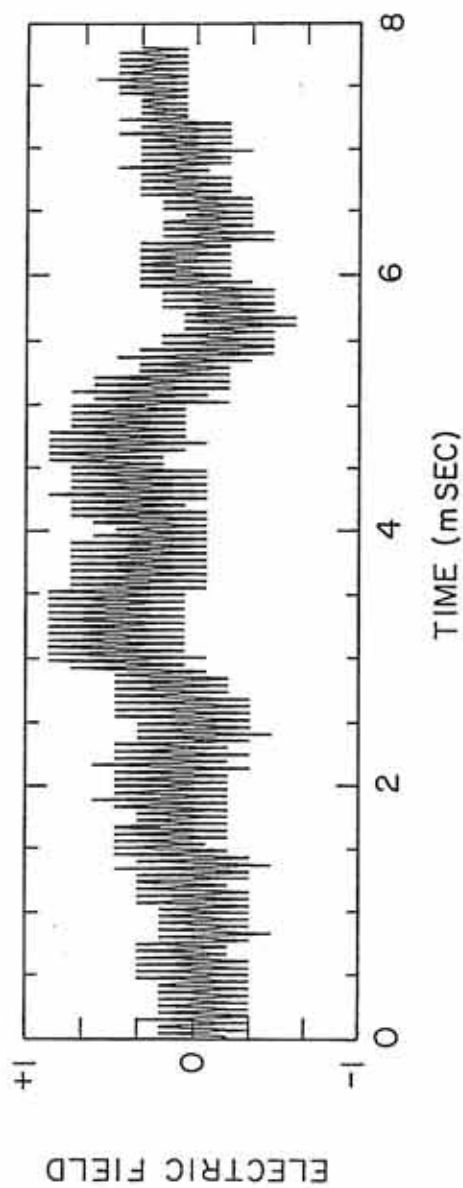
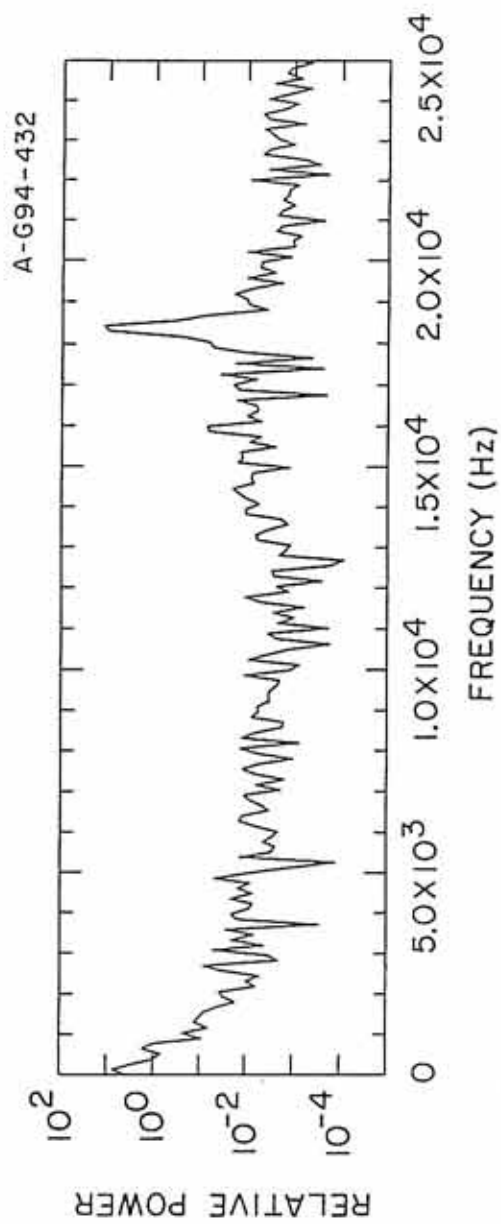
Figure 57. An example of a chaotic-type waveform (bottom panel) and its spectrum (top panel). The spectrum consists of two broadband signals, both exhibiting a great deal of structure. Similar chaotic-type waveforms have been observed at Venus (Figures 24b and 26) and during the first Earth flyby (Figure 43), and make up most of the waveforms observed during the second Earth flyby.

A-G94-431



GALILEO, 1856:17.611, DAY 343, DEC 8, 1992

Figure 58. The bottom panel is an example of a "constant over 8 ms" waveform.
The top panel is the spectrum of the waveform.

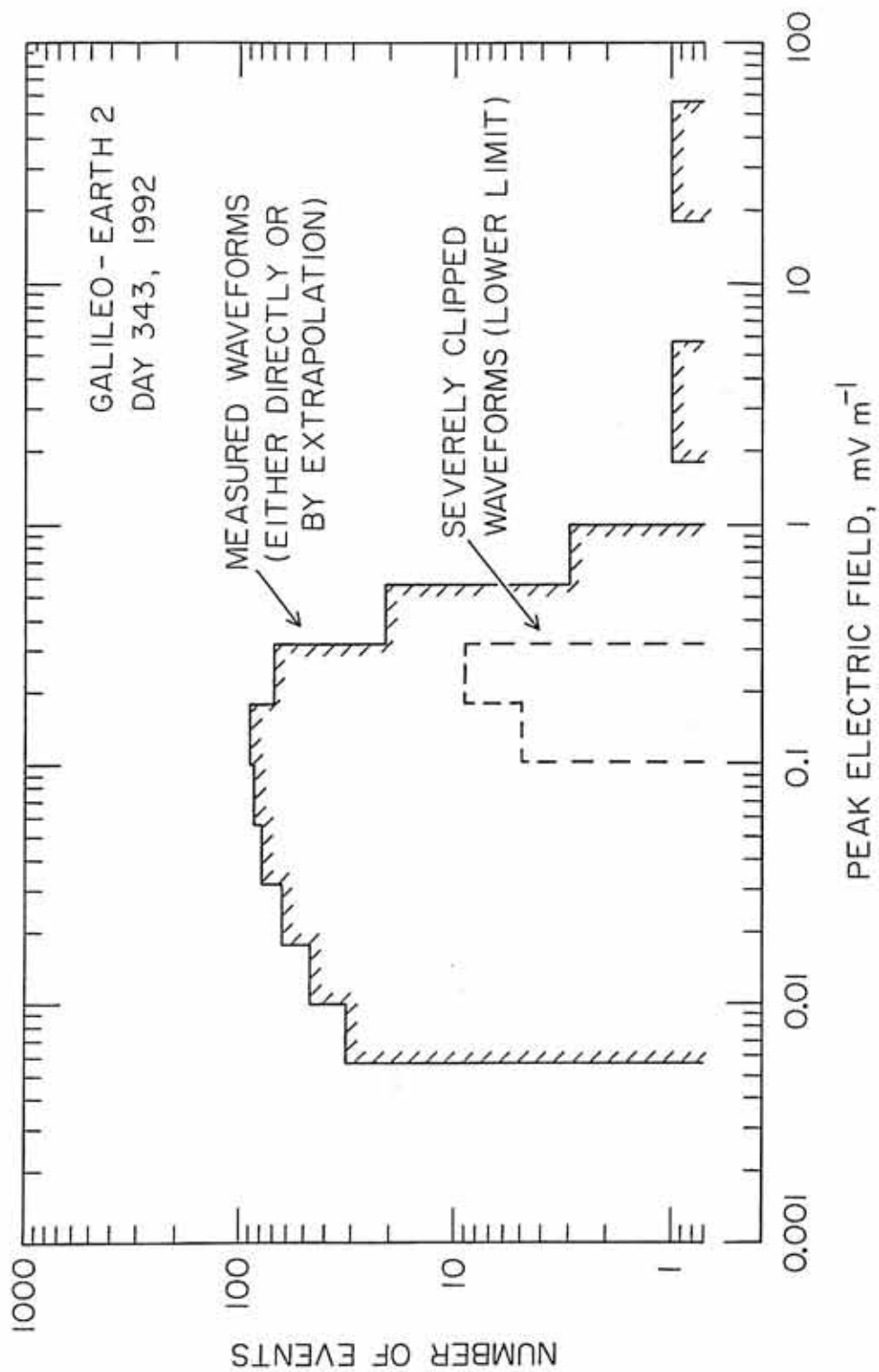


GALILEO, 1824:59.012, DAY 343, DEC 8, 1992

Figure 59. The number of waveform blocks as a function of peak electric field strength. The solid line gives the peak field strength for the waveforms measured directly (unclipped) or by extrapolation (moderately clipped). The dashed line gives the lower limit to the field strengths for severely clipped waveforms.

B-G94-435

GALILEO - EARTH 2
DAY 343, 1992



REFERENCES

- Alvarez, H., F. T. Haddock, and R. P. Lin, Evidence for electron excitation of type III radio burst emission, Solar Physics, 26, 468, 1972.
- Anderson, R. R. G. K. Parks, T. E. Eastman, D. A. Gurnett, and L. A. Frank, Plasma Waves Associated With Energetic Particles Streaming Into the Solar Wind From the Earth's Bow Shock, J. Geophys. Res., 86, 4493, 1981.
- Bardwell, S., and M. V. Goldman, Three-dimensional Langmuir wave instabilities in type III solar radio bursts, Astrophys. J., 209, 912, 1976.
- Bohm, D., and E. P. Gross, Theory of plasma oscillations: A, Origin of medium-like behavior; B, Excitation and damping of oscillations, Phys. Rev., 75, 1851, 1949a.
- Bohm, D., and E. P. Gross, Theory of plasma oscillations: B, Excitation and damping of oscillations, Phys. Rev., 75, 1864, 1949b.
- Cairns, I. H., Fundamental plasma emission involving ion sound waves, J. Plasma Phys., 38, 169, 1987a.
- Cairns, I. H., Second harmonic plasma emission involving ion sound waves, J. Plasma Phys., 38, 179, 1987b.
- Cairns, I. H., A theory for the Langmuir waves in the electron foreshock, J. Geophys. Res., 92, 2329, 1987c.
- Cairns, I. H., A semiquantitative theory for the $2f_p$ radiation observed upstream of the Earth's bow shock, J. Geophys. Res., 93, 3958, 1988.
- Cairns, I. H., Electrostatic wave generation above and below the plasma frequency by electron beams, Phys. Fluids B, 1, 204, 1989.
- Cairns, I. H. and S. F. Fung, Growth of electron plasma waves above and below f_p in the electron foreshock, J. Geophys. Res., 93, 7307, 1988.
- Cairns, I. H. and D. B. Melrose, A theory for the $2f_p$ radiation upstream of the Earth's bow shock, J. Geophys. Res., 90, 6637, 1985.
- Cairns, I. H. and P. A. Robinson, Strong Langmuir turbulence at Jupiter, Geophys. Res. Lett., 19, 1069, 1992a.

- Cairns, I. H. and P. A. Robinson, Theory for low-frequency modulated Langmuir wave packets, Geophys. Res. Lett., **19**, 2187, 1992b.
- Canu, P., N. Cornilleau-Wehrlin, C. de Villedary, P.J. Kellogg, C. C. Harvey, and R. J. MacDowall, Observations of electron plasma waves upstream of the Jovian bow shock, Planet. Space Sci., **41**, 811, 1993.
- Crawford, G. K., R. J. Strangeway, and C. T. Russell, Electron plasma oscillations in the Venus foreshock, Geophys. Res. Lett., **17**, 1805, 1990.
- Crawford, G. K., R. J. Strangeway, and C. T. Russell, Variations in plasma wave intensity with distance along the electron foreshock boundary at Venus, Adv. Space Res., **11**, (9)93, 1991.
- Crawford, G. K., R. J. Strangeway, and C. T. Russell, VLF emissions in the Venus foreshock: Comparison with terrestrial observations, J. Geophys. Res., **98**, 15305, 1993a.
- Crawford, G. K., R. J. Strangeway, and C. T. Russell, VLF image of the Venus foreshock, in press Geophys. Res. Lett., 1993b.
- Dum, C. T., Simulations of plasma waves in the electron foreshock: The generation of Langmuir waves by a gentle bump-on-tail electron distribution, J. Geophys. Res., **95**, 8095, 1990a.
- Dum, C. T., Simulations of plasma waves in the electron foreshock: The transition from reactive to kinetic instability, J. Geophys. Res., **95**, 8111, 1990b.
- Dum, C. T., Simulations of plasma waves in the electron foreshock: The generation of downshifted oscillations, J. Geophys. Res., **95**, 8123, 1990c.
- Escande, D. F. and G. V. de Genouillac, Electron burst relaxation in a fluctuating plasma, Astron. Astrophys., **68**, 405, 1978.
- Etcheto, J., and M. Faucheux, Detailed study of electron plasma waves upstream of the Earth's bow shock, J. Geophys. Res., **89**, 6631, 1984.
- Fainberg, J., and R. G. Stone, Satellite observations of type III solar radio bursts at low frequencies, Space Sci. Rev., **16**, 145, 1974.
- Filbert, P. C., and P. J. Kellogg, Electrostatic noise at the plasma frequency beyond the Earth's bow shock, J. Geophys. Res., **84**, 1369, 1979.
- Fitzenreiter, R. J., J. D. Scudder, and A. J. Klimas, Three-dimensional analytical model for the spatial variation of the foreshock electron distribution function: Systematics and comparisons with ISEE observations, J. Geophys. Res., **95**, 4155, 1990.

- Frank, L. A., W. R. Paterson, K. L. Ackerson, F. V. Coroniti, V. M. Vasyliunas, Plasma observations at Venus with Galileo, Science, 252, 1528, 1991.
- Fredricks, R. W., F. L. Scarf, and L. A. Frank, Nonthermal electrons and high frequency waves in the upstream solar wind, 2, Analysis and interpretation, J. Geophys. Res., 76, 6691, 1971.
- Fredricks, R. W., F. L. Scarf, C. T. Russell and M. Neugebauer, Detection of solar-wind electron plasma frequency fluctuations in an oblique nonlinear magnetohydrodynamic wave, J. Geophys. Res., 77, 3598, 1972.
- Freund, H. P., and K. Papadopoulos, Oscillating two-stream and parametric decay instability in a weakly magnetized plasma, Phys. Fluids, 23, 139, 1980.
- Fried, B. D., T. Ikemura, K. Nishikawa, and G. Schmidt, Parametric instabilities with finite wavelength pump, Phys. Fluids, 19, 1975, 1976.
- Fuselier, S. A., D. A. Gurnett, and R. J. Fitzenreiter, The downshift of electron plasma oscillations in the electron foreshock region, J. Geophys. Res., 90, 3935, 1985.
- Galeev, A. A., R. Z. Sagdeev, Yu. S. Sigov, V. D. Shapiro, and V. I. Shevchenko, Nonlinear theory for the modulational instability of plasma waves, Sov. J. Plasma Phys. Engl. Transl., 1, 5, 1975.
- Ginzburg, V. L., and V. V. Zheleznyakov, On the possible mechanism of sporadic solar radio emission (radiation in an isotropic plasma), Sov. Astron., AJ2, 653, 1958.
- Goldman, M. V. Progress and problems in the Theory of Type III Solar Radio Emission, Solar Physics, 89, 403, 1983.
- Goldman, M. V. Strong turbulence of plasma waves, Rev. Mod. Phys., 56, 709, 1984.
- Goldman, M. V., G. F. Reiter, and D. R. Nicholson, Radiation from a strongly turbulent plasma: Application to electron beam-excited solar emissions, Phys. Fluids, 23, 388, 1980.
- Goldstein, M. L., R. A. Smith, and K. Papadopoulos, Nonlinear stability of solar type III radio bursts, II, Application to observations near 1 AU, Astrophys. J., 234, 683, 1979.
- Grognard, R. J-M., Deficiencies of the asymptotic solutions commonly found in quasilinear relaxation theory, Aust. J. Phys., 28, 731, 1975.
- Grognard, R. J-M., Numerical Simulation of the Weak Turbulence Excited by a Beam of Electrons in the Interplanetary Plasma, Solar Physics, 81, 173, 1982.

- Gurnett, D. A., The Earth as a radio source: The nonthermal continuum, J. Geophys. Res., 80, 2751, 1975.
- Gurnett, D. A., and R. R. Anderson, Electron plasma oscillations associated with type III radio bursts, Science, 194, 1159, 1976.
- Gurnett, D. A., and R. R. Anderson, Plasma wave electric fields in the solar wind: Initial results from Helios 1, J. Geophys. Res., 82, 632, 1977.
- Gurnett, D. A., R. R. Anderson, F. L. Scarf, and W. S. Kurth, The heliocentric radial variation of plasma oscillations associated with type III radio bursts, J. Geophys. Res., 83, 4147, 1978.
- Gurnett, D. A., R. R. Anderson, and R. L. Tokar, Plasma oscillations and the emissivity of type III radio bursts, Radio Physics of the Sun, Edited by M. R. Kundu and T. E. Gergely, Reidel Publishing Co., Dordrecht, Holland, 369, 1980.
- Gurnett, D. A., and L. A. Frank, Electron plasma oscillations associated with type III radio emissions and solar electrons, Solar Physics, 45, 477, 1975.
- Gurnett, D. A., and L. A. Frank, Ion acoustic waves in the solar wind, J. Geophys. Res., 83, 58, 1978.
- Gurnett, D. A., G. B. Hospodarsky, W. S. Kurth, D. J. Williams, and S. J. Bolton, The fine structure of Langmuir waves produced by a solar electron event, J. Geophys. Res., 98, 5631, 1993.
- Gurnett, D. A., W. S. Kurth, R. L. Poynter, L. J. Granroth, I. H. Cairns, W. M. Macek, S. L. Moses, F. V. Coroniti, C. F. Kennel, and D. D. Barbosa, First Plasma Wave Observations at Neptune, Science, 246, 1494, 1989.
- Gurnett, D. A., W. S. Kurth, A. Roux, R. Gendrin, C. F. Kennel, and S. J. Bolton, Lightning and plasma wave observations from the Galileo flyby of Venus, Science, 253, 1522, 1991.
- Gurnett, D. A., W. S. Kurth, and F. L. Scarf, Plasma wave observations near Jupiter: Initial Results from Voyager 2, Science, 206, 987, 1979b.
- Gurnett, D. A., W. S. Kurth, and F. L. Scarf, Plasma waves near Saturn: Initial results from Voyager 1, Science, 212, 235, 1981b.
- Gurnett, D. A., W. S. Kurth, F. L. Scarf, and R. L. Poynter, First plasma wave observations at Uranus, Science, 233, 106, 1986.

- Gurnett, D. A., W. S. Kurth, R. R. Shaw, A. Roux, R. Gendrin, C. F. Kennel, F. L. Scarf, and S. D. Shawhan, The Galileo plasma wave investigation, Space Sci. Rev., **60**, 341, 1992.
- Gurnett, D. A., J. E. Maggs, D. L. Gallagher, W. S. Kurth, and F. L. Scarf, Parametric interaction and spatial collapse of beam-driven Langmuir waves in the solar wind, J. Geophys. Res., **86**, 8833, 1981a.
- Gurnett, D. A., E. Marsch, W. Pilipp, R. Schwenn, and H. Rosenbauer, Ion acoustic waves and related plasma observations in the solar wind, J. Geophys. Res., **84**, 2029, 1979a.
- Hoang, S., J. Fainberg, J. L. Steinberg, R. G. Stone, and R. H. Zwickl, The $2f_p$ circumterrestrial radio radiation as seen from ISEE 3, J. Geophys. Res., **86**, 4531, 1981.
- Hospodarsky, G. B., D. A. Gurnett, W. S. Kurth, M. G. Kivelson, R. J. Strangeway, and S. J. Bolton, The fine structure of Langmuir waves observed upstream of the bow shock at Venus, J. Geophys. Res., **99**, 13363, 1994.
- Kellogg, P. J., K. Goetz, R. L. Howard, and S. J. Monson, Evidence for Langmuir wave collapse in the interplanetary plasma, Geophys. Res. Lett., **19**, 1303, 1992.
- Kivelson, M. G., C. F. Kennel, R. L. McPherron, C. T. Russell, D. J. Southwood, R. J. Walker, C. M. Hammond, K. K. Khurana, R. J. Strangeway, P. J. Coleman, Magnetic field studies of the solar wind interaction with Venus from the Galileo flyby, Science, **253**, 1518, 1991.
- Kivelson, M. G., K. K. Khurana, J. D. Means, C. T. Russell, and R. C. Snare, The Galileo magnetic field investigation, Space Sci. Rev., **60**, 357, 1992.
- Kurth, W. S., D. A. Gurnett, and F. L. Scarf, High-resolution spectrograms of ion acoustic waves in the solar wind, J. Geophys. Res., **84**, 3413, 1979.
- Lacombe, C. A., A. Mangency, C. C. Harvey, and J. D. Scudder, Electron plasma waves upstream of Earth's bow shock, J. Geophys. Res., **90**, 73, 1985.
- Leckband, J. A., Magnetohydrodynamic Wave-Associated Plasma Density Fluctuations in the Earth's Foreshock Region, Ph.D. Thesis, University of Iowa, 1992.
- Lin, R. P., The emission and propagation of 40 keV solar flare electrons, Solar Phys., **12**, 266, 1970.
- Lin, R. P., W. K. Levedal, W. Lotko, D. A. Gurnett, and F. L. Scarf, Evidence for nonlinear wave-wave interactions in solar type III radio bursts, Astrophys. J., **308**, 954, 1986.

- Lin, R. P., D. W. Potter, D. A. Gurnett, and F. L. Scarf, Energetic electrons and plasma waves associated with a solar type III radio burst, Astrophys. J., 251, 364, 1981.
- Magelssen, G. R., and D. F. Smith, Non relativistic electron stream propagation in the solar atmosphere and type III radio bursts, Solar Physics, 55, 211, 1977.
- McLean, D. J. and N. R. Labrum, Solar Radiophysics, Cambridge University Press, New York, 1985.
- Melrose, D. B., Fundamental emission for type III bursts in the interplanetary medium; the role of ion-sound turbulence, Solar Physics, 79, 173, 1982.
- Melrose, D. B., Instabilities in Space and Laboratory Plasmas, Cambridge University Press, New York, 1986.
- Melrose, D. B., Plasma Emission: A Review, Solar Physics, 111, 89, 1987.
- Melrose, D. B., The brightness temperature of solar type III bursts, Solar Physics, 120, 369, 1989.
- Melrose, D. B., Particle Beams in the Solar Atmosphere: General Overview, Solar Physics, 130, 3, 1990.
- Melrose, D. B., G. A. Dulk, and I. H. Cairns, Clumpy Langmuir waves in type III solar radio bursts, Astron. Astrophys., 163, 229, 1986.
- Melrose, D. B., and M. V. Goldman, Microstructures in Type III Events in the Solar Wind, Solar Physics, 107, 329, 1987.
- Meyer-Vernet N., and C. Perche, Tool kit for antennae and thermal noise near the plasma frequency, J. Geophys. Res., 94, 2405, 1989.
- Muschiatti, L., Electron Beam Formation and Stability, Solar Physics, 130, 201, 1990.
- Muschiatti, L., M. V. Goldman, and D. Newman, Quenching of the Beam-Plasma Instability by Large-scale Density Fluctuations in 3 Dimensions, Solar Physics, 96, 181, 1985.
- Nicholson, D. R., Introduction to Plasma Theory, John Wiley & Sons, New York, 1983.
- Nicholson, D. R., M. V. Goldman, P. Hoyng, and J. C. Weatherall, Nonlinear Langmuir waves during type III solar radio bursts, Astrophys. J., 223, 605, 1978.
- Onsager, T. G. and R. H. Holzworth, Measurement of the electron beam mode in Earth's foreshock, J. Geophys. Res., 95, 1990.

- Papadopoulos, K., On the physics of strong turbulence for electron plasma waves, in Proceedings of the Varenna School on Plasma Physics, Pergamon Press, N. York, 355, 1978.
- Papadopoulos, K., M. L. Goldstein, and R. A. Smith, Stabilization of electron streams in type III solar radio bursts, Astrophys. J., **190**, 175, 1974.
- Reiner, M. J., K. A. Anderson, E. Roelof, T. Armstrong, G. B. Hospodarsky, J. Fainberg, R. G. Stone, L. Lanzerotti, D. A. Gurnett, M. Pick, J. L. Phillips, and R. Forsyth, Ulysses/Galileo observations of type III radio bursts and associated in-situ electrons and Langmuir waves, Space Sci. Rev., submitted.
- Robinson, P. A., Transit-time damping and the arrest of wave collapse, Phys. Fluids B, **3**, 545, 1991.
- Robinson, P. A., Clumpy Langmuir waves in Type III radio sources, Sol. Phys., **139**, 147, 1992.
- Robinson, P. A., I. H. Cairns, and D. A. Gurnett, Connection between ambient density fluctuations and clumpy Langmuir waves in the Type III radio sources, Astrophys. J., **387**, L101-L104, 1992.
- Robinson, P. A., I. H. Cairns, and A. J. Willies, Dynamics and efficiency of type III solar radio emission, Astrophys. J., **422**, 870, 1994.
- Robinson, P. A. and D. L. Newman, Strong plasma turbulence in the Earth's electron foreshock, J. Geophys. Res., **96**, 17733, 1991.
- Robinson, P. A., A. J. Willies, and I. H. Cairns, Dynamics of Langmuir and ion-sound waves in type III solar radio sources, Astrophys. J., **408**, 720, 1993.
- Rodriguez, P. and D. A. Gurnett, Correlation of bow shock plasma wave turbulence with solar wind parameters, J. Geophys. Res., **81**, 2871, 1976.
- Rodriguez, P. and D. A. Gurnett, Electrostatic and electromagnetic turbulence associated with the Earth's bow shock, J. Geophys. Res., **80**, 19, 1975.
- Scarf, F. L., R. W. Fredricks, L. A. Frank, and M. Neubauer, Nonthermal electrons and high frequency waves in the upstream solar wind, 1, Observations, J. Geophys. Res., **76**, 5162, 1971.
- Scarf, F. L., D. A. Gurnett, and W. S. Kurth, Jupiter plasma wave observations: An initial Voyager 1 overview, Science, **204**, 991, 1979.
- Scarf, F. L., D. A. Gurnett, W. S. Kurth, and R. L. Poynter, Voyager 2 plasma wave observations at Saturn, Science, **215**, 587, 1982.

- Scarf, F. L., W. W. L. Taylor, C. T. Russell, and R. C. Elphic, Pioneer Venus plasma wave observations: The solar wind-Venus interaction, J. Geophys. Res., **85**, 7599, 1980.
- Shapiro, V. D., and V. I. Shevchenko, Strong Turbulence of Plasma Oscillations, Handbook of Plasma Physics, Vol. 2, Basic Plasma Physics, ed. by A. A. Galeev and R. N. Sudan, North Holland, 124, 1984.
- Smith, R. A., M. L. Goldstein, and K. Papadopoulos, Nonlinear stability of solar type III radio bursts, I, Theory, Astrophys. J., **234**, 348, 1979.
- Sturrock, P. A., Type III solar radio bursts, in Proc. AAS-NASA Symposium on the Physics of Solar Flares, ed. W. N. Hess, NASA SP-50, Washington D.C., 357, 1964.
- Solar-Geophysical Data prompt reports, National Geophysical Data Center, Boulder, CO, Number 557-Part 1, January, 1991.
- Takakura, T. and H. Shibahashi, Dynamics of a cloud of fast electrons travelling through the plasma, Solar Physics, **46**, 323 1976.
- Thiessen, J. P., and P. K. Kellogg, Langmuir wave decay and collapse in the Jovian foreshock, Planet. Space Sci., **41**, 823, 1993.
- Tokar, R. L., and D. A. Gurnett, The volume emissivity of type III radio bursts, J. Geophys. Res., **85**, 2353, 1980.
- Tonks, L., and I. Langmuir, Oscillations in ionized gases, Phys. Rev., **33**, 195, 1929.
- Wild, J. P., Observations of the spectrum of high-intensity solar radiation at metre wavelengths, III, Isolated bursts, Aust. J. Sci. Res. Ser. A, **3**, 541, 1950.
- Williams, D. J., R. W. McEntire, S. Jaskulek, and B. Wilken, The Galileo energetic particles detector, Space Sci. Rev., **60**, 385, 1992.
- Williams, D. J., R. W. McEntire, S. M. Krimigis, E. C. Roelof, S. Jaskulek, B. Tossman, B. Wilken, W. Stüdemann, T. P. Armstrong, T. A. Fritz, L. J. Lanzerotti, and J. G. Roederer, Energetic particles at Venus: Galileo results, Science, **203**, 1525, 1991.
- Wong, A. Y., and B. H. Quon, Spatial collapse of beam-driven plasma waves, Phys. Rev. Lett, **34**, 1499, 1975.
- Zakharov, V. E., Collapse of Langmuir waves, Sov. Phys. JETP Engl. Transl., **35**, 908, 1972.

Zhang, T-L., K. Schwingenschuh, C. T. Russell, and J. G. Luhmann, Asymmetries in the location of the Venus and Mars bow shock, Geophys. Res. Lett., **18**, 127, 1991.